Cosmological signature of Primordial Black Hole (PBH) dark matter and its form in early universe

A Thesis

Submitted for the Degree of

Doctor of Philosophy

in

The Department of Physics,

Pondicherry University,

Puducherry - 605 014, India



by

Amlan Chakraborty

Indian Institute of Astrophysics,

Bengaluru - 560 034, India



February 2026

Cosmological signature of Primordial Black Hole (PBH) dark matter and its form in early universe

Amlan Chakraborty
Indian Institute of Astrophysics



Indian Institute of Astrophysics
Bengaluru - 560 034, India

Thesis title	:	**Cosmological signature of Primordial Black Hole (PBH) dark matter and its form in early universe**
Author	:	**Amlan Chakraborty**
Address	:	Indian Institute of Astrophysics II Block, Koramangala Bengaluru - 560 034, India
Email	:	amlan.chakraborty@iiap.res.in; amlanchakra@gmail.com
Supervisor	:	**Prof. Subinoy Das**
Address	:	Indian Institute of Astrophysics II Block, Koramangala Bengaluru - 560 034, India
Email	:	subinoy@iiap.res.in

Declaration of Authorship

I hereby declare that the research contained in this thesis is the result of the investigations carried out by me at the Indian Institute of Astrophysics, Bengaluru, under the supervision of **Prof. Subinoy Das**. This work has not been submitted for awarding a degree or any other qualification either in this university or any other institution.

Amlan Chakraborty
PhD Student, IIA,
Bengaluru-560034, India

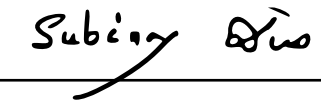
Signed: 

Date: 16.02.2026

Certificate

This is to certify that the thesis titled **"Cosmological signature of Primordial Black Hole (PBH) dark matter and its form in early universe"** submitted to the Pondicherry University by Mr. Amlan Chakraborty for the award of the degree of Doctor of Philosophy, is based on the results of the investigations carried out by him under my supervision and guidance, at the Indian Institute of Astrophysics. This thesis has not been submitted to any other university or institute for the award of any degree, diploma, fellowship, etc.

Prof. Subinoy Das
Thesis Supervisor,
Indian Institute of Astrophysics,
Bengaluru-560034, India

Signed: 

Date: 16.02.2026

List of Publications

A). Publications included in this thesis

1. **Formation and Abundance of Late-forming Primordial Black Holes as Dark Matter** ; **Amlan Chakraborty**, Prolay K. Chanda, Kanhaiya Lal Pandey, Subinoy Das *The Astrophysical Journal* **932**(2), 119 (2022), DOI:10.3847/1538-4357/ac6ddd

2. **Cosmological constraints on mass-varying dark matter** ; **Amlan Chakraborty**, Anirban Das, Subinoy Das, Shiv K. Sethi, *Physical Review D* **111**(6), 063515 (2025), DOI:10.1103/PhysRevD.111.063515

3. **DESI results: hint towards coupled dark matter and dark energy** ; **Amlan Chakraborty**, Prolay Chanda, Subinoy Das, Koushik Dutta, *Journal of Cosmology and Astroparticle Physics (JCAP)* **2025**(11), 047 (2025), DOI: 10.1088/1475-7516/2025/11/047

4. **Hint of dark matter-dark energy interaction in DESI DR2 and current cosmological dataset?** ; **Amlan Chakraborty**, Tulip Ray, Subinoy Das, Arka Banerjee, Vidhya Ganesan, *The Astrophysical Journal* **998**(1), 83 (2026), DOI:10.3847/1538-4357/ae2ff8

B). Other contributed publications [Not part of this thesis]

1. **The prior dependence of the DESI results** ; Vrund Patel, **Amlan Chakraborty**, Luca Amendola, *Under review at Physics Letters B*, arXiv: 2407.06586

2. **Neutrino mass constraints in the context of 4-parameter dark energy equation of state and DESI DR2 observations** ; Gowri S. Nair, **Amlan Chakraborty**, Luca Amendola, Subinoy Das, *Under review at Journal of Cosmology and Astroparticle Physics (JCAP)*, arXiv:2512.08752

List of other non-refereed publications, such as White Papers etc. can be found in this iNSPIRE-HEP public library: https://inspirehep.net/authors/2771617

Presentations at Conferences/Schools/Colloquia

1. **Participant** in *Rethinking Cosmology* conference, organized at *Raman Research Institute (RRI)* in *December 2025*

2. **Contributed student talk** given on "***A New Mechanism for Dynamical Dark Energy to Explain DESI Observations***" in *The Dark Universe, Les Houches Summer School*, organized at *Ecole de Physique des Houches* in *July 2025*

3. **Colloquium talk** given on "***A New Mechanism for Dynamical Dark Energy to Explain DESI Observations***", organized at *Universität Heidelberg, RWTH, Aachen, University of Geneva* in *June-July 2025*

4. **Invited talk** given on "***Can Cosmology Allow a Mass-Varying Dark Matter?***" in *21st Century Cosmology: Tensions, Anomalies and New Physics*, conference organized at *Ashoka University* in *August 2024*

5. **Colloquium talk** given on "***Can Cosmology Allow a Mass-Varying Dark Matter?***", organized at *Universität Heidelberg* in *June 2024*

6. **Colloquium talk** given on "***Formation and Abundance of Late-Forming Primordial Black Holes as Dark Matter***", organized at *Laboratoire Univers et Particules de Montpellier (LUPM), Montpellier* in *May 2024*

7. **Contributed talk** given on "***Can Cosmology Allow a Mass-Varying Dark Matter?***" in *Neighbourhood Cosmology Meeting (NCM)*, organized at *Raman Research Institute (RRI)* in *November 2023*

8. **Contributed talk** given on "***Formation and Abundance of Late-Forming Primordial Black Holes as Dark Matter***" in *Less Travelled Path in the Dark Universe*, conference organized at *International Centre for Theoretical Sciences (ICTS)* in *March 2023*

9. **Poster** presented on " ***Formation and Abundance of Late-Forming Primordial Black Holes as Dark Matter***", in the *In-House Symposium* meeting, organized at *Indian Institute of Astrophysics (IIA)* in *March 2023.*

10. **Contributed talk** given on "***Formation and Abundance of Late-Forming Primordial Black Holes as Dark Matter***" in *32nd Indian Association for General Relativity and Gravitation (IAGRG) Meeting*, conference organized at *Indian Institute of Science Education and Research (IISER), Kolkata* in *December 2022*

11. **Invited colloquium talk** given on "***Formation and Abundance of Late-Forming Primordial Black Holes as Dark Matter***" in *IPM, Tehran Weekly Seminar*, organized virtually in *June 2022*

Attended Schools/Workshops

1. **Participant** in *The Dark Universe, Les Houches Summer School* organized at *Ecole de Physique des Houches* in *July 7 - August 2, 2025*

2. **Participant** in *3rd IAGRG School on Gravitation and Cosmology* organized at *International Centre for Theoretical Sciences (ICTS)* in *October 14 - 25, 2024*

3. **Participant** in *Largest Cosmological Surveys and Big Data Science Workshop* organized at *International Centre for Theoretical Sciences (ICTS)* in *May 9 - 12, 2023*

4. **Participant** in *Physics of the Early Universe* school, attended virtually in *January 3-12, 2022*

5. **Participant** in *Gravitational Wave Probes of Physics Beyond the Standard Model* workshop, held virtually in *July 12-16 2021*

Acknowledgements

The journey that culminates in this thesis did not begin with equations or data, but with curiosity—an enduring desire to understand the Universe at its most fundamental level. Cosmology, for me, has never been merely a scientific discipline; it has been a lens through which wonder, doubt, and perseverance coexist. This thesis is therefore not only a record of scientific work, but also a reflection of the people and experiences that shaped my path toward becoming a researcher.

First and foremost, I express my deepest gratitude to my PhD supervisor, *Prof. Subinoy Das*. At a time when opportunities were scarce and the odds seemed stacked against me, he gave me the chance to pursue research in cosmology and trusted me with the freedom to explore it fully. He consistently encouraged independent thinking and gave me complete freedom to collaborate with researchers of my choice, which greatly broadened my scientific perspective. His unwavering support, patience, and belief in my abilities have been the cornerstone of my PhD journey. From him, I learned not only how to formulate meaningful scientific problems, but also how to think carefully about their physical foundations before delving into detailed calculations. He also taught me how to communicate science effectively—how to present my work clearly and confidently, and how to speak before an audience with composure. Beyond research, I always cherished our long discussions, which often extended beyond physics to life and career choices. His emphasis on clarity of thought, physical intuition, and intellectual honesty has left a lasting imprint on how I approach science, and these lessons will continue to guide me throughout my career.

I am sincerely grateful to my collaborators *Prof. Arka Banerjee* and *Prof. Shiv K. Sethi*. Every discussion with them was a learning experience. Their sharp insights, breadth of understanding, and ability to view problems from first principles

consistently inspired me to aspire to their level of scientific maturity. Interacting with them shaped my thinking in ways that extend far beyond the scope of this thesis.

This thesis would not have been possible without the guidance and support of my close collaborators and mentors, *Prof. Kanhaiya Lal Pandey, Prof. Anirban Das, and Dr. Prolay K. Chanda*. During my first research project, *Kanhaiya* was a postdoctoral researcher at IIA and mentored me with exceptional dedication. He guided me through every step of executing a research problem properly, introduced me to high-performance computing clusters, and clarified numerous conceptual questions in fundamental cosmology. I was always inspired by his analytical rigor, careful reasoning, and resilience in the face of repeated setbacks—qualities that I now believe define an excellent researcher.

Anirban da played a crucial role in shaping my academic writing and presentation skills. His advice on structuring papers, refining arguments, and producing publication-quality figures significantly improved my scientific communication and confidence as a researcher.

The successful completion of the latter half of my PhD owes an enormous debt to *Prolay da*. His profound command over both cosmology and particle physics, combined with his calm and methodical approach to problem-solving, provided me with stability during some of the most challenging phases of my research. His suggestions often proved to be pivotal turning points in my work, and his composure in navigating difficulties taught me how to endure uncertainty with clarity and focus.

I gratefully acknowledge *DST* and *DAAD* for supporting my research visits to *Prof. Luca Amendola's* group at the *University of Heidelberg* during my PhD tenure. Traveling abroad for the first time was an overwhelming experience, but

Luca's warmth and hospitality immediately made me feel at home. Working with him and his group—*Ziyang, Vrund, Tijark, and Angela*—was intellectually enriching and personally memorable. *Luca* and his wife *Manuela* welcomed me with incredible kindness and showed me the beauty of Heidelberg, making those months among the most cherished memories of my life. I also consider myself fortunate to have witnessed the rare spectacle of the Aurora Borealis during this period—an experience I will never forget.

I thank *ICTS, Bangalore*, which became a second home during my PhD due to the many schools and conferences hosted there. ICTS provided an environment where long conversations, new ideas, and meaningful connections flourished. I am particularly grateful to *Prof. David Marsh (Doddy)*; spending time with him in Bangalore, discussing science and life, left a deep impression on me. His perspective on doing meaningful research influenced my approach in subtle but enduring ways.

Among all the schools I attended, *Les Houches* remains unparalleled. Living in the Alpine valley for a month, immersed in intense discussions with fellow cosmologists, was one of the highlights of my research life. The challenging problems posed by lecturers, the collaborative spirit among participants, and the shared hikes—during which I saw the Milky Way for the first time—made this experience unforgettable. I am especially thankful to *Prof. Florent Leclercq* and *Prof. Guilhem Lavaux* for organizing and leading the hikes. I also cherish the friendships formed there with *Rahul, Amrita, Anoma, Aritra, Anupama, Utkarsh, Erik, Daniel, Shambel, Ashutosh, Pierre, Murali, and Tejas*, and I hope these bonds lead to many future collaborations.

At IIA, I am grateful to my batchmates *Sipra, Soumyaranjan, Amrutha, Judhajeet, Anisha, and Neeraj* for their companionship and support, and to my seniors *Fazlu, Swastik, and Siorre* for their guidance. I am particularly thankful to *Ravi Kumar*

Sharma, whose selfless help made him my go-to person for almost every technical challenge. His guidance in learning CLASS and MontePython was invaluable. I also enjoyed mentoring junior students and interns, especially *Bhaskar*, with whom I shared many long discussions and continue to stay connected.

My academic foundation was built long before my PhD. I am deeply grateful for my time at *Scottish Church College* and especially for my postgraduate years at *JNU*, without which my dream of pursuing cosmology would never have materialized. I owe a profound debt to *Prof. Debashis Ghoshal* and *Prof. Prasenjit Sen* in JNU. *Prof. Ghoshal's* classes were foundational and inspiring; his analytical clarity and mastery of fundamentals taught me how to truly understand physics. He was the one who encouraged me to pursue cosmology. *Prof. Sen* taught me how to be a resilient researcher and how to conduct world-class research even with limited resources—lessons that became essential throughout my career. I cherish my postgraduate life at *JNU*, from my first hostel experience to long night walks across campus. I am grateful to my friends *Amit, Debamalya, Kavind, Alfayet, Souvik, Ritam, and Palash,* who remain an integral part of my life.

I am also fortunate to have had inspiring teachers during my undergraduate years, particularly *Prof. Suman Mukhopadhaya* and *Prof. Rajsekhar Bhattacharya*, whose teaching beautifully balanced physical intuition and problem-solving skills. My undergraduate friends—*Sumit, Arijit, Pradipta, Avik, Tamal, Ritesh, and Aritra*—challenged me intellectually and motivated me to become a better physicist.

My earliest inspiration came from my school years. I am deeply grateful to *Mr. Arun Paul*, my first physics teacher, whose unorthodox teaching style and friendly nature ignited my curiosity and love for physics. I was fortunate to have *Mr. Jayanta Bhattacharya and Mr. Ajay Dhar* as mentors; *Jayanta sir* nurtured my problem-solving skills, while *Ajay sir* emphasized developing physical intuition before mathematical formalism. Their influence played a decisive role in shaping

my path toward research. I also thank my school teachers *Subhra Bhattacharya, Prakash Bhattacharya, Pranab Kar, and Sujit Sasmal*, and I remain eternally grateful to *Mr. Kamal Adhikary*, whose teaching of mathematics from my elementary years laid the foundation for my journey in physics.

Finally, I owe everything to my family. My parents, *Mita Chakraborty and Sajal Kumar Chakraborty*, have been my greatest pillars of strength. My mother held our family together with unwavering love and sacrifices. She was the first person with whom I shared my desire to become a physicist during my school days. My father has always supported me silently yet steadfastly, ensuring that I never worried about financial uncertainty, even after his retirement. His wisdom during times of crisis helped me overcome countless challenges. I am deeply grateful to my uncle *Krishnenendu Chakraborty*, who nurtured my curiosity through everyday questions and practical problem-solving. His habit of asking why things work the way they do and his intuitive approach to applied physics played a crucial role in developing my physical intuition, particularly in classical mechanics. I am also inspired by my cousin *Saptarshi Chakraborty*, whose mathematical rigor and perseverance I have always admired. I thank my extended family—*Dadu, Mammam, Mamuni, Jethu, Bunty didi, Babui, my "colorful" mashis,* and my cousins *Sumitabha Bhowmick, Suvoprasad Chakraborty, Sourajeet Chakraborty, and Sudeshna Thakurta*—for their constant love and encouragement.

To everyone whose name I may have inadvertently missed, I remain deeply grateful. I consider myself incredibly fortunate to have been surrounded by so many people who helped me discover and pursue my first love—Physics. I am thankful that I could follow my passion, and I sincerely hope that these bonds endure for a lifetime.

– Amlan Chakraborty

★❤

***To my dear* parents, family,**

&

teachers

—who shaped my thinking, perseverance, and sense of wonder.

Abstract

The nature of the dark sector remains one of the central open problems in modern cosmology. While the standard ΛCDM model provides an excellent description of a wide range of observations, recent high-precision data increasingly motivate extensions in which the properties of dark matter and dark energy deviate from their minimal assumptions. In this thesis, we investigate a class of scenarios in which scalar–fermion interactions modify both the early-time behavior of dark matter and the late-time dynamics of dark energy, and we confront these models with current cosmological data using Bayesian inference.

We first examine whether the assumption that dark matter was cold and non-relativistic prior to recombination is directly required by existing observations. In a phenomenological mass-varying dark matter (MVDM) framework, we allow the dark matter mass to undergo a rapid transition from zero to a finite value at high redshift. The resulting free-streaming suppression of small-scale power produces characteristic phase shifts and power suppression in the CMB angular power spectra and reduces the late-time clustering amplitude. Using Planck 2018 CMB data supplemented by BAO, supernovae, and weak-lensing priors, we derive a lower bound on the transition redshift and find a mild reduction in S_8 relative to ΛCDM. Including high-multipole measurements from ACT significantly improves the constraints and yields a mild preference for the MVDM model over ΛCDM. We find a lower bound $\log_{10} z_t > 4.55$ and a mild preference for an eV-scale dark matter mass, with $M \simeq 20$–$40\,\mathrm{eV}$ depending on the dataset combination. The inclusion of KIDS1000+BOSS+2dfLenS weak-lensing priors further reduces the inferred value of S_8, demonstrating that early-time departures from cold dark matter can partially alleviate the clustering tension.

Building on this phenomenological framework, we then construct a concrete microscopic realization in which a Yukawa-type scalar–fermion interaction leads to the late formation of primordial black holes (PBHs). In this scenario, dark matter becomes non-relativistic at $z_T \sim 10^6$, triggering an exponential growth of perturbations in the radiation-dominated era due to a force stronger than gravity. This mechanism produces early dense halos that cool through scalar radiation and collapse into PBHs. We derive a non-monochromatic PBH mass function and show that it is narrow, with a peak in the sublunar window $M_{\rm BH} \sim 10^{-16}$–$10^{-14}\, M_\odot$ for $z_T \simeq 10^6$. We find that these PBHs can constitute nearly the entire dark matter abundance, $f(M) \simeq 1$, while remaining consistent with current observational constraints. We further demonstrate the existence of a temporary static configuration in which an attractive scalar force balances Fermi pressure, and show that the resulting PBHs are expected to possess significant spin, providing a potential observational signature for future gravitational-wave experiments.

In the second part of the thesis, we explore the implications of similar Yukawa-type interactions for late-time cosmic acceleration in light of recent DESI observations. We first study an interacting quintessence scenario in which the scalar field retains non-zero kinetic energy at the present epoch. The interaction modifies the relation between the microscopic equation of state of the field and the effective equation of state inferred by an observer, allowing the effective equation of state $w_{\rm eff}$ to cross the phantom divide while maintaining $w_\phi > -1$ at all times. Solving the modified Klein–Gordon equation for exponential and polynomial self-interaction potentials, we show that $w_{\rm eff}$ crosses -1 around $z \sim 0.5$, transitions from $w_{\rm eff} < -1$ in the past to $w_{\rm eff} > -1$ today, and can reach present-day values as large as $w_{\rm eff} \sim -0.8$. We find that the model remains consistent within the 2σ DESI confidence regions for a wide range of parameters, demonstrating that interacting quintessence with finite kinetic energy provides a viable explanation of the DESI-inferred dark energy evolution without introducing phantom instabilities.

Finally, we perform a full Markov Chain Monte Carlo analysis of the chameleon dark energy model in which the scalar field oscillates around the evolving minimum of an effective potential and settles with vanishing velocity at the present epoch. Using combinations of Planck, SDSS BAO, DESI DR2 BAO, Pantheon+, and SH_0ES data, we obtain fully constrained posteriors for the dark-sector coupling without invoking any sign-switching mechanism or additional exotic assumptions. Dataset combinations including DESI DR2 BAO or SH_0ES show a mild preference for a non-zero interaction, with $\beta = 0.256^{+0.092}_{-0.063}$ for Planck+DESI DR2 BAO+Pantheon+ and $\beta = 0.335^{+0.082}_{-0.054}$ for Planck+SDSS BAO+Pantheon+SH_0ES. For these combinations, we obtain $\Delta\chi^2_{\rm min} = -4.75, -6.41$ and $\Delta{\rm AIC} = -0.75, -2.41$, corresponding to weak-to-positive statistical evidence relative to ΛCDM. Although the present-day equation of state asymptotically approaches $w_{\rm eff} \to -1$, the scalar dynamics exhibit phantom crossing near $z \sim 0.5$, in qualitative agreement with the DESI reconstruction.

Taken together, the four investigations presented in this thesis establish a unified picture in which scalar–fermion interactions influence both the early thermal history of dark matter and the late-time dynamics of dark energy. The same physical mechanism is shown to generate early departures from cold dark matter, produce a viable primordial black hole population, and induce an effective phantom crossing in the dark energy sector. This unified perspective suggests that early- and late-time cosmological anomalies may share a common microscopic origin within the dark sector, and provides a concrete framework for testing this possibility with forthcoming cosmological surveys.

Contents

Abstract i

List of Figures vii

List of Tables xi

1 Introduction 1
- 1.1 Basic Cosmology . . . 2
- 1.2 Horizons and Distances in Cosmology . . . 7
- 1.3 Thermal History of the Universe . . . 11
- 1.4 Cosmological Observables . . . 16
- 1.5 The Standard Model of Cosmology . . . 21
- 1.6 The S_8 Tension . . . 24
- 1.7 Motivation for Physics Beyond the Standard Cosmological Model . 25
- 1.8 Dark Matter: Observational Evidence and Basic Properties . . . 26
- 1.9 Dark Matter Candidates . . . 31
- 1.10 Primordial Black Holes as Dark Matter Candidates . . . 36
- 1.11 Dark Energy: Observational Motivation and Theoretical Overview . 43
- 1.12 Outlines . . . 55

2 Statistical Methods 57
- 2.1 Introduction . . . 57
- 2.2 Probability and the Frequentist Approach . . . 59
- 2.3 Bayesian Probability and Bayes' Theorem . . . 61
- 2.4 Prior, Likelihood, Posterior and Evidence . . . 62
- 2.5 Goodness of fit, χ^2, confidence regions, and marginalisation . . . 64
- 2.6 Monte Carlo Methods and Markov Chain Monte Carlo . . . 67
- 2.7 Model comparison and information criteria . . . 78
- 2.8 Application in Cosmology . . . 79

3 Cosmological constraints on mass-varying dark matter 81
- 3.1 Introduction . . . 81

3.2 Background Density Evolution and Perturbations 84
3.3 Method 90
3.4 Results 91
3.5 Summary 101
3.6 Tables of χ^2 104

4 Formation and Abundance of *Late Forming* Primordial Black Holes as Dark Matter 105
4.1 Introduction 105
4.2 Late Forming PBH: The mechanism 108
4.3 Static Structure of primordial Halo 112
4.4 PBH mass function and PBH DM abundance 116
4.5 Summary 122
4.6 Details of derivations 124

5 DESI results: Hint towards coupled dark matter and dark energy 127
5.1 Introduction 127
5.2 Model Set Up 130
5.3 Perturbations for dark matter-dark energy fluid 136
5.4 Model Implementation 139
5.5 Results 142
5.6 Summary 146

6 Hint of dark matter-dark energy interaction in DESI DR2 and current cosmological dataset? 149
6.1 The Chameleon Model 152
6.2 Model Implementation: Shooting Algorithm 160
6.3 Method 162
6.4 Results 164
6.5 Summary 174

7 Summary and Future Work 177
7.1 Summary 177
7.2 Future Work 180

Bibliography 183

List of Figures

1.1 Planck 2018 Temperature anisotropy power spectrum with Y-axis $D_\ell^{TT} = \frac{\ell(\ell+1)c_\ell^{TT}}{2\pi}$. THe top panel shows the theoretically predicted power spectra for ΛCDM model on top of measured values and the bottom panel shows the corresponding residuals. It has been taken from Aghanim et al. (2020) 17

1.2 Two-point correlation function of Bright Galaxy Sample (BGS) from DESI is shown here. The upper and lower panel plots the monopole and quadrupole moments of the correlation function, respectively. The bump at the higher s value corresponds to the BAO scale. Figure credit: Abdul Karim et al. (2025) 19

1.3 In the left panel, a schematic diagram of a spiral galaxy embedded in a dark matter halo is shown. The centre plots the density profiles of different components of a galaxy, with the NFW profile chosen for dark matter. In the right panel, the rotation velocity is plotted as a function of distance for different components. The figure is taken from Balazs et al. (2026) 27

1.4 Left panel shows an image of the Bullet cluster overlapped with an X-ray image (in red) from Baryons and gravitational lensing from dark matter (in blue). Right panel shows a schematic diagram of observed Bullet cluster in both with and without dark matter in the universe. The right panel figure is taken from Balazs et al. (2026) respectively. 28

1.5 An Illustration of the large range of possible dark matter masses is shown here, along with different candidates at different mass scales. The figure is obtained from Balazs et al. (2026) 29

1.6 Various possible dark matter candidates shown schematically. Credit: Bertone & Tait (2018) 31

1.7 Current bounds on WIMPs detection. The shaded regions are excluded. Only a small window is left. The yellow shaded area refers to the Neutrino floor, where the detection of WIMPs is indistinguishable from that of neutrinos. The figure is obtained from Baudis (2014). 33

1.8 Left panel shows the standard formation mechanism of PBH through a peak in standard scale invariant inflationary power spectra (credit: Solbi & Karami (2021)), and the right panel shows a drop in pressure during QCD phase transition through a drop in equation of state parameter w (credit: Byrnes et al. (2018)). 38
1.9 State-of-the-art constraints on PBH being dark matter, taken from Carr et al. (2021). The shaded regions exclude PBH from being a dark matter candidate. Only a small window remains open for PBH to contribute to the total dark matter density. 42
1.10 Obtained from Suzuki et al. (2012), the left panel shows the confidence region of Ω_Λ and Ω_m for ΛCDM model for CMB, BAO and SNe-Ia datsets. The right panel shows the confidence region for wCDM model where it shows that the data prefers cosmological constant, i.e. $w = -1$ as dark energy. 44
1.11 The evolution of equation of state parameter for quintessence dark energy field is shown here. Left panel shows freezing model and right panel shows the thawing model, which is obtained from Tsujikawa (2013a). 47
1.12 The upper panel depicts evolution of dark energy equation of state parameter reconstructed from MCMC analysis for w_0w_aCDM model using CMB, DESI, and Union 3 dataset. The lower panel shows the evolution of dark energy density normalized to its present-day energy density $f_{\rm DE} = \frac{\rho_{\rm DE}(z)}{\rho^0_{\rm DE}}$. The image is taken from Lodha et al. (2025a). 53

3.1 Variation of mass of MVDM particle is plotted for mass $M = 25\,\text{eV}$ for a transitional redshift $z_t = 10^5$. 84
3.2 Evolution of background energy density with redshifts is plotted for mass $M = 100\,\text{eV}$ for a transitional redshift $z_t = 10^5$. 85
3.3 The relative change in the CMB TT and EE power spectra with respect to ΛCDM is plotted for mass $M = 25,\ 50$ and $100\,\text{eV}$ for a transitional redshift $z_t = 10^5$. 87
3.4 Relative change in matter power spectra with respect to ΛCDM is plotted for mass $M = 25,\ 50$ and $100\,\text{eV}$ for a transitional redshift $z_t = 10^5$. 88
3.5 Reconstructed 2D and 1D marginalized posterior distributions of $\log_{10} z_t, M(\,\text{eV}), \Omega_\text{m}, S_8$ with 68% and 95% confidence level. The weak lensing measurement of S_8 is shown as grey bands (68% and 95%). Here we considered Pantheon+ dataset for "SN-Ia". 92
3.6 The 2D and 1D marginalized posterior distributions of $\log_{10} z_t, M, \Omega_\text{m}, S_8$ with 68% and 95% confidence level for three different S_8 priors as mentioned in Sec. 3.3. 96
3.7 Reconstructed 2D marginalized posterior distributions of Ω_m and S_8 with 68% and 95% confidence levels. 97

3.8 Residuals of the CMB TT, EE (top panel) and matter (bottom panel) power spectra with respect to ΛCDM in the best fit MVDM model for Planck, Planck+S_8, ACT, ACT+S_8 and Planck+BAO+SN-Ia data set. Here we considered Pantheon+ dataset for "SN-Ia". For better visualisation, the observed Planck and ACT CMB data points in the top panels have been rebinned into wider multipole intervals. This rebinning is used only for visualisation and does not affect the likelihood analysis or parameter constraints. 99

4.1 $|\delta|$ vs scale factor a for a typical wave number which is inside the Compton scale of the scalar field around the PBH formation redshift $z_T = 10^6$. We can see that the growth of the $|\delta_\Phi|$ is exponential which makes this mode go non-linear and finally collapse to form PBHs. 107
4.2 The contours above delineate different PBH masses in the solar units as a function of the $T - m_\phi$ parameter space, derived using eq. (4.5) where T is the temperature of the Universe at epoch of formation of PBH and m_ϕ is the mass of the scalar field mediating the fifth force. 112
4.3 Schematic representation of PBH formation mechanism discussed in this chapter. 113
4.4 In the above, we demonstrate the static profile, which is obtained by solving eqns. (4.10), and, (4.9). The plot at the left shows the static profile for the scalar field, ϕ, and the plot at the right delineates the density profile, ρ, of the resulted dark matter halo. As discussed in the main text, this halo may later collapse due to cooling through scalar radiation and eventually form PBH (Flores & Kusenko 2021a). 115
4.5 Schematic representation of multiple PBH formation in a single horizon 120
4.6 Plot of the late forming PBH mass function, $f(\tilde{M})$, shown in cyan, suggests that the PBH density can attribute to the entire dark matter density in the universe. PBH mass function shown in this figure is for $f_{\max}(\tilde{M}) = 1$ (ie., $f_{\rm PBH} \approx 1$) for redshift of formation $z_T \sim 10^6$. 121

5.1 Schematic plot of $V_{\rm eff}(\phi) = V(\phi) + \rho_{\rm DM} f(\phi)$. 133
5.2 A typical dynamics of ϕ and $\phi' = \frac{d\phi}{da}$ with the scale factor for the polynomial self-interaction potential is shown here with different initial positions of the field. The left (right) figure depicts the dynamics for a field that starts on the right (left) side of the effective minimum for $\alpha = 0.14$ and $\beta = 0.45$, with initial field value $\phi_{\rm initial} = 0.15 M_{\rm pl}(0.05 M_{\rm pl})$ and final value $\phi_0 = 0.28 M_{\rm pl}(0.30 M_{\rm pl})$. Here $M_{\rm pl}$ is the reduced Planck mass. 141

5.3 Fitting of $w(z)$ for polynomial self-interaction potential within the 2-σ contours of DESI (light purple) and DESI+Union3+Planck (light grey). The initial value of phi, $\phi_{\rm in}$ is considered as $0.15M_{\rm pl}$(top-left), $0.15M_{\rm pl}$ (top-right), $0.15M_{\rm pl}$ (bottom-left) and $0.21M_{\rm pl}$ (bottom-right). 143
5.4 Fitting of $w(z)$ for exponential self-interaction potential within the 2-σ contours of DESI (light purple) and DESI+Union3+Planck (light gray). The initial value of phi, $\phi_{\rm in}$ is considered as $0.08M_{\rm pl}$(top-left), $0.05M_{\rm pl}$ (top-right), $0.05M_{\rm pl}$ (bottom-left) and $0.025M_{\rm pl}$ (bottom-right). 144

6.1 Schematic diagram of effective potential with evolving minima . . . 153
6.2 Two-dimensional marginalized posterior distributions of the model parameters ($\omega_{\rm dm}$, H_0, α, β, Ω_m, and S_8) obtained from our MCMC analysis with contours having 68% and 95% C.L. Different colors represent different dataset combinations: Planck-only, Planck+SDSS BAO, Planck+SDSS BAO+Pantheon+, Planck+DESI DR2 BAO+Pantheon+, and Planck+SDSS BAO+Pantheon+ + SH_0ES. 165
6.3 The scalar field dynamics with redshift is plotted here for best-fit values obtained from MCMC analysis for different combinations of datasets. The left panel shows the field value normalized to its initial value at the initial redshift, and the corresponding initial value is provided in the legend box. The right panel shows the corresponding dynamics of field velocity for the same set of best-fit values. Here $\dot{\phi}$ means derivative with respect to conformal time. . . 171
6.4 The effective dark energy equation of state for the chameleon model is plotted with redshift for best-fit values obtained from MCMC analysis for different combinations of datasets. It highlights a phantom crossing at low redshift. 172

List of Tables

3.1 Obtained parameter values with mean (best-fit) $\pm 1\sigma$ error in the ΛCDM and MVDM model from the analysis of Planck Aghanim et al. (2020) and Planck+S_8Heymans *et al.* (2021) data. Lower limits are obtained at half of the peak posterior value of the respective parameter. 93

3.2 Obtained parameter values with mean (best-fit) $\pm 1\sigma$ error in the ΛCDM and MVDM model from the analysis of ACT Aiola et al. (2020); Louis et al. (2017) and ACT+S_8Heymans *et al.* (2021) data. Lower limits are obtained at half of the peak posterior value of the respective parameter. 94

3.3 Obtained parameter values with mean (best-fit) $\pm 1\sigma$ error in the ΛCDM and MVDM model from the analysis of combined Planck + BAO + Pantheon+ dataset. Lower limits are obtained at half of the peak posterior value of the respective parameter. 95

3.4 Obtained parameter values with mean (best-fit) $\pm 1\sigma$ error in the MVDM model from the analysis of Planck+S_8^+ Amon et al. (2022), Planck+S_8Heymans *et al.* (2021) and Planck+S_8^- Asgari, Marika et al. (2021) data. Lower limits are obtained at half of the peak posterior value of the respective parameter. 98

3.5 Comparison of $\Delta\chi^2_{\rm min}$ and ΔAIC per experiment for MVDM and ΛCDM models. 101

3.6 Best-fit $\chi^2_{\rm min}$ per experiment (and total) for both the model 104

3.7 Best-fit $\chi^2_{\rm min}$ per experiment (and total) for both the model 104

6.1 Prior ranges considered for MCMC analysis for the cosmological parameters of Chameleon and ΛCDM model. 163

6.2 The mean (bestfit) $\pm 1\sigma$ error for the cosmological parameters constrained with the datasets Planck and Planck + SDSS BAO for the ΛCDM model and Chameleon model are shown in this table. The 1σ error is obtained at 68% confidence level. The corresponding χ^2_{min} and $\Delta\chi^2_{min}$ values are also shown. Upper bounds are obtained from the marginalized distribution such that 95% of the samples lie below the quoted value, corresponding to the 95% credible level. . . 167

6.3 Obtained parameter values with mean (bestfit) $\pm 1\sigma$ error using the datasets Planck + SDSS BAO + Pantheon Plus and Planck + SDSS BAO + Pantheon Plus + SH_0ES for the ΛCDM model and Chameleon model are shown in this table. The 1σ error is obtained at 68% confidence level. The corresponding χ^2_{min} and $\Delta\chi^2_{min}$ values are also shown. Upper bounds are obtained from the marginalized distribution such that 95% of the samples lie below the quoted value, corresponding to the 95% credible level. 168

6.4 Obtained parameter values with mean (bestfit) $\pm 1\sigma$ error using with the datasets Planck + DESI DR2 BAO + Pantheon Plus for the ΛCDM model and Chameleon model are shown in this table. The 1σ error is obtained at 68% confidence level. The corresponding χ^2_{min} and $\Delta\chi^2_{min}$ values are also shown. Upper bounds are obtained from the marginalized distribution such that 95% of the samples lie below the quoted value, corresponding to the 95% credible level. . . 170

6.5 Comparison of $\Delta\chi^2_{\rm min}$ and ΔAIC per experiment for Chameleon and ΛCDM models. 173

Chapter 1

Introduction

Modern cosmology seeks to provide a quantitative and self-consistent description of the origin, composition, and evolution of the Universe across an enormous range of physical scales and cosmic times. Over the past few decades, a remarkable concordance has emerged between theoretical predictions based on general relativity and a diverse set of high-precision observations, including cosmic microwave background, galaxy surveys, distance measurements using standard candles and rulers, etc. These developments have established a minimal cosmological framework, the so-called ΛCDM model, which successfully accounts for a wide variety of observational phenomena with a small set of parameters.

Despite its empirical success, the standard cosmological model rests on the existence of two dominant components whose physical nature remains unknown: dark matter and dark energy. Together they make up more than 95% of the present energy budget of the Universe, yet neither has been directly detected in laboratory experiments. This conceptual gap has motivated an extensive exploration of extensions of the minimal model, involving new particle candidates, modified gravitational dynamics, and non-trivial interactions within the dark sector.

The aim of this thesis is to investigate several such extensions, with particular emphasis on non-standard dark matter scenarios, interacting dark energy models, and primordial black holes as possible dark matter candidates. Before introducing these specific models, it is useful to summarize the basic theoretical framework of homogeneous and isotropic cosmology, the key observables that constrain it, and the standard picture of the cosmic constituents and their evolution. This chapter provides a brief overview of the basics of modern cosmology, the observational and theoretical motivations that underlie the studies presented in the subsequent chapters.

1.1 Basic Cosmology

Homogeneity, Isotropy, and the FLRW Metric

The observed Universe on large scales is spatially homogeneous and isotropic. This is known as the "Copernican Principle". These symmetries imply that the space-time metric can be written in the most generalised way, i.e., Friedmann–Lemaître–Robertson–Walker (FLRW) form Robertson (1935); Walker (1937); Lemaître (1931); Friedmann (1924),

$$ds^2 = -dt^2 + a^2(t)\left[\frac{dr^2}{1-kr^2} + r^2\left(d\theta^2 + \sin^2\theta\, d\phi^2\right)\right], \tag{1.1}$$

$a(t)$ represents the scale factor; $k = 0, \pm 1$ denotes the spatial curvature corresponding to flat, closed, and open, respectively.

Although the general FLRW metric is presented here for flat, open, and closed spatial geometries, all cosmological analyses in this thesis assume a spatially flat Universe, $k = 0$. We therefore adopt the conventional normalisation of the scale

factor today $a_0 = 1$ throughout the remainder of the thesis. The expressions for $k = \pm 1$ are included only for completeness and are not used in the subsequent calculations.

The evolution of the universe is governed by Einstein's field equations Einstein (1916); Carroll (2019),

$$G_{\mu\nu} = 8\pi G\, T_{\mu\nu}, \tag{1.2}$$

where $T_{\mu\nu}$ is the energy–momentum tensor of the cosmic fluid. For perfect fluid, the Einstein equations reduce to the two Friedmann equations,

$$H^2 \equiv \left(\frac{\dot{a}}{a}\right)^2 = \frac{8\pi G}{3}\rho - \frac{k}{a^2}, \tag{1.3}$$

$$\frac{\ddot{a}}{a} = -\frac{4\pi G}{3}\left(\rho + 3p\right), \tag{1.4}$$

where ρ is the energy density, p is the pressure of the fluid; $H(t)$ is the Hubble parameter.

Critical Density and Density Parameters

It is convenient to define the critical energy density required for spatially flat Universe,

$$\rho_{\rm c}(t) \equiv \frac{3H^2(t)}{8\pi G}. \tag{1.5}$$

The fractional energy density of each component i is then given by

$$\Omega_i(t) \equiv \frac{\rho_i(t)}{\rho_{\rm c}(t)}. \tag{1.6}$$

Then the Friedmann equation becomes

$$\sum_i \Omega_i(t) + \Omega_k(t) = 1, \tag{1.7}$$

where $\Omega_k(t) \equiv -k/(a^2H^2)$ measures the contribution of spatial curvature. Usually, we ignore the spatial curvature component as observations suggest the universe to be spatially flat. So the total fractional energy density becomes $\Omega_{\rm tot} = \frac{\rho_{\rm tot}}{\rho_c}$.

Now, a flat, open, or closed Universe corresponds to $\Omega_{\rm tot} = 1$, $\Omega_{\rm tot} < 1$, and $\Omega_{\rm tot} > 1$, respectively.

Continuity Equation and Equation of State

Energy–momentum conservation, $\nabla_\mu T^{\mu\nu} = 0$, implies the continuity equation,

$$\dot{\rho} + 3H(\rho + p) = 0. \tag{1.8}$$

For a fluid characterized by a constant equation of state parameter

$$w \equiv \frac{p}{\rho}, \tag{1.9}$$

this equation admits the solution

$$\rho(a) = \rho_0\, a^{-3(1+w)}. \tag{1.10}$$

The corresponding evolution of the scale factor for a single-component Universe with $w \neq -1$ is

$$a(t) \propto t^{\frac{2}{3(1+w)}}, \tag{1.11}$$

while for $w = -1$ one obtains an exponential expansion,

$$a(t) \propto e^{Ht}. \tag{1.12}$$

Main Components of the Universe

The cosmic expansion history is governed by the relative contributions of the different energy components that fill the Universe. In the standard cosmological framework, the dominant constituents are radiation, non-relativistic matter, and dark energy. Each component is characterized by a specific equation of state parameter $w = p/\rho$, which determines how its energy density evolves with the scale factor through the continuity equation,

$$\rho(a) = \rho_0 \, a^{-3(1+w)}. \tag{1.13}$$

This simple relation encodes the essential physical differences between relativistic and non-relativistic species, and between ordinary matter and vacuum energy.

Radiation. For ultra-relativistic particles, such as photons and relativistic neutrinos, the pressure satisfies $p = \rho/3$, corresponding to $w_r = 1/3$. The energy density then follows as

$$\rho_r(a) \propto a^{-4}. \tag{1.14}$$

The factor a^{-3} arises from the dilution of particle number due to the expansion of volume, while the additional factor a^{-1} reflects the redshifting of each particle's energy as its wavelength is stretched by the expansion. As a result, radiation dominates the energy budget of the very early Universe. In a radiation-dominated epoch, the scale factor evolves as

$$a(t) \propto t^{1/2}, \tag{1.15}$$

corresponding to a rapidly decelerating expansion.

Non-relativistic matter. For pressureless matter, including baryons and cold dark matter, the pressure is negligible compared to the energy density, $p \simeq 0$, and hence $w_m = 0$. The energy density scales as

$$\rho_m(a) \propto a^{-3}, \tag{1.16}$$

reflecting purely the dilution of particle number with the expansion, since the rest mass energy of each particle remains constant. In a matter-dominated Universe, the Friedmann equations imply

$$a(t) \propto t^{2/3}. \tag{1.17}$$

This slower expansion rate allows small primordial density perturbations to grow efficiently under gravitational instability, leading to the formation of cosmic structures such as galaxies and clusters.

Dark energy. A cosmological constant is characterized by a constant energy density and negative pressure, $p = -\rho$, corresponding to $w_\Lambda = -1$. In this case,

$$\rho_\Lambda(a) = \text{const.} \tag{1.18}$$

Unlike radiation and matter, the energy density of dark energy does not dilute as the Universe expands. When dark energy dominates the total energy budget, the expansion becomes accelerated, with

$$a(t) \propto e^{Ht}. \tag{1.19}$$

More generally, any fluid with equation of state parameter $w < -1/3$ leads to accelerated expansion and can act as a dark energy candidate.

Cosmic epochs. The different scalings of $\rho_r(a)$, $\rho_m(a)$, and $\rho_\Lambda(a)$ imply that the dominant component of the Universe changes with time. At early times, radiation dominates, followed by a transition to matter domination at matter–radiation equality. At late times, the nearly constant dark energy density eventually overtakes the matter density, leading to the present epoch of accelerated expansion. This sequence provides the basic backbone of the standard thermal and dynamical history of the Universe.

1.2 Horizons and Distances in Cosmology

A central task of observational cosmology is to relate measurable quantities, such as redshifts, angles, and fluxes, to the underlying geometry and expansion history of the Universe. This requires a precise definition of cosmological distances and horizons, which encode both the kinematics of cosmic expansion and the causal structure of spacetime.

Redshift and the Scale Factor

The cosmological redshift z is defined as

$$1 + z \equiv \frac{\lambda_{\rm obs}}{\lambda_{\rm em}} = \frac{a(t_0)}{a(t_{\rm em})}, \tag{1.20}$$

where $\lambda_{\rm em}$ and $\lambda_{\rm obs}$ denote the emitted and observed wavelengths, respectively, $a(t_{\rm em})$ is the scale factor at the time of emission, and $a(t_0) \equiv 1$ today. The redshift thus provides a direct measure of the cosmic expansion between the time of emission and observation.

In an expanding Friedmann–Lemaître–Robertson–Walker spacetime, light propagates along null geodesics satisfying

$$ds^2 = -dt^2 + a^2(t)\left[d\chi^2 + S_k^2(\chi)d\Omega^2\right] = 0, \tag{1.21}$$

where χ denotes the comoving radial coordinate and $S_k(\chi)$ encodes the spatial curvature through $d\chi = dr/\sqrt{1-kr^2}$ and

$$S_k(\chi) = \sinh\chi, \qquad k = -1, \tag{1.22}$$

$$= \chi, \qquad k = 0, \tag{1.23}$$

$$= \sin\chi \qquad k = +1 \tag{1.24}$$

Comoving Distance

The comoving distance $\chi(z)$ to an object observed at redshift z is defined as the coordinate distance traveled by a photon emitted at time $t_{\rm em}$ and observed today,

$$\chi(z) = \int_{t_{\rm em}}^{t_0} \frac{c\,dt}{a(t)} = \int_0^z \frac{c\,dz'}{H(z')}, \tag{1.25}$$

$H(z) = \dot{a}/a$ is the Hubble expansion rate. The comoving distance is independent of the epoch at which it is evaluated and provides a convenient measure of spatial separation in an expanding Universe.

For a spatially flat Universe, the comoving distance directly determines the transverse comoving separation between two objects separated by an angle $\Delta\theta$ as

$$r_\perp = \chi(z)\,\Delta\theta. \tag{1.26}$$

Particle Horizon

Particle horizon defines the maximum comoving distance from which light has reached an observer since the beginning of the universe.

$$\chi_{\mathrm{p}}(t) = \int_{t_{\mathrm{i}}}^{t} \frac{c\,dt'}{a(t')}, \tag{1.27}$$

t_{i} denotes the initial time, often taken to be the end of inflation or the Big Bang. The particle horizon thus characterizes the size of the causally connected region of the Universe at a given cosmic time.

The existence of a finite particle horizon underlies the horizon problem of standard cosmology and motivates the introduction of an early inflationary phase.

Sound Horizon

Of particular importance for both cosmic microwave background and baryon acoustic oscillation observations is the sound horizon. Prior to recombination, photons and baryons form a tightly coupled plasma in which pressure supports acoustic oscillations. The comoving sound horizon at time t is defined as the maximum distance traveled by a sound wave,

$$r_s(t) = \int_{t_{\mathrm{i}}}^{t} \frac{c_s(t')}{a(t')}\,dt' = \int_{z}^{\infty} \frac{c_s(z')}{H(z')}\,dz', \tag{1.28}$$

where c_s is the sound speed of the photon–baryon fluid. Evaluated at the photon decoupling or baryon drag epoch, the sound horizon sets a standard ruler that is imprinted in both the angular power spectrum of the CMB and the clustering of galaxies at late times.

Angular Diameter Distance

The angular diameter distance $D_A(z)$ is defined as

$$D_A(z) = \frac{l}{\theta}. \tag{1.29}$$

Here l denotes physical transverse size of an object, θ is its observed angular size. In a general FLRW spacetime, it becomes

$$D_A(z) = \frac{1}{1+z}\, S_k(\chi(z))\,, \tag{1.30}$$

Here $(1+z)^{-1}$ accounts for the expansion between emission and observation. The angular diameter distance plays a central role in interpreting the angular scale of Cosmic Microwave Background peaks and transverse BAO feature in galaxy surveys.

Luminosity Distance

The luminosity distance $D_L(z)$ relates the intrinsic luminosity L of a source to the observed flux F according to

$$F = \frac{L}{4\pi D_L^2(z)}. \tag{1.31}$$

In an expanding Universe, the luminosity distance and comoving distance are correlated through

$$D_L(z) = (1+z)\, S_k(\chi(z))\,. \tag{1.32}$$

The additional factor of $(1+z)$ arises from the redshifting of photon energies and the time dilation of the photon arrival rate. Luminosity distances are the primary observable in Type-Ia supernova cosmology.

Distance Duality Relation

A fundamental relation between angular diameter and luminosity distances is provided by the Etherington reciprocity theorem,

$$D_L(z) = (1+z)^2 D_A(z), \tag{1.33}$$

This is a very generic relation that provides an important internal consistency check for cosmological observations.

Together, these distance measures and horizons form the geometrical backbone of modern observational cosmology. They allow the expansion history and curvature of the Universe to be inferred from CMB anisotropies, baryon acoustic oscillations, and supernova observations, which will be discussed in the following sections.

1.3 Thermal History of the Universe

The large-scale properties of the present Universe come out of a sequence of well-defined physical processes that occurred as the cosmic plasma cooled and expanded from its initial hot and dense state. The thermal history of the Universe provides the framework that connects high-energy particle physics to cosmological observables, and determines the initial conditions for structure formation.

In this section we briefly review the major epochs of cosmic evolution, from the early radiation-dominated era to the present accelerated expansion.

Early Radiation-Dominated Epoch

At a sufficiently early Universe, relativistic species provided the dominant contribution to the total energy density, and the expansion rate was governed by the radiation component,

$$\rho_{\rm rad}(a) \propto a^{-4}, \qquad H(a) \simeq H_0 \sqrt{\Omega_{\rm r}}\, a^{-2}. \tag{1.34}$$

The additional factor of a^{-1} compared to matter dilution arises from the redshifting of particle momenta in an expanding spacetime. During this epoch, the temperature scales as $T \propto a^{-1}$, and the Universe can be accurately described as a nearly homogeneous thermal bath in local equilibrium.

Electroweak and QCD Phase Transitions

Baryogenesis at early times leads to a baryon asymmetry, in which matter components begin to dominate over antimatter Sakharov (1991); Riotto (1998); Trodden (1999). At temperatures of order $T \sim 100\,\mathrm{GeV}$ and $z \sim 10^{15}$, the electroweak symmetry is broken Englert & Brout (1964); Guralnik et al. (1964) through the Higgs mechanism Higgs (1964), endowing the W and Z bosons and fermions with mass . Although this transition is a smooth crossover in the Standard Model, it may play an important role in baryogenesis in extensions of particle physics.

At $T \sim 150\,\mathrm{MeV}$ and $z \sim 10^{12}$, the strong interaction undergoes the QCD phase transition Gross & Wilczek (1973), during which quarks and gluons become confined into hadrons. The effective number of relativistic degrees of freedom drops rapidly across this epoch, modifying the expansion rate and leaving a small imprint on the evolution of density perturbations.

Neutrino Decoupling and Electron–Positron Annihilation

At temperatures $T \sim 1\,\mathrm{MeV}$ and $z \sim 5 \times 10^9$, weak interaction rates fall below the Hubble expansion rate, and neutrinos decouple from the primordial plasma Mangano et al. (2005); Hannestad & Madsen (1995). Shortly thereafter, electrons and positrons annihilate. Their entropy transfers primarily to photons. As a result, the photon temperature becomes higher than the neutrino temperature,

$$T_\nu = \left(\frac{4}{11}\right)^{1/3} T_\gamma, \tag{1.35}$$

a relation that remains valid to the present epoch and plays a central role in precision cosmology.

Big Bang Nucleosynthesis

Between temperatures of $T \sim 1\,\mathrm{MeV}$ and $T \sim 0.01\,\mathrm{MeV}$, light nuclei are synthesized through a network of nuclear reactions, known as Big Bang Nucleosynthesis (BBN) Tytler et al. (2000); Fields & Sarkar (2006). It predicts the primordial abundances of deuterium, helium, and lithium as a function of the baryon-to-photon ratio and expansion rate. The remarkable agreement between theoretical predictions and observed light element abundances provides one of the earliest and most robust confirmations regarding the model of hot Big Bang.

Matter–Radiation Equality

With the expansion of the universe, the radiation energy density decreases faster than the matter. The epoch of matter–radiation equality is defined by

$$\rho_{\rm m}(a_{\rm eq}) = \rho_{\rm r}(a_{\rm eq}), \tag{1.36}$$

and marks the transition from radiation-dominated to matter-dominated expansion. This epoch plays a crucial role in the growth of density perturbations and shapes the matter power spectrum.

Prior to equality, perturbations in the matter component grow only logarithmically, while after equality they grow approximately linearly with the scale factor.

Recombination and Photon Decoupling

At redshift $z \simeq 1100$, the temperature drops sufficiently for electrons and protons to combine into neutral hydrogen, as a result of a reduction in photon encounters to ionize them at $T = 0.3$ eV. Eventually, the free electron abundance decreases, the photon mean free path increases dramatically, and photons decouple from the baryon fluid because the Thompson scattering rate between photons and baryons falls below the Hubble expansion rate at $T = 0.25$ eV. These photons form the cosmic microwave background observed today Penzias & Wilson (1965).

The last scattering surface defines a nearly spherical shell at comoving distance $\chi(z_{\rm rec})$, and the acoustic oscillations of the photon–baryon plasma at this epoch are imprinted as a series of peaks in the CMB angular power spectrum.

Ater photon decoupling, the baryons feels a drag from photon due to baryon to photon ratio being small. Around $z_d \sim 1060$ and $T = 0.20$ eV, the baryon drag epoch, at which baryons are released from the scattering with photons and begin to fall into the potential wells of dark matter. The comoving sound horizon at this epoch sets the standard ruler measured by baryon acoustic oscillations.

Dark Ages, Cosmic Dawn, and Reionization

Following recombination, the Universe enters the so-called dark ages Miralda-Escude (2003); Natarajan & Yoshida (2014), during which neutral hydrogen dominates and luminous sources have not yet formed. Formation of first stars and galaxies marks the beginning of cosmic dawn, leading eventually to the reionization Barkana & Loeb (2001); Zaroubi (2013) of the intergalactic medium, through the ionization of the neutral hydrogen.

Reionization is completed by redshift $z \sim 6$, and leaves an imprint on the CMB through Thomson scattering, characterized by the optical depth parameter τ.

Matter–Dark Energy Equality and Late-Time Acceleration

At relatively recent times, the energy density of dark energy becomes comparable to that of matter,

$$\rho_{\rm m}(a_\Lambda) = \rho_{\rm de}(a_\Lambda), \tag{1.37}$$

marking the onset of accelerated expansion Riess et al. (1998). For a cosmological constant, this occurs at redshift $z \sim 0.3$.

During this epoch, the growth of cosmic structures is gradually suppressed, and the expansion history departs significantly from the matter-dominated solution.

The Present Epoch

Today, the Universe is observed to be dominated by dark energy, with a subdominant matter component and a negligible radiation contribution. The present cosmic expansion rate is characterized by the Hubble constant H_0, and precision observation from cosmic microwave background, large-scale structure, and supernova distances provide a consistent picture of the late-time Universe within the standard cosmological framework.

1.4 Cosmological Observables

The remarkable progress of modern cosmology is driven by a small number of precision observables that directly probe the expansion history of the Universe and the structure formation. Among these, the cosmic microwave background, baryon acoustic oscillations, and Type-Ia supernovae are the cornerstones of current observational framework.

These three probes are complementary in both redshift coverage and physical origin, and together they provide a tightly constrained and internally consistent description of the Universe from recombination to the present epoch.

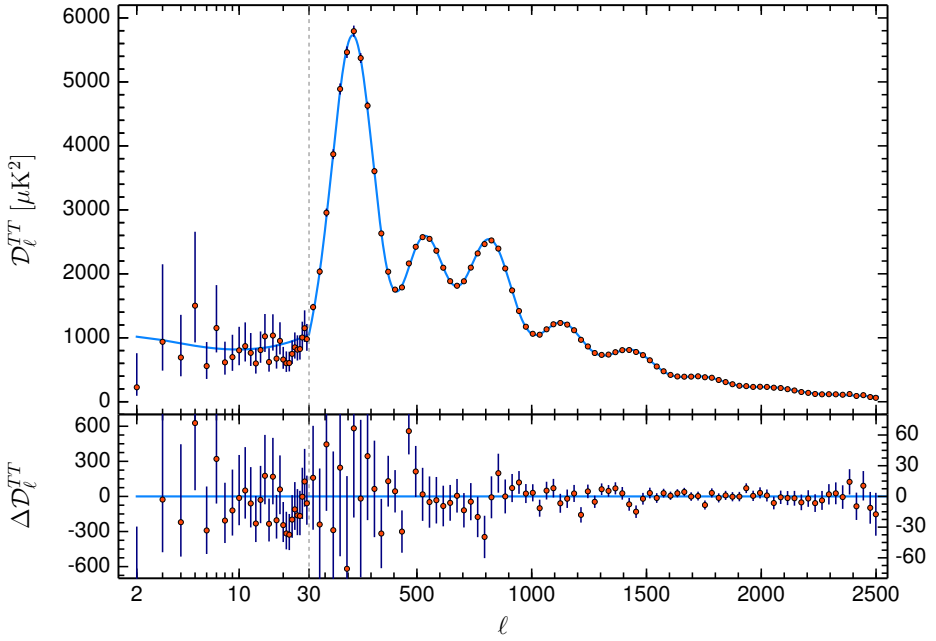


FIGURE 1.1: Planck 2018 Temperature anisotropy power spectrum with Y-axis $D_\ell^{TT} = \frac{\ell(\ell+1)c_\ell^{TT}}{2\pi}$. THe top panel shows the theoretically predicted power spectra for ΛCDM model on top of measured values and the bottom panel shows the corresponding residuals. It has been taken from Aghanim et al. (2020)

Cosmic Microwave Background

Cosmic microwave background (CMB) is the relic photons released at the epoch of photon decoupling, such that the universe is cooled down sufficiently for protons and electrons to combine into neutral hydrogen. At this stage, the mean free path of photons increased dramatically and radiation began to propagate freely through the expanding Universe.

Prior to decoupling, photons and baryons formed a tightly coupled plasma, supported against gravitational collapse by radiation pressure. Density perturbations in this fluid executed acoustic oscillations under the competition between gravitational infall and photon pressure. These oscillations were frozen at the moment of decoupling and are observed today as temperature anisotropies on the celestial sphere. They can be represented through spherical harmonicsY_ℓ^m,

$$\frac{\delta T}{T}(\theta, \phi) = \sum_{\ell=0}^{\infty} \sum_{m=-\ell}^{m=\ell} a_{\ell m} Y_{\ell}^{m}(\theta, \phi) \tag{1.38}$$

These anisotropies are described by the angular power spectrum,

$$C_{\ell} = \langle |a_{\ell m}|^2 \rangle, \tag{1.39}$$

which exhibits a characteristic series of acoustic peaks. The temperature anisotropy power spectra from Planck 2018 is illustrated in Figure 1.1.

Angular position of the first peak is set by the ratio

$$\theta_* = \frac{r_s(z_*)}{D_A(z_*)}, \tag{1.40}$$

where $r_s(z_*)$ is comoving sound horizon during recombination at z_*, $D_A(z_*)$ represents angular diameter distance to the last scattering surface. This quantity fixes the geometric scale of the Universe at $z \simeq 1100$.

In addition to temperature anisotropies, the CMB exhibits linear polarization generated by Thomson scattering in the presence of a local quadrupole anisotropy. The polarization spectra provide independent information on the ionization history and the amplitude of primordial fluctuations.

Measurements of the CMB therefore encode both the initial conditions of structure formation and the geometry of the Universe at early times. Satellite missions like *COBE* Smoot et al. (1992), *WMAP* Kogut et al. (2003), and *Planck* Aghanim et al. (2020) have progressively mapped these anisotropies with increasing precision, establishing the CMB as the primary probe of the early Universe.

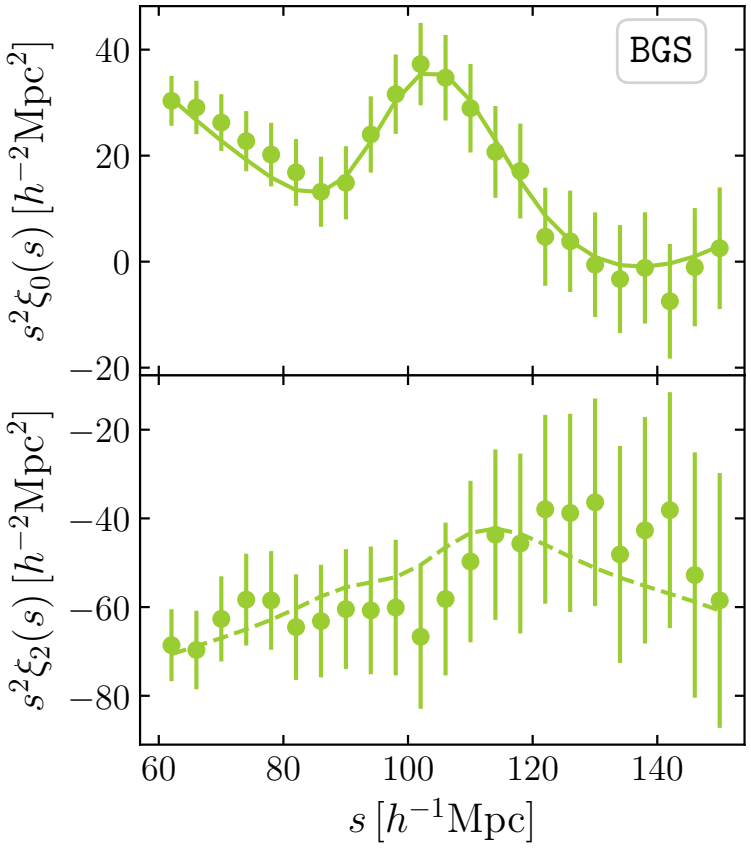


FIGURE 1.2: Two-point correlation function of Bright Galaxy Sample (BGS) from DESI is shown here. The upper and lower panel plots the monopole and quadrupole moments of the correlation function, respectively. The bump at the higher s value corresponds to the BAO scale. Figure credit: Abdul Karim et al. (2025)

Baryon Acoustic Oscillations

Baryon acoustic oscillations originate from the same acoustic waves in the photon–baryon plasma that give rise to the CMB anisotropies. However, the imprint observed in the late-time matter distribution is set not at recombination, but at a slightly later epoch known as the drag epoch.

While recombination marks the moment when photons decouple from baryons, baryons continue to experience residual Compton drag from the photon bath for a short time thereafter. The drag epoch, denoted by redshift z_d, corresponds to

the moment when this momentum exchange becomes negligible and baryons are released from radiation pressure.

The characteristic comoving scale imprinted in the matter distribution is therefore the sound horizon during drag epoch,

$$r_d = \int_{z_d}^{\infty} \frac{c_s(z)}{H(z)}\, dz, \tag{1.41}$$

which is slightly larger than the sound horizon at recombination.

After this epoch, baryons fall into dark matter potential wells, and the overdensity at separation r_d is preserved as a small enhancement in the two-point correlation function of galaxies, as shown in Figure 1.2. This feature acts as a standard ruler whose physical length is fixed by early-Universe physics.

In observations, BAO measurements constrain combinations of distances through

$$D_M(z) = (1+z)D_A(z), \qquad D_H(z) = \frac{c}{H(z)}, \tag{1.42}$$

or through the isotropic volume-averaged distance $D_V(z)$.

Because the BAO scale is calibrated by the same pre-recombination physics as the CMB, BAO measurements provide a direct geometric probe of the late-time expansion history anchored to early-Universe initial conditions.

Large spectroscopic surveys such as *BOSS* Alam et al. (2017a), *eBOSS*,Zhao et al. (2022) and the Dark Energy Spectroscopic Instrument (DESI) Abdul Karim et al. (2025) have measured the BAO feature over a wide redshift range. In particular, DESI has achieved percent-level precision in distance measurements from $z \simeq 0.1$ to $z \simeq 3$, enabling stringent tests of the expansion history and providing first evidence of possible deviations from a cosmological constant.

Type-Ia Supernovae

Type-Ia supernovae are standard candles, whose intrinsic luminosities can be calibrated using empirical correlations between light-curve shape and peak brightness. The primary observable is the distance modulus,

$$\mu(z) = m - M = 5 \log_{10} \left(\frac{D_L(z)}{10\,\mathrm{pc}} \right), \tag{1.43}$$

where $D_L(z)$ is the luminosity distance.

The luminosity distance is defined through

$$D_L(z) = (1+z) \int_0^z \frac{c}{H(z')}\, dz'. \tag{1.44}$$

Measurements of supernova distances directly probe the integrated expansion rate and were the first to establish the accelerated expansion of the Universe. Modern compilations, such as the Pantheon+ Brout et al. (2022), Union3 Rubin et al. (2025), and DES Abbott et al. (2022)samples, provide hundreds of well-calibrated supernovae extending to redshifts $z \sim 2$.

Supernova data are particularly sensitive to the late-time behavior of dark energy and play a crucial role in breaking degeneracies between cosmological parameters when combined with CMB and BAO observations.

1.5 The Standard Model of Cosmology

The remarkable success of modern cosmology rests on a minimal phenomenological model known as the ΛCDM model. Despite its simplicity, this framework provides

an accurate description of a variety of cosmological observations, from the CMB to the galaxy distribution and the late-time accelerated expansion of the Universe.

ΛCDM assumes that the cosmic energy budget is dominated by four components: radiation, baryons, cold dark matter, and cosmological constant Λ representing dark energy. The geometry is taken to be spatially flat, and the primordial perturbations are assumed to be adiabatic, Gaussian, and nearly scale-invariant.

Within these assumptions, the entire background evolution and linear perturbation dynamics are specified by a small set of parameters. In its minimal version, the ΛCDM model is characterized by six independent parameters.

The Six Cosmological Parameters

The first two parameters describe the physical matter content of the Universe,

$$\omega_b \equiv \Omega_b h^2, \tag{1.45}$$

$$\omega_{cdm} \equiv \Omega_{cdm} h^2, \tag{1.46}$$

where Ω_b and Ω_c are the present-day density fractions of baryons and cold dark matter, and $h = H_0/(100\,\mathrm{km\,s^{-1}Mpc^{-1}})$.

The angular size of the sound horizon at recombination,

$$\theta_s \equiv \frac{r_s(z_*)}{D_A(z_*)}, \tag{1.47}$$

where $r_s(z_*)$: comoving sound horizon at the redshift of photon decoupling z_*; $D_A(z_*)$: corresponding angular diameter distance. It represents the geometric scale of the universe.

The next two parameters describe the statistical properties of primordial curvature perturbations generated during inflation. The amplitude of the primordial power spectrum is parameterized by A_s, while its scale dependence is described by the spectral index n_s, defined through

$$\mathcal{P}_{\mathcal{R}}(k) = A_s \left(\frac{k}{k_*}\right)^{n_s - 1}, \tag{1.48}$$

where k_* is a chosen pivot scale. These parameters determine the initial conditions for all subsequent structure formation.

The sixth parameter is the optical depth to reionization, τ, which quantifies the integrated Thomson scattering probability between recombination and today. This parameter controls the suppression of primary CMB anisotropies on small angular scales and the amplitude of large-scale polarization.

Together, the parameter set

$$\{\omega_b,\, \omega_{cdm},\, \theta_s,\, A_s,\, n_s,\, \tau\} \tag{1.49}$$

completely specifies the homogeneous expansion history and the linear evolution of perturbations in the ΛCDM framework.

Remarkably, this minimal six-parameter model provides an excellent simultaneous fit to a wide variety of independent observations. The success of ΛCDM in describing both early- and late-time cosmology establishes it as the current standard model of cosmology. At the same time, the phenomenological nature of the cosmological constant and the unknown particle nature of dark matter indicate that ΛCDM should be regarded as an effective description rather than a fundamental theory.

1.6 The S_8 Tension

Despite its overall success, the ΛCDM model has in recent years been confronted with a number of mild but persistent discrepancies between different cosmological probes. One of the most extensively discussed among these is the so-called S_8 tension Abdalla et al. (2022), where early- and late-time observations show a mismatch in the amplitude of matter fluctuations.

The clumpiness of the matter distribution in our Universe is parameterized by

$$S_8 \equiv \sigma_8 \left(\frac{\Omega_m}{0.3}\right)^{1/2}, \tag{1.50}$$

where σ_8 is the root mean square of matter fluctuations at the length scale of $8h^{-1}$Mpc, and Ω_m is the matter density at present-day.

In ΛCDM, Planck observation yields $S_8 = 0.832 \pm 0.013$ Aghanim et al. (2020). The observation of weak lensing of galaxies from the CFHTLenS collaboration initially pointed to a higher $S_8 = 0.799 \pm 0.015$ at 2σ Heymans *et al.* (2013); MacCrann et al. (2015) in the framework of ΛCDM. However, a re-analysis with the combination of DES data Abbott *et al.* (2018) and KiDS/Viking H. Hildebrandt *et al.* (2020); S. Joudaki *et al.* (2020) established the tension at the 3σ level with the value $S_8 = 0.755^{+0.019}_{-0.021}$ S. Joudaki *et al.* (2020). The tension arises due to a lower matter clustering at scales $k \approx 0.1 - 1h\text{Mpc}^{-1}$, and a reduction in the amplitude of matter fluctuations on those scales can effectively resolve it. For several years, this discrepancy persisted, motivating extensive investigations into extensions of the standard cosmological model.

More recent measurements from KIDS have found $S_8 = 0.81^{+0.016}_{-0.021}$ and reduced the statistical significance to 0.7σ of this discrepancy Wright et al. (2025). While the tension is no longer regarded as a decisive anomaly, its earlier persistence played an

important role in motivating systematic studies of non-standard growth histories.

In this thesis, the implications of the S_8 tension are explored in the context of interacting dark matter models in Chapter 3, where departures from the standard growth of structure are investigated as a possible mechanism to alleviate discrepancies between early- and late-time probes.

1.7 Motivation for Physics Beyond the Standard Cosmological Model

Despite ΛCDM being successful at describing various observations, it is currently confronted with several persistent, increasingly precise anomalies that motivate the exploration of physics beyond the minimal framework.

Perhaps the most prominent of these is the Hubble tension, namely a long-standing mismatch between the Hubble constant measured from early-Universe probes from CMB, with direct measurement from late-Universe distance indicators. This tension of $> 5\sigma$ has proven remarkably stable against improvements in both observational data and analysis techniques, and has resisted explanations within simple extensions of the standard model (see the recent comprehensive review Di Valentino et al. (2025) on this topic).

In addition, recent observations from the *James Webb Space Telescope* have revealed the presence of unexpectedly massive and evolved galaxies at very high redshift Naidu et al. (2022). These findings suggest a more rapid formation of structure in the early Universe than is typically predicted within standard ΛCDM, raising important questions about the timing of galaxy formation and the underlying properties of the dark sector.

At the same time, increasingly precise measurements of baryon acoustic oscillations from the Dark Energy Spectroscopic Instrument (DESI) are beginning to probe the late-time expansion history with unprecedented accuracy. Recent analyses have reported evidence of departures from a pure cosmological constant description of dark energy, suggesting the possibility of evolving dark energy dynamics at low redshift Adame et al. (2024); Abdul Karim et al. (2025).

Taken together, these observational developments do not yet provide conclusive evidence for a breakdown of ΛCDM. However, their collective presence across independent probes of the early and late Universe provides strong motivation to examine extensions of the standard model involving non-trivial dark matter and dark energy physics. In the following sections, we therefore present an overview of the current theoretical understanding of the dark sector, review the leading candidate models, and outline the physical motivations that underlie the investigations presented in the subsequent chapters of this thesis.

1.8 Dark Matter: Observational Evidence and Basic Properties

The existence of dark matter is one of the central pillars of modern cosmology. Without it, formation of structure can not be possible. The dark matter consists of almost 95% of the total matter component of the universe, and baryons follow the gravitational potential well formed by dark matter to create the structures we see today. In contrast to baryonic matter, dark matter exhibits no confirmed non-gravitational interactions with Standard Model particles, except only through gravity, which confirms its presence and likely plays a crucial role in the structure

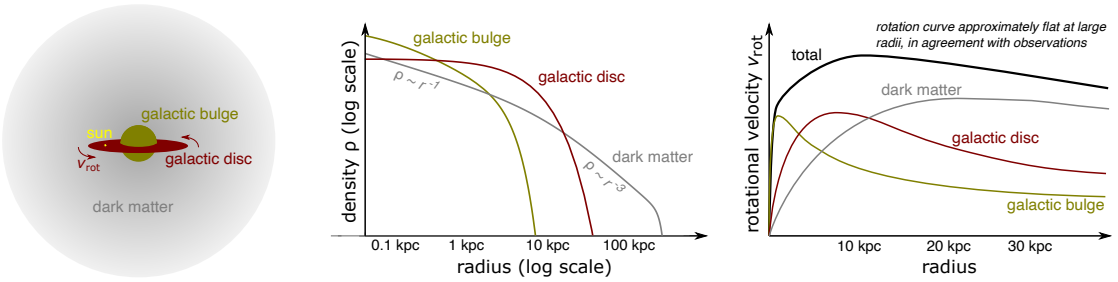


FIGURE 1.3: In the left panel, a schematic diagram of a spiral galaxy embedded in a dark matter halo is shown. The centre plots the density profiles of different components of a galaxy, with the NFW profile chosen for dark matter. In the right panel, the rotation velocity is plotted as a function of distance for different components. The figure is taken from Balazs et al. (2026)

formation. A wide range of independent observations, spanning galactic to cosmological scales, consistently point toward the presence of a dominant non-luminous matter component.

Gravitational Evidence for Dark Matter

One of the earliest and most direct indications for dark matter arises from the study of galaxy rotation curves Rubin & Ford (1970); Freeman (1970). For a test particle orbiting in a spherically symmetric gravitational potential, Newtonian dynamics predicts a circular velocity profile

$$v(r) = \sqrt{\frac{GM(r)}{r}}, \tag{1.51}$$

where $M(r)$ represents enclosed mass within radius r. If the mass distribution follows observed luminous matter, one expects $M(r)$ to approach a constant beyond the optical extent of the galaxy, leading to a Keplerian decline $v(r) \propto r^{-1/2}$.

Observations, however, reveal that rotation curves of spiral galaxies remain approximately flat out to the largest measured radii. This implies that $M(r)$ continues to grow roughly linearly with r, requiring the presence of an extended,

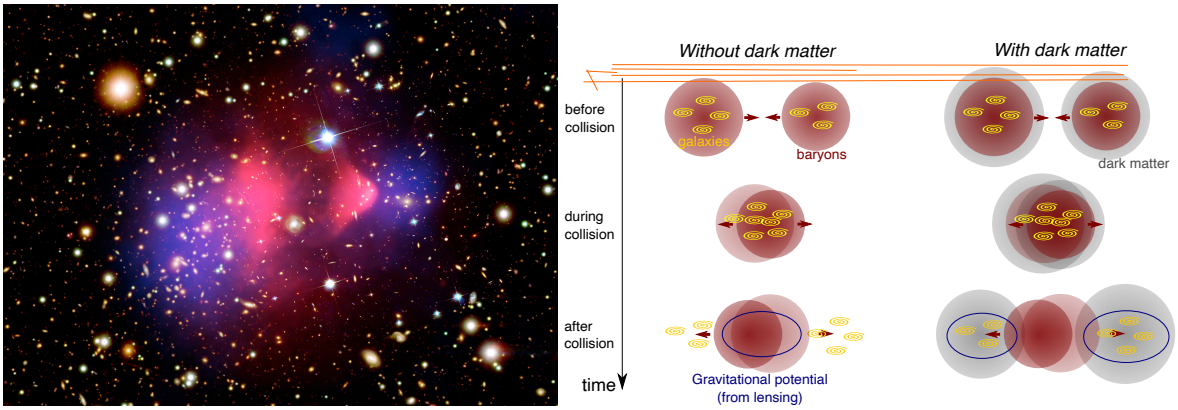


FIGURE 1.4: Left panel shows an image of the Bullet cluster overlapped with an X-ray image (in red) from Baryons and gravitational lensing from dark matter (in blue). Right panel shows a schematic diagram of observed Bullet cluster in both with and without dark matter in the universe. The right panel figure is taken from Balazs et al. (2026) respectively.

non-luminous halo whose mass far exceeds that of the visible components. This behavior is observed across a wide range of galaxy masses and morphologies as shown in Figure 1.3, indicating that dark matter is a generic feature of galactic dynamics rather than a peculiarity of individual systems.

A particularly striking demonstration of the collisionless nature of dark matter is offered by merging galaxy clusters, most notably the Bullet Cluster Harvey et al. (2015). In this system, the baryonic component, traced by X-ray emitting gas, is spatially separated from the dominant mass component inferred from gravitational lensing. The fact that the gravitational potential follows the galaxies rather than the gas strongly suggests that the dominant matter component interacts primarily through gravity, with negligible non-gravitational self-interactions or coupling to baryons on cluster scales. This has been shown in Figure 1.4.

Finally, cosmological observations provide independent and consistent evidence for dark matter. Measurements of the cosmic microwave background anisotropies require a non-baryonic matter density to explain the heights and positions of the acoustic peaks, while large-scale structure surveys confirm that the growth of density perturbations is consistent with a pressureless matter component that

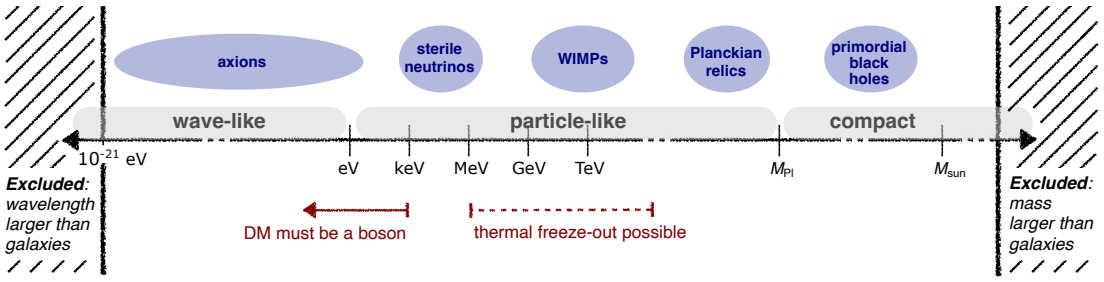


FIGURE 1.5: An Illustration of the large range of possible dark matter masses is shown here, along with different candidates at different mass scales. The figure is obtained from Balazs et al. (2026)

began to dominate the energy budget after matter–radiation equality.

Mass Scales and Quantum Constraints

Independently of any specific particle model, very general bounds can be placed on the mass of a dark matter particle Profumo (2017). A lower bound arises from quantum mechanical considerations. Requiring the de Broglie wavelength of a dark matter particle to be smaller than the typical size of dwarf galaxies leads to

$$m_{\rm dm} \gtrsim 10^{-22}\ \text{eV}, \tag{1.52}$$

below which quantum pressure would prevent the formation of observed small-scale structures.

An upper bound can be inferred from the requirement that dark matter behaves as a macroscopic object on astrophysical scales, where encountering a globular cluster does not get destabilized by encountering a dark matter, leading to

$$m_{\rm dm} \lesssim 10^{60}\ \text{GeV}, \tag{1.53}$$

Between these extremes lies an enormous range of viable mass scales, spanning more than eighty orders of magnitude as shown in Figure 1.5, reflecting the deep

theoretical uncertainty surrounding the microscopic nature of dark matter.

Basic Physical Properties of Dark Matter

Taken together, these observations constrain the fundamental properties of dark matter in a largely model-independent way. At the background and linear perturbation level, dark matter must behave as a pressureless fluid. In addition, the success of the standard cosmological model in describing the cosmic microwave background and large-scale structure requires dark matter to be effectively cold and collisionless at least from the epoch of recombination onward. In particular:

- Dark matter must be non-relativistic before matter–radiation equality in order to seed the observed hierarchy of cosmic structures.
- Its self-interactions must be sufficiently weak to avoid significant deviations from collisionless dynamics on galactic and cluster scales.
- Its coupling to photons and baryons must be extremely suppressed, consistent with the absence of electromagnetic signatures.
- It should be long-lived, cold, and collisionless, and should not possess any color charge.

Within the Standard Model of particle physics, no known particle satisfies all of these requirements, with the partial exception of neutrinos. They were initially named as "Hot dark matter". However, the measured neutrino masses imply that they remain relativistic until relatively late times and possess large thermal velocities, thereby suppressing structure formation on small scales. cosmological

observations constrain the sum of neutrino masses to $\sum m_\nu \lesssim 0.1$–0.2 eV, implying that neutrinos account for at most a few percent of the total dark matter abundance and cannot account for the dominant cold component.

1.9 Dark Matter Candidates

The observational evidence reviewed in the previous section establishes the existence of a dominant, non-baryonic matter component with well-defined macroscopic properties. However, these constraints leave the microscopic nature of dark matter largely unconstrained. A wide variety of candidates, shown in Figure 1.6, have therefore been proposed, spanning many orders of magnitude in mass and interaction strength. In this section, we briefly review the principal classes of dark matter candidates that are most relevant for cosmology, with particular emphasis on those scenarios that motivate the investigations presented in the later chapters of this thesis.

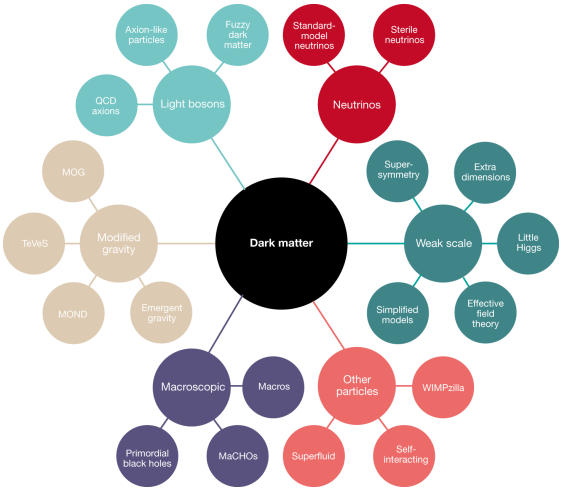


FIGURE 1.6: Various possible dark matter candidates shown schematically. Credit: Bertone & Tait (2018)

Weakly Interacting Massive Particles (WIMPs) and the WIMP Miracle

Perhaps the most extensively studied dark matter candidate is the weakly interacting massive particle (WIMP) Salucci (2019). WIMPs are assumed to be stable, electrically neutral particles with masses in the range

$$m_{\text{wimp}} \sim 10 \text{ GeV}, \tag{1.54}$$

and interaction strengths characteristic of the weak scale.

The central appeal of WIMPs lies in the thermal freeze-out mechanism, which naturally produces a relic abundance of the observed order of magnitude. In the early Universe, WIMPs are assumed to be in thermal equilibrium with the primordial plasma. As the temperature drops below the WIMP mass, their equilibrium number density becomes Boltzmann suppressed,

$$n_{\text{eq}}(T) \propto \left(\frac{mT}{2\pi}\right)^{3/2} e^{-m/T}. \tag{1.55}$$

As long as the annihilation rate

$$\Gamma_{\text{ann}} = n\langle\sigma v\rangle \tag{1.56}$$

exceeds the Hubble expansion rate $H(T)$, WIMPs remain in chemical equilibrium. Freeze-out occurs when

$$n_{\text{f}}\langle\sigma v\rangle \simeq H(T_{\text{f}}), \tag{1.57}$$

after which the comoving number density becomes approximately conserved.

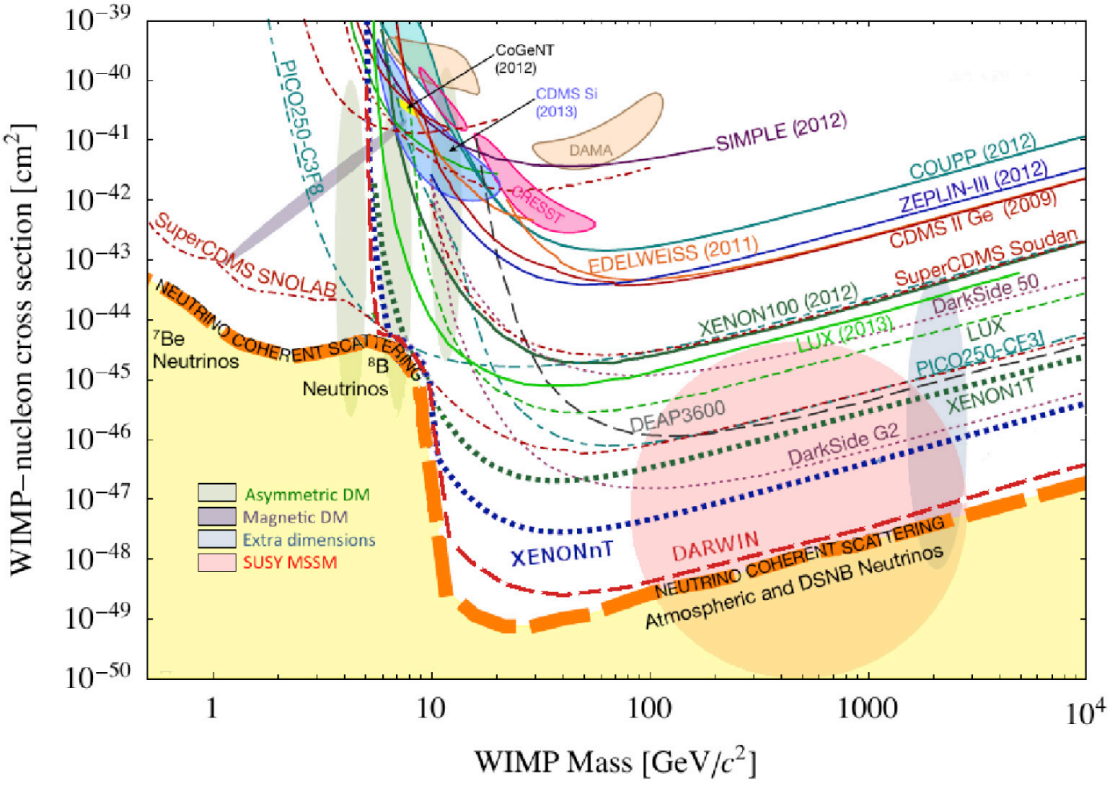


FIGURE 1.7: Current bounds on WIMPs detection. The shaded regions are excluded. Only a small window is left. The yellow shaded area refers to the Neutrino floor, where the detection of WIMPs is indistinguishable from that of neutrinos. The figure is obtained from Baudis (2014).

Solving the Boltzmann equation for the WIMP abundance yields a present-day relic density

$$\Omega_{\rm wimp}h^2 \simeq \frac{3\times10^{-27}\ {\rm cm}^3\ {\rm s}^{-1}}{\langle\sigma v\rangle}. \tag{1.58}$$

Remarkably, for an annihilation cross section of order

$$\langle\sigma v\rangle \sim 10^{-26}\ {\rm cm}^3\ {\rm s}^{-1}, \tag{1.59}$$

characteristic of weak interactions, one obtains $\Omega_{\rm wimp}h^2 \sim 0.1$, in excellent agreement with the observed dark matter abundance. This numerical coincidence is commonly referred to as the *WIMP miracle*.

Motivated by this result, an extensive experimental program has been pursued over the past decades, including direct detection, indirect detection, and collider

searches. Despite steadily improving sensitivities, no conclusive signal of WIMPs has been observed so far, with current status is shown in Figure 1.7. This absence of detection has significantly weakened the original motivation for WIMPs and prompted renewed interest in alternative dark matter scenarios.

Warm Dark Matter

Warm dark matter occupies an intermediate regime between hot and cold dark matter. Warm candidates become non-relativistic earlier than neutrinos but still possess non-negligible thermal velocities at early times. Their free-streaming suppresses structure formation below a characteristic scale, potentially alleviating some small-scale challenges associated to CDM model Viel et al. (2013a); Holm et al. (2022); Blinov et al. (2020); Alexander et al. (2023).

The comoving free-streaming length for warm dark matter can be estimated as

$$\lambda_{\rm fs} \sim 0.1 \left(\frac{1\ \text{keV}}{m_{\rm wdm}}\right)^{4/3} \text{Mpc}, \tag{1.60}$$

which leads to a linear matter power spectrum, where on small length scales powers are suppressed.

Observations of Lyman-α forest place strong lower bounds on the warm dark matter particle mass, typically

$$m_{\rm wdm} \gtrsim 3 - 5\ \text{keV}, \tag{1.61}$$

severely restricting the parameter space in which warm dark matter can differ significantly from cold dark matter. While warm dark matter remains a viable alternative, its impact on cosmological observables is tightly constrained.

Fuzzy and Ultra-Light Dark Matter

At the opposite extreme of the mass spectrum lie ultra-light scalar field candidates, often referred to as fuzzy dark matter Hu et al. (2000), where dark matter mass can be as small as

$$m_{\rm fdm} \sim 10^{-22}\ {\rm eV}, \tag{1.62}$$

such that the de Broglie wavelength becomes astrophysically relevant Dutta Chowdhury et al. (2023); Dalal & Kravtsov (2022); Marsh & Niemeyer (2019),

$$\lambda_{\rm dB} \sim \frac{h}{mv} \sim {\rm kpc}. \tag{1.63}$$

Quantum pressure associated with the wave nature of the field suppresses structure formation below this scale and leads to characteristic solitonic cores in dark matter halos. Constraints from galaxy dynamics, Lyman-α forest data, and CMB observations place increasingly strong limits on the viable parameter space of fuzzy dark matter, though a narrow window around $m \sim 10^{-22}$–10^{-21} eV remains of interest.

While cold dark matter successfully describes observations from recombination onward, its behavior at earlier times remains poorly constrained. This motivates scenarios such as the mass-varying dark matter framework studied in Chapter 3. Beyond particle candidates, primordial black holes offer a distinct possibility for dark matter, and in Chapter 4 we explore a new formation mechanism based on Yukawa-type interactions. In the following section, we therefore give a brief overview of primordial black holes as dark matter candidates.

1.10 Primordial Black Holes as Dark Matter Candidates

Primordial black holes (PBHs) constitute a conceptually distinct class of dark matter candidates in which the dark matter is not composed of new elementary particles, but instead consists of compact objects formed through gravitational collapse in the early Universe. Unlike stellar black holes, whose formation is tied to the late-time evolution of massive stars, primordial black hole dark matter may form at very early epochs, when the cosmic density is extremely high, and the Hubble horizon mass is correspondingly small. As a result, PBHs can span an enormous range of masses, from sub-gram scales to many solar masses, depending on the formation time and the underlying physical mechanism.

The possibility that PBHs could contribute to the cosmic dark matter density was first proposed shortly after the development of modern cosmology, motivated by the realization that sufficiently large density fluctuations in the early Universe could undergo gravitational collapse Carr & Hawking (1974); Carr (1975). Since then, PBHs have been studied both as dark matter candidates and as probes of early-Universe physics, providing a unique window into small-scale primordial perturbations, phase transitions, and non-standard dynamics in the radiation-dominated era.

At the background level, primordial black holes behave as pressureless matter and redshift as a^{-3} once formed. However, their compact nature leads to distinctive signatures on small scales and in high-energy and gravitational-wave observations, allowing them to be strongly constrained over much of the mass range. Despite these constraints, a large mass window remains in which PBHs may contribute to the total of dark matter density today.

Basic Criterion for PBH Formation

Primordial black holes are generally produced from the collapse of inhomogeneities in the early universe, unlike stellar black holes, which form from the collapse of a star. Denoting by $\delta(\mathbf{x})$ the density contrast smoothed on the horizon scale, collapse occurs when

$$\delta(\mathbf{x}) > \delta_{\rm c}, \tag{1.64}$$

where $\delta_{\rm c}$ is a critical threshold of order unity that depends on the equation of state of the background fluid. Simulations of relativistic collapse in a radiation-dominated Universe typically find $\delta_{\rm c} \simeq 1.5$–$2.0$ Carr et al. (2021); Amendola et al. (2018).

The mass of the resulting black hole is set by horizon mass at the time of formation Carr & Hawking (1974); Carr et al. (2021),

$$M_{\rm PBH} \simeq \gamma M_{\rm H}(t_{\rm f}) = \gamma \frac{c^3 t_{\rm f}}{G}, \tag{1.65}$$

where $t_{\rm f}$ is the formation time and $\gamma \lesssim 1$ encodes the efficiency of collapse. This relation implies a direct mapping between PBH mass and formation epoch: lighter PBHs form earlier, while heavier PBHs form later.

A more refined treatment takes into account the phenomenon of critical collapse, in which the PBH mass depends continuously on the distance from the collapse threshold Choptuik (1993),

$$M_{\rm PBH} = k M_{\rm H} (\delta - \delta_{\rm c})^{\eta}, \tag{1.66}$$

with $\eta \simeq 0.36$ for a radiation background. This leads naturally to extended mass functions even when perturbations are generated on a narrow range of scales.

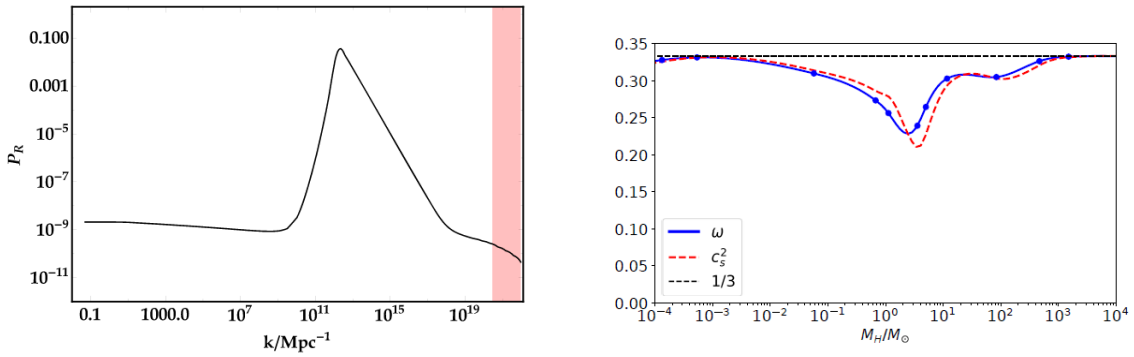


FIGURE 1.8: Left panel shows the standard formation mechanism of PBH through a peak in standard scale invariant inflationary power spectra (credit: Solbi & Karami (2021)), and the right panel shows a drop in pressure during QCD phase transition through a drop in equation of state parameter w (credit: Byrnes et al. (2018)).

Formation Mechanisms

Several physical mechanisms can generate the large density fluctuations required for PBH formation.

The most widely studied channel relies on enhanced primordial curvature perturbations produced during inflation Carr & Lidsey (1993), Ivanov et al. (1994), Sasaki et al. (2018), Ashoorioon et al. (2018), Bhattacharya et al. (2021a). If the power spectrum $\mathcal{P}_\mathcal{R}(k)$ develops a pronounced peak on small scales. shown in the left panel of Figure 1.8, (García-Bellido et al. 1996; Clesse & García-Bellido 2015; García-Bellido & Ruiz Morales 2017; Kannike et al. 2017; Ezquiaga et al. 2018; Ballesteros & Taoso 2018; Franciolini et al. 2018; Pi et al. 2018; Ashoorioon et al. 2021) that are insensitive to CMB observations, sufficiently large perturbations collapse into PBHs when those modes re-enter the horizon. This implies the density contrast to be very high at those scales, and that gives the perfect environment for the formation of PBH when those modes enter horizon.

But an alternative route is to keep the success of the simple inflationary model with scale-invariant power spectra as it is, but creating high sub-horizon scale density

contrast with some phase transition that naturally takes place as the universe cools down. For example, QCD PBH are formed due to the temporary drop in the pressure around epoch of QCD phase transition Jedamzik (1997); Widerin & Schmid (1998); Jedamzik (1998); Hindmarsh & Philipsen (2005); Byrnes et al. (2018), shown in the right panel of Figure 1.8. However since the QCD PBHs will have masses of the order $\sim 0.1 - 10\ M_{\odot}$, which can not account for total dark matter because of current constraints on $f(M)$ for these masses (see Fiq.4.6).

Other first-order phase transition driven by bubble nucleation or bubble collision can also create PBHs Crawford & Schramm (1982), Hawking et al. (1982),La & Steinhardt (1989), Moss (1994), Konoplich et al. (1998), Konoplich et al. (1999), Kodama et al. (1982), Kusenko et al. (2020), Gross et al. (2021), Baker et al. (2021),Kawana & Xie (2022). Existence of attractive long range fifth force Das et al. (2021) or scalar field fragmentation Cotner & Kusenko (2017a), Cotner & Kusenko (2017b), Cotner et al. (2018), Cotner et al. (2019) can also lead to PBH dark matter formation in the pre-BBN era. Once PBHs form through the above process, typically, the PBH mass is of the order of horizon size at the formation epoch. Thus, knowing the formation epoch more or less fixes the PBH mass.

PBH Mass Functions

A central theoretical ingredient is the PBH mass function, which describes the fraction of dark matter in PBHs per logarithmic mass interval Carr et al. (2021),

$$f_{\rm PBH}(M) \equiv \frac{1}{\Omega_{\rm DM}} \frac{d\Omega_{\rm PBH}}{d\ln M}. \tag{1.67}$$

Early studies often assumed a monochromatic mass function,

$$f_{\rm PBH}(M) = f_{\rm PBH}\,\delta(\ln M - \ln M_0), \tag{1.68}$$

corresponding to PBHs forming at a single epoch. However, realistic formation mechanisms generically predict extended mass distributions due to the finite width of the primordial power spectrum peak and the effects of critical collapse.

Extended mass functions are typically modeled as log-normal or power-law distributions. The precise shape of $f_{\rm PBH}(M)$ encodes information about the primordial perturbations and the collapse process, and plays a crucial role in comparing PBH scenarios with observational constraints.

PBH Abundance and the Fraction $\beta(M)$

The initial abundance of PBHs is commonly expressed in terms of the mass fraction at formation,

$$\beta(M) \equiv \frac{\rho_{\rm PBH}(t_{\rm f})}{\rho_{\rm tot}(t_{\rm f})}. \tag{1.69}$$

For Gaussian density fluctuations, $\beta(M)$ can be estimated using a Press–Schechter–type approach Press & Schechter (1974),

$$\beta(M) = 2\int_{\delta_{\rm c}}^{\infty} \frac{1}{\sqrt{2\pi}\sigma(M)} \exp\left(-\frac{\delta^2}{2\sigma^2(M)}\right) d\delta, \tag{1.70}$$

where $\sigma(M)$ is the variance of density contrast smoothed on the horizon scale.

The present-day fraction of dark matter in monochromatic PBHs is related to $\beta(M)$ by redshifting from formation to matter–radiation equality with $M_{\rm eq}$ being the horizon mass at that epoch, and $\Omega_{\rm cdm}$ is the dark matter density at present-day

Byrnes et al. (2018).

$$f_{\rm PBH}(M) \simeq \frac{\beta(M)}{\Omega_{\rm cdm}} \left(\frac{M}{M_{\rm eq}}\right)^{-1/2}. \tag{1.71}$$

This strong scaling implies that even extremely small initial abundances can translate into an appreciable dark matter fraction today. The expression changes for $f_{\rm PBH}(M)$ in case of non-monochromatic PBHs, and it has been discussed extensively in Chapter 4.

Observational Constraints

There have been extensive efforts to search for the PBHs using various observations. These include observations of the extragalactic γ-ray background, gravitational microlensing experiments (e.g., OGLE-I-IV, using Kepler objects, Eridanus-II star clusters), cosmic microwave background experiments, dynamical constraints, and accretion constraints (Laha 2019; Laha et al. 2020; Dasgupta et al. 2020; Carr & Kühnel 2020; Carr et al. 2021a, and the references therein) etc. More recently, gravitational wave astronomy has opened up a new avenue for the search of primordial black holes through the gravitational waves generated either by their coalescence or associated with their generation (Bird et al. 2016; Sasaki et al. 2016, 2018; Kapadia et al. 2020, 2021; Hütsi et al. 2021, and references therein).

Though PBH is a simple and well-motivated DM candidate, the present PBH dark matter density is subject to stringent constraints from various observational and theoretical studies Carr et al. (2021a). Although low mass PBHs are expected to evaporate via Hawking radiation faster, they are constrained by the extragalactic gamma-ray background, cosmic-ray measurements, and Big Bang nucleosynthesis. Those with initial mass $\gtrsim 10^{15}$ g have lifetime longer than the age of the Universe

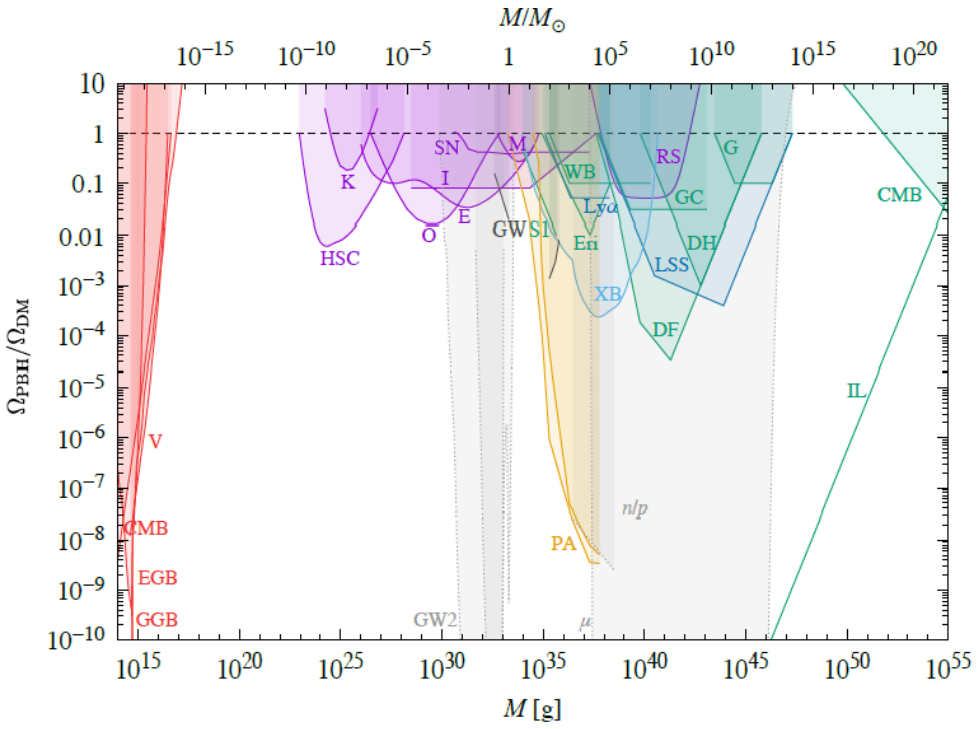


FIGURE 1.9: State-of-the-art constraints on PBH being dark matter, taken from Carr et al. (2021). The shaded regions exclude PBH from being a dark matter candidate. Only a small window remains open for PBH to contribute to the total dark matter density.

(Hawking 1974, 1975). Intermediate-mass PBHs are constrained by microlensing surveys, including EROS, MACHO, OGLE, and Kepler, as well as by dynamical heating of star clusters and wide binaries. Heavier PBHs are constrained by accretion effects on the CMB, large-scale structure, and by the stochastic gravitational-wave background and merger rates observed by LIGO–Virgo–KAGRA.

Figure 1.9 gives a nice overview of the current status of the PBH abundance constraints over all the possible mass ranges. From the figure, one can find that the potential allowed mass range over which PBHs can still make up for the entire dark matter belongs to the 10^{17}g - 10^{24}g ($10^{-16}M_\odot$ - $10^{-10}M_\odot$).

Cosmological Role of PBHs

In principle, at the time of their generation, PBHs could have masses starting from the Planck mass (10^{-5}g) to stupendously large masses such as $\sim 10^{17} M_{\odot}$, the horizon mass at the time of matter–radiation equality (Carr et al. 2021b). On a cosmological scale, PBH dark matter would behave almost like dark particle matter; however, depending on their mass, on galactic and smaller scales, it can have characteristic observable consequences. PBHs can also have implications in early black hole seeding, and formation of the first stars and galaxies, accretion onto massive enough PBHs can account for the detected X-ray and infrared backgrounds and their cross-correlation (Cappelluti et al. 2022, and references therein).

For these reasons, PBHs occupy a special place at the intersection of cosmology, astrophysics, and fundamental physics, and remain a subject of active theoretical and observational investigation.

1.11 Dark Energy: Observational Motivation and Theoretical Overview

The discovery that the expansion of the Universe is currently accelerating represents one of the central milestones of modern cosmology. Observations of distant Type Ia supernovae revealed that high-redshift supernovae appear systematically dimmer than expected in a decelerating universe, implying that the cosmic expansion rate has increased over the past few billion years Riess et al. (1998). Within the framework of General Relativity, this observation requires the presence of an energy component with sufficiently negative pressure to drive accelerated expansion.

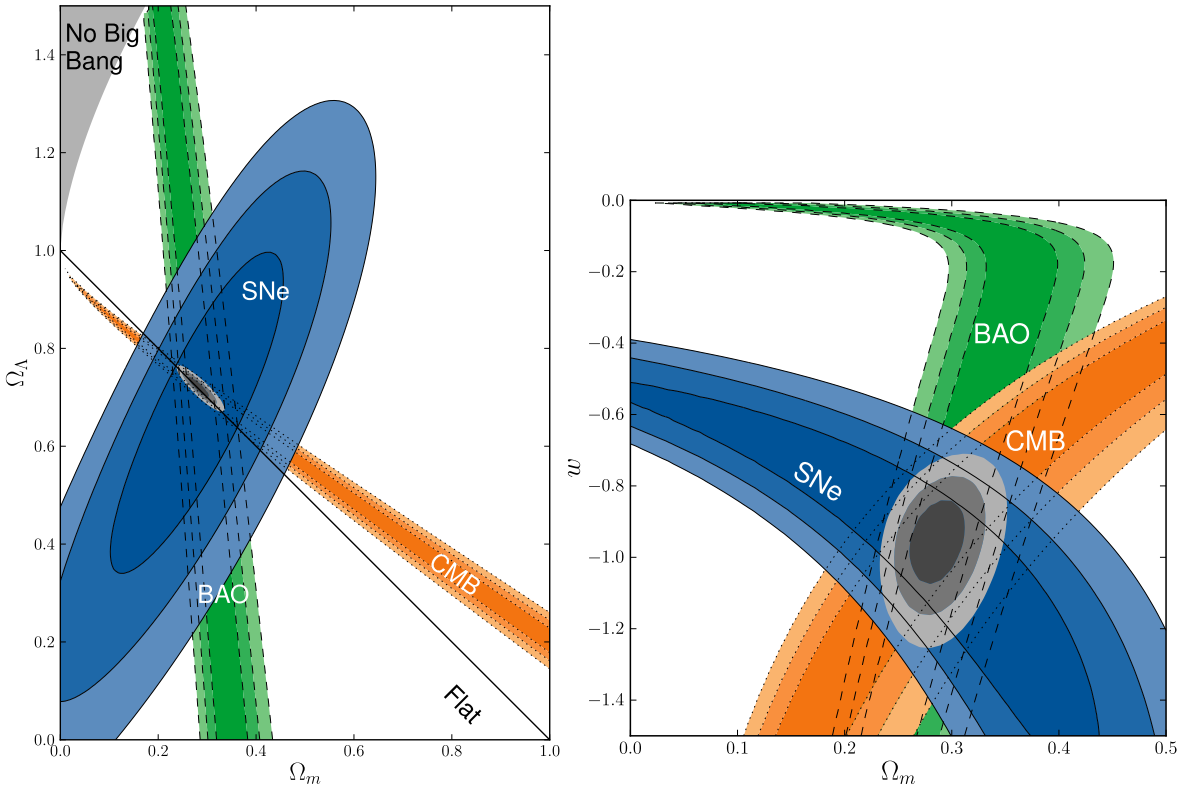


FIGURE 1.10: Obtained from Suzuki et al. (2012), the left panel shows the confidence region of Ω_Λ and Ω_m for ΛCDM model for CMB, BAO and SNe-Ia datsets. The right panel shows the confidence region for wCDM model where it shows that the data prefers cosmological constant, i.e. $w = -1$ as dark energy.

The condition for acceleration follows directly from the second Friedmann equation,

$$\frac{\ddot{a}}{a} = -\frac{4\pi G}{3} \sum_i \left(\rho_i + 3p_i\right), \tag{1.72}$$

where $a(t)$ is the scale factor and the sum runs over all cosmic components. Accelerated expansion, $\ddot{a} > 0$, therefore requires

$$\rho + 3p < 0 \quad \Longleftrightarrow \quad w \equiv \frac{p}{\rho} < -\frac{1}{3}. \tag{1.73}$$

Any component satisfying this inequality acts as a source of cosmic acceleration and is generically referred to as dark energy.

Cosmological Constant and the Vacuum Energy Interpretation

The simplest realization of dark energy is the cosmological constant Λ, corresponding to strictly constant vacuum energy density. In this case, the energy–momentum tensor takes the form

$$T^{\mu}_{\ \nu} = -\rho_\Lambda \, \delta^{\mu}_{\ \nu}, \tag{1.74}$$

with

$$p_\Lambda = -\rho_\Lambda, \qquad w_\Lambda = -1, \tag{1.75}$$

and a constant energy density $\rho_\Lambda = \Lambda/(8\pi G)$.

In the ΛCDM model, the late-time expansion history is governed by

$$H^2(a) = H_0^2 \left[\Omega_{\rm r} a^{-4} + \Omega_{\rm m} a^{-3} + \Omega_\Lambda \right], \tag{1.76}$$

which provides an excellent description of current observations over a wide range of redshifts Suzuki et al. (2012), as shown in Figure 1.10.

Despite its empirical success, the cosmological constant interpretation raises deep theoretical problems. From the perspective of quantum field theory, vacuum fluctuations generically contribute to the energy density with magnitude

$$\rho_{\rm vac}^{(\rm theory)} \sim \int^{\Lambda_{\rm UV}} \frac{d^3k}{(2\pi)^3} \, \frac{1}{2} \sqrt{k^2 + m^2}, \tag{1.77}$$

which, for any reasonable ultraviolet cutoff, exceeds the observed value

$$\rho_\Lambda^{(\rm obs)} \simeq 10^{-120} \, \rho_{\rm vac}^{(\rm theory)} \tag{1.78}$$

by many orders of magnitude. Explaining this enormous discrepancy constitutes the cosmological constant problem.

A second conceptual difficulty is the coincidence problem. While matter density scales as $\rho_{\rm m} \propto a^{-3}$ and radiation as $\rho_{\rm r} \propto a^{-4}$, the vacuum energy remains constant. The near equality

$$\rho_{\rm m}(a_0) \sim \rho_\Lambda \tag{1.79}$$

at the present epoch (shown in the left panel of Figure 1.10), therefore appears accidental, requiring an explanation of why cosmic acceleration begins only recently in cosmic history.

Dynamical Dark Energy and Quintessence

These theoretical difficulties motivate the exploration of dynamical alternatives to a constant vacuum energy Odintsov et al. (2025). The simplest class of such models is quintessence Copeland et al. (2006a); Ratra & Peebles (1988); Zlatev et al. (1999), in which the scalar field ϕ being the dark energy is minimally coupled to gravity and evolves in a potential $V(\phi)$, represented through the lagrangian,

$$\mathcal{L}_\phi = \frac{1}{2} g^{\mu\nu} \partial_\mu \phi \, \partial_\nu \phi - V(\phi). \tag{1.80}$$

From the corresponding energy-momentum tensor, we can derive the following expressions

$$\rho_\phi = \frac{1}{2}\dot{\phi}^2 + V(\phi) \qquad p_\phi = \frac{1}{2}\dot{\phi}^2 - V(\phi) \tag{1.81}$$

Here ρ_ϕ is the energy density and p_ϕ is the pressure of field ϕ. This leads to an equation of state

$$w_\phi = \frac{\frac{1}{2}\dot{\phi}^2 - V(\phi)}{\frac{1}{2}\dot{\phi}^2 + V(\phi)} \tag{1.82}$$

For a positive kinetic energy, $w_\phi \gtrsim -1$ Accelerated expansion requires the potential energy to dominate over the kinetic term, $\dot{\phi}^2 \ll V(\phi)$, so that $w_\phi \approx -1$ Tsujikawa

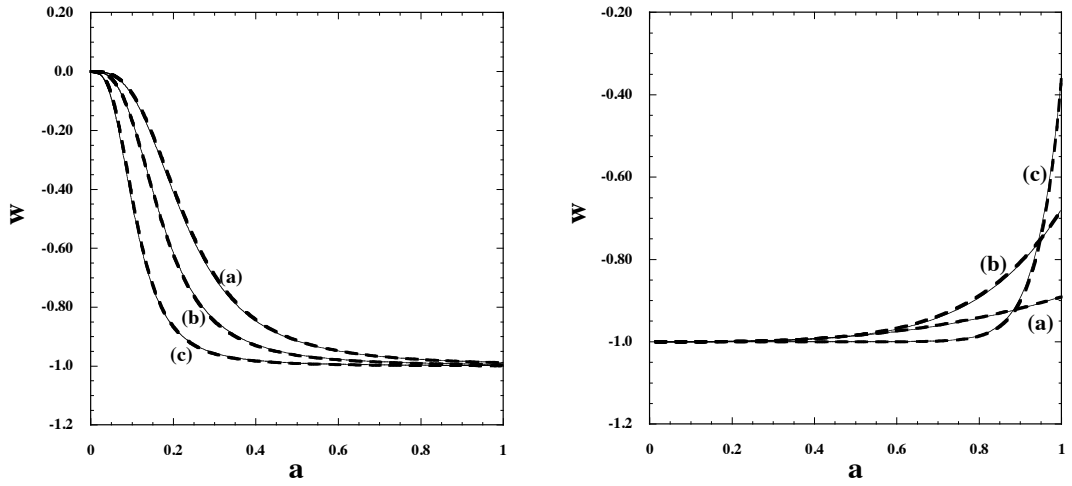


FIGURE 1.11: The evolution of equation of state parameter for quintessence dark energy field is shown here. Left panel shows freezing model and right panel shows the thawing model, which is obtained from Tsujikawa (2013a).

(2013b); Cahn et al. (2008); Bhattacharya et al. (2024a).

The scalar field obeys the Klein–Gordon equation,

$$\ddot{\phi} + 3H\dot{\phi} + \frac{dV}{d\phi} = 0, \tag{1.83}$$

which admits a wide variety of evolutionary behaviors depending on the form of $V(\phi)$.

A useful phenomenological classification distinguishes between freezing models, in which the field slows down and approaches $w \to -1$ at late times, and thawing models, where the field remains frozen by Hubble friction until recent epochs and only then begins to evolve Caldwell & Linder (2005); Linder (2006, 2015); Berbig (2025). These two behaviors lead to distinct evolution of w with scale factor, shown in Figure 1.11 and provide a framework for confronting dynamical dark energy with observations.

From a theoretical perspective, quintessence models require an extremely light scalar field with mass of order the present Hubble scale,

$$m_\phi^2 \sim \frac{d^2V}{d\phi^2} \sim H_0^2, \tag{1.84}$$

raising naturalness concerns regarding radiative stability and the suppression of couplings to visible matter. Also, the initial conditions, such as field position and velocity, are extremely fine-tuned to match the observed accelerating expansion of the universe at present epoch.

Phantom Dark Energy and Stability Issues

An even more exotic possibility is phantom dark energy, characterized by $w < -1$ Caldwell (2002). In a field-theoretic description, this requires a Lagrangian with negative kinetic energy Ludwick (2017); Caldwell et al. (2003),

$$\mathcal{L} = -\frac{1}{2}(\partial\phi)^2 - V(\phi) \tag{1.85}$$

leading to

$$\rho_\phi = -\frac{1}{2}\dot{\phi}^2 + V(\phi) \qquad p_\phi = -\frac{1}{2}\dot{\phi}^2 - V(\phi) \tag{1.86}$$

and hence $w_\phi < -1$ whenever the kinetic term is non-zero.

Such theories suffer from ghost instabilities and violate the null energy condition. For this reason, phantom dark energy is generally regarded as an effective description that may arise from more complete theories, rather than as a fundamental model.

Coupled Dark Energy and Interacting Models

Interacting dark energy models have also been an important extension of the dark energy paradigm by allowing energy exchange between dark energy and dark matter, a possibility motivated by theoretical arguments that a scalar field naturally couples to other sectors unless protected by symmetry Amendola (2000); Amendola et al. (2003a); Amendola & Quercellini (2003a); Amendola (2001). In such coupled dark energy models, the conservation equations are modified according to

$$\nabla_\mu T^{\mu\nu}_{(\mathrm{dm})} = +Q^\nu, \tag{1.87}$$

$$\nabla_\mu T^{\mu\nu}_{(\phi)} = -Q^\nu, \tag{1.88}$$

where Q^ν encodes the energy–momentum transfer between dark matter and dark energy.

At the background level, this leads to

$$\dot{\rho}_{\mathrm{dm}} + 3H\rho_{\mathrm{dm}} = +Q, \tag{1.89}$$

$$\dot{\rho}_\phi + 3H(\rho_\phi + p_\phi) = -Q, \tag{1.90}$$

so that the dilution of dark matter energy density and the scalar field evolution are both modified.

Such interactions can generate scaling solutions in which the ratio $\rho_{\mathrm{dm}}/\rho_\phi$ remains approximately constant over extended periods. As a result, the scalar field tracks the evolution of the dominant component of the universe, offering a dynamical mechanism to address the coincidence problem. Moreover, coupled models exhibit distinctive observational signatures, including the CMB, large-scale structure, and expansion history that can be probed with recent datasets with higher precision.

Consequently, numerous scalar-tensor theories have been proposed in the literature to model such interacting scenarios, opening up a rich phenomenological landscape to explore Damour et al. (1990); Casas et al. (1992); Anderson & Carroll (1998); Amendola & Tocchini-Valentini (2001); Bean (2001); Damour et al. (2002); Comelli et al. (2003); Amendola et al. (2003b); Chimento et al. (2003); Amendola & Quercellini (2003b); França & Rosenfeld (2004); Khoury & Weltman (2004a,b); Brax et al. (2004); Farrar & Peebles (2004); Gubser & Khoury (2004); Kaplan et al. (2004); Olivares et al. (2005); Wei & Cai (2005); Peccei (2005); Fardon et al. (2006); von Marttens et al. (2020b); Baker et al. (2022); Zhang (2022); Piedipalumbo et al. (2023); Brax et al. (2024); Käding et al. (2023); Singh et al. (2023); Burgess & Quevedo (2022); Brax et al. (2023); van der Westhuizen & Abebe (2024); Di Valentino et al. (2020); Bolotin et al. (2014); Pan et al. (2020); Lucca & Hooper (2020); Di Valentino et al. (2020, 2021); Liu et al. (2022); Li et al. (2020a); Bachega et al. (2020); Li et al. (2020b); Mukhopadhyay et al. (2020); von Marttens et al. (2020a); Kase & Tsujikawa (2020a); Liu et al. (2020); Kase & Tsujikawa (2020b); Chamings et al. (2020); Benisty et al. (2020a); Amendola & Tsujikawa (2020); Benisty et al. (2020b); Yang et al. (2020); Barrow & Kittou (2020); Silva et al. (2024); Shah et al. (2023); de Souza et al. (2024); Halder et al. (2024); Shah et al. (2024, 2025a). Beyond these phenomenological and scalar–tensor theories, several recent studies have developed DM-DE interaction models based directly on particle physics and string-theoretic frameworks Khoury et al. (2025); Bedroya et al. (2025). These works provide concrete examples of theoretically motivated interactions that can naturally lead to evolving dark energy behavior, including trends broadly consistent with the departures from ΛCDM suggested by recent DESI measurements.

Motivation from Recent Observations

While the ΛCDM model remains consistent with current data at the background level, recent high-precision measurements have begun to test the assumption that dark energy is exactly constant. Very recently, Baryon Acoustic Oscillation (BAO) measurements from the first year results from DESI have injected new momentum into dark energy model building Adame et al. (2025); Calderon et al. (2024); Lodha et al. (2025b); Abdul Karim et al. (2025); Lodha et al. (2025c). The latest results from the DESI collaboration indicate strong deviations from a pure constant $w = -1$ behavior, with hints of redshift evolution of the equation of state, shown in Figure 1.12. With a strong statistical significance of these deviations, they motivate a systematic exploration of alternative dark energy models.

BAO provides a standard ruler imprinted in the late-time clustering of matter. The physical length of this ruler is set by comoving sound horizon at baryon drag epoch,

$$r_d \equiv r_s(z_d) = \int_{z_d}^{\infty} \frac{c_s(z)}{H(z)}\, dz, \qquad c_s(z) = \frac{c}{\sqrt{3\,[1+R(z)]}}, \qquad R(z) = \frac{3\rho_b(z)}{4\rho_\gamma(z)}. \tag{1.91}$$

Here z_d (the drag epoch) denotes the redshift below which Compton drag becomes inefficient and baryons are no longer tightly coupled to photons. In practice, r_d controls the BAO scale in the late-time galaxy distribution.

Observationally, BAO analyses extract the location of the acoustic feature in the two-point statistics of galaxies (or quasars / Lyman-α tracers) both transverse and radial to the line of sight. This yields constraints on the dimensionless combinations

$$\frac{D_M(z)}{r_d}, \qquad \frac{D_H(z)}{r_d}, \tag{1.92}$$

where

$$D_H(z) = \frac{c}{H(z)}, \qquad D_M(z) = (1+z)\, D_A(z) \;=\; c \int_0^z \frac{dz'}{H(z')} \quad \text{(spatially flat)}. \tag{1.93}$$

Some analyses also report an isotropic BAO distance,

$$D_V(z) \equiv \left[z\, D_M^2(z)\, D_H(z) \right]^{1/3}, \tag{1.94}$$

which compresses the anisotropic information into a single scale. Because $D_M(z)$ and $D_H(z)$ are integrals (or inverse) of $H(z)$, BAO measurements directly probe the expansion history and therefore constrain dark energy through its impact on $H(z)$ at low redshift. In combination with a prior on r_d (often supplied by early-universe physics as constrained by the CMB), BAO becomes a sharp test of late-time acceleration.

DESI measures BAO across a wide redshift range using multiple tracers like galaxies, quasars, Lyman-α observations, etc., thereby mapping $D_M(z)/r_d$ and $D_H(z)/r_d$ with high statistical precision. These measurements, when combined with complementary probes such as Type Ia supernovae and CMB constraints on the early Universe, yield constraints on the expansion history at late times, specifically probing the behaviour of dark energy.

First of all, along with several other combinations of data sets like Type Ia supernova (SN Ia) and CMB, if DESI data is fitted with a dark energy sector with a *constant* equation of state parameter w (namely wCDM model), it is fully consistent with $w = -1$. This hints towards a cosmological constant.

Relying on the poor theoretical understanding of the origin of the cosmological constant Martin (2012); Bamba et al. (2012), in particular, its required magnitude, the data is fitted with a dark energy sector, which is dynamical Adame et al. (2025); Abdul Karim et al. (2025). Considering that the origin of the dark sector

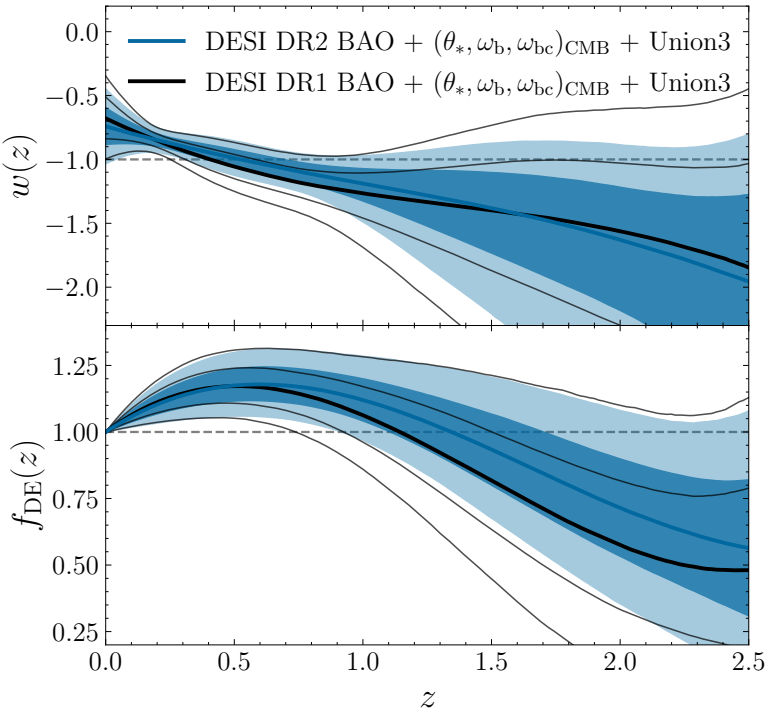


FIGURE 1.12: The upper panel depicts evolution of dark energy equation of state parameter reconstructed from MCMC analysis for w_0w_aCDM model using CMB, DESI, and Union 3 dataset. The lower panel shows the evolution of dark energy density normalized to its present-day energy density $f_{DE} = \frac{\rho_{DE}(z)}{\rho^0_{DE}}$. The image is taken from Lodha et al. (2025a).

is still unknown, it was parameterized by two constant parameters (known as CPL parameterization Chevallier & Polarski (2001); Linder (2003)) w_0 and w_a, in the following manner,

$$w(a) = w_0 + w_a(1 - a), \tag{1.95}$$

Depending on various SN Ia data combinations with CMB, DESI data found that $w_0 > -1$ and $w_a < 0$ with a significance varying from 2.5σ to 3.9σ *. For completeness, the specific quoted constraints from the DESI analysis when CMB and Pantheon+ datasets are combined,

$$w_0 = -0.838 \pm 0.055, \qquad w_a = -0.62^{+0.22}_{-0.19}, \tag{1.96}$$

*Interpreting DESI results in terms of a specific parameterization has been criticized at Shlivko & Steinhardt (2024a); Cortês & Liddle (2024); Gialamas et al. (2025); Huang et al. (2025); Roy Choudhury & Okumura (2024); Colgáin & Sheikh-Jabbari (2024); Park & Ratra (2025); Park et al. (2024a); Banerjee et al. (2021); Lee et al. (2022).

as reported in Adame et al. (2025); Abdul Karim et al. (2025). The time evolution of the equation of state parameter and fractional energy density normalized to present epoch has been shown in Figure 1.12.

This interpretation of data means that ΛCDM is disfavored at ~ 2.8–4.2σ. Moreover, the above constraint on w_0 and w_a would mean that the dark energy sector had an equation of state $w < -1$ for $z > 1$ that crossed $w = -1$ phantom barrier at some recent past with its present value $w_0 > -1$ Linder (2024). To bolster the above arguments, the DESI collaboration reconstructed the equation of state of the dark energy sector by writing its equation of state $w(z)$ in terms of orthogonal polynomials Calderon et al. (2024); Lodha et al. (2025c). It was reported that the data favors evolving dark energy with cosmological constant lying outside 2-σ confidence contour for some redshift ranges. Moreover, the findings agree with the interpretation in terms of w_0 and w_a. A similar conclusion, albeit depending on the dataset used, was drawn in Mukherjee & Sen (2024); Jiang et al. (2024); Ye et al. (2024); Wolf et al. (2025b,a); Ferrari et al. (2025). Also, non-DESI data has been used to confirm and strengthen the DESI 2024 Park et al. (2024b). Moreover, DESI has been tested against several other parameterizations than CPL, and all lead towards dynamical dark energy Giarè et al. (2024a).

In short, DESI collaboration results hint towards tantalizing evidence for evolving dark energy that shows phantom crossing. In this thesis, we focus on a class of coupled dark energy scenarios arising from Yukawa-type interactions between a scalar field and dark matter fermions. These models provide a concrete realization in which the effective equation of state can cross the phantom divide without introducing fundamental instabilities, and allow a unified treatment of background evolution and structure formation. The theoretical formulation and observational consequences of these models are investigated in detail in Chapters 5 and 6.

1.12 Outlines

The thesis is organized as follows. Chapter 2 introduces the statistical framework used for parameter inference and model comparison. Chapter 3 studies mass-varying dark matter and early-time deviations from the standard cold dark matter paradigm. Chapter 4 is devoted to primordial black holes as dark matter candidates and to a novel formation mechanism driven by Yukawa-type interactions. Chapters 5 and 6 present the formulation and cosmological implications of coupled dark energy models having a similar type of Yukawa interactions to explain DESI observations. Finally, Chapter 7 summarizes the main results of the thesis and discusses possible future works.

Chapter 2

Statistical Methods

2.1 Introduction

Modern cosmology is an intrinsically statistical science. Unlike laboratory experiments, where physical systems can be prepared repeatedly under controlled conditions, cosmological observations provide us with a single realization of the Universe, observed through incomplete, noisy, and indirect measurements. Fundamental quantities such as the dark matter abundance, the properties of dark energy, or the amplitude of primordial fluctuations cannot be measured directly, but must instead be inferred by confronting theoretical models with observational data across a wide range of cosmic probes.

As a consequence, progress in cosmology relies not only on the construction of physically motivated models, but equally on the development of robust statistical frameworks capable of extracting reliable information from high-dimensional and imperfect datasets. Parameter estimation, uncertainty quantification, and model comparison play a central role in all stages of cosmological analysis, from the

interpretation of cosmic microwave background anisotropies to the study of large-scale structure and gravitational lensing. In this context, statistical inference is not merely a technical tool, but an essential component of the scientific methodology underlying precision cosmology Heavens (2010); Verde (2007); Trotta (2008).

The rapid increase in the volume and quality of cosmological data over the past two decades has further amplified the importance of advanced statistical techniques. Current experiments routinely constrain models with ten or more free parameters, often in the presence of strong degeneracies and non-Gaussian likelihoods. Exploring such parameter spaces exhaustively using deterministic methods is computationally expensive, making stochastic sampling techniques indispensable. In particular, Markov Chain Monte Carlo (MCMC) algorithms Metropolis et al. (1953); Hastings (1970) have become the standard approach for parameter inference in cosmology.

The analyses presented in this thesis rely extensively on Bayesian inference and MCMC sampling to extract constraints on cosmological parameters and to assess the statistical viability of different theoretical models. Numerical pipelines such as `CLASS` Lesgourgues (2011) for the computation of cosmological observables and `MontePython` Brinckmann & Lesgourgues (2018) for Bayesian parameter estimation form the backbone of this approach. These tools allow one to construct a likelihood function for a given dataset, explore the corresponding posterior distribution in a high-dimensional parameter space, and derive statistically meaningful constraints on both background and perturbation-level quantities.

Beyond parameter estimation, modern cosmology increasingly demands a careful assessment of competing theoretical frameworks. When extending the standard ΛCDM model, for instance by introducing new dark sector interactions or additional degrees of freedom, it is not sufficient to demonstrate an improved fit to a given dataset. One must also quantify whether the increased model complexity is

justified by the data. Model comparison criteria, such as the Akaike Information Criterion (AIC) Akaike (1974), provide a principled way to balance goodness of fit against the number of free parameters, and play an important role in the interpretation of the results presented in later chapters of this thesis. This chapter establishes the statistical and computational framework that will be used throughout this thesis to extract robust cosmological constraints from observational data.

2.2 Probability and the Frequentist Approach

The starting point of any statistical analysis is the mathematical definition of probability. In its most elementary form, probability is introduced through the concept of relative frequency. Consider an experiment with N identical and independent trials, in which a particular event A occurs n times. The probability of the event A is then defined as

$$P(A) = \lim_{N\to\infty} \frac{n}{N}, \tag{2.1}$$

provided that the limit exists. This definition, familiar from elementary probability theory, identifies probability with the long-run frequency of occurrence of an event in a large ensemble of repeated experiments.

In a more general and abstract formulation, probability is defined as a measure satisfying a set of axioms. Let Ω denote the sample space of all possible outcomes and let A and B be subsets of Ω. A probability measure P assigns to each event

$A \subset \Omega$ a real number $P(A)$ such that

$$P(A) \geq 0, \tag{2.2}$$

$$P(\Omega) = 1, \tag{2.3}$$

$$P(A \cup B) = P(A) + P(B), \qquad \text{for } A \cap B = \varnothing. \tag{2.4}$$

For a continuous random variable x, probability is described by a probability density function $p(x)$, normalized according to

$$\int_{-\infty}^{+\infty} p(x)\, dx = 1, \tag{2.5}$$

such that the probability for x to lie in an interval $[a, b]$ is given by

$$P(a \leq x \leq b) = \int_a^b p(x)\, dx. \tag{2.6}$$

The interpretation underlying these definitions is known as the frequentist interpretation of probability. In this viewpoint, probability is not a degree of belief but a property of an ensemble of repeated experiments. Randomness is associated with the outcome of the experiment, while the parameters describing the underlying physical model are regarded as fixed but unknown constants.

Within the frequentist framework, statistical inference is based on the hypothetical repetition of the same experiment an infinite number of times under identical conditions. In cosmology, this concept is commonly implemented by treating different regions of the Universe, Fourier modes, or large samples of astrophysical objects as an effective ensemble, relying on ergodicity. However, within this framework, model parameters are regarded as fixed but unknown quantities, and probability statements are assigned only to data realizations, so that confidence intervals do not directly represent probabilities for the parameters themselves. Moreover, the

incorporation of prior theoretical information and the comparison of non-nested models are not naturally formulated in the frequentist approach. For these reasons, although frequentist methods remain valuable in cosmological data analysis, it is often advantageous to adopt a Bayesian framework, in which probability is interpreted as a degree of belief conditioned on available information. In the next section, we introduce the Bayesian interpretation of probability and Bayes' theorem as the basis of the inference methods used throughout this thesis.

2.3 Bayesian Probability and Bayes' Theorem

In the Bayesian framework, probability is interpreted as a quantitative measure of plausibility assigned to a proposition, given a specified state of information. This interpretation extends the elementary definition of probability as a frequency ratio and allows probabilities to be assigned to hypotheses, model parameters, and theoretical statements, in addition to repeatable random events.

Let A and B denote two propositions, and let $\mathcal{I}$ represent the background information. The conditional probability $P(A|B,\mathcal{I})$ is defined as the probability that A is true given that B and $\mathcal{I}$ are true. The axioms of probability theory imply the product rule,

$$P(A,B|\mathcal{I}) = P(A|B,\mathcal{I})\,P(B|\mathcal{I}), \tag{2.7}$$

which expresses the joint probability of A and B. By symmetry, the joint probability can equally be written as

$$P(A,B|\mathcal{I}) = P(B|A,\mathcal{I})\,P(A|\mathcal{I}). \tag{2.8}$$

Since the left-hand sides of Eqs. (2.7) and (2.8) are identical, equating the right-hand sides yields

$$P(A|B,\mathcal{I})\,P(B|\mathcal{I}) = P(B|A,\mathcal{I})\,P(A|\mathcal{I}). \tag{2.9}$$

Rearranging this expression leads directly to Bayes' theorem,

$$P(A|B,\mathcal{I}) = \frac{P(B|A,\mathcal{I})\,P(A|\mathcal{I})}{P(B|\mathcal{I})}. \tag{2.10}$$

In statistical inference, the abstract propositions are replaced by a set of model parameters $\boldsymbol{\theta}$ and an observed data set $\mathcal{D}$, under an assumed model $\mathcal{M}$. Bayes' theorem then takes the form

$$P(\boldsymbol{\theta}|\mathcal{D},\mathcal{M}) = \frac{P(\mathcal{D}|\boldsymbol{\theta},\mathcal{M})\,P(\boldsymbol{\theta}|\mathcal{M})}{P(\mathcal{D}|\mathcal{M})}. \tag{2.11}$$

This equation provides the mathematical foundation of Bayesian parameter inference, describing how prior knowledge about the parameters is updated in the light of new data.

2.4 Prior, Likelihood, Posterior and Evidence

Equation (2.11) decomposes Bayesian inference into four distinct ingredients, each of which plays a well-defined conceptual and practical role in statistical analysis.

The quantity

$$P(\boldsymbol{\theta}|\mathcal{M}) \tag{2.12}$$

is the *prior* distribution. It encodes the knowledge on parameters $\boldsymbol{\theta}$ before the

data are analyzed, under the assumption of the model $\mathcal{M}$. In cosmological applications, priors are typically chosen to be uniform over physically allowed ranges or motivated by independent measurements, so as to avoid introducing unwarranted information into the analysis.

The factor

$$P(\mathcal{D}|\boldsymbol{\theta}, \mathcal{M}) \tag{2.13}$$

is the *likelihood*. For a fixed parameter set, it quantifies the probability of obtaining the observed data under the assumed model. As a function of $\boldsymbol{\theta}$, the likelihood measures the relative support that the data provide for different regions of parameter space. It is not a probability distribution over the parameters, but rather a probability distribution over the data, evaluated at the observed realization.

The quantity

$$P(\boldsymbol{\theta}|\mathcal{D}, \mathcal{M}) \tag{2.14}$$

is the *posterior* distribution. It represents the probability density of the parameters after the information contained in the data has been taken into account. All parameter constraints, confidence regions, and derived quantities reported in Bayesian analyses are obtained from this posterior distribution.

The denominator in Bayes' theorem,

$$P(\mathcal{D}|\mathcal{M}) = \int P(\mathcal{D}|\boldsymbol{\theta}, \mathcal{M})\, P(\boldsymbol{\theta}|\mathcal{M})\, \mathrm{d}\boldsymbol{\theta}, \tag{2.15}$$

is known as *evidence*. It ensures the proper normalization of the posterior. Beyond normalization, the evidence plays a central role in Bayesian model comparison, since it quantifies the overall probability of the data under a given model after averaging over its parameter space.

Equation (2.11) makes explicit how information is updated in the Bayesian framework. The posterior combines the information carried by the data, summarized by the likelihood, with the prior knowledge encoded in the prior distribution. In the limit of highly informative data, the posterior becomes largely insensitive to the prior, while in poorly constrained directions of parameter space the posterior retains sensitivity to prior assumptions.

2.5 Goodness of fit, χ^2, confidence regions, and marginalisation

A central goal of statistical analysis in cosmology is to quantify how well a theoretical model reproduces a given set of observational data, and to determine the range of parameter values that are consistent with the data within specified level of statistical uncertainty. These tasks are commonly formulated in terms of goodness-of-fit measures, confidence regions, and marginalised probability distributions.

The χ^2 statistic and goodness of fit

Consider a data vector $\mathbf{d} = \{d_i\}$ consisting of N measured data points, and a theoretical model $\mathbf{m}(\boldsymbol{\theta}) = \{m_i(\boldsymbol{\theta})\}$ depending on a set of parameters $\boldsymbol{\theta}$. If the measurement errors are assumed to be Gaussian and characterized by a covariance matrix $\mathbf{C}$, the likelihood becomes

$$\mathcal{L}(\boldsymbol{\theta}) \propto \exp\left[-\frac{1}{2}\chi^2(\boldsymbol{\theta})\right] \tag{2.16}$$

where the χ^2 statistic is defined by

$$\chi^2(\boldsymbol{\theta}) = \sum_{i,j=1}^{N} \left[d_i - m_i(\boldsymbol{\theta})\right] C_{ij}^{-1} \left[d_j - m_j(\boldsymbol{\theta})\right]. \tag{2.17}$$

The quantity $\chi^2(\boldsymbol{\theta})$ measures the weighted squared distance between the data and the model predictions. The best-fit parameters $\boldsymbol{\theta}_{\rm bf}$ are obtained by minimizing $\chi^2(\boldsymbol{\theta})$, or equivalently by maximizing the likelihood.

The goodness of fit of a model is commonly assessed using the minimum value $\chi^2_{\rm min} = \chi^2(\boldsymbol{\theta}_{\rm bf})$. For a model with k free parameters fitted to N data points, the number of degrees of freedom is $\nu = N - k$, and the reduced chi-square is defined as

$$\chi^2_{\rm red} = \frac{\chi^2_{\rm min}}{\nu}. \tag{2.18}$$

A value $\chi^2_{\rm red} \simeq 1$ indicates an acceptable fit under the assumption of correctly estimated Gaussian errors, while significantly larger or smaller values may indicate a poor model fit or misestimated uncertainties.

Confidence regions from the likelihood

In parameter estimation, one is often interested in determining the region of parameter space that is consistent with the data at a given confidence level. For Gaussian-distributed errors, confidence regions can be constructed from the variation of χ^2 around its minimum.

For a set of parameters $\boldsymbol{\theta}$, the confidence region at a given confidence level is defined by the condition

$$\Delta\chi^2(\boldsymbol{\theta}) \equiv \chi^2(\boldsymbol{\theta}) - \chi^2_{\min} \leq \Delta\chi^2_\alpha, \tag{2.19}$$

where the threshold $\Delta\chi^2_\alpha$ depends on the desired confidence level and on the number of parameters being considered.

For example, for one parameter of interest, the standard values are

$$\Delta\chi^2 = \begin{cases} 1.00, & 68.3\% \text{ confidence}, \\ 4.00, & 95.4\% \text{ confidence}, \\ 9.00, & 99.7\% \text{ confidence}, \end{cases} \tag{2.20}$$

corresponding to the familiar 1σ, 2σ, and 3σ intervals for a Gaussian distribution. For two parameters of interest, the corresponding values are $\Delta\chi^2 = 2.30, 6.18$, and 11.83, defining elliptical confidence contours in the parameter plane.

These confidence regions provide a frequentist interpretation of parameter uncertainties under the assumption that the likelihood is well approximated by a multivariate Gaussian near its maximum.

Marginalisation over nuisance parameters

In cosmological analyses, the parameter vector $\boldsymbol{\theta}$ typically contains both parameters of direct physical interest and nuisance parameters that encode astrophysical or instrumental uncertainties. To obtain constraints on a subset of parameters, it is necessary to marginalise over the remaining degrees of freedom.

In the Bayesian framework, the marginal posterior for a parameter θ_i is obtained by integrating the full posterior over all other parameters:

$$P(\theta_i|\mathcal{D},\mathcal{M}) = \int P(\boldsymbol{\theta}|\mathcal{D},\mathcal{M})\, d\theta_1 \cdots d\theta_{i-1}\, d\theta_{i+1} \cdots d\theta_n. \tag{2.21}$$

This procedure yields the probability distribution for θ_i after accounting for the uncertainties and correlations associated with all other parameters. From the marginal posterior, one can define credible intervals by enclosing a specified fraction of the total probability, such as 68% or 95%.

In the special case where the posterior is Gaussian, marginalisation corresponds to projecting the multivariate Gaussian onto the subspace of interest. In general cosmological applications, however, the posterior is non-Gaussian and high-dimensional, and the marginalisation integrals in Eq. (2.21) cannot be performed analytically.

This motivates the use of numerical sampling techniques, such as Markov Chain Monte Carlo methods, which allow one to estimate marginal distributions, confidence regions, and parameter correlations directly from samples drawn from the posterior distribution.

2.6 Monte Carlo Methods and Markov Chain Monte Carlo

In Bayesian parameter estimation, the central task is to characterize the posterior probability distribution $P(\boldsymbol{\theta} \mid D)$ over a multidimensional parameter space. In realistic cosmological applications this distribution is not available in analytic form

and can only be evaluated numerically at discrete points. Monte Carlo methods provide a general strategy to extract statistical information from such distributions by generating ensembles of parameter values whose empirical distribution reproduces the posterior. In practice, this is achieved using Markov Chain Monte Carlo techniques, which construct correlated sequences of samples with the desired stationary distribution. In this section, we introduce the MCMC framework employed in this thesis.

Monte Carlo error estimation

In parameter estimation problems, it is useful to adopt an ensemble interpretation of what is meant by a "measured" set of cosmological parameters. Let $\boldsymbol{\alpha}_{\rm true}$ denote the unknown true values of the parameters that describe the physical Universe. These parameters are realized in a particular cosmological history, and the observer measures a single data set $\mathbf{D}_0$, affected by instrumental noise, cosmic variance, and other sources of statistical uncertainty. From this single realization, one constructs an estimator $\boldsymbol{\alpha}_0$ by minimizing a χ^2 function or maximizing a likelihood.

Conceptually, however, $\mathbf{D}_0$ is only one element of a hypothetical ensemble of possible data sets that could have been obtained from the same underlying model. If the Universe could be observed repeatedly under identical physical conditions but with independent realizations of the statistical noise, one would obtain a sequence of data sets

$$\mathbf{D}_0,\ \mathbf{D}_1,\ \mathbf{D}_2,\ \ldots, \tag{2.22}$$

leading to a corresponding sequence of parameter estimates

$$\boldsymbol{\alpha}_0,\ \boldsymbol{\alpha}_1,\ \boldsymbol{\alpha}_2,\ \ldots. \tag{2.23}$$

The statistical uncertainty of the measurement is encoded in the distribution of $\boldsymbol{\alpha}_i - \boldsymbol{\alpha}_{\rm true}$ over this ensemble. In the ideal limit, the expectation value of this distribution satisfies

$$\langle \boldsymbol{\alpha}_i \rangle = \boldsymbol{\alpha}_{\rm true}, \tag{2.24}$$

while its covariance determines the error bars and correlations of the inferred parameters.

In practice, the true parameters $\boldsymbol{\alpha}_{\rm true}$ are unknown and the ensemble of repeated Universes is not accessible. Monte Carlo error estimation provides a practical strategy to approximate this ensemble distribution using numerical simulations. The basic assumption is that the measured best-fit parameters $\boldsymbol{\alpha}_0$ are sufficiently close to $\boldsymbol{\alpha}_{\rm true}$ that one may treat $\boldsymbol{\alpha}_0$ as a fiducial model for the purpose of estimating uncertainties.

One then generates a large number of synthetic data sets by simulating the observation process under the assumption that $\boldsymbol{\alpha}_0$ is the true underlying model. For each synthetic realization $\mathbf{D}_i^{(\rm sim)}$, the full parameter estimation procedure is repeated, yielding a sequence of simulated estimates $\boldsymbol{\alpha}_i^{(\rm sim)}$. The distribution of the differences

$$\boldsymbol{\alpha}_i^{(\rm sim)} - \boldsymbol{\alpha}_0 \tag{2.25}$$

provides an empirical approximation to the unknown distribution of $\boldsymbol{\alpha}_i - \boldsymbol{\alpha}_{\rm true}$. In this way, the sampling distribution of the estimator is reconstructed without explicit knowledge of the true parameters Verde (2007).

This approach allows one to determine confidence regions, parameter correlations, and potential biases in a controlled manner, provided that the simulation accurately reproduces the statistical properties of the data and the relevant observational effects. Monte Carlo error estimation therefore plays a central role in

modern cosmological analyses, both as a validation tool for analytical error estimates and as a benchmark for more sophisticated Bayesian sampling methods introduced in the following sections.

Markov chains and posterior sampling

In Bayesian inference, the central object of interest is the posterior distribution $P(\boldsymbol{\theta} \mid \mathbf{D})$, which encodes all statistical information about the model parameters $\boldsymbol{\theta}$ given the observed data $\mathbf{D}$. For realistic cosmological models, this distribution is typically defined in a high-dimensional parameter space and has no closed analytic form. Direct numerical integration of the posterior is therefore impractical, and one must resort to sampling methods to explore its structure.

A powerful class of algorithms for this purpose is based on Markov chains. A Markov chain is a stochastic sequence of points $\{\boldsymbol{\theta}_0, \boldsymbol{\theta}_1, \boldsymbol{\theta}_2, \ldots\}$ in parameter space with the property that the probability of moving to the next point depends only on the current position,

$$P(\boldsymbol{\theta}_{n+1} \mid \boldsymbol{\theta}_n, \boldsymbol{\theta}_{n-1}, \ldots) = P(\boldsymbol{\theta}_{n+1} \mid \boldsymbol{\theta}_n). \tag{2.26}$$

The chain is constructed in such a way that, after a sufficiently long evolution, the distribution of sampled points converges to a stationary distribution equal to the target posterior,

$$\lim_{n\to\infty} P(\boldsymbol{\theta}_n \in d\boldsymbol{\theta}) = P(\boldsymbol{\theta} \mid \mathbf{D})\, d\boldsymbol{\theta}. \tag{2.27}$$

Once this stationary regime is reached, simple averages over the chain provide unbiased estimates of posterior expectation values. For any function $f(\boldsymbol{\theta})$, one

has

$$\langle f(\boldsymbol{\theta}) \rangle \simeq \frac{1}{N} \sum_{n=1}^{N} f(\boldsymbol{\theta}_n), \tag{2.28}$$

where the $\boldsymbol{\theta}_n$ are samples drawn from the stationary part of the chain. In this way, multidimensional integrals over the posterior are replaced by averages over a discrete sequence of sampled points.

The construction of a Markov chain with the desired stationary distribution is achieved by defining a suitable transition probability between points in parameter space. Among the many possible algorithms, the Metropolis–Hastings method is the most widely used in cosmological parameter estimation and forms the basis of modern sampling codes such as `MontePython`.

The Metropolis–Hastings algorithm

A Markov chain is built by proposing a new point in parameter space from the current point and then deciding whether to accept the move. If one were to accept *only* moves that increase the target probability, the chain would quickly get trapped near a local maximum and fail to explore the full posterior volume. The Metropolis–Hastings (MH) algorithm Metropolis et al. (1953); Hastings (1970) provides a simple acceptance rule that permits occasional moves to lower probability regions, thereby ensuring efficient exploration and, under mild conditions, convergence to the desired stationary distribution.

Let $\boldsymbol{\theta}_i$ denote the current parameter vector, and let the target distribution be the posterior

$$P(\boldsymbol{\theta} \mid \mathbf{D}) \propto \mathcal{L}(\mathbf{D} \mid \boldsymbol{\theta})\, \pi(\boldsymbol{\theta}), \tag{2.29}$$

which is proportional to the product of likelihood and prior. A proposal distribution $q(\boldsymbol{\theta}^* \mid \boldsymbol{\theta}_i)$ is used to generate a candidate point $\boldsymbol{\theta}^*$.

The MH algorithm proceeds as follows:

1. Choose an initial point $\boldsymbol{\theta}_i$ in parameter space and evaluate the unnormalised posterior

$$\tilde{P}_i \equiv \mathcal{L}(\mathbf{D} \mid \boldsymbol{\theta}_i)\, \pi(\boldsymbol{\theta}_i). \tag{2.30}$$

2. Given the current point $\boldsymbol{\theta}_i$, draw a candidate $\boldsymbol{\theta}^*$ from the proposal density

$$\boldsymbol{\theta}^* \sim q(\boldsymbol{\theta}^* \mid \boldsymbol{\theta}_i), \tag{2.31}$$

   and compute the corresponding unnormalised posterior

$$\tilde{P}_* \equiv \mathcal{L}(\mathbf{D} \mid \boldsymbol{\theta}^*)\, \pi(\boldsymbol{\theta}^*). \tag{2.32}$$

3. Form the acceptance ratio

$$r \;=\; \frac{\tilde{P}_*\, q(\boldsymbol{\theta}_i \mid \boldsymbol{\theta}^*)}{\tilde{P}_i\, q(\boldsymbol{\theta}^* \mid \boldsymbol{\theta}_i)}, \tag{2.33}$$

   and define the acceptance probability

$$p(X) \;=\; \min\left(1,\, r\right). \tag{2.34}$$

4. If $p(\boldsymbol{\theta}^*) > p(\boldsymbol{\theta}_i)$ then accept the proposal and set

$$\boldsymbol{\theta}_{i+1} = \boldsymbol{\theta}^*, \qquad \tilde{P}_{i+1} = \tilde{P}_*. \tag{2.35}$$

5. If $p(\boldsymbol{\theta}^*) < p(\boldsymbol{\theta}_i)$, then consider $\alpha = \frac{p(\boldsymbol{\theta}^*)}{p(\boldsymbol{\theta}_i)}$ and draw a random number n from uniform distribution $n \sim \mathcal{U}[0, 1]$. If $\alpha > n$, accept the proposal and fix

$$\boldsymbol{\theta}_{i+1} = \boldsymbol{\theta}^*, \qquad \tilde{P}_{i+1} = \tilde{P}_*. \tag{2.36}$$

Otherwise reject the proposal and keep the current state,

$$\boldsymbol{\theta}_{i+1} = \boldsymbol{\theta}_i, \qquad \tilde{P}_{i+1} = \tilde{P}_i. \tag{2.37}$$

6. Repeat steps (2)–(5) until the chain contains a sufficiently large number of samples. After discarding an initial burn-in phase, the remaining samples are used to estimate posterior moments and credible regions.

In practice, the posterior is only known up to a normalisation constant, and the acceptance ratio can be evaluated using the unnormalised posterior,

$$P(\boldsymbol{\theta} \mid \mathbf{D}) \propto \mathcal{L}(\mathbf{D} \mid \boldsymbol{\theta})\, \pi(\boldsymbol{\theta}), \tag{2.38}$$

so that the Bayesian evidence cancels out of the acceptance probability. This makes the algorithm particularly well suited for high-dimensional cosmological applications.

The efficiency of the sampling depends crucially on the choice of proposal distribution. If the proposed steps are too small, the chain explores parameter space slowly and successive samples are highly correlated. Very large steps make acceptance rate go very low, leading to a poor mixing of chain. In practice, the proposal covariance is tuned adaptively to achieve an acceptance rate of order 20–30%, which is close to optimal for multivariate targets.

Burn-in, Autocorrelation, and Convergence

In practice, the initial part of the chain depends on the arbitrary starting point and does not represent the stationary distribution. This initial phase, known as the burn-in period, must be discarded before performing any statistical analysis.

Moreover, successive samples in an MCMC chain are generally correlated. The efficiency of the chain is characterized by the autocorrelation time, which measures the number of steps required to obtain approximately independent samples. Parameter uncertainties and confidence regions must be estimated using the effective number of independent samples rather than the total chain length.

To assess convergence, it is common to run multiple independent chains starting from different initial conditions and compare their statistical properties. Convergence is typically assessed using the Gelman–Rubin $\hat{R}$ statistic, which measures the relative consistency of multiple chains through a comparison of intra-chain and inter-chain variances. Convergence is typically declared when $\hat{R}$ is sufficiently close to unity for all parameters.

Convergence diagnostics and the Gelman–Rubin criterion

A crucial aspect of Markov Chain Monte Carlo sampling is the assessment of convergence. Before the samples can be used to estimate posterior quantities, one must verify that the chain has reached its stationary regime and that the distribution of sampled points is independent of the initial conditions.

A widely used diagnostic is the Gelman–Rubin convergence criterion, which is based on running multiple independent chains starting from different initial points in parameter space. Suppose that M chains are evolved, each producing N samples $\{\boldsymbol{\theta}_i^{(m)}\}$, where $m = 1, \ldots, M$ labels the chain and $i = 1, \ldots, N$ labels the iteration.

For a given parameter θ, one first computes the mean of each chain,

$$\bar{\theta}^{(m)} = \frac{1}{N} \sum_{i=1}^{N} \theta_i^{(m)}, \tag{2.39}$$

and the mean over all chains,

$$\bar{\theta} = \frac{1}{M} \sum_{m=1}^{M} \bar{\theta}^{(m)}. \tag{2.40}$$

Two complementary estimates of the variance are then constructed. The *within-chain variance* measures the typical fluctuation of each chain around its own mean,

$$W = \frac{1}{M} \sum_{m=1}^{M} \left[\frac{1}{N-1} \sum_{i=1}^{N} \left(\theta_i^{(m)} - \bar{\theta}^{(m)} \right)^2 \right]. \tag{2.41}$$

The *between-chain variance* measures the dispersion of the chain means,

$$B = \frac{1}{M-1} \sum_{m=1}^{M} \left(\bar{\theta}^{(m)} - \bar{\theta} \right)^2. \tag{2.42}$$

For converged chains with same stationary distribution, the within-chain and between-chain variances should agree up to statistical fluctuations. An unbiased estimator of the total posterior variance is then given by

$$\hat{V} = \left(1 - \frac{1}{N} \right) W + \left(1 + \frac{1}{M} \right) B. \tag{2.43}$$

The potential scale reduction factor is defined as

$$\hat{R} = \frac{\hat{V}}{W} \tag{2.44}$$

In the limit of perfect convergence, one expects $B/N \simeq W$ and therefore $\hat{R} \to 1$. Values $\hat{R} > 1$ indicate that the chains have not yet fully mixed and that their means still retain memory of the initial conditions. In practical cosmological analyses,

convergence is typically declared when Gelman & Rubin (1992a)

$$|\hat{R} - 1| < 0.01 \tag{2.45}$$

for all parameters.

This criterion, called the Gelman–Rubin criterion, provides a simple and robust test of convergence by comparing fluctuations within individual chains to fluctuations across different chains. It is routinely implemented in cosmological sampling codes and constitutes a standard diagnostic for the reliability of MCMC-based parameter estimation.

Analysis of Markov Chain Monte Carlo outputs

Once convergence has been established and the initial burn-in phase has been removed, the Markov chains provide a discrete sampling of the posterior probability distribution in the parameter space. The purpose of the chain analysis is to extract reliable estimates of parameter values, uncertainties, and correlations from this sample.

For a parameter vector $\boldsymbol{\theta}$ with posterior distribution $P(\boldsymbol{\theta} \mid D)$, expectation values of any function $f(\boldsymbol{\theta})$ can be approximated by Monte Carlo averages over the converged chain,

$$\langle f(\boldsymbol{\theta}) \rangle \simeq \frac{1}{N} \sum_{i=1}^{N} f(\boldsymbol{\theta}_i), \tag{2.46}$$

where $\{\boldsymbol{\theta}_i\}_{i=1}^{N}$ denotes the retained samples after burn-in and thinning. In particular, posterior means and variances are estimated as

$$\langle \theta_a \rangle \simeq \frac{1}{N} \sum_{i=1}^{N} \theta_{a,i}, \tag{2.47}$$

$$\sigma^2(\theta_a) \simeq \frac{1}{N-1} \sum_{i=1}^{N} (\theta_{a,i} - \langle \theta_a \rangle)^2. \tag{2.48}$$

The joint structure of the posterior is characterized through the covariance matrix,

$$\mathrm{Cov}(\theta_a, \theta_b) = \langle \theta_a \theta_b \rangle - \langle \theta_a \rangle \langle \theta_b \rangle, \tag{2.49}$$

which quantifies parameter degeneracies and correlations. These correlations play a central role in the interpretation of cosmological constraints, where multiple parameters often remain partially degenerate.

In practice, one-dimensional marginalized posterior distributions are obtained by projecting the full posterior onto a single parameter,

$$P(\theta_a \mid D) = \int d\boldsymbol{\theta}_{\setminus a}\, P(\boldsymbol{\theta} \mid D), \tag{2.50}$$

where the integration is performed over all parameters except θ_a. Similarly, two-dimensional marginalized distributions are used to construct joint credible contours in selected parameter planes.

Credible intervals are defined directly from the marginalized posterior. For a chosen credibility level C, the interval $[\theta_a^-, \theta_a^+]$ satisfies

$$\int_{\theta_a^-}^{\theta_a^+} P(\theta_a \mid D)\, d\theta_a = C, \tag{2.51}$$

with the additional requirement that the interval contains the region of highest posterior density.

The full set of posterior summaries — means, standard deviations, correlation matrices, and marginalized distributions — provides a complete statistical characterization of the parameter constraints derived from the MCMC analysis. These quantities form the basis for all parameter estimates reported in the subsequent chapters.

2.7 Model comparison and information criteria

Beyond parameter estimation within a given model, an important task in cosmological data analysis is the quantitative comparison of competing theoretical models. Since models with a larger number of free parameters can generally achieve better fits to the data, any comparison must penalize unnecessary model complexity in order to avoid overfitting.

For this reason, approximate information criteria are widely used as practical tools for model comparison. In this work, we employ the Akaike Information Criterion (AIC) Akaike (1974), which is defined as

$$\mathrm{AIC} = -2 \ln \mathcal{L}_{\max} + 2k \tag{2.52}$$

where $\mathcal{L}_{\max}$ is the maximum value of the likelihood achieved by the model, and k is the number of free parameters. The first term measures the goodness of fit, while the second term penalizes model complexity.

Model comparison is then performed using the difference

$$\Delta\text{AIC} = \text{AIC}_{\text{model}} - \text{AIC}_{\text{ref}}, \tag{2.53}$$

with respect to a chosen reference model, typically ΛCDM. By convention, values $\Delta\text{AIC} \lesssim 2$ indicate statistically indistinguishable models, $2 \lesssim \Delta\text{AIC} \lesssim 6$ indicate moderate preference for the reference model, and $\Delta\text{AIC} \gtrsim 10$ indicate strong disfavour of the alternative model.

The AIC provides an efficient and robust criterion for assessing whether the improvement in fit achieved by an extended model justifies the introduction of additional parameters. In the following chapters, we use ΔAIC as the primary tool to quantify the relative performance of models with respect to the standard ΛCDM cosmology.

2.8 Application in Cosmology

In cosmological parameter estimation, MCMC methods are routinely used to explore posterior distributions in parameter spaces of dimension six or higher. Publicly available codes such as `MontePython` Brinckmann & Lesgourgues (2018) implement efficient MCMC samplers that interface Boltzmann solvers with observational likelihoods.

In the analyses presented in this thesis, MCMC techniques are employed to sample the posterior distributions of cosmological parameters, to compute marginal constraints, and to quantify parameter degeneracies. The resulting chains form the basis for all parameter inference and model comparison results discussed in the following chapters. Although Bayesian evidence is introduced in this chapter

for completeness, it is not evaluated in the present analysis; model comparison is instead performed using the Akaike Information Criterion (AIC).

Chapter 3

Cosmological constraints on mass-varying dark matter *

3.1 Introduction

Building on the standard cosmological framework and the overview of dark matter candidates presented in Chapter 1, observations of the CMB establish that dark matter constitutes the dominant matter component of the Universe and is well described by a cold, collisionless fluid within the ΛCDM paradigm Aghanim et al. (2020). Despite this success, the microscopic nature of dark matter remains unknown, and small-scale challenges in structure formation motivate the exploration of controlled departures from the standard cold dark matter picture within a cosmological setting.

Warm dark matter (WDM) and mixed dark matter, which is a combination of hot dark matter (HDM) and WDM or CDM, have been proposed as alternatives to

*This chapter is based on publication Chakraborty et al. (2025c)

CDM to solve small-scale problems due to their free-streaming properties, which result in less structure formation at small scales Viel et al. (2013a); Holm et al. (2022); Blinov et al. (2020); Alexander et al. (2023). It reduces the number of satellite galaxies in halos and suppresses the halo mass function. However, in addition to these small-scale problems, the standard ΛCDM model has been challenged by cosmological tensions such as the Hubble tension and the S_8 tension Abdalla et al. (2022) discussed in Chapter 1.

Despite numerous attempts, alternative CDM scenarios such as WDM or mixed dark matter models have failed to resolve the S_8 tension. Adding massive thermal neutrinos, one of the proposed solutions does not alleviate the tension. This is because an increase in $\Delta N_{\rm eff}$ can raise σ_8 and lower $\Omega_{\rm m}$, which exacerbates the tension Aghanim et al. (2020); Poulin et al. (2018). Various approaches have been explored, such as decaying dark matter Enqvist et al. (2015); Poulin et al. (2016); Vattis et al. (2019); Haridasu & Viel (2020); Clark et al. (2021); Pandey et al. (2020); Abellán et al. (2022, 2021) and non-thermal dark matter models Poulin et al. (2018); Kreisch et al. (2020); Murgia et al. (2016); Archidiacono et al. (2019); Becker et al. (2021); Kumar & Nunes (2016), to address this issue.

In this chapter, we investigate the cosmological signatures of a novel scenario of mass-varying DM (MVDM) that is a natural generalization of the extra radiation $N_{\rm eff}$ and the WDM models. While the standard CDM framework reviewed in the previous chapter fits the observations at and after recombination very well, the properties of dark matter at earlier epochs remain largely unconstrained by direct observations. In this work, we plan to explore whether data allow for a scenario in which dark matter is relativistic at early times in a model-independent manner. The realisation of an MVDM scenario has been previously suggested in many particle physics models Agarwal et al. (2015); Das & Weiner (2011); Chanda & Das (2017); Ganesan et al. (2024). However, in this work, we refrain from assuming any particular model and assume a phenomenological relation proposed

in Das et al. (2023).

Previously, cosmological effects of late formation of massive DM were studied in Refs. Sarkar et al. (2015); Das et al. (2019, 2023); Das & Nadler (2021a). Similar phenomenon can also occur in models with late primordial black hole formation Bhattacharya et al. (2021b); Chakraborty et al. (2022a). Particularly in Ref. Das et al. (2023), some of the authors showed in a model-independent approach that the Lyman-α data from small scale places strong constraint on the transition redshift z_t. Here, we follow a similar phenomenological approach to model the time-variation of DM mass from zero to a finite value.

We perform a comprehensive Bayesian analysis of this model using the latest cosmic microwave background (CMB) data from Planck and ACT. Our study reveals a lower bound on the transition redshift z_t ($\log_{10} z_t > 4.55$) and a mild preference for a DM mass of 41.7 eV when the Planck Aghanim et al. (2020) and KIDS1000+BOSS+2dfLenS weak lensing data Heymans *et al.* (2021) are taken into account. The results indicate that the weak lensing data favors this model. Moreover, the inclusion of weak lensing data significantly reduces the S_8 tension as compared to the case when only Planck data is considered. While this analysis remains deliberately model-independent, the phenomenological mass variation considered here naturally admits concrete microscopic realizations, which we explore in the next chapter in the context of Yukawa-type scalar–fermion interactions and primordial black hole dark matter formation.

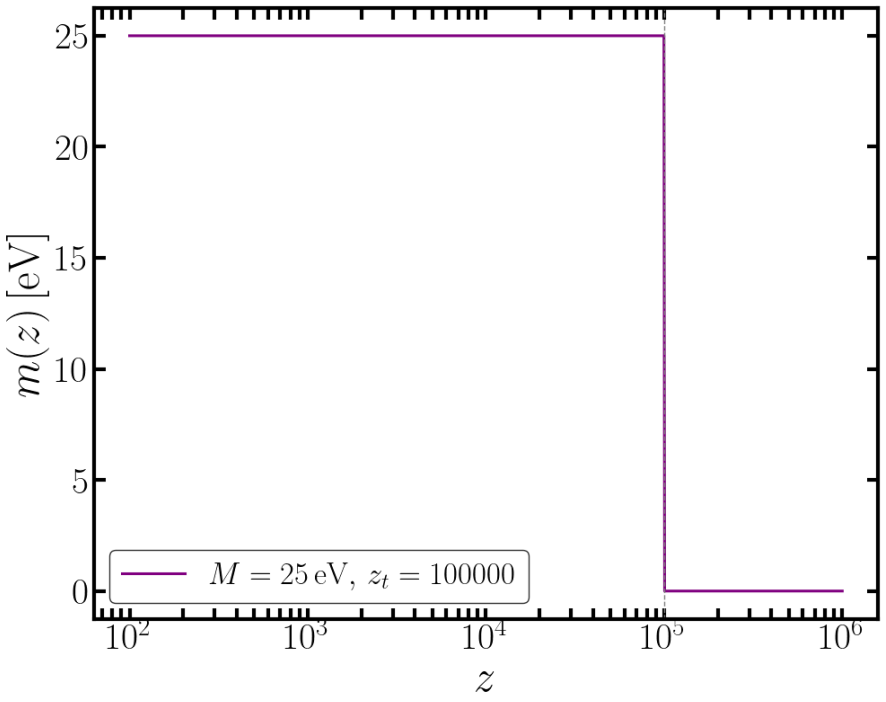


FIGURE 3.1: Variation of mass of MVDM particle is plotted for mass $M = 25\,\mathrm{eV}$ for a transitional redshift $z_t = 10^5$.

3.2 Background Density Evolution and Perturbations

In this study, we consider MVDM to be a fermionic particle with a temperature T. We do not commit to a particular particle physics model for the mass variation of DM. Instead, we adopt the phenomenological relation proposed in Ref. Das et al. (2023). The essential concept is that DM was massless and relativistic in the early time, and at a transition redshift of z_t, it underwent an instantaneous transition to become non-relativistic. The form of $m(z)$ considered in this analysis is as follows

$$m(z) = \frac{M}{2}\left[1 - \tanh\left(\frac{z - z_t}{\Delta z}\right)\right]. \tag{3.1}$$

Here, M denotes the final mass of MVDM, whereas the redshift duration of the transition is represented by Δz. The variation of the mass has been plotted in

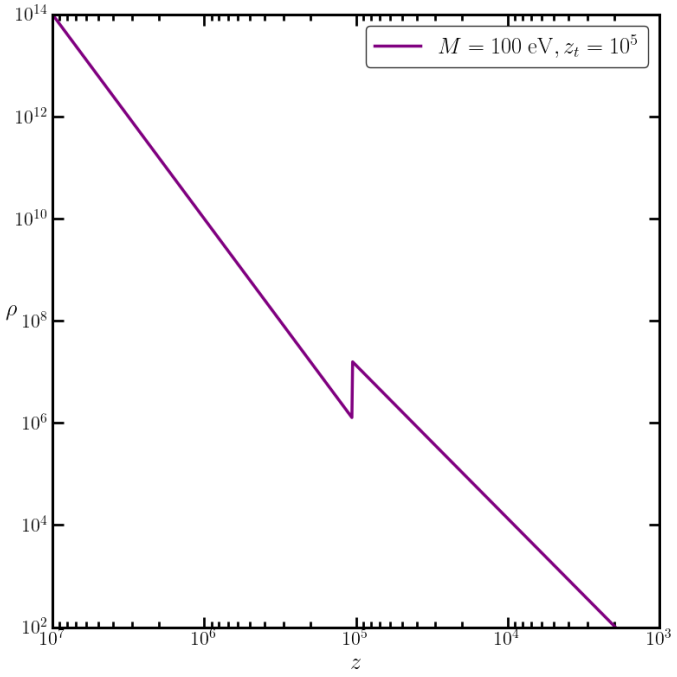


FIGURE 3.2: Evolution of background energy density with redshifts is plotted for mass $M = 100\,\mathrm{eV}$ for a transitional redshift $z_t = 10^5$.

Figure 3.1 for $M = 25\,\mathrm{eV}$ and $z_t = 10^5$. We note that, due to our assumption of the instantaneous nature of the transition, the value of Δz is considerably smaller than that of z_t ($\Delta z \ll z_t$) and we fix $\Delta z = 1$ throughout our analysis. Consequently, the DM instantaneously loses its relativistic nature, necessitating the ratio of the final mass (M) to the transition temperature (T_t) to be significantly greater than unity, i.e., $M/T_t \gg 1$. It is very straightforward to calculate the energy density of MVDM from the following equation:

$$\rho_{\mathrm{MVDM}} = a^{-4} \int dq\, d\Omega\, q^2 f(q/T) \epsilon \tag{3.2}$$

Where $\epsilon = \sqrt{q^2 + a^2 m(a)^2}$ is the energy of the particle with q being the comoving momentum and $f(q/T)$ is the phase space distribution function.

We take the phase space distribution of MVDM to be Fermi-Dirac, which enables

us to calculate the energy density and other higher moments of the distribution. Due to the rapid transition, the energy density exhibits a jump during its evolution at z_t, which can be expressed as the quantity $\rho^{\rm NR}_{\rm MVDM}(z \to z_t^+/\rho^{\rm R}_{\rm MVDM}(z \to z_t^-) = M/T_t$. This phenomenon is accurately depicted in Figure 3.2 for a particular value of z_t. The increase in the MVDM energy density should be understood as an effective description of the energy transfer associated with the underlying mass-generation process. In a complete microscopic realization, the MVDM component would not be separately conserved during the transition; rather, the energy gained through the increase in its rest mass would be compensated by a corresponding change in the sector responsible for generating the mass, such that the total energy–momentum tensor remains conserved. Since the present analysis is deliberately model-independent, the microscopic dynamics of this additional sector are not specified explicitly.

For the remainder of this chapter, we have set the MVDM temperature to $T = T_\gamma/10$ in the relativistic phase as a representative value. The mass of a light, Fermionic dark matter particle can be constrained by Tremaine-Gunn bound Peebles (1993). This bound can be cast in terms of the value of the initial (fine-grained) phase space distribution function (Ref. Peebles (1993), Eq.(18.64)). The constraint depends on the ratio M/T, which means the bounds need to be scaled by the corresponding factor for our choice of temperature, T. We note that the parameter space studied in the thesis is consistent with this bound.

Because of its relativistic nature before z_t, MVDM will contribute to the total radiation energy density, thereby affecting the evolution of the universe and leaving an imprint on observables such as the CMB and the matter power spectra. This contribution can be quantified as an additional relativistic degree of freedom, $\Delta N_{\rm eff}$, given by Das et al. (2023),

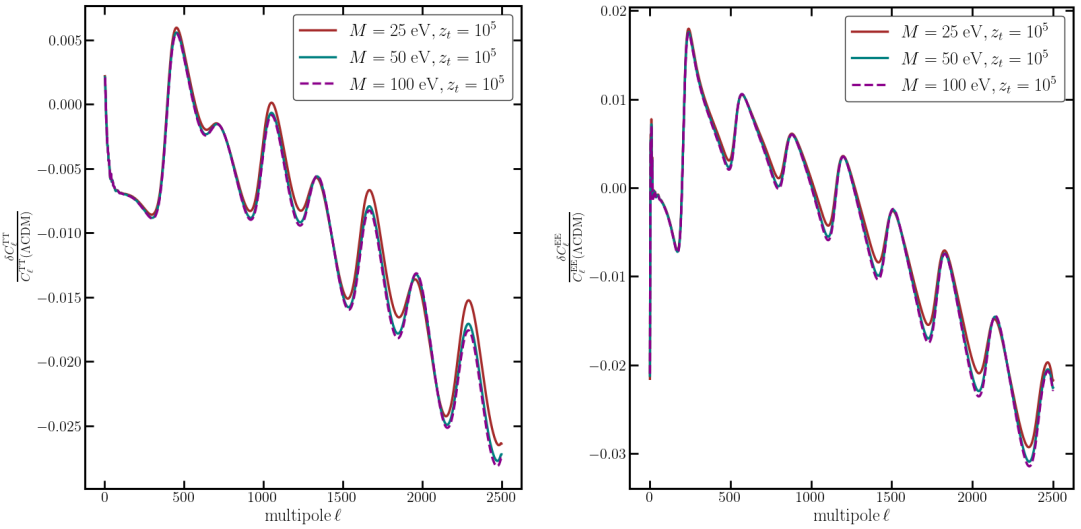


FIGURE 3.3: The relative change in the CMB TT and EE power spectra with respect to ΛCDM is plotted for mass $M = 25,\ 50$ and $100\,\mathrm{eV}$ for a transitional redshift $z_t = 10^5$.

$$\Delta N_{\rm eff} \approx \frac{\rho_{\rm MVDM}(z=0)}{\rho_\nu^{\rm th}(z=0)} \frac{T_t}{M} \frac{1}{1+z_t} \tag{3.3}$$

This model shows observable effects at the perturbation level as well. The transition of DM from relativistic to non-relativistic phase introduces a cut-off scale, denoted by k_t, in our model, which corresponds to the fluctuations that entered the horizon at the transition redshift z_t. We can obtain the evolution of perturbations from Boltzmann hierarchies in synchronous gauge:

$$\begin{aligned}
\dot{\Psi}_0 &= -\frac{qk}{\epsilon}\Psi_1 + \frac{1}{6}\dot{h}\frac{d\ln f_0}{d\ln q}\,, \\
\dot{\Psi}_1 &= \frac{qk}{3\epsilon}\left(\Psi_0 - 2\Psi_2\right)\,, \\
\dot{\Psi}_2 &= \frac{qk}{5\epsilon}\left(2\Psi_1 - 3\Psi_3\right) - \left(\frac{1}{15}\dot{h} + \frac{2}{5}\dot{\eta}\right)\frac{d\ln f_0}{d\ln q}\,, \\
\dot{\Psi}_\ell &= \frac{qk}{(2\ell+1)\epsilon}\left[\ell\Psi_{\ell-1} - (\ell+1)\Psi_{\ell+1}\right]\,, \quad l \geq 3\,.
\end{aligned} \tag{3.4}$$

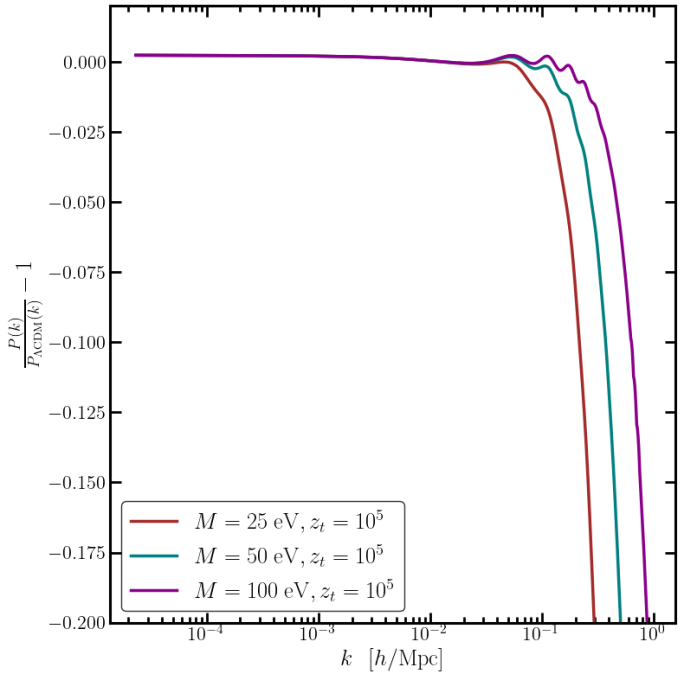


FIGURE 3.4: Relative change in matter power spectra with respect to ΛCDM is plotted for mass $M = 25,\ 50$ and $100\,\mathrm{eV}$ for a transitional redshift $z_t = 10^5$.

Where ψ_ℓ are the ℓ-th multipole of the perturbed phase space distribution; h and η are metric perturbations; f_0 is the background Fermi-Dirac distribution function. The corresponding perturbed energy density $\delta\rho$, pressure δP, bulk velocity θ_h, and anisotropic stress σ_h can be obtained from these hierarchies using the following equations:

$$\begin{aligned}
\delta\rho &= 4\pi a^{-4} \int q^2 dq\, \epsilon f_0(q) \Psi_0\,, \\
\delta P &= \frac{4\pi}{3} a^{-4} \int q^2 dq\, \frac{q^2}{\epsilon} f_0(q) \Psi_0\,, \\
(\rho + P)\theta_h &= 4\pi k a^{-4} \int q^2 dq\, q f_0(q) \Psi_1\,, \\
(\rho + P)\sigma_h &= \frac{8\pi}{3} a^{-4} \int q^2 dq\, \frac{q^2}{\epsilon} f_0(q) \Psi_2\,.
\end{aligned} \tag{3.5}$$

In this work, the non-vanishing particle mass prevents an exact analytic evaluation

of these integrals, and the system must be treated numerically. In addition to the perturbations, the unperturbed temperature T enters through the background Fermi–Dirac distribution, so that the relevant dimensionless variables are naturally expressed in terms of the q/T, ϵ/T, and at late time it becomes $m(z)/T$.

Prior to the transition redshift, DM was relativistic and free streaming, prohibiting the growth of structure for the modes that entered before z_t. This results in a suppression of power for $k > k_t$ in the matter power spectra shown in Figure 3.4. For a lower transition redshift, the suppression moves to larger scales, implying the structure is washed away at lower k modes. Furthermore, the free streaming length is directly proportional to the thermal velocity of DM particles, i.e., $v_{th} = \frac{\langle p \rangle}{m}$. Therefore, the cut-off scale k_t, which is determined from the free-streaming length during the transition, is also dependent on the final mass of the DM Hu et al. (1998); Lesgourgues & Pastor (2006); Viel et al. (2013b); Abazajian et al. (2015). Consequently, we obtain smaller k_t values for DM with lighter mass. This suppression of power is also reflected in the CMB temperature and polarization anisotropy power spectrum at higher ℓ, as shown in Figure 3.3.

The presence of free-streaming dark matter (DM) particles during their relativistic phase causes a small but non-zero $\Delta N_{\rm eff}$, which exerts an additional drag on the metric perturbation via gravity during the radiation-dominated era. This results in an extra phase shift in the acoustic oscillation of the photon-baryon plasma that can be detected in both the cosmic microwave background (CMB) and the matter power spectrum as small wiggles, which can be seen in both Figure 3.3 & 3.4.

3.3 Method

We use the Boltzmann hierarchy for the MVDM model and implement it in CLASS following Ref. Das et al. (2023) to compute the CMB anisotropy power spectra and the matter power spectrum Lesgourgues (2011).

We perform a comprehensive MCMC analysis of the model using the following datasets:

- Planck 2018 measurements of the low-ℓ CMB TT, EE, and high-ℓ TT, TE, EE power spectra Aghanim et al. (2020).
- The BAO measurements from 6dFGS Beutler et al. (2011b) and SDSS DR7 MGS Ross et al. (2015b) for low redshift $z < 0.2$ comprises the likelihood for "Bao-smallz-2014". In addition to this we also use BOSS DR12 at $z = 0.38, 0.51$ and 0.61 Alam et al. (2017b).
- We use the S_8-prior from the KIDS1000+BOSS+2dfLenS weak lensing data with $S_8 = 0.766^{+0.02}_{-0.014}$ Heymans *et al.* (2021). In this work, we use the S_8 value obtained as a prior for our MCMC analysis. In order to gain an understanding of the effect of prior, we also consider different S_8 prior values obtained from different weak lensing measurements. We use a higher S_8 prior i.e. $S_8^+ = 0.772^{+0.018}_{-0.017}$ obtained from shear-shear analysis from DES Y3 survey Amon et al. (2022) as well as a lower prior $S_8^- = 0.759^{+0.024}_{-0.021}$ obtained from KIDS1000-cosmic shear analysis Asgari, Marika et al. (2021).
- ACT data from ACT collaboration, which includes the DR4 data release Aiola et al. (2020). We use `actpollite dr4` likelihood code which contains TT measurements ($600 < \ell < 4126$) and TE and EE measurements ($350 < \ell < 4126$). Since it does not have large-scale data, constraining reionization

optical depth $\tau_{\rm reio}$ is not possible. So a Gaussian prior is also added, centered at $\tau_{\rm reio} = 0.06 \pm 0.01$ while analyzing ACT data alone Louis et al. (2017).

- Type-Ia supernova (SN-Ia) catalogue Pantheon+ spanning in redshift $0.001 < z < 2.26$. Brout et al. (2022)

In this study, we adopt the standard ΛCDM model as our base framework, which comprises of the six parameters: $\omega_b, \omega_{\rm cdm}, 100\theta_s, \ln 10^{10} A_s, n_s, \tau_{\rm reio}$. To incorporate our MVDM model, we introduce two additional parameters $\log_{10} z_t$, M in conjunction with the six aforementioned parameters.

The MCMCs are executed using the MontePython-v3 Brinckmann & Lesgourgues (2018) code with the Metropolis-Hasting algorithm. We utilize our modified CLASS version to interface with the MCMCs. We obtain all the reported χ^2_{min} values using the Python package iMinuit James & Roos (1975). We use the Choleski decomposition Lewis et al. (2000) and consider the convergence criteria $R - 1 \lesssim 0.01$ from Gelman & Rubin (1992b) for convergence of the chains.

3.4 Results

For the Planck-only analysis with the MVDM cosmology, shown in Figure 3.5 and in Table 3.1, we were able to obtain a bound on the mass $M > 23\,\text{eV}$ and $\log_{10} z_t > 4.72$ (obtained at half of the peak posterior value of the respective parameter). Our analysis yields $S_8(\text{MVDM}) = 0.822^{+0.0236}_{-0.0179}$, which is to be compared with $S_8(\Lambda\text{CDM}) = 0.831^{+0.0164}_{-0.0165}$. MVDM shifts S_8 downward almost by $\sim 0.5\sigma$, thus effectively reducing the level of S_8 tension from $\sim 2.7\sigma$ to $\sim 2.2\sigma$. So, MVDM prefers a slightly lower value of S_8, and the minimum χ^2 shows a slight improvement compared to the standard ΛCDM model i.e. $\Delta\chi^2_{\rm min} = \chi^2_{\rm min}(MVDM) - \chi^2_{\rm min}(\Lambda CDM) = -1.23$.

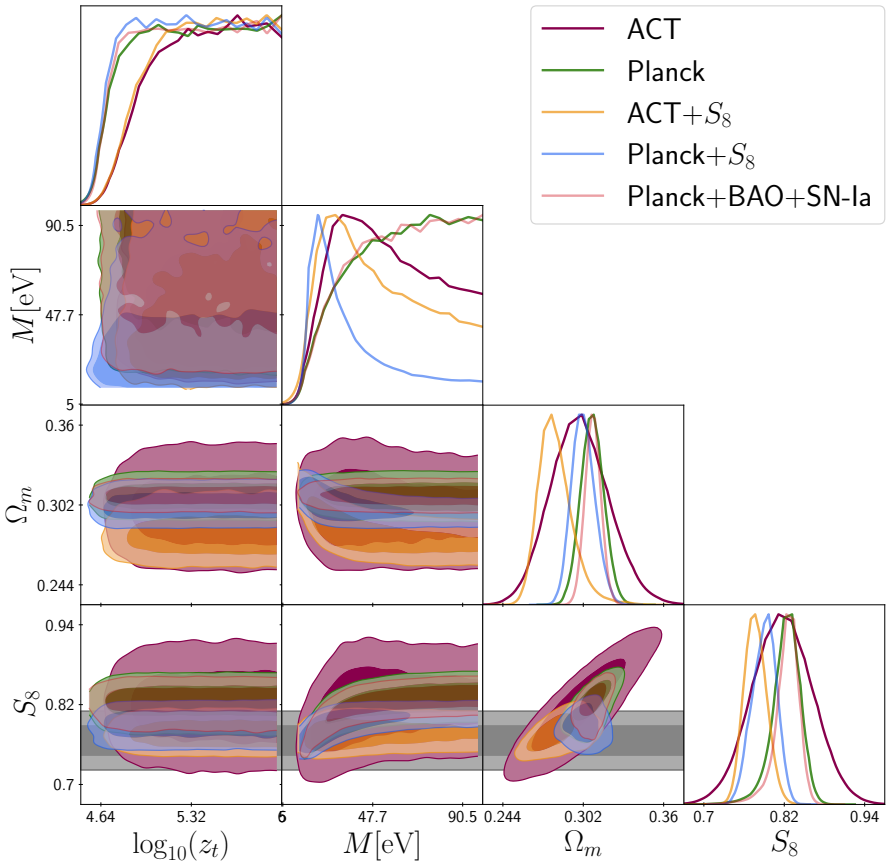


FIGURE 3.5: Reconstructed 2D and 1D marginalized posterior distributions of $\log_{10} z_t, M(\,\mathrm{eV}), \Omega_\mathrm{m}, S_8$ with 68% and 95% confidence level. The weak lensing measurement of S_8 is shown as grey bands (68% and 95%). Here we considered Pantheon+ dataset for "SN-Ia".

The inclusion of the S_8 prior in our analysis yields significant changes in the results. Specifically, we observe a mild preference for dark matter final mass $M = 41.7^{+7.81}_{-27.5}\,\mathrm{eV}$ and a tighter constraint on $\log_{10} z_t > 4.67$ in the MVDM model. We get $S_8(\mathrm{MVDM}) = 0.79^{+0.0209}_{-0.0167}$ in this likelihood combination, which can be compared with our baseline $S_8(\Lambda\mathrm{CDM}) = 0.805^{+0.0126}_{-0.0129}$. Consequently, the χ^2_{min} in the combined analysis decreases for the MVDM case, with $\Delta\chi^2_{\mathrm{min}} = \chi^2_{\mathrm{min}}(MVDM) - \chi^2_{\mathrm{min}}(\Lambda CDM) = -3.81$. Further, we note that the overall χ^2_{min} is less impacted by the inclusion of the S_8 prior in the MVDM case (+3.78) as compared to that in the ΛCDM case (+6.36). This finding indicates that the MVDM model is better suited to explain both CMB and weak lensing data compared to ΛCDM. We also report the individual contribution from each dataset in each run

TABLE 3.1: Obtained parameter values with mean (best-fit) $\pm 1\sigma$ error in the ΛCDM and MVDM model from the analysis of Planck Aghanim et al. (2020) and Planck+S_8Heymans *et al.* (2021) data. Lower limits are obtained at half of the peak posterior value of the respective parameter.

Model	ΛCDM		MVDM	
Parameter	Planck	Planck+S_8	Planck	Planck+S_8
$100\omega_b$	$2.24(2.2334)^{+0.0154}_{-0.0155}$	$2.25(2.2528)^{+0.0145}_{-0.0146}$	$2.24(2.239)^{+0.0153}_{-0.0157}$	$2.25(2.245)^{+0.0152}_{-0.0156}$
$\omega_{\rm dm}$ †	$0.12(0.1199)^{+0.00141}_{-0.0014}$	$0.118(0.1178)^{+0.00114}_{-0.00118}$	$0.12(0.1208)^{+0.00141}_{0.00143}$	$0.119(0.12)^{+0.00134}_{-0.00158}$
$100\times\theta_s$	$1.04(1.04184)^{+0.000304}_{-0.0003}$	$1.04(1.04215)^{+0.000301}_{-0.000294}$	$1.04(1.042)^{+0.000322}_{-0.000353}$	$1.04(1.0419)^{+0.000317}_{-0.000362}$
n_s	$0.965(0.96754)\pm 0.00453$	$0.969(0.972)^{+0.00421}_{-0.00422}$	$0.968(0.9655)^{+0.00466}_{-0.00503}$	$0.97(0.965)^{+0.00493}_{-0.00511}$
$\ln 10^{10}A_s$	$3.04(3.0391)^{+0.0156}_{-0.0162}$	$3.04(3.021)^{+0.0159}_{-0.0158}$	$3.05(3.0442)^{+0.0162}_{-0.0173}$	$3.04(3.042)^{+0.0158}_{-0.0171}$
τ_{reio}	$0.0541(0.0517)^{+0.00763}_{-0.00786}$	$0.0521(0.0507)^{+0.00799}_{-0.00785}$	$0.0546(0.0547)^{+0.00786}_{-0.00847}$	$0.0538(0.05198)^{+0.00758}_{-0.00826}$
$\log_{10} z_t$	—	—	> 4.72	> 4.67
M[eV]	—	—	> 23	$41.7(23.87)^{+7.81}_{-27.5}$
S_8	$0.831(0.827)^{+0.0164}_{-0.0165}$	$0.805(0.8114)^{+0.0126}_{-0.0129}$	$0.822(0.821)^{+0.0236}_{-0.0179}$	$0.79(0.776)^{+0.0209}_{-0.0167}$
$\Omega_{\rm m}$	$0.315(0.3138)^{+0.00852}_{-0.00867}$	$0.303(0.3064)^{+0.00672}_{-0.00712}$	$0.309(0.301)^{+0.00823}_{-0.00884}$	$0.302(0.311)^{+0.00759}_{-0.0095}$
H_0[Km/s/Mpc]	$67.3(67.35)^{+0.602}_{-0.643}$	$68.2(67.88)^{+0.528}_{-0.527}$	$67.9(67.52)^{+0.638}_{-0.636}$	$68.4(67.96)^{+0.695}_{-0.606}$
$\chi^2_{\rm min}$	2771.78	2778.14	2770.55	2774.33

† For ΛCDM model, the 'dm' subscript means the Cold Dark Matter (CDM), and for the MVDM model, it means the mass varying dark matter considered in this chapter.

for both of the models, which are reported in Table 3.6 in Section 3.6.

The analysis of Planck data reveals comparatively higher values of S_8 , indicating an increased amplitude of matter fluctuations at the $8h^{-1}$Mpc scale. In contrast, the MVDM model exhibits a suppression of fluctuations at smaller length scales, resulting in a reduced amplitude of matter fluctuations. Consequently, the incorporation of S_8 priors significantly affects the posterior distributions, demonstrating a mild preference for detecting the mass of dark matter, an aspect that the Planck data alone does not exhibit. Given the substantial impact on the result of MCMC analysis, we performed an additional set of analyses utilizing different S_8 priors

TABLE 3.2: Obtained parameter values with mean (best-fit) $\pm 1\sigma$ error in the ΛCDM and MVDM model from the analysis of ACT Aiola et al. (2020); Louis et al. (2017) and ACT+S_8Heymans *et al.* (2021) data. Lower limits are obtained at half of the peak posterior value of the respective parameter.

Model	ΛCDM		MVDM	
Parameter	ACT	ACT+S_8	ACT	ACT+S_8
$100\omega_b$	$2.15(2.1471)^{+0.0308}_{-0.0318}$	$2.16(2.1561)^{+0.0307}_{-0.0314}$	$2.16(2.166) \pm 0.0317$	$2.17(2.1698)^{+0.0304}_{-0.0323}$
$\omega_{\rm dm}$ ‡	$0.118(0.1171)^{+0.00373}_{-0.00384}$	$0.114(0.11401)^{+0.00162}_{-0.00177}$	$0.118(0.11839)^{+0.00379}_{-0.00385}$	$0.115(0.1168)^{+0.00179}_{-0.00266}$
$100 \times \theta_s$	$1.04(1.0433)^{+0.000728}_{-0.000708}$	$1.04(1.04385)^{+0.000666}_{-0.000686}$	$1.04(1.0436)^{+0.000723}_{-0.000727}$	$1.04(1.0436)^{+0.000691}_{-0.000698}$
n_s	$1.01(1.0092)^{+0.0156}_{-0.0159}$	$1.02(1.0177)^{+0.0142}_{-0.0144}$	$1.01(1.00945)^{+0.0154}_{-0.0164}$	$1.02(1.0131)^{+0.0147}_{-0.0149}$
$\ln 10^{10} A_s$	$3.04(3.04165)^{+0.0224}_{-0.0238}$	$3.03(3.0332)^{+0.0209}_{-0.0223}$	$3.04(3.0421)^{+0.0225}_{-0.0239}$	$3.03(3.029)^{+0.0209}_{-0.0232}$
τ_{reio}	$0.0604(0.06058)^{+0.00927}_{-0.01}$	$0.0601(0.06145)^{+0.00897}_{-0.0102}$	$0.0606(0.05936)^{+0.00922}_{-0.0103}$	$0.0604(0.05645)^{+0.00914}_{-0.0102}$
$\log_{10} z_t$	—	—	> 5.1	> 5.2
M[eV]	—	—	> 27	$51.2(25.31)^{+16}_{-33.5}$
S_8	$0.826(0.8169)^{+0.0419}_{-0.044}$	$0.777(0.78)^{+0.016}_{-0.0183}$	$0.817(0.8159)^{+0.0452}_{-0.046}$	$0.777(0.7711)^{+0.0159}_{-0.0183}$
$\Omega_{\rm m}$	$0.303(0.2986)^{+0.0202}_{-0.023}$	$0.279(0.2822)^{+0.00842}_{-0.00955}$	$0.3(0.2998)^{+0.0203}_{-0.0226}$	$0.283(0.2913)^{+0.00916}_{-0.0143}$
H_0[Km/s/Mpc]	$67.9(68.11)^{+1.51}_{-1.55}$	$69.6(69.384)^{+0.736}_{-0.699}$	$68.4(68.339)^{+1.51}_{-1.58}$	$69.6(68.95)^{+1.06}_{-0.768}$
$\chi^2_{\rm min}$	280.0495	281.8939	275.7832	276.7859

‡ For ΛCDM model, the 'dm' subscript means the Cold Dark Matter (CDM), and for the MVDM model, it means the mass varying dark matter considered in this chapter.

derived from various weak lensing measurements, as elaborated in Section 3.3. The outcomes of this analysis are illustrated in Figure 3.6 and Table 3.4. Notably, the posterior distributions indicate that variations in the priors do not lead to significant changes in the results, which is why the minimum χ^2 has not been computed.

To gain a deeper understanding of the results obtained from the MCMC analysis, we present residual plots in Figure 3.8 for the CMB TT, EE power spectra, and the matter power spectra with respect to ΛCDM in the best-fit mass-varying dark matter (MVDM) model obtained when Planck, Planck+S_8, and

TABLE 3.3: Obtained parameter values with mean (best-fit) $\pm 1\sigma$ error in the ΛCDM and MVDM model from the analysis of combined Planck + BAO + Pantheon+ dataset. Lower limits are obtained at half of the peak posterior value of the respective parameter.

Dataset	Planck + BAO + Pantheon+	
Parameter	ΛCDM	MVDM
$100\omega_b$	$2.24(2.2403)^{+0.0136}_{-0.0138}$	$2.24(2.249)^{+0.0137}_{-0.0140}$
$\omega_{\rm dm}$ [§]	$0.12(0.1201)^{+0.000981}_{-0.000997}$	$0.121(0.1186)^{+0.000982}_{-0.000964}$
$100 \times \theta_s$	$1.04(1.0419)^{+0.000284}_{-0.000289}$	$1.04(1.0420)^{+0.000311}_{-0.000342}$
n_s	$0.966(0.9645)^{+0.00376}_{-0.00387}$	$0.967(0.9618)^{+0.00387}_{-0.00427}$
$\ln 10^{10} A_s$	$3.04(3.038)^{+0.0161}_{-0.0168}$	$3.05(3.045)^{+0.0157}_{-0.0166}$
τ_{reio}	$0.0546(0.051609)^{+0.00756}_{-0.00809}$	$0.0547(0.05589)^{+0.00755}_{-0.00798}$
$\log_{10} z_t$	—	> 4.75
M[eV]	—	> 26
S_8	$0.826(0.828)^{+0.0127}_{-0.0128}$	$0.824(0.819)^{+0.0203}_{-0.0132}$
$\Omega_{\rm m}$	$0.312(0.315)^{+0.00591}_{-0.00605}$	$0.309(0.301)^{+0.00579}_{-0.00588}$
H_0[Km/s/Mpc]	$67.5(67.408)^{+0.442}_{-0.441}$	$67.9(68.45)^{+0.427}_{-0.443}$
$\chi^2_{\rm min}$	4189.92	4189.66

[§] For ΛCDM model, the 'dm' subscript means the Cold Dark Matter (CDM), and for the MVDM model, it means the mass varying dark matter considered in this chapter.

Planck+BAO+Pantheon+ datasets are considered. Notably, the suppression of power at small length scales (i.e., large k modes and large ℓ's) is a crucial factor in mitigating the tension.

As mentioned in Section 3.2 and Das et al. (2023), this suppression is attributed to the fact that the MVDM stays relativistic until the transition redshift z_t, contributing to the relativistic energy density, which can be quantified through additional degrees of freedom in Equation 3.3. This effect washes away all perturbations

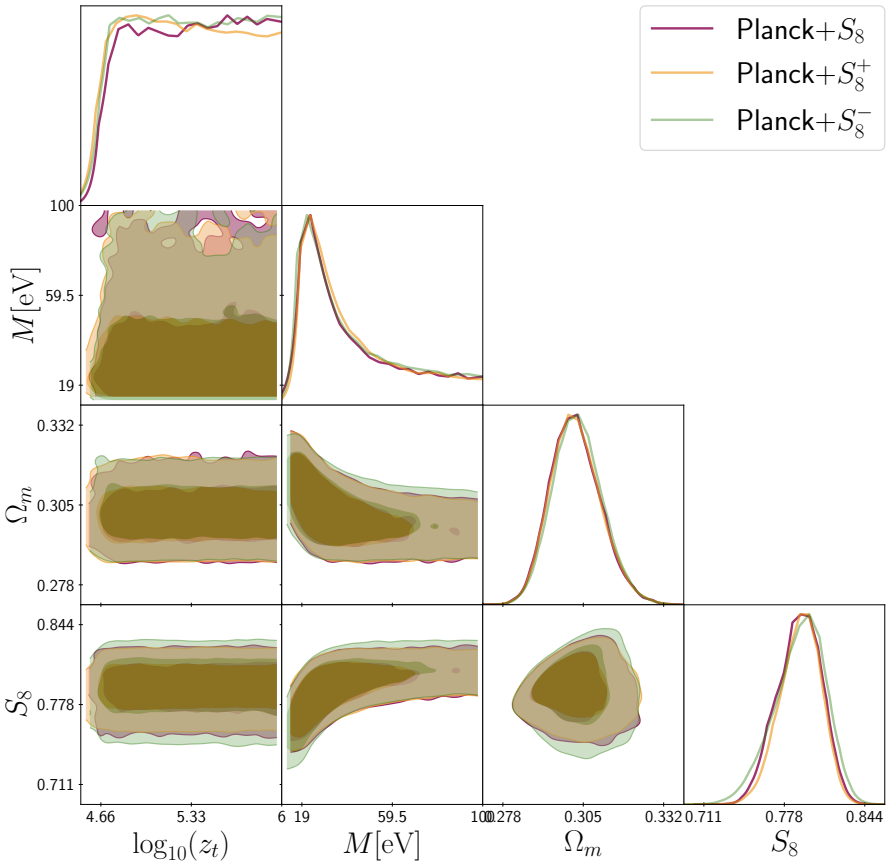


FIGURE 3.6: The 2D and 1D marginalized posterior distributions of $\log_{10} z_t, M, \Omega_\mathrm{m}, S_8$ with 68% and 95% confidence level for three different S_8 priors as mentioned in Sec. 3.3.

at very small length scales, as evidenced by the matter power spectra residual plot and CMB TT, EE residual plots in Figure 3.8. Consequently, we observe a reduction in the S_8 value relative to Planck due to the reduction in fluctuation amplitude on scales $k \approx 0.1-1h\,\mathrm{Mpc}^{-1}$ as discussed in the Introduction. The addition of S_8 prior yields a mild preference for the mass of MVDM at around 23.87 eV (best-fit value), as shown in Figure 3.5. These results clearly demonstrate that the KIDS1000+BOSS+2dfLenS weak lensing data mildly prefers the MVDM model. It should be noted that the error bars in the angular power spectra from Planck are larger at higher ℓ owing to the Planck beam, which makes it difficult to put a stringent bound on the Dark Matter mass. This is because significant deviations from the standard ΛCDM paradigm occur only at small length scales, as is evident from the matter power spectra residual plot.

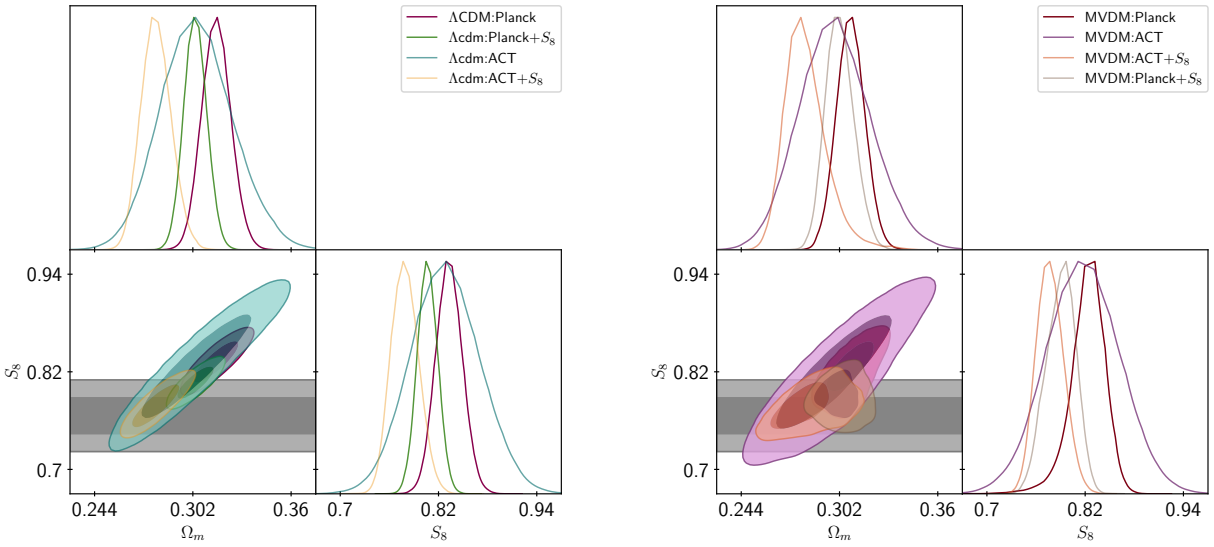


FIGURE 3.7: Reconstructed 2D marginalized posterior distributions of $\Omega_{\rm m}$ and S_8 with 68% and 95% confidence levels.

To address this issue, we have also done our MCMC analysis using ACT data, which has better angular resolution than Planck and has measured the CMB power spectra up to $\ell \simeq 4000$. The results are also included in Figure 3.5 and in Table 3.2, where it is clear that the ACT data does a slightly better job in constraining the mass of dark matter and lowering the S_8 value than Planck. ACT data provides a lower limit on the mass $M > 27\,\mathrm{eV}$ and $\log_{10} z_t > 5.1$ (obtained at half of the peak posterior values of the respective parameters). Our analysis also shows $S_8(\mathrm{MVDM}) = 0.817^{+0.0452}_{-0.046}$, compared to $S_8(\Lambda\mathrm{CDM}) = 0.826^{+0.0419}_{-0.044}$ where MVDM lowers S_8 by 0.2σ. We also observe an improvement in minimum χ^2 over ΛCDM, i.e. $\Delta\chi^2_{\rm min} = \chi^2_{\rm min}(MVDM) - \chi^2_{\rm min}(\Lambda CDM) = -4.2663$. The modest improvement in the ACT-only fit can be attributed to the suppression in the high-ℓ CMB spectra induced by the relativistic phase and rapid transition of MVDM. Since ACT measures these small angular scales with higher precision than Planck, it is more sensitive to such features, allowing a comparatively better fit to the data.

In addition to the S_8 value, we find a tighter lower bound on $\log_{10} z_t > 5.2$. It also tightens the constraint on the dark matter mass $M = 51.2\,(25.31)^{+16}_{-33.5}\,\mathrm{eV}$,

TABLE 3.4: Obtained parameter values with mean (best-fit) $\pm 1\sigma$ error in the MVDM model from the analysis of Planck+S_8^+ Amon et al. (2022), Planck+S_8Heymans *et al.* (2021) and Planck+S_8^- Asgari, Marika et al. (2021) data. Lower limits are obtained at half of the peak posterior value of the respective parameter.

Model	MVDM		
Parameter	Planck+S_8^+	Planck+S_8	Planck+S_8^-
$100\omega_b$	$2.25(2.2527)^{+0.0156}_{-0.0153}$	$2.25(2.245)^{+0.0152}_{-0.0156}$	$2.25(2.247)^{+0.0153}_{-0.0154}$
$\omega_{\rm dm}$ *	$0.119(0.1189)^{+0.00132}_{-0.00158}$	$0.119(0.12)^{+0.00134}_{-0.00158}$	$0.119(0.1194)^{+0.00133}_{0.00153}$
$100 \times \theta_s$	$1.04(1.0422)^{+0.000329}_{-0.000359}$	$1.04(1.0419)^{+0.000317}_{-0.000362}$	$1.04(1.0418)^{+0.000323}_{-0.000344}$
n_s	$0.97(0.97133)^{+0.00503}_{-0.00513}$	$0.97(0.965)^{+0.00493}_{-0.00511}$	$0.97(0.9722)^{+0.00484}_{-0.00503}$
$\ln 10^{10} A_s$	$3.04(3.0499)^{+0.0159}_{-0.0168}$	$3.04(3.042)^{+0.0158}_{-0.0171}$	$3.04(3.0568)^{+0.0161}_{-0.0166}$
τ_{reio}	$0.0535(0.0564)^{+0.00773}_{-0.00811}$	$0.0538(0.05198)^{+0.00758}_{-0.00826}$	$0.0536(0.0595)^{+0.00777}_{-0.008}$
$\log_{10} z_t$	> 4.72	> 4.67	> 4.75
M[eV]	$41.6(26.59)^{+7.26}_{-26.9}$	$41.7(23.87)^{+7.81}_{-27.5}$	$41.6(23.5)^{+8.51}_{-28.4}$
S_8	$0.791(0.787)^{+0.0191}_{-0.0155}$	$0.79(0.776)^{+0.0209}_{-0.0167}$	$0.79(0.782)^{+0.0248}_{-0.0178}$
$\Omega_{\rm m}$	$0.302(0.3018)^{+0.00763}_{-0.00935}$	$0.302(0.311)^{+0.00759}_{-0.0095}$	$0.303(0.305)^{+0.00783}_{-0.00906}$
H_0[Km/s/Mpc]	$68.4(68.46)^{+0.685}_{-0.603}$	$68.4(67.96)^{+0.695}_{-0.606}$	$68.4(68.12)^{+0.664}_{-0.614}$

* For ΛCDM model, the 'dm' subscript means the Cold Dark Matter (CDM), and for the MVDM model, it means the mass varying dark matter considered in this chapter.

compared to previous ACT analysis, but this constraint is much weaker than that of Planck+S_8. We find S_8(MVDM)= $0.777^{+0.0159}_{-0.0183}$ in comparison with S_8(ΛCDM)= $0.777^{+0.016}_{-0.0183}$, showing no significant change in the S_8 values in either of the models except for their best-fit values, as given in Table 3.2. However, the addition of prior reduces the S_8 tension significantly compared to all the previous analyses considered in this work. For example, χ^2_{min} in the combined analysis decreases for the MVDM case, with $\Delta\chi^2_{\rm min} = \chi^2_{\rm min}(MVDM) - \chi^2_{\rm min}(\Lambda CDM) = -5.108$.

The individual contribution from each dataset in each run for both models is reported in Table 3.7 in Section 3.6. We show the posteriors of S_8 and Ω_m for each dataset in Figure 3.7, which provides a comparison between MVDM and ΛCDM models across various datasets. Additionally, we have included the residual plots for both the ACT and ACT+S_8 datasets along with the other datasets previously mentioned in Figure 3.8.

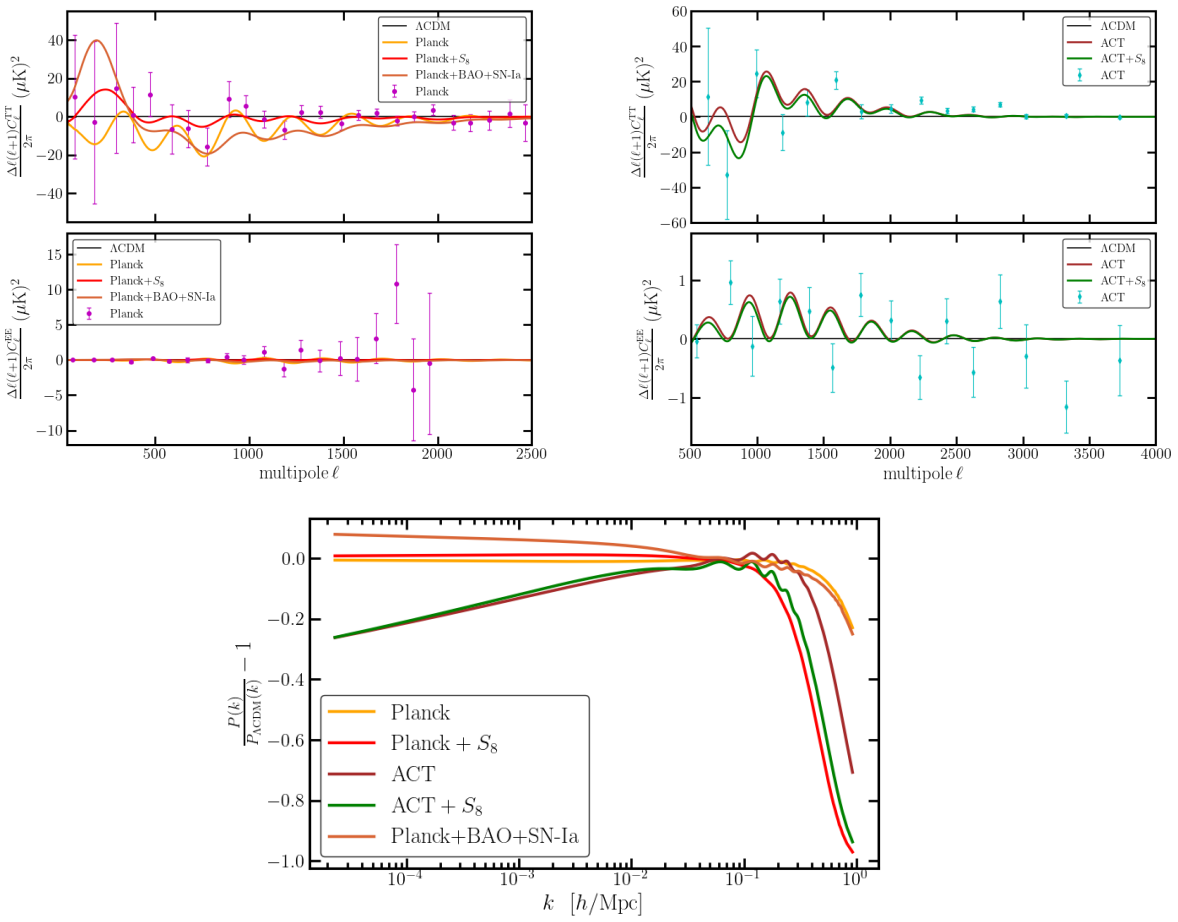


FIGURE 3.8: Residuals of the CMB TT, EE (top panel) and matter (bottom panel) power spectra with respect to ΛCDM in the best fit MVDM model for Planck, Planck+S_8, ACT, ACT+S_8 and Planck+BAO+SN-Ia data set. Here we considered Pantheon+ dataset for "SN-Ia". For better visualisation, the observed Planck and ACT CMB data points in the top panels have been rebinned into wider multipole intervals. This rebinning is used only for visualisation and does not affect the likelihood analysis or parameter constraints.

We have also performed a comprehensive analysis by integrating the Planck, BAO,

and Pantheon+ datasets. The mean and best-fit values of the cosmological parameters derived from this combined analysis are presented in Table 3.3. The results show no significant changes compared to the Planck-only analysis, both in terms of the posterior distributions and the estimated values of the cosmological parameters, as shown in figure 3.5.

We found the lowest lower limit on the transition redshift $\log_{10} z_t > 4.55$ among all combinations of datasets. It is worth noting that the lower bound must be higher than the redshift of recombination to avoid significant impacts on the CMB power spectra. We have also performed an MCMC analysis by considering all of the datasets into account (i.e. both Planck+ACT and Planck+ACT+S_8). However, no significant change in the result was observed.

We computed the Akaike Information Criterion (AIC) to investigate any preference of the data for the MVDM model over ΛCDM. It is a statistical tool for evaluating the relative quality of different models when applied to a specific dataset. The difference in AIC between two models is given by

$$\Delta\text{AIC} = \chi^2_{\text{min,Model}} - \chi^2_{\text{min,}\Lambda\text{CDM}} + 2(N_{\text{Model}} - N_{\Lambda\text{CDM}})\,. \tag{3.6}$$

The $\Delta\chi^2_{\text{min}}$ and ΔAIC for each dataset combination are given in Table 3.5. We see that the ACT data exhibits a mild preference for MVDM over ΛCDM, which is not the case for Planck. This result can also be attributed to the smaller error bars of ACT at high-ℓ compared to Planck, as the changes in the power spectrum for MVDM come from the small scales.

TABLE 3.5: Comparison of $\Delta\chi^2_{\rm min}$ and ΔAIC per experiment for MVDM and ΛCDM models.

Dataset	MVDM	
	$\Delta\chi^2_{\rm min}$	ΔAIC
Planck	-1.23	+2.77
Planck+S_8	-3.81	+0.19
ACT	-4.2663	-0.2663
ACT+S_8	-5.108	-1.108
Planck+BAO+SN-Ia	-0.26	+3.74

3.5 Summary

In this study, we explored the model of a mass-varying dark matter (MVDM), where it transitions from a relativistic to a nonrelativistic phase in the early Universe, and derived constraints using cosmological observation data. We assumed a phenomenological relation of dark matter mass as a function of redshift without invoking any specific particle physics model. We focused only on fast transitions in this work. The large free streaming velocity in the relativistic phase of DM at early time washes out the structures at small scales and manifests its effect in easing the tension between the amplitude of matter fluctuations (S_8) determined from local Heymans *et al.* (2021); Heymans *et al.* (2013); MacCrann et al. (2015); H. Hildebrandt *et al.* (2020); S. Joudaki *et al.* (2020); Abbott *et al.* (2018) and high redshift probes Aghanim et al. (2020), as depicted in Figure 3.5. Our Bayesian analysis with the MVDM model reveals a slight reduction in S_8 when only Planck CMB data is used, and the result does not change significantly when BAO and supernova datasets are included. However, the inclusion of S_8 prior, obtained from KIDS1000+BOSS+2dfLenS weak lensing measurements, significantly reduces the value of S_8. Furthermore, the model puts a lower bound on the transition redshift

and shows a mild preference for the mass of the dark matter to be 23.87 eV. Similar $\sim$ eV order warm dark matter mass has also been predicted in other models Rogers & Poulin (2023). This work uses S_8 prior throughout the analysis to test the potential of the MVDM model to alleviate the S_8 tension and constrain the final mass of the dark matter. However a comprehensive analysis would require using the lensing and clustering data directly to get a robust inference on the model parameters. We keep this for future work.

The MVDM model shows new features at high multipoles of the CMB anisotropic power spectra. Because of its relatively larger error bars at high multipoles, Planck-only analysis yields poorer constraints on the DM mass. Since ACT data provides those measurements at higher multipoles with comparatively better precision, our MCMC analysis showed better constraining of mass M compared to Planck. This is also reflected in the ΔAIC calculations. Including prior from KIDS1000+BOSS+2dfLenS weak lensing data even further reduces the S_8 as expected.

Future experiments, such as CMB-S4 Abazajian et al. (2016, 2022), are expected to achieve higher precision measurements at high multipoles, specifically for goals related to de-lensing the inflationary B-modes, constraining $N_{\rm eff}$ and Σm_ν, among others. Such experiments are expected to provide insight into the detailed small-scale physics of the CMB data, which could aid in the detection and proper constraint of the DM mass M of our model. In this regard, a Fisher forecast can also be conducted in the future. Another way to probe such a model is through CMB spectral distortion as shown in Sarkar et al. (2017a), which might also be detected in future experiments.

As previously mentioned, we did not invoke any specific particle physics model to explain the mass variation of dark matter. However, considering a particular particle physics model could potentially introduce additional model-dependent

effects beyond those reported in this work. The residual plots of CMB power spectra and matter power spectra, as shown in Figure 3.8 and referenced in Das et al. (2023), exhibit oscillatory structures resulting from the additional drag force exerted by the relativistic DM, leading to a phase shift in the baryon acoustic oscillation. A similar phenomenon could occur in the dark sector, too. This model could also be employed to constraint the dark acoustic oscillation Schaeffer & Schneider (2021); Parashari & Laha (2023). Additionally, the present model could be tested by the small-scale Lyman-α forest data in line with recent works Archidiacono et al. (2019); Miller et al. (2019); Wang et al. (2013); Murgia et al. (2017); Baur et al. (2017); Murgia et al. (2018); Palanque-Delabrouille et al. (2020); Enzi et al. (2021).

3.6 Tables of χ^2

We report the $\chi^2_{\rm min}$ for each MCMC analysis performed:

TABLE 3.6: Best-fit $\chi^2_{\rm min}$ per experiment (and total) for both the model

Experiment	ΛCDM			MVDM		
Planck high-ℓ TT,TE,EE	2353.36	2354.37	2358.06	2350.87	2352.13	2353.6
Planck low-ℓ EE	395.75	395.85	395.8	396.15	396.82	395.84
Planck low-ℓ TT	22.67	22.70	21.9	23	23.35	23.6
KiDS/BOSS/2dFGS	–	–	2.38	–	–	1.29
BAO-boss-dr12	–	4.10	–	–	4.09	–
BAO-smallz-2014	–	1.31	–	–	1.32	–
Pantheon+	–	1411.59	–	–	1411.95	–
Total	2771.78	4189.92	2778.14	2770.55	4189.66	2774.33

TABLE 3.7: Best-fit $\chi^2_{\rm min}$ per experiment (and total) for both the model

Experiment	ΛCDM		MVDM	
ACTPol lite DR4	280.0462	281.1964	275.7791	276.5869
$\tau_{\rm reio}$ prior	0.0033	395.8	0.0041	0.1261
KiDS/BOSS/2dFGS	–	0.6766	–	0.0729
Total	280.0495	281.8939	275.7832	276.7859

Chapter 4

Formation and Abundance of *Late Forming* Primordial Black Holes as Dark Matter *

4.1 Introduction

As reviewed in Chapter 1, the microscopic nature of dark matter remains unknown, and the absence of signals in direct and collider searches motivates the exploration of its viable alternative candidates. Among these, primordial black holes constitute a particularly well-motivated possibility, formed from the collapse of large density perturbations in the deep radiation-dominated era Zel'dovich & Novikov (1967); Hawking (1971) and behaving as pressureless matter at the background level. Depending on their mass and formation epoch, primordial black holes can leave distinctive signatures on small scales and in gravitational wave observations, making them a powerful probe of early-Universe physics.

*This chapter is based on publication Chakraborty et al. (2022b)

Primordial black holes are generally formed due to the collapse of inhomogeneities in the early universe. There are several mechanisms to form PBH. Possible formation mechanisms are extensively discussed in Chapter 1. Usually, the mass of the formed PBHs is of the order of the horizon mass during their formation. So a large range of masses of PBH are possible to form and the later they form, the higher their mass. If the PBHs form during radiation dominated era, the PBH mass, $M_{\rm BH}$, differs from the horizon mass, $M_{\rm H}$, by only a factor of unity $\gamma \lesssim 1$ (Carr et al. 2021a),

$$M_{\rm BH} = \gamma M_{\rm H} = \frac{\gamma c^3 t}{G} \approx 2.03 \times 10^5 \gamma \left(\frac{t}{1\ {\rm s}}\right) M_\odot. \tag{4.1}$$

But in this work, we break this simple relation between PBH mass and formation red-shift by introducing a new scale in the formation process. The main goal here is to form PBH at a later epoch (between BBN and CMB decoupling epoch) but with the PBH masses much lesser than horizon mass at the time of formation. In standard ΛCDM cosmology, it is not possible to form PBH during this epoch as gravity is not strong enough to overcome radiation pressure. But the presence of a new additional force stronger than gravity can make the story different (Savastano et al. 2019; Das et al. 2021). For example, recently, it was pointed out (Savastano et al. 2019) that an early dense DM halo can form deep in a radiation-dominated era when an attractive scalar force makes the dark matter perturbation grow much faster $\delta \sim a^p$ than standard logarithmic growth. As a follow-up work on this (Flores & Kusenko 2021a), it was further demonstrated that these early halos could lose energy through scalar radiation and can indeed form PBH as a viable dark matter candidate. This mechanism provides a concrete microscopic realization of the phenomenological mass-varying dark matter framework discussed in the previous chapter, in which dark matter transitions from relativistic to non-relativistic behavior.

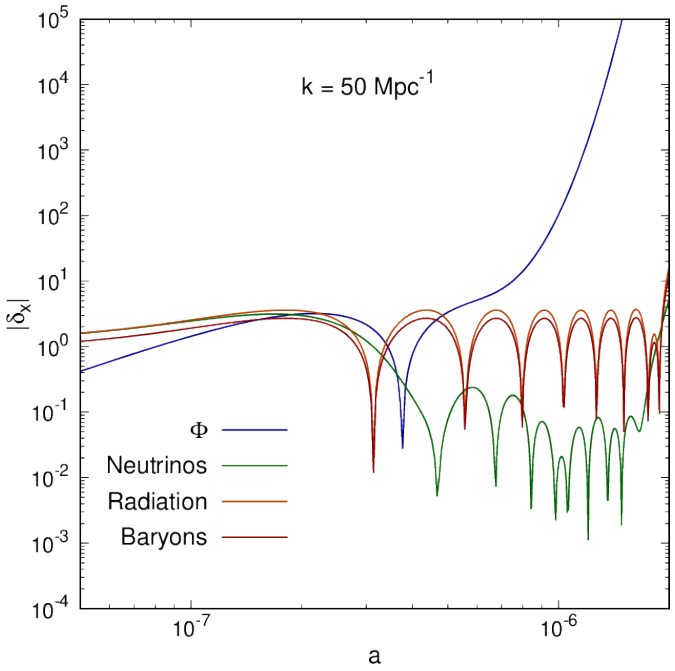


FIGURE 4.1: $|\delta|$ vs scale factor a for a typical wave number which is inside the Compton scale of the scalar field around the PBH formation redshift $z_T = 10^6$. We can see that the growth of the $|\delta_\Phi|$ is exponential which makes this mode go non-linear and finally collapse to form PBHs.

Here we propose a scenario where the growth rate of primordial inhomogeneities of a fermionic particle coupled with a scalar field can even grow much faster than polynomial. We show that exponential growth is well possible in a Yukawa-type scalar-fermion interaction Gogoi et al. (2021). This exponential growth occurs when our keVmass fermionic particle turns non-relativistic around $z_T \sim 10^6$ and sound speed of DM perturbation turns imaginary Afshordi et al. (2005). We derive the matter power spectrum for the above mentioned exponential growth scenario and do a detailed calculation of the PBH mass function in this scenario using the scaling relation for a critical gravitational collapse of a massless scalar field given by Choptuik (1993) and the Press-Schechter formalism Press & Schechter (1974). We find that for the $z_T \simeq 10^6$ the peak of the PBH mass function lies between $10^{-15} - 10^{-12} M_\odot$ and therefore it can account for almost entire dark matter in the universe ($f(M) \simeq 1$) given the current constraints on the PBH abundances.

4.2 Late Forming PBH: The mechanism

This thesis proposes a novel mechanism for forming PBH at a late epoch (around $z \simeq 10^4 - 10^7$). But later, we will see if we want PBH to make up for the entire DM from cosmological constraints $z \geq 10^6$. The key ingredient is – a dark matter fermion that couples to a long-range scalar. Due to the presence of coupling to matter, scalar field evolution is controlled by an effective potential $V^{\text{eff}}(\phi)$ Das et al. (2006a). Typically, the shape of the effective potential has a minimum, and the scalar field adiabatically follows that minima Khoury & Weltman (2004c) of the effective potential. The dynamics of scalar with a self-interacting potential in such chameleon theories can also give rise to a temporary epoch of early dark energy before CMB Karwal et al. (2021); Gogoi et al. (2021) and can relax Hubble tension. It was explicitly shown for the case of usual dark energy Afshordi et al. (2005) that such a system of interacting dark matter-scalar fluid would encounter a perturbative instability when matter particle turns non-relativistic. In Gogoi et al. (2021), the same mechanism was extended for early dark energy theories, and it was shown that even in radiation dominated era, the EDE phase would encounter exponential instability in dark matter perturbation when it turns non-relativistic. In our case, the DM mass is of the order of KeV–so one would expect the instability to occur around $z_T \simeq 10^6 - 10^7$.

To find the exact epoch when fluctuation grows non-linear, one needs to solve for the linear perturbation equations- evolving it from big bang to a redshift around z_T. We adopt the generalized dark matter(GDM) formalism for our DM-scalar fluid as done in Hu (1998). In this formalism, the background fluid equation state parameter, $w_{\phi-\psi}$, evolves with redshift z. In the early epoch, the fluid was relativistic, so the dark matter and the scalar field are not coupled (as it couples through the trace of energy-momentum tensor). So, we take $w_{\phi-\psi_1} \sim \frac{1}{3}$ at high redshifts, and as the dark matter tends to become non-relativistic around a redshift z_T, the effective coupling turns on. For a quadratic self-interacting

scalar potential, the fermion-scalar fluid effectively behaves like early dark energy for a short duration - soon after, the fluid sound speed square c_s^2 turns negative, which results in a strong instability in the fluid perturbation. For details of the evolution of c_s^2 and $w_{\phi-\psi_1}$ we refer to the work Gogoi et al. (2021); Afshordi et al. (2005). It was shown there that the DM-scalar fluid perturbation starts to grow exponentially even in radiation dominated era once the sound speed becomes imaginary. In this work, we show that this mechanism would form a dense early DM halo which finally collapses into PBH due to cooling through scalar radiation Flores & Kusenko (2021a).

In applying the GDM formalism, we approximate the coupled fermion–scalar system as a single effective perfect fluid. We neglect anisotropic stress and non-adiabatic pressure perturbations, and define the physical sound speed in the rest frame, or equivalently the comoving frame, of the effective fluid, identifying it with the adiabatic sound speed, $c_s^2 = c_a^2 = \dot{P}/\dot{\rho}$. Under these assumptions, the perturbation equations in synchronous gauge within the GDM formalism are given by Gogoi et al. (2021):

$$\dot{\delta} = -(1+w)\left(\theta + \frac{\dot{h}}{2}\right) - 3(c_s^2 - w)H\delta \tag{4.2}$$

$$\dot{\theta} = -(1-3c_s^2)H\theta + \frac{c_s^2 k^2}{1+w}\delta \tag{4.3}$$

We implement the model in the Boltzmann code CLASS (Lesgourgues 2011; Blas et al. 2011). In As shown in Figure 4.1, around z_F, the density perturbation of the coupled fluid increases compared to those of the other components. This exponential growth makes the perturbation turn non-linear very fast, followed by the formation of dense early halos, which evolve into PBH (Flores & Kusenko 2021a) by loose energy through scalar radiation.

There are two main concerns related to the formation of dark matter PBH at

such a late epoch few *e-foldings* prior to CMB. First of all, one needs to check if the appearance of dark matter so late in the universe is at all viable from CMB and structure formation perspective. From the recent studies it seems, if DM is produced earlier than $z \geq 10^6$, one can satisfy both CMB Sarkar et al. (2017b); Agarwal et al. (2015), Large Scale Structure Sarkar et al. (2017b, 2016, 2017b) observations as well as constraints from local Milky Way satellite observations Das & Nadler (2021b).

The second challenge is the horizon size around this late redshift is very large, and if one produces horizon size PBH, the PBH mass would be stupendously big ($M > 10^{11} M_\odot$, known as SLAB- the Stupendously Large Black Holes). This will be subject to many constraints arising from dynamical friction and destruction of galaxies in the cluster $f_{PBH} \lesssim 10^{-3}$ (Carr et al. 2021b). But we will show how the scalar field mass in our example is typically higher compared to the local Hubble constant. So the Compton wavelength or the range of the fifth force is much smaller than the horizon. As an attractive fifth force is the main reason for forming PBH-the size of the PBH is much smaller compared to horizon mass at the formation epoch.

During the radiation domination, $H = (2t)^{-1}$, such that the Universe's age t is a function of the temperature of the thermal bath T as the following,

$$t \approx 2.42\ g_*^{-1/2} \left(\frac{T}{1\ \text{MeV}}\right)^{-2} \text{s}. \tag{4.4}$$

Using eqns. (4.1), and (4.4), we find that for such a PBH being formed at a redshift $z_T \simeq 10^6$, is expected to have a horizon size mass, $M_{\rm BH} \sim 10^{12} M_\odot$, as evaluated from eq. (4.1) which is much heavier than the mass window mentioned above. But as in our case, only a fraction of horizon mass (enclosed in the Compton volume

of the scalar) collapses into the black hole, we find

$$M_{\rm BH} = \frac{\gamma c^3 t}{G} \approx 2.03 \times 10^5 \gamma \left(\frac{t}{1\ {\rm s}}\right) M_\odot \left(\frac{m_\phi}{H}\right)^{-3}, \tag{4.5}$$

where, m_ϕ is the mass of the scalar field. The term $(m_\phi/H)^{-3}$ provides with an extra parameter for tweaking $M_{\rm BH}$, as can be seen from Fig.4.2.

We discuss a scenario where the PBHs form at a temperature, $\sim$ 1 keV in the presence of a scalar field of mass, $m_\phi \sim 10^{-13}$ eV, so that the factor $(H/m_\phi)^3$ corresponds to a value $\sim 10^{-25}$. The density of the thermal bath derived as the function of the Hubble parameter, $3H^2 M_{\rm Pl}^2/8\pi$, is evaluated as $\sim 10^{12}$ eV^4 during this time period. Assuming a monochromatic mass function the masses of the PBHs formed can be estimated as the mass enclosed within the Hubble horizon, $M_H \sim (H^{-1})^3 \rho \sim M_{\rm Pl}^2/H$, multiplied by the factor, $(H/m_\phi)^3$. With the choice of the parameter space as discussed above, the PBHs are expected to form with a mass, $M_{\rm BH} \sim 10^{-14}\ M_\odot$. This mass corresponds to a Schwarzschild radius, $\sim M_{\rm BH}/M_{\rm Pl}^2 \sim 10^{-9}$ cm, far below the distance measures of this study.

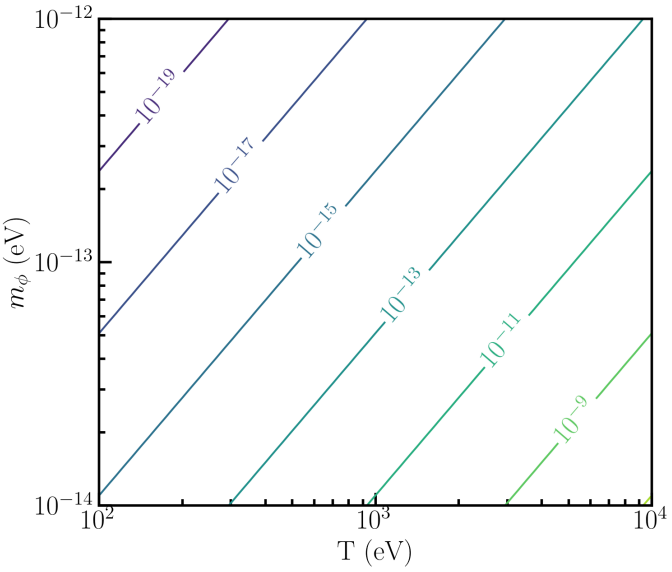


FIGURE 4.2: The contours above delineate different PBH masses in the solar units as a function of the $T - m_\phi$ parameter space, derived using eq. (4.5) where T is the temperature of the Universe at epoch of formation of PBH and m_ϕ is the mass of the scalar field mediating the fifth force.

4.3 Static Structure of primordial Halo

It was pointed out in Flores & Kusenko (2021a) that in the presence of an attractive long-range force mediated by a scalar field, an intermediate state of a dark matter halo forms, as this attractive 'fifth force' is balanced by the Fermi pressure. Accelerated dark matter particles moving in the halo will emit scalar radiation due to the long-range interaction, resulting in the halo losing energy so that it may collapse rapidly to form PBH. This has been schematically shown in Figure 4.3. The dipole radiation due to the coherent motion of the particles should vanish because the particles are identical, while the higher moments are expected to be negligible. On the other hand, where the radiation is due to particles behaving as incoherent sources, the radiated power depends linearly on the number of dark matter particles in the halo. The halo can also lose energy through scalar bremsstrahlung radiation, where the dominating radiation is quadruple as the dark matter particles are identical Maxon & Corman (1967); Maxon (1972). As the halo decreases

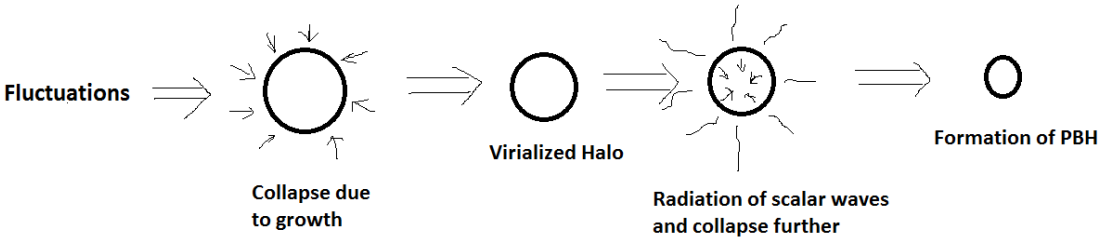


FIGURE 4.3: Schematic representation of PBH formation mechanism discussed in this chapter.

in size, the collapse timescale increases, the diffusion timescale decreases, and at some point, the diffusion becomes slower than the collapse. This results in the radiation being trapped, and the cooling happens from the surface. A dark matter halo can collapse into a black hole only if the rate of energy loss, $\tau_{\rm loss}$, is less than the expansion rate of the Universe, $\sim H^{-1}$.

In this section, we numerically show that, indeed, the temporary static phase is possible where fermi degeneracy pressure balances scalar forces. Numerically we solve for the static profile for the ϕ field. Derivations of these equations are provided in Brouzakis & Tetradis (2006); Lee & Pang (1987); Chanda & Das (2017). We consider the dark matter to be a fermion field, ψ, self-interacting through a scalar field ϕ. We discuss a more general interaction as compared to the first work on this type of model (Fardon et al. 2004) which considers Majorana mass as a linear function of ϕ. In this analysis we introduce a function $f(\phi)$ so that the dark matter mass is obtained as, $m_\psi = m_D^2/f(\phi)$, where, m_D is the Dirac mass. We choose the self-interaction to have the form, $f(\phi) = \lambda_\psi \phi$.

Prior to the phase transition, an effective potential controls the dynamics of the ϕ (Fardon et al. (2004))

$$V_{\rm eff} = \rho_\psi + V(\phi). \tag{4.6}$$

In our analysis, we use, $V(\phi) = m_\phi^2 \phi^2$, where, m_ϕ is the scalar field mass.

We assume the dark matter particles to be weakly interacting and non-scattering such that the motion of the ψ particles can be determined using the Thomas-Fermi approximation Brouzakis & Tetradis (2006), that is, the physical parameters such as density, pressure, and number density are characterized by the distribution, $\sim [1+\exp(\epsilon_F/T)]^{-1}$, where, the Fermi energy, $\epsilon_F = \sqrt{p_F^2+m_\psi^2}$; p_F being the Fermi momentum. We consider a simpler scenario by doing the calculations in the zero temperature limit Brouzakis & Tetradis (2006), and, obtaining the form of the trace of the energy-momentum tensor, $T^\mu_\mu = \rho - 3p$:

$$T^\mu_\mu = \frac{m_\psi^2}{2\pi^2}\left(p_F\sqrt{p_F^2+m_\psi^2} - m_\psi^2 \ln\left(\frac{p_F+\sqrt{p_F^2+m_\psi^2}}{m_\psi}\right)\right), \tag{4.7}$$

and the pressure

$$p = \frac{m_\psi^2}{8\pi^2}\left[\frac{2p_F^3}{3m_\psi^2}\sqrt{p_F^2+m_\psi^2} - \left(p_F\epsilon_F - m_\psi^2\ln\left(\frac{p_F+\epsilon_F}{m_\psi}\right)\right)\right], \tag{4.8}$$

where, $\epsilon_F = \sqrt{p_F^2+m_{\psi_1}^2}$.

In the weak GR limit, the KG equation becomes,

$$\phi'' + \frac{2}{r}\phi' = \frac{dV(\phi)}{d\phi} - \frac{d\ln[m_\psi]}{d\phi}T^\mu_\mu, \tag{4.9}$$

and the Euler equation for pressure, p,

$$\frac{dp}{d\phi} = \frac{d\left[\ln m_\psi\right]}{d\phi}T^\mu_\mu. \tag{4.10}$$

We obtain a static solution for ϕ as demonstrated in Fig. 4.4, which is determined by balance between the attractive fifth force and the local Fermi pressure as derived from the Euler equation, (4.10), and the Klein-Gordon equation (4.9). The mass enclosed in the dark matter halo corresponds to a Schwarzschild radius of

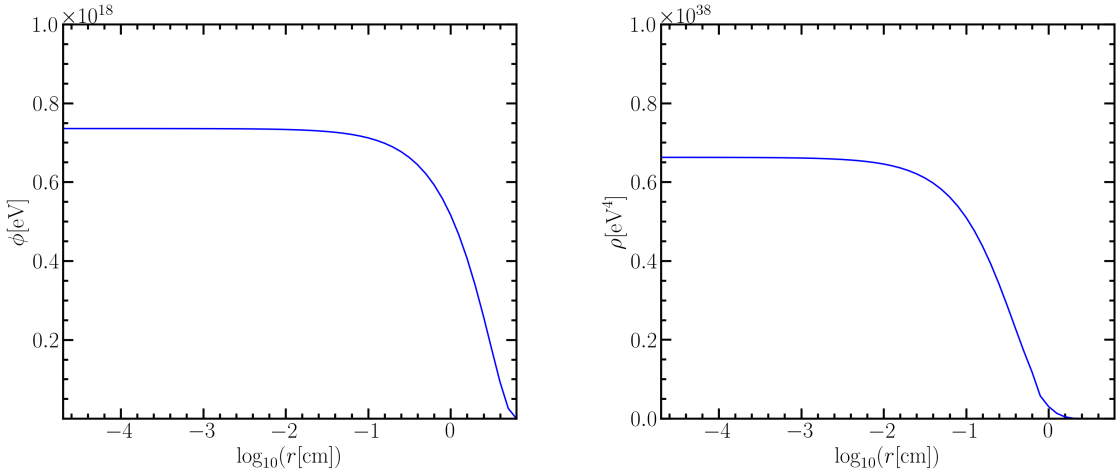


FIGURE 4.4: In the above, we demonstrate the static profile, which is obtained by solving eqns. (4.10), and, (4.9). The plot at the left shows the static profile for the scalar field, ϕ, and the plot at the right delineates the density profile, ρ, of the resulted dark matter halo. As discussed in the main text, this halo may later collapse due to cooling through scalar radiation and eventually form PBH (Flores & Kusenko 2021a).

$\sim 10^{-9}$ cm, which is much smaller than the size of the halo. The density at the core of the profile can be predicted without explicitly carrying out the numerical calculations. Because of the self-interactions through the ϕ field, the density of dark matter particles near the core of the profile should be much denser by a factor of $(m_\phi/H)^3$. Therefore, for PBHs formed at ~ 1 keV for dark matter particles self-interacting through a scalar of mass, $m_\phi \sim 10^{-13}$ eV, the core density should be, $\sim 10^{12}$ eV^4 $(m_\phi/H)^3 \sim 10^{37}$ eV^4, which, agrees very well with the results from the numerical studies. We should remind ourselves from the earlier calculations that at ~ 1 keV, the factor, $(m_\phi/H)^3 \sim 10^{25}$, for the given scalar mass, and, the factor 10^{12} eV^4 is the density of the thermal bath evaluated at the same temperature.

4.4 PBH mass function and PBH DM abundance

In this section, we focus on estimating the dark matter abundance of PBH from the collapse of primordial fluctuations in the radiation-dominated era. Though we concentrate mostly on the cosmology with the exponential growth of perturbation prior to the phase transition, our treatment and numerical code developed in the current section is kept generic and can be applied for calculating PBH abundance with different perturbations growth rate. It is instructive to note that here in this work, we consider a non-monochromatic mass function, i.e., the mass of PBH formed from collapse does not necessarily have to be equal to the horizon mass.

The mass distribution of PBH is usually stated in terms of $f(M)$, the fraction of CDM made up of PBHs of a given mass M, and is given by (Byrnes et al. 2018),

$$f(M) = \frac{1}{\Omega_{\rm CDM}} \frac{d\Omega_{\rm PBH}}{d\ln M} \tag{4.11}$$

where $\Omega_{\rm CDM}$ and $\Omega_{\rm PBH}$ are the abundances of CDM and PBH respectively.

Using Press-Schechter formalism Press & Schechter (1974) and taking into account the mass fraction of the Universe that collapses to form PBHs at the time of formation, we can write expression for $\beta(M)$ as,

$$\beta(M) = 2\int_{\delta_{\rm c}}^{\infty} \frac{M}{M_h} Pr(\delta)\, d\delta \tag{4.12}$$

where $\delta_{\rm c}$ is the critical value of δ at the time of horizon entry for PBH formation, and $Pr(\delta)$ is the probability density function of the density contrast. Assuming a Gaussian distribution of density fluctuations, $Pr(\delta)$ can be given as,

$$Pr(\delta) = \frac{1}{\sqrt{2\pi\sigma^2(R)}} \exp(-\frac{\delta^2}{2\sigma^2(R)}) \tag{4.13}$$

where $\sigma(R)$ is smoothed density fluctuations over a smoothing radius R and can be given as,

$$\sigma^2(R) = \int_0^\infty \frac{dk}{k} \Delta(k) W_R^2(k) \tag{4.14}$$

here $W_R^2(k)$ is the window function of smoothing radius R which we take as a step function, is given by,

$$W_R(k) = \theta\left(\frac{1}{R} - k\right) \tag{4.15}$$

The smoothing radius R can be related to horizon mass M_h using the following relation, (see, Appendix 4.6)

$$\frac{1}{R} = \frac{k_B T_0}{2} \left(\frac{g_{*,s}(T_0)}{g_{*,s}(T_h)}\right)^{1/3} \left(\frac{g_{*,\rho}(T_h)}{45\hbar^3 c^3 \pi G}\right)^{1/4} \frac{1}{\sqrt{M_h}} \tag{4.16}$$

The dimensionless power spectra $\Delta(k)$ in Equation 4.14 can be written as,

$$\Delta(k, z) = \frac{k^3 P(k, z)}{2\pi^2} = A_s \delta^2(k, z) \tag{4.17}$$

where, $P(k)$ is the density power spectra and A_s is the primordial power spectrum amplitude.

Now considering the formation of PBH from the gravitational collapse of primordial density fluctuations in the radiation dominated phase of the early universe as a critical phenomenon, we can write the following equation for the PBH mass at its formation (Choptuik 1993),

$$M = K M_h (\delta - \delta_c)^\gamma \tag{4.18}$$

where M is the mass of the primordial black hole; δ is the density contrast, and

δ_c is the critical value of δ at the time of horizon entry, M_h is the horizon mass at the time the fluctuation entered the horizon, K and γ are constants which depend on the shape of the fluctuations and background equation of state respectively.

The above equation can be inverted to give δ as a function of M as,

$$\delta = \left(\frac{M}{KM_h}\right)^{1/\gamma} + \delta_c = \mu^{1/\gamma} + \delta_c \tag{4.19}$$

where, $\mu = M/(KM_h)$. Now using Eq 4.11, 4.12 and 4.19 we can write $f(M)$ as (Byrnes et al. 2018),

$$f(M) = \frac{2}{\Omega_{\rm CDM}} \int_{-\infty}^{\infty} Pr(M_h) \frac{M}{\gamma M_h} \mu^{1/\gamma} \left(\frac{M_{\rm eq}}{M_h}\right)^{1/2} d\ln M_h \tag{4.20}$$

where $Pr(M_h)$ is the probability density function of the density contrast in terms of M_h,

$$Pr(M_h) = \frac{1}{\sqrt{2\pi\sigma^2(M_h)}} \exp\left(-\frac{(\delta_c + \mu^{1/\gamma})^2}{2\sigma^2(M_h)}\right) \tag{4.21}$$

Power spectrum $P(k)$ for exponentially growing δ

In this section, we discuss the case where the density contrast grows exponentially, i.e., $\delta \propto \exp(\lambda k c_s t)$, where c_s is the sound speed, and λ is a constant and has been tuned to a suitable value such that the formed PBH fractional abundances $f(M)$ are within 1. In this case, in which the scaling (the exponential growth) regime starts from $z_{\rm in}$ and lasts till redshift z_T, we find the linear matter power spectrum

as

$$P(k,z) = \begin{cases} \frac{2\pi^2 A_s}{k^3} & \text{if } k \leq k(z_T), \\ \frac{2\pi^2 A_s}{k^3} \exp(\frac{2\ c_m}{(1+z_T)^2}) \exp(-\frac{2\ c_m}{(1+z(k))^2}) & \text{if } k(z_T) < k \leq k(z_{\rm in}), \\ \frac{2\pi^2 A_s}{k^3} \exp(\frac{2\ c_m}{(1+z_T)^2}) \exp(-\frac{2\ c_m}{(1+z_{\rm in})^2}) \left(\frac{\log(1+z_{\rm in})}{\log(1+z(k))}\right)^2 & \text{if } k > k(z_{\rm in}) \end{cases} \tag{4.22}$$

The above power spectrum is evaluated at redshift $z = z_T$ with $c_m = \lambda k c_s / 2\sqrt{\Omega_{r,0}} H_0$ and where z as a function of k can be given as, (see, Appendix 4.6)

$$1 + z(k) = \frac{k}{k_B T_0} \left(\frac{g_{*,s}(T_0)}{g_{*,s}(T_h)}\right)^{-1/3} g_{*,\rho}^{-1/4}(T_h) \left(\frac{4\pi^3 H_0^2\, G\, \Omega_{r,0}}{45\, \hbar^3 c^9}\right)^{-1/4} \tag{4.23}$$

In $z(k)$, the redshift is the horizon-entry redshift associated with the comoving mode k, defined by $k = a[z(k)]H[z(k)]$. $k(z_T)$ and $k(z_{\rm in})$ are different wave numbers that just entered the horizon corresponding to their respective redshifts, $z_{\rm in}$ is the redshift at which this growth starts and ends at a redshift z_T. In the equation 4.22 the first case ($k \leq k(z_T)$) represents the scales which are still outside the horizon at the redshift z_T, the second case ($k(z_T) < k \leq k(z_{\rm in})$) represents the scales that have entered during the exponential growth period, and the last case ($k > k(z_{\rm in})$) represents the scales which entered before the growth period and grew logarithmically in the initial phase following the standard ΛCDM cosmology driven growth. After that all the scales grow by equal amount in the exponentially growing regime. For our calculation we have taken $z_{\rm in} = 3 \times 10^7$. We cut the power spectrum for $k > k(z_{\rm in})$ as these modes enter the horizon before the exponential growth regime starts.

Results

We compute the PBH mass function $f(M)$ using Equations 4.20 and 4.21 in which for $\sigma(M_h)$ we use Equations 4.14, 4.16 and 4.22. For our calculation we have used

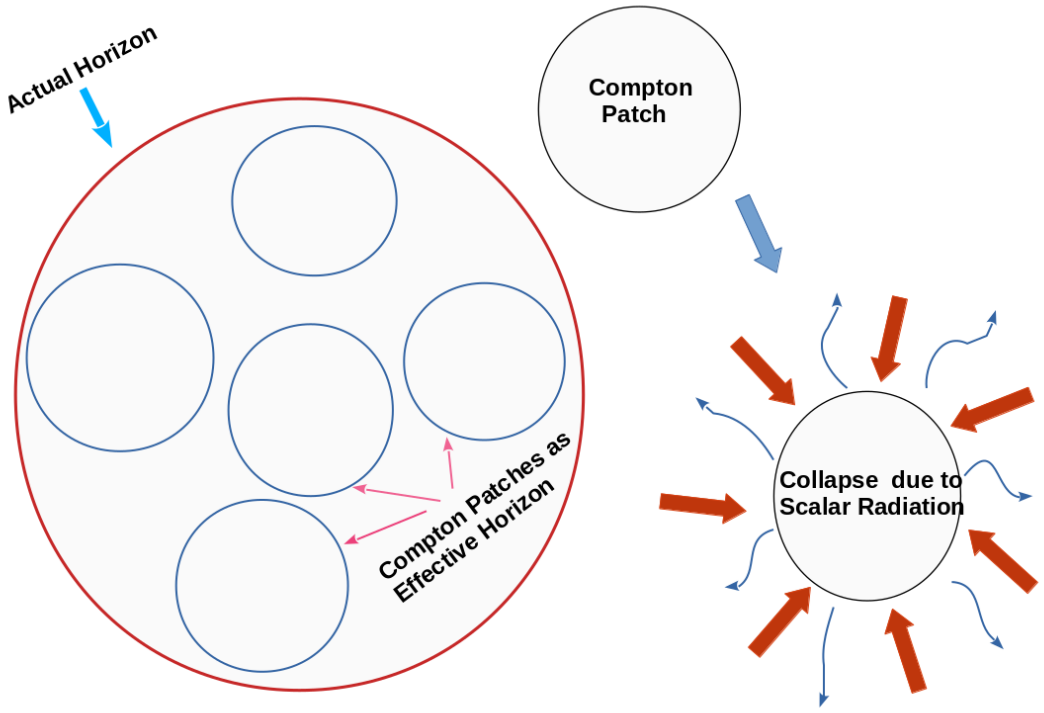


FIGURE 4.5: Schematic representation of multiple PBH formation in a single horizon

$K = 11.9$, $\gamma = 0.37$ as suggested by Green & Liddle (1999) and $\delta_c = 2.07$ from Savastano et al. (2019). The corresponding plots is shown in the Figure 4.6. In this figure all the constraints plot are taken from Flores & Kusenko (2021a) . For this calculation, we have not taken the whole horizon to be under the influence of the exponential growth but rather taken a small fraction of it, which is basically the ratio between the range of the scalar field, i.e., Compton-scale and the Hubble radius ($(m_\phi/H)^{-1}$). This is taken into account in the calculation as a factor of $(m_\phi/H)^{-3} \sim 10^{-25}$ to the black hole mass evaluated in our calculation and the plot in Figure 4.6. Also, since the Compton scale is smaller than the horizon scale, at any epoch, there will be multiple numbers of Compton patches that will contribute to the formation of PBH, which has been represented schematically in Figure 4.5. We have incorporated this into the calculation by multiplying a factor of $(m_\phi/H)^3 \sim 10^{25}$ in the expression of $f(M)$ in equation 4.20. Therefore the modified expression becomes,

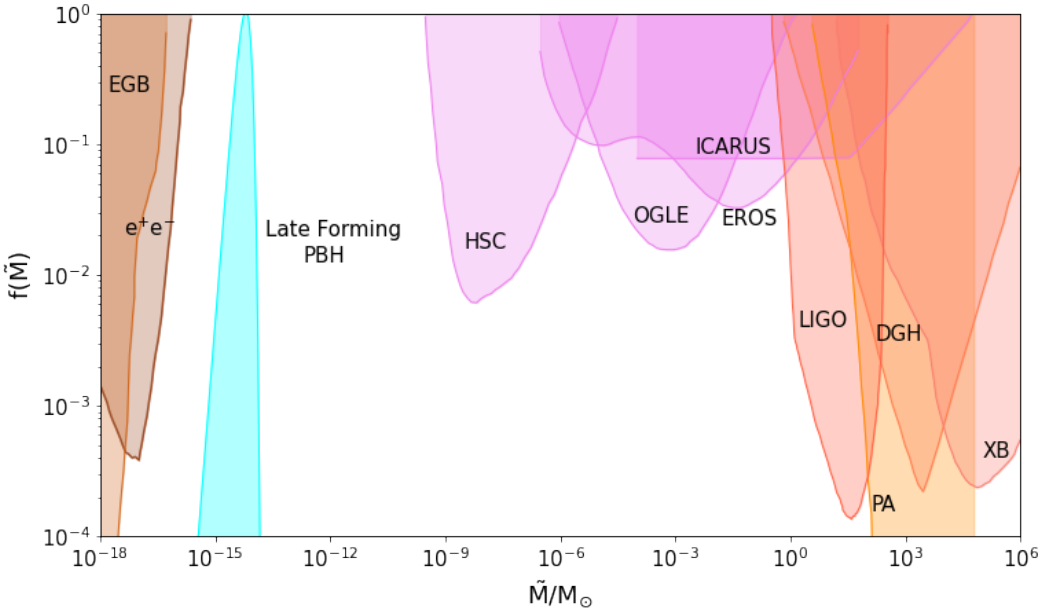


FIGURE 4.6: Plot of the late forming PBH mass function, $f(\tilde{M})$, shown in cyan, suggests that the PBH density can attribute to the entire dark matter density in the universe. PBH mass function shown in this figure is for $f_{\max}(\tilde{M}) = 1$ (ie., $f_{\rm PBH} \approx 1$) for redshift of formation $z_T \sim 10^6$.

$$f(\tilde{M}) = \left(\frac{m_\phi}{H}\right)^3 \frac{2}{\Omega_{\rm CDM}} \int_{-\infty}^{\infty} Pr(M_h) \frac{\tilde{M}}{\gamma M_h} \tilde{\mu}^{1/\gamma} \left(\frac{M_{\rm eq}}{M_h}\right)^{1/2} d\ln M_h \tag{4.24}$$

where, $\tilde{M} = M\left(\frac{m_\phi}{H}\right)^{-3}$ which is defined as the actual black hole mass when a Compton range of collapse is considered and $\tilde{\mu} = \tilde{M}/(KM_h)$. One can think this treatment is analogous to the modified definition of β for non-monochromatic mass function, given in equation (4.12) as opposed to, in Press-Schechter theory, the factor M/M_h in β never appears, due to assumption of the monochromatic mass function. Also, hypothetically one can think of the constant Compton scale as our effective horizon. There is a sharp exponential growth in the power spectrum inside this effective horizon, and it reflects an approximate sharp peak in $f(\tilde{M})$, which we have got in our plot.

The plot in figure 4.6 shows a peak $f(\tilde{M})$ for a certain PBH mass for which the PBH contributes to the total dark matter density in the universe. Since the Compton scale remains constant with time, the ratio between the Compton scale

and the Hubble radius ($(m_\phi/H)^{-1}$) decreases with time. This ratio takes the highest value in our calculation at the beginning of the growth regime. For this reason, the $f(\tilde{M})$ gets the highest contribution from the PBH mass corresponding to this scale. We find that, given enough span for the exponential growth regime ($z_T \sim 10^6$) our model can give $f_{\rm max}(\tilde{M}) = 1$ which is a good approximation to $f_{\rm PBH} = 1$, suggesting that these PBHs can make up for all the dark matter in this case. Increasing the termination redshift of the growth regime, z_T beyond $\sim 10^6$, decreases the abundance of the PBHs, and hence the corresponding $f_{\rm PBH}$ goes below 1.

4.5 Summary

In this chapter, we present a novel mechanisms for late forming ($z_T \sim 10^6$) PBHs. Keeping the scale-invariant inflationary primordial power as it is, here we show that a late phase transition in a fermion-scalar fluid can produce dark matter PBHs due to the formation of early dense halo in radiation dominated era, which evolves into PBH by cooling though scalar radiation. We also do a detailed analytical calculation of the PBH mass function for these cases and show that, in principle, these PBHs can even make up for almost all of the dark matter. The PBH masses in these models are in the range of $\sim 10^{-16} - 10^{-14} M_\odot$.

In standard ΛCDM cosmology, the growth function being logarithmic in the radiation-dominated era, gravity alone can not clump the matter to collapse into PBH. In this work, we have considered a scenario where the growth rate of the primordial inhomogeneities is exponential. This can happen in a scenario where a force stronger than gravity emerges due to interaction between an additional scalar field and a beyond standard model fermionic particle. The exponential growth of perturbations occurs when the fermionic particles become non-relativistic at

around $z \sim 10^6$. This can lead to the formation of numerous low mass dark matter halos, which can further collapse due to scalar radiation and form primordial black holes of similar masses. We also do a detailed calculation of the PBH mass function for this model. Though Flores & Kusenko (2021a) also worked out the PBH fraction for a similar PBH formation mechanism (though in a different model context), there an approximate estimation using Press-Schechter theory was used. In this chapter, we have presented a detailed and thorough calculation of f(M) for the first time in our knowledge of early DM halo formation.

There is an allowed mass range for PBH around $10^{-16} - 10^{-10} M_\odot$ (sublunar mass range), where the constraints on $f_{\rm PBH}$ are almost non-existent. Though this mass range was previously constrained due to femtolensing, optical microlensing, white-dwarf survival and neutron star capture is no longer constrained in the light of recent studies Katz et al. (2018); Montero-Camacho et al. (2019). Our model allows the formation of PBH in this window for a keV mass fermion and with other viable model parameters- therefore, these PBHs can make up for all the dark matter. In principle we should use non-monochromatic constraints (Carr et al. 2017) to compare with our $f(M)$, however since our $f(M)$ turns out to be very narrow (if we approximate our $f(M)$ with a log-normal distribution the corresponding σ would be $\lesssim 0.2$) in which case monochromatic constraints will be a good approximation to the non-monochromatic constraints derived using the method provided by Carr et al. (2017) (for example the non-monochromatic constraints given for the log-normal distribution $\sigma = 2$ case in Figure 20 of Carr et al. (2021a)).

These PBHs are not expected to either evaporate or even accrete mass significantly in a Hubble time scale (Rice & Zhang 2017; Pandey & Mangalam 2018) which makes these PBHs a very good candidate for dark matter. Though some works considering the capture of PBHs by white dwarfs and neutron stars suggests strong bounds on the sublunar mass PBHs (Pani & Loeb 2014), recent studies (Defillon

et al. 2014) dispute these bounds on the grounds of recent understanding of dark matter density in globular clusters which is now known to be much lower than assumed in these analyses (Ibata et al. 2013). Though the constraints on PBH is a rapidly evolving field of research and thus the current PBH abundance constraint over various mass windows should be taken as an order of magnitude estimate, future more detailed studies will be able to put more robust bounds around this mass window.

Also, in our model, the PBHs form through the scalar radiation of dense halos, which are just clumps of matter and have a distribution of initial angular momentum. As a result, these PBH would have considerable spin, which in principle can be detected through future gravity wave observation Flores & Kusenko (2021b).

4.6 Details of derivations

Relation between smoothing radius R and halo mass M_h: Eq 4.16

Using the Friedmann's equation $H^2 = 8\pi G\rho/3c^2$, we can write the energy density ρ as,

$$\rho = \frac{\pi^2 g_{*,\rho}(T)}{30\hbar^3 c^3}(k_B T)^4 \tag{4.25}$$

where, $k = aH/c$ and the scale-factor a in terms of temperature T of the thermal bath as,

$$a = \left(\frac{g_{*,s}(T_0)}{g_{*,s}(T)}\right)^{1/3} \frac{T_0}{T} \tag{4.26}$$

where T_0 is the temperature at $a = 1$. Now, the horizon mass can be obtained by,

$$M_h = \frac{4}{3}\pi \left(\frac{c}{H}\right)^3 \frac{\rho}{c^2} = \frac{4\pi c}{3}\frac{\rho}{H^3} \tag{4.27}$$

from equation (4.27) and using the Friedmann's equation we get,

$$H = \frac{c^3}{2GM_h} \tag{4.28}$$

Now using equations (4.25) and (4.28) we get,

$$M_h = \left(\frac{45\hbar^3 c^{11}}{16\pi^3 G^3 k_B^4}\right)^{1/2} \left(\frac{1}{g_{*,\rho}(T_h)}\right)^{1/2} \frac{1}{T_h^2} \tag{4.29}$$

Here T_h is the temperature corresponding to the horizon mass M_h. Since we know the length x corresponding to wave number k can be written as, $1/R = aH/(2\pi c)$. Now using equations (4.26), (4.28) and (4.29), we get,

$$\frac{1}{R} = \left(\frac{k_B T_0}{2}\right) \left(\frac{g_{*,s}(T_0)}{g_{*,s}(T_h)}\right)^{1/3} \left(\frac{g_{*,\rho}(T_h)}{45\pi G\hbar^3 c^3}\right)^{1/4} \frac{1}{\sqrt{M_h}} \tag{4.30}$$

Relation between wave-number k and redshift z: Eq. 4.23

In radiation dominated era, $H = 1/(2t)$ and $a = (4\Omega_{r,0}H_0^2)^{1/4}\sqrt{t}$. Now using $k = \frac{2\pi}{R}$ and equations (4.28) and (4.30) we finally get,

$$k = (k_B T_0) \left(\frac{g_{*,s}(T_0)}{g_{*,s}(T_h)}\right)^{1/3} (g_{*,\rho}(T_h))^{1/4} \left(\frac{4\pi^3 H_0^2\, G\, \Omega_{r,0}}{45\,\hbar^3 c^9}\right)^{1/4} (1+z) \tag{4.31}$$

or, the $1+z(k)$ can be written as,

$$1 + z(k) = \frac{k}{k_B T_0} \left(\frac{g_{*,s}(T_0)}{g_{*,s}(T_h)}\right)^{-1/3} g_{*,\rho}^{-1/4}(T_h) \left(\frac{4\pi^3 H_0^2\, G\, \Omega_{r,0}}{45\,\hbar^3 c^9}\right)^{-1/4} \tag{4.32}$$

Chapter 5

DESI results: Hint towards coupled dark matter and dark energy*

5.1 Introduction

The nature of dark energy remains one of the central open problems in modern cosmology. Although the standard ΛCDM model continues to provide an excellent fit to most available data, recent baryon acoustic oscillation measurements from DESI have raised the possibility that the dark energy equation of state may evolve with cosmic time Adame et al. (2025); Calderon et al. (2024); Lodha et al. (2025b) and hint towards tantalizing evidence for evolving dark energy that shows phantom crossing †. These results have been extensively discussed in Chapter 1.

*This chapter is based on publication Chakraborty et al. (2025a)

†Within three days of the manuscript's publication on ArXiv, the results from the DESI DR2 dataset were released Abdul Karim et al. (2025), providing significantly stronger evidence for an evolving dark energy. The model-independent reconstruction of the dark energy equation of state with the DR2 dataset yields a 2-σ bound Lodha et al. (2025c) that remains consistent with

Various dark energy models have been explored in light of possible departures from $w = -1$ Odintsov et al. (2025). A well-studied class is quintessence Copeland et al. (2006a); Ratra & Peebles (1988); Zlatev et al. (1999), a slowly rolling scalar field producing time-varying dark energy pressure. In quintessence models, the dynamics fall into two broad categories: freezing, where the field slows and approaches $w \to -1$, and thawing, where it begins frozen at $w \approx -1$ and only recently started evolving Caldwell & Linder (2005); Linder (2006, 2015); Berbig (2025). While many potentials, exponential, power-law, etc., have been studied, they all yield $-1 \leq w < -1/3$ Tsujikawa (2013b); Cahn et al. (2008); Bhattacharya et al. (2024a), ensuring accelerated expansion but preventing a crossing into the phantom regime, $(w < -1)$, thus not suitable to explain the DESI anomaly Wolf et al. (2024a); Ramadan et al. (2024); Bhattacharya et al. (2024b). The evolution of dark energy from quintessence to explain DESI observations has been examined, but it eventually becomes phantom-like in the past Tada & Terada (2024).

Meanwhile, phantom dark energy models Caldwell (2002) extend into $w < -1$ but at the cost of violating the null energy condition, requiring exotic physics such as a negative kinetic term Ludwick (2017); Caldwell et al. (2003). The models where dark energy originates from a phase transition like vacuum metamorphosis Parker & Raval (2000); Caldwell et al. (2006); Di Valentino et al. (2018), or "quintom" scenarios Guo et al. (2005); Yang et al. (2025), struggles to explain the DESI anomaly either from an observational point of view or from model building aspects, pointing to the need for new or more complex dynamics Lodha et al. (2025b); Shlivko & Steinhardt (2024b); Fikri et al. (2024); Wolf et al. (2024b); Hernández-Almada et al. (2024); Cai et al. (2010); Yin (2022, 2024); Heckman et al. (2025). However, it has been shown that using a modified gravity model (e.g., a general Horndeski scalar-tensor theory) can provide a viable explanation for the DESI observations Chudaykin & Kunz (2024); Ye et al. (2024); Ferrari et al. (2025); Chudaykin et al. (2025).

their findings from DESI DR1, indicating compatibility of our model (to be discussed in the next section) with the newly released dataset.

From the perspective developed in the earlier chapters, in which scalar–dark matter interactions modify the behavior of the dark sector at early times, it is natural to ask whether similar interactions can also account for the emerging evidence for evolving dark energy in late-time observations such as DESI. In this Chapter, we consider interactive dark energy models as an economical solution to DESI observations deploying a similar Yukawa-type interaction. Recent analyses indicate that a non-gravitational interaction in the dark sector is still consistent with current observations Chakraborty et al. (2026); Gómez-Valent et al. (2020, 2022); Goh et al. (2023)and might even help relieve tensions in the standard ΛCDM model Wang et al. (2024); Cai et al. (2021); Benisty et al. (2023a); Benisty & Davis (2022); Benisty et al. (2023b); Sabogal et al. (2024); Shah et al. (2024, 2025b). Notably, a joint analysis of DESI Year 1 BAO and Planck 2018 CMB data shows a preference for dark sector interaction at greater than 95% confidence, with a coupling parameter shifting H_0 toward the locally measured value Giarè et al. (2024b), offering an intriguing hint of interacting dark sector Lewis & Chamberlain (2024); Gao et al. (2025); Li et al. (2025, 2024a,b); Sabogal et al. (2025a) frameworks alongside more conventional models. Implications of DESI results for the Hubble tension have also been explored in Wang & Piao (2024).

In this work, we propose an interacting dark sector model, especially a chameleon model Khoury & Weltman (2004b); Paliathanasis (2024, 2020), as an economical solution to DESI anomaly. By allowing dark energy to exchange energy with dark matter, our framework naturally mimics phantom-like behavior without invoking a fundamental phantom field Das et al. (2006a). We introduce an interaction term modifying the effective equation of state while maintaining theoretical stability. Unlike standard chameleon models Das et al. (2006a); Khoury & Weltman (2004b); Paliathanasis (2023a,b), where the scalar field settles at a potential minimum with vanishing kinetic energy, our approach allows for continued evolution, ensuring non-zero kinetic energy at present. This setup accommodates an evolving history,

permitting early phantom behavior followed by a transition to quintessential behavior today, which is consistent with DESI findings. The two most important points in our paper are the following:

- Due to the dark matter and dark energy interacting with each other, the inferred equation of state by an observer is different from the equation of state of the scalar field w_ϕ.
- Along with the interactions, the finite kinetic energy of the scalar field at the present epoch allows the effective (observed) equation of state to cross the phantom barrier.

While this framework shows how a chameleon-type interaction can reproduce the phenomenology suggested by DESI, the more decisive question—whether current data require a non-zero dark-sector coupling—is addressed in the next chapter using DESI DR2 and complementary datasets.

5.2 Model Set Up

In the section, we revisit the model proposed in Das et al. (2006a) where the quintessence dark energy model of a scalar field ϕ with canonical *positive* kinetic energy term interacts with dark matter in Einstein gravity. We will argue that the model can easily *mimic* effective (observable) dark energy equation of state parameter $w(z)$ that crosses the phantom divide in the recent past and reaches its present value $w_0 > -1$. Therefore, the setup is ideally suited to explain the observations made by DESI. We will show explicit examples of dark energy sectors and how they fit the data.

This study considers a quintessence scalar field ϕ, representing dark energy, which has a Yukawa-like interaction with the dark matter (fermion) field ψ Das et al. (2006a) [‡],

$$\mathcal{L}_{\rm int} = -f(\phi/M_{\rm Pl})\bar{\psi}\psi \ . \tag{5.1}$$

We note that the interaction term makes the dark matter mass quintessence field dependent[§]. In effect, the non-relativistic dark matter energy density does not redshift as a^{-3} as for the case of ordinary matter, but evolves as follows.

$$\rho_{\rm DM} \sim f(\phi)/a^3 \ , \tag{5.2}$$

where, a is the scale factor, with the present value of the scale factor normalized as $a_0 = 1$, and the field is denoted as ϕ_0. We begin with a general form of $f(\phi)$, but observational requirements will fix the properties of the function, as we will see later.

In this case, the Hubble parameter is determined by the following expression.

$$3H^2 M_{\rm Pl}^2 = \rho_\phi + \frac{\rho_{\rm DM}^{(0)}}{a^3}\frac{f(\phi)}{f_0} + \frac{\rho_B^{(0)}}{a^3}, \tag{5.3}$$

where, $\rho_{\rm DM}^{(0)}$ and $\rho_B^{(0)}$ are the present-day dark matter density and baryon density, respectively, and $f_0 = f(\phi_0)$, and $M_{\rm Pl}$ is the reduced Planck mass. The dark energy density is given as the sum of the kinetic and potential terms originating from the quintessence field.

$$\rho_\phi = \frac{1}{2}\dot{\phi}^2 + V(\phi) \ . \tag{5.4}$$

[‡]Here, the nature of the dark matter is not so important. The setup could well be generalized to bosonic dark matter with different interaction terms.

[§]Note that the dark energy field is coupled only with the dark matter. Although moduli fields can in principle couple universally to all matter sectors, we assume that the visible sector exhibits a Damour–Polyakov least-coupling mechanism Damour & Polyakov (1994b), which dynamically suppresses baryonic interactions and keeps them within equivalence-principle bounds. The dark sector, however, can retain a non-vanishing coupling, as expected in sequestered or hidden-sector realizations.

By varying the action related to ϕ we obtain the following modified Klein-Gordon (KG) equation of motion,

$$\ddot{\phi} + 3H\dot{\phi} = -V_{,\phi}(\phi) - \frac{\rho^{(0)}_{\rm DM}}{a^3}\frac{f_{,\phi}(\phi)}{f(\phi_0)} \ , \tag{5.5}$$

where interaction between dark matter and the quintessence field invokes the last term and '$,\phi$' in the subscript to any quantity corresponds to the derivative of the quantity w.r.t. ϕ. The above equation tells us that the dynamics of the field are determined by an effective potential, $V_{\rm eff} = V(\phi) + \rho^{(0)}_{\rm DM} f(\phi)/a^3 f_0$. This is schematically shown in Fig. 5.1 where $V(\phi)$ is a falling function of ϕ and $f(\phi)$ is a growing function of ϕ. Two competing behaviors of the functions create a minimum of the potential. It is important to note that the minimum of the potential moves as the strength of the growing function determined by dark matter density dilutes with the expansion of the Universe. Depending on the choices of these two functions and initial conditions, the quintessence field may either sit at the minimum of the effective potential or show some additional dynamics around the minimum. In the first case, the effective mass of the field being heavy, the field tracks the minimum adiabatically. We will see later that to mimic DESI results, the field must not sit at its effective minimum and, therefore, violate the adiabatic condition.

At this moment, we note that the total Hubble parameter and its integrals determine the cosmological observables. Therefore, any inference on dark energy properties from cosmological observables is only indirect. In our case, an observer would be unaware of the interactions between dark matter and dark energy. Any individual observer will infer the properties of dark energy using the following expressions for the same Hubble equation of (5.3)

$$3H^2 M_{\rm Pl}^2 = \rho^{\rm eff}_{\rm DE} + \frac{\rho^{(0)}_{\rm DM}}{a^3} + \frac{\rho^{(0)}_{\rm B}}{a^3} \ . \tag{5.6}$$

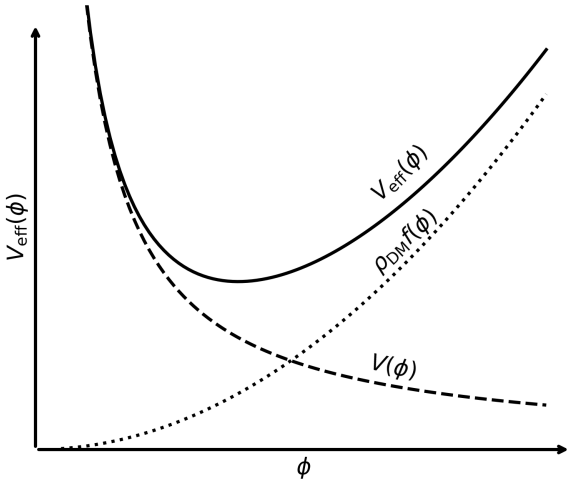


FIGURE 5.1: Schematic plot of $V_{\rm eff}(\phi) = V(\phi) + \rho_{\rm DM} f(\phi)$.

Here, $\rho_{\rm DE}^{\rm eff}$ satisfies the energy conservation equation

$$\frac{d}{dt}(\rho_{\rm DE}^{\rm eff}) + 3H(1 + w_{\rm eff})\rho_{\rm DE}^{\rm eff} = 0 \ , \tag{5.7}$$

where, $w_{\rm eff}$ is the effective equation of the state of the dark energy as perceived or measured by an observer. Take note that the above two equations are written in a way such that there seems to be no interaction between the dark matter (represented by $\rho_{\rm DM}$) and the dark energy (represented by $\rho_{\rm DE}^{\rm eff}$).

It has been shown Das et al. (2006a) that the effective equation of state of the dark energy can be written as

$$w_{\rm eff} = \frac{w_\phi}{1 - x} \ , \tag{5.8}$$

where

$$x = -\frac{\rho_{\rm DM}^0}{a^3 \rho_\phi} \left(\frac{f(\phi)}{f_0} - 1 \right) \ , \tag{5.9}$$

and

$$w_\phi = \frac{\left(\dot{\phi}^2/2 - V(\phi)\right)}{\left(\dot{\phi}^2/2 + V(\phi)\right)}. \tag{5.10}$$

is the usual equation of state parameter for a dark energy field with a canonical kinetic energy term. We consider dynamics of ϕ such that $f(\phi)$ is increasing with time, and it ensures that $x > 0$. In the case of nearly flat potentials, $w_\phi \approx -1$, and, therefore, in the past, observationally inferred $w_{\rm eff}$ can have values smaller than -1. Note that this requires a phantom field that needs the kinetic energy to be negative. Moreover, the setup has broad structural flexibility to cross $w_{\rm eff} < -1$ in the recent past by appropriately adjusting w_ϕ and x.

Let us first note that if the dark energy sector is modeled by a cosmological constant with $w_\phi = -1$ for all time and the coupling to the dark matter sector is also non-dynamical, it means $x = 0$. That leads to $w_{\rm eff} = -1$ for all the time. This is not suitable for explaining the DESI results. On the other hand, if a thawing quintessence field models the dark energy sector, the field starts to roll as the Universe expands, and it was stuck at its potential at earlier times Caldwell & Linder (2005); Tsujikawa (2013b); Linder (2006, 2015). As representative examples, if w_ϕ changes from -1 to -0.8 with an intermediate value of -0.5 while x changes from 0.9 to 0 while $x = 0.5$ at the intermediate value, it can be easily checked from Eq. (6.10) that the $w_{\rm eff}$ shows phantom barrier crossing in some recent past with $w_{\rm eff} > -1$ today. At the same time, the behavior of phantom crossing can also be reproduced when w_ϕ changes from -1 to -0.9 to -0.8 while x changes from 0.9 to 0.1 to 0. Note that in the first case, the field crosses its minimum and thus reduces the value of w_ϕ as the field loses its kinetic energy. In the second case, the field does not cross the minimum. It is instructive to note that the above example points are intended to illustrate, in principle, the flexibilities of the setup. Later, we will show explicit numerical examples that reproduce DESI results of $w_{\rm eff}$.

Our investigation is especially motivated by theoretical insights derived from String

theory compactifications, which propose a relationship between the cosmological scalar field and the geometry of compactified dimensions Damour & Polyakov (1994b). In pursuit of this, we have introduced a coupling function, denoted $f(\phi)$, to mathematically represent these interactions,

$$f(\phi) = \exp\left(\frac{\beta\phi}{\sqrt{8\pi}M_{\rm Pl}}\right), \tag{5.11}$$

where β represents the strength of the coupling. This approach is similar to that utilized by Das et al. (2006a), but has been specifically adapted to align with the intricacies of our requirements to suit the DESI data. Regarding the self-interaction potential of the scalar field, we have chosen a polynomial form :

$$V(\phi) = M^4\left(\frac{M_{\rm Pl}}{\phi}\right)^{\alpha}, \tag{5.12}$$

and an exponential form expressed as

$$V(\phi) = M^4 \exp\left(-\frac{\alpha\phi}{\sqrt{8\pi}M_{\rm Pl}}\right). \tag{5.13}$$

Here, the parameter M has a dimension of energy, and the α parameter governs the steepness of the potential. Note that a combination of Eq. (5.11) and one of the expressions of Eq. (5.12) or Eq. (5.13) produces the desired result of Fig. 5.1.

The scalar field evolves under the influence of an effective potential towards a dynamically evolving minimum. Prior studies in Das et al. (2006a) have established that the effective equation of state parameter $w_{\rm eff}$ tends to -1.0 in the present cosmological epoch. This trend is attributed to the specific setup, in which the scalar field reaches equilibrium at the minimum of the potential with $w_\phi = -1$ at the present epoch with $x = 0$. However, this alignment with $w_{\rm eff} = -1$ does not fully accord with recent observations from DESI Adame et al. (2025). To remedy the situation, our work introduces a nuanced revision to the above framework. Our hypothesis suggests that by allowing the scalar field not to stop at the potential

minimum at the present epoch, we endow our model with the versatility necessary to better correlate with the findings from the DESI survey. This adjustment allows the equation of the state parameter, $w_{\rm eff}$, to exceed the limit -1, thus providing a credible interpretation of recent observational evidence. Through this refined methodology, we endeavor to bridge the gap between the evolving theories of dark energy and the most current empirical data.

5.3 Perturbations for dark matter-dark energy fluid

The presence of an additional interaction in the dark matter-dark energy fluid naturally gives rise to modified perturbation equations, whose equation of motion is presented as follows,

$$\begin{aligned}\dot{\delta}_{\rm DM} &= -\left(\frac{\theta_{\rm DM}}{a}+\frac{\dot{\tilde{h}}}{2}\right)+\frac{\tilde{\beta}}{M_{\rm Pl}}\delta\dot{\phi}\ ,\\ \dot{\theta}_{\rm DM} &= -H\theta_{\rm DM}+\frac{\tilde{\beta}}{M_{\rm Pl}}\left(\frac{k^2}{a}\delta\phi-\dot{\phi}\theta_{\rm DM}\right)\ ,\end{aligned} \tag{5.14}$$

Where, $\tilde{\beta}=\frac{\beta}{\sqrt{8\pi}}$. Also, the perturbed Klein-Gordon equation becomes,

$$\ddot{\delta\phi}+3H\dot{\delta\phi}+\left(\frac{k^2}{a^2}+V_{,\phi\phi}\right)\delta\phi+\frac{1}{2}\dot{\tilde{h}}\dot{\phi}=-\frac{\tilde{\beta}}{M_{\rm Pl}}\rho_{\rm DM}\delta_{\rm DM}\ , \tag{5.15}$$

where $\tilde{h}\equiv\tilde{h}^{i}{}_{i}$ is the trace of metric perturbation $\tilde{h}_{ij}$ in synchronous gauge.

Similarly, the perturbed Einstein equation determining the evolution of metric perturbation gets modified too in the following manner,

$$k^2\eta - \frac{1}{2}a^2H\dot{\tilde{h}} = -\frac{a^2}{2M_{\rm Pl}^2}\left(\sum_{i=\gamma,\nu,{\rm B},{\rm DM}}\rho_i\delta_i + \delta\rho_\phi\right), \tag{5.16}$$

$$k^2\dot{\eta} = \frac{a}{2M_{\rm Pl}^2}\left(\sum_{i=\gamma,\nu,{\rm B},{\rm DM}}(\rho_i + P_i)\theta_i + ak^2\dot{\phi}\delta\phi\right), \tag{5.17}$$

$$\ddot{\tilde{h}} + 3H\dot{\tilde{h}} - 2\frac{k^2}{a^2}\eta = -\frac{3}{M_{\rm Pl}^2}\left(\sum_{i=\gamma,\nu,{\rm B},{\rm DM}}\delta P_i + \dot{\phi}\delta\dot{\phi} - V_{,\phi}\delta\phi\right), \tag{5.18}$$

where $\delta\rho_\phi = \dot{\phi}\delta\dot{\phi} + V_{,\phi}\delta\phi$.

Since the field behaves similarly to a thawing quintessence model, but with dynamics governed by an effective potential—where the field begins to roll only at very late times ($z \sim 4$)—the field's kinetic energy remains subdominant compared to potential energy. This is consistent with evolution of w_ϕ, shown later in Figures 5.3 and 5.4 in Section 5.5, where the equation of state does not vary significantly, changing from -1 to approximately -0.8 within the redshift range 0–4. It can be shown that the kinetic energy remains smaller than the potential energy as long as w_ϕ stays negative. Therefore, in the perturbation equation, we can safely consider $\dot{\phi}$ to be small and assume $\ddot{\delta\phi} = \dot{\delta\phi} = 0$. The perturbation equation for the growth of dark matter then becomes,

$$\ddot{\delta}_{\rm DM} + \left(2H + \frac{\tilde{\beta}\dot{\phi}}{M_{\rm Pl}}\right)\dot{\delta}_{\rm DM} + \frac{1}{2}\left(\dddot{\tilde{h}} + \left(2H + \frac{\tilde{\beta}\dot{\phi}}{M_{\rm Pl}}\right)\ddot{\tilde{h}}\right) \approx \frac{\tilde{\beta}^2}{M_{\rm Pl}^2}\frac{\rho_{\rm DM}\delta_{\rm DM}}{1 + a^2V_{,\phi\phi}/k^2} + \frac{\frac{1}{2}\frac{\tilde{\beta}\dot{\phi}}{M_{\rm Pl}}\dot{\tilde{h}}}{1 + a^2V_{,\phi\phi}/k^2}, \tag{5.19}$$

We kept the terms proportional to $\dot{\phi}$, to quantify the effect on the growth of perturbation when the scalar field has a small velocity. Here, we ignore other components in the perturbation equation for simplicity.

Now initially, the field is stuck at the initial point and only starts to roll from redshift $z \sim 4$. So before that, the perturbation growth follows the following equation,

$$\ddot{\delta}_{\rm DM} + 2H\dot{\delta}_{\rm DM} + \frac{1}{2}\left(\ddot{\tilde{h}} + 2H\dot{\tilde{h}}\right) \approx \frac{\tilde{\beta}^2}{M_{\rm Pl}^2}\frac{\rho_{\rm DM}\delta_{\rm DM}}{1 + a^2 V_{,\phi\phi}/k^2} \ , \tag{5.20}$$

The right-hand side term arises due to the extra fifth force in the system. The denominator of this term quantifies the screening of this force, which shows the comoving range of this force $\lambda_{\rm F}(a) \equiv a^{-1}V_{,\phi\phi}^{-1/2}$. So only the modes $k > \lambda_{\rm F}^{-1}$ will be affected by this extra force, in turn enhancing the growth at those scales. The perturbation growth of the modes till $z \sim 4$ is similar to the growth shown and argued in Das et al. (2006a); Boriero et al. (2015b).

Now, after redshift $z = 4$, the field starts rolling and starts gaining kinetic energy. So this scenario can be thought of as a correction to the growth dynamics discussed in Das et al. (2006a); Boriero et al. (2015b). Comparing Equation 5.19 with 5.20, we see some extra contributions are coming from the velocity of the field. As argued before, the field velocity remains comparatively small throughout the field evolution, suggesting a small correction to the dynamics in the growth of the perturbation.

The L.H.S of Equation 5.19, shows an extra damping term proportional to $\tilde{\beta}\dot{\phi}$, which shows an overall supression at scales of dark matter perturbation, however, $\frac{\tilde{\beta}\dot{\phi}}{M_{\rm Pl}} \ll 2H$, due to both $\beta < 0.5$ and velocity of the field being small. So we expect the extra suppression due to field velocity to be very tiny. Following the same argument, we can also infer that the expression $\left(\ddot{\tilde{h}} + \left(2H + \frac{\tilde{\beta}\dot{\phi}}{M_{\rm Pl}}\right)\dot{\tilde{h}}\right)$ predominantly should depend on $\propto -\rho_{\rm DM}\delta_{\rm DM}$, which acts as a source term for the growth of the perturbation.

In the R.H.S of Equation 5.19, there is an extra velocity-dependent source term in addition to the standard fifth force source term. Now this term also acts source of growth of perturbation but within the co-moving range of the fifth force $\lambda_{\rm F}$. So it enhances the growth for scales $k > \lambda_{\rm F}^{-1}$. We can gain some intuition regarding the physical in this type of coupled dark sector model, through analytically deriving the perturbation equation of growth of perturbation equation under some assumptions. However, to truly get an idea of how different modes get affected, one should implement the model in a Boltzmann code `CLASS` to generate the matter power spectrum, which is beyond the scope of this paper, but we keep it for our future study.

5.4 Model Implementation

In exploring scalar field cosmological models, the choice of exponential and polynomial potential presents significant challenges, especially in determining the final scalar field value analytically, ϕ_0. Since our model does not require ϕ_0 to coincide with the effective potential minima to match DESI observations, we adopt arbitrary values for ϕ_0, along with the parameters α and β. This model combines thawing and interaction scenarios, where the field stays frozen at its initial position from an early time and begins rolling at late times ($a = 0.2$), leaving the early universe cosmology largely unchanged.

In our study, we have numerically solved the Klein-Gordon (KG) equation 5.5 using a Python code, appropriately calculating the Hubble parameter at each epoch through the Friedmann equation 5.3 to understand the late-time dynamic behavior of the scalar field. We appropriately fix the parameters M and ϕ_0 as well as α and β. Instead of employing automated optimization methods like the shooting algorithm, we manually set the initial conditions for the field's value

and velocity for a fixed M and ϕ_0. We fix the initial velocity of the field to be zero and vary only the initial position of the field such that the present-day position of the field matches with ϕ_0, within an accuracy of 0.01 and at the same time, the corresponding kinetic and potential energy of the field adds up to the observed present-day dark energy density, $\rho_{\rm DE}$, within a level of precision of 0.01. Following the obtained dynamics of the scalar field, i.e., its position and velocity for each epoch, as depicted in Figure 5.2, we proceed to calculate the equation of state parameter for the field, w_ϕ, using equation 6.9. We also determined the effective equation of state, $w_{\rm eff}$, by applying equations 5.9 and 6.10, with the results presented in Figure 5.3 & 5.4. To assess the validity of our model, we compared the $2-\sigma$ bound on the reconstructed dark energy equation of state $w(z)$, inferred from DESI observations Calderon et al. (2024), against $w_{\rm eff}(z)$. We repeat the whole process by varying the parameters α, β, M, ϕ_0, until the obtained $w_{\rm eff}(z)$ properly fits within the $2-\sigma$ bound provided by DESI.

Our methodology follows the formalism established by Das et al. (2006a) where the kinetic energy of the scalar field is set to zero upon reaching the potential minima (i.e., ϕ_0 in their case) in the present-day universe, making its potential energy the sole contributor to the dark energy density. However, our model introduces more flexible dynamics of the scalar field. Choosing the model parameters suitably and letting the field be at an arbitrary position in the present epoch permits the scalar field to efficiently cross the minima of the effective potential, reducing the self-interacting potential energy relative to the observed dark energy density. Consequently, this difference in energy density can be attributed to the scalar field's kinetic energy.

Next, the late-time dynamics are governed by an effective potential arising from the self-interaction of the field and its coupling to dark matter. This creates an evolving effective minima that the field is attracted to over time. For $\alpha = 0.14$, $\beta = 0.45$, $M = 2.14 \times 10^{-3}$ eV, and $\phi_0 = 0.28 M_{\rm pl}$, starting from a stationary

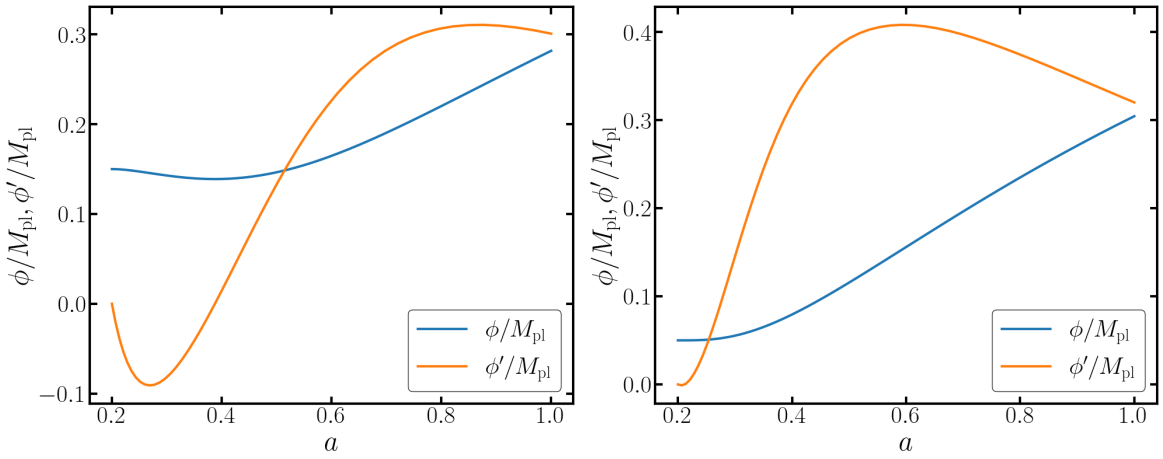


FIGURE 5.2: A typical dynamics of ϕ and $\phi' = \frac{d\phi}{da}$ with the scale factor for the polynomial self-interaction potential is shown here with different initial positions of the field. The left (right) figure depicts the dynamics for a field that starts on the right (left) side of the effective minimum for $\alpha = 0.14$ and $\beta = 0.45$, with initial field value $\phi_{\rm initial} = 0.15 M_{\rm pl}(0.05 M_{\rm pl})$ and final value $\phi_0 = 0.28 M_{\rm pl}(0.30 M_{\rm pl})$. Here $M_{\rm pl}$ is the reduced Planck mass.

point on the right side of the potential, with $\phi_{\rm initial} = 0.15 M_{\rm pl}$, as shown in the left panel of Figure 5.2, the field rolls down toward the minimum, leading to a decrease in both its position and velocity. As the minima evolves to a higher value, the field starts to roll up the left side of the potential upon crossing it, eventually losing all of its kinetic energy. Subsequently, it starts to move back towards the minima, such that the field value and its velocity continue to increase until it crosses the minima again, showcasing an oscillatory pattern in the scalar field dynamics. As another example, for the right panel of Figure 5.2 with the same choice of α, β and M, the field starts rolling from the left side of the potential, with $\phi_{\rm initial} = 0.05 M_{\rm pl}$, moves towards the evolving minima and eventually crosses it with an ever-increasing field value to reach the chosen $\phi_0 = 0.30 M_{\rm pl}$ in this case. The velocity, however, increases until the field crosses the minima and then decreases.

5.5 Results

In this section, we show results for the interacting quintessence dark matter scenario described by Eq. (5.1), Eq. (5.11), and Eq. (5.12) or Eq. (5.13). In particular, we solve the dynamics of the quintessence field following the procedure outlined in the previous section and plot $w_{\rm eff}$ and w_ϕ as a function of redshift z and confront them with the DESI results. We show illustrative examples of parameters for which predictions fall within the 2-σ bounds.

The DESI collaboration has reconstructed the dark energy equation of state by expanding it in Chebyshev polynomials up to fourth order and constrained its coefficients via Monte Carlo Markov Chain (MCMC) analysis Calderon et al. (2024). It provided strong evidence for the late-time dynamical behavior of dark energy. The 2-σ confidence interval they obtained from various datasets has been crucial for our study. Rather than conducting a separate MCMC analysis, we focus on verifying whether our prediction from the model is consistent with the observation from DESI and other key datasets (e.g., Union3, Planck). At the moment, it is important to remind ourselves that $w_{\rm eff}$ (not w_ϕ) must be compared with the data.

We first focus on the model described by the potential given by Eq. (5.12). This model combines thawing quintessence and interaction scenarios, where the field stays frozen at its initial position from an early time and begins rolling at late times, leaving the early universe cosmology largely unchanged. The results are illustrated in Fig. 5.3 for different values of the model parameters. The shaded areas indicate the 2-σ confidence region as per various datasets, as provided in Calderon et al. (2024). In all cases, the continuous violet line corresponds to $w_{\rm eff}$, where the blue dashed line delineates w_ϕ. Furthermore, we include a reference line at $w = -1$ to highlight the significance of phantom crossing, which is crucial for interpreting the DESI observation Adame et al. (2025); Calderon et al. (2024). Note that w_ϕ never crosses the phantom barrier, but the observable $w_{\rm eff}$ does.

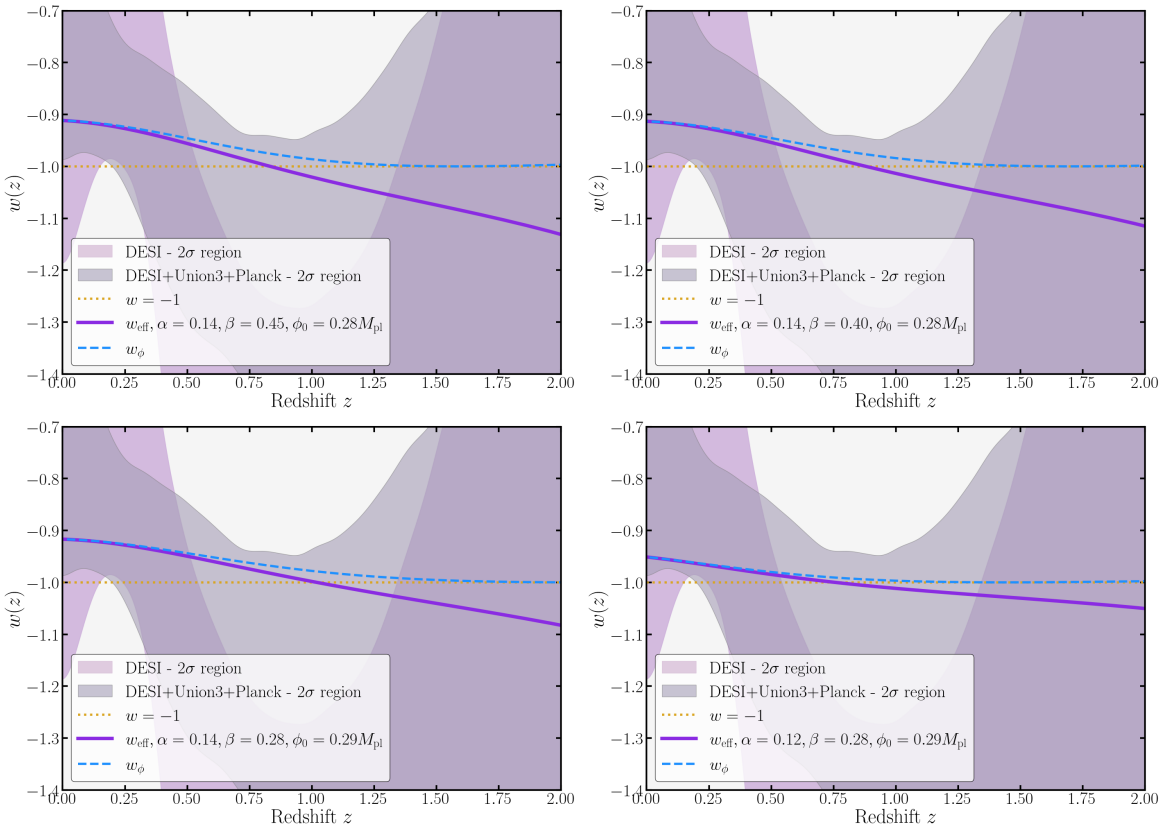


FIGURE 5.3: Fitting of $w(z)$ for polynomial self-interaction potential within the 2-σ contours of DESI (light purple) and DESI+Union3+Planck (light grey). The initial value of phi, $\phi_{\rm in}$ is considered as $0.15M_{\rm pl}$(top-left), $0.15M_{\rm pl}$ (top-right), $0.15M_{\rm pl}$ (bottom-left) and $0.21M_{\rm pl}$ (bottom-right).

In the top panels of Figure 5.3, we show predictions of the model for $\alpha = 0.14, \beta = 0.45$ (top-left) and $\alpha = 0.14, \beta = 0.40$ (top-right) using a polynomial self-interaction potential of Eq. (5.12) with $M = 2.14 \times 10^{-3}$ eV, $\phi_{\rm in} = 0.15M_{\rm pl}$ and $\phi_0 = 0.28M_{\rm pl}$. It is not surprising that the value of M is close to the dark energy scale. We find that the prediction is not consistent with only DESI results depicted by the purple-shaded regions in the top panel. However, in the same panels, the gray-shaded regions show allowed space for the data combinations of DESI + Union3 + Planck, and we see that it fits very well within the $2-\sigma$ bounds, with $w_{\rm eff}$ crosses the phantom divide within $z \sim 0.75 - 1.00$.

The figures in the lower left and lower right illustrate scenarios for $\alpha = 0.14$ and $\alpha = 0.12$, keeping β and ϕ_0 fixed at 0.28 and $0.29M_{\rm pl}$, respectively. Both show

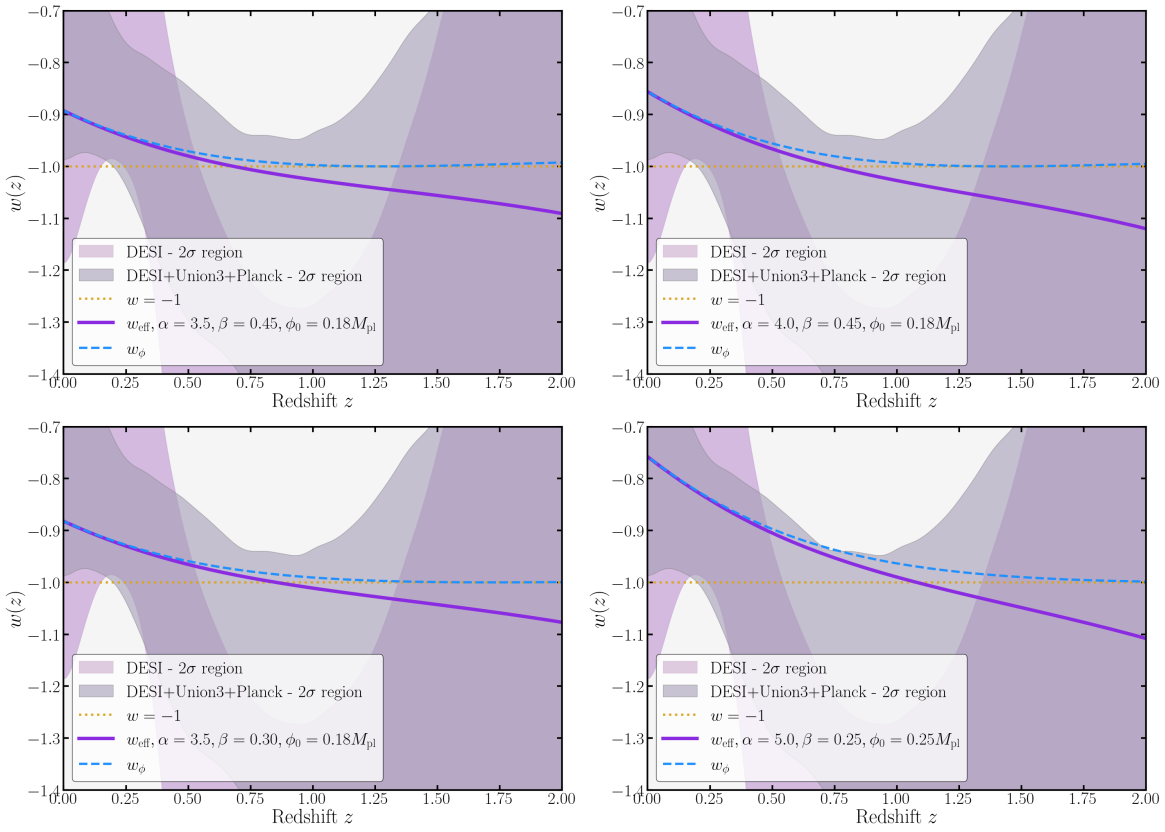


FIGURE 5.4: Fitting of $w(z)$ for exponential self-interaction potential within the 2-σ contours of DESI (light purple) and DESI+Union3+Planck (light gray). The initial value of phi, $\phi_{\rm in}$ is considered as $0.08M_{\rm pl}$(top-left), $0.05M_{\rm pl}$ (top-right), $0.05M_{\rm pl}$ (bottom-left) and $0.025M_{\rm pl}$ (bottom-right).

perfect alignment within the allowed region of the combined data sets and are not consistent with DESI-only bounds, similar to the top panels. A higher value of α (for a fixed β) implies a higher steepness in the self-interaction potential, leading to a higher kinetic energy as the field rolls down rapidly. This behavior is reflected in w_ϕ, where higher α consistently results in higher w_ϕ throughout all epochs presented in the plots. Consequently, $w_{\rm eff}$ also reaches a higher value in the present epoch for $\alpha = 0.14$ compared to $\alpha = 0.12$. If we compare the top right and left panels of the figure where α remains fixed at 0.14 and β varies from 0.45 to 0.40, we find that $w_{\rm eff}$ drops sharply at higher redshifts for higher β. In this case, the dependence of $w_{\rm eff}$ on the quantity x, which is directly influenced by β, through Eq. (5.9) becomes crucial. An increase in β leads to a higher value of x at earlier epochs, with x asymptotically approaching zero in the present epoch. The

increase in x decreases $w_{\rm eff}$. This explains the observed trend. The most important aspect of the plots in Figure 5.3 is that we have explicit examples of a coupled dark matter quintessence model where $w_{\rm eff} < -1$ for higher redshift with crossing $w_{\rm eff} = -1$ at a recent time and reaching $w_{\rm eff} > -1$ at the present epoch. This is exactly the behavior that the DESI data seeks. We achieve this without any field theoretic pathologies in the quintessence dark energy sector whose equation of state always remains larger than -1.

We have also explored the dynamics of w_ϕ and $w_{\rm eff}$ for an exponential self-interaction potential of the form of Eq. (5.13) using $M = 2.35 \times 10^{-3}$eV and $\phi_0 = 0.18 M_{\rm pl}$ for the top and bottom left panel of the figure whereas the bottom right panel considers $\phi_0 = 0.25 M_{\rm pl}$. The results are illustrated in Fig. 5.4. The behavior of w_ϕ and $w_{\rm eff}$ exhibits similar sensitivities to variations in parameters α and β as in Fig. 5.3. However, the order of magnitude of α is considerably larger for the exponential potential compared to the polynomial potential, reflecting their distinct functional forms. The steeper nature of the exponential potential enhances the kinetic energy of the scalar field, causing $w_{\rm eff}$ to exceed -0.8 at the current epoch while it crosses the phantom divide around $z \sim 1.00$. This has been shown in the bottom right panel of Fig. 5.4.

In both Figure 5.3 and 5.4, our result does not properly fit the DESI-only 2σ contour for any of the benchmark points considered. We don't isolate any parameter combination consistent with the DESI-only bounds. However, it's worth noting that fitting with DESI alone does not provide new insights, since the limited number of data points introduces large uncertainties in parameter inference, as reflected in the broad error bars of $w(z)$. In the era of multi-probe cosmology, priority should be given to the consistency with combined datasets – which our model shows good agreement.

We would like to conclude the section with some comments about the nature of

the potential that is suitable to fit the DESI results in this coupled scenario. Both the examples we have worked with correspond to the thawing quintessence model, where the field was stuck at its potential at some early epoch and has only started to roll recently. The equation of state behavior reported by DESI will be difficult to reproduce in a freeze-in type of dark energy model where the potential is such that the field frees into a smaller velocity as the Universe expands. In this case, the scalar field must roll down from an early redshift and come to a stop in the present day, which results in $w_\phi > -1$ at high redshift and $w_\phi \simeq -1$ at the present day. Moreover, since ϕ must monotonically increase with time within the observational range of DESI, it becomes impossible to implement the freezing scenario in this context. The DESI reconstruction of the equation of state excludes $w = -1$ from the $0 < z < 0.25$ range at a $2 - \sigma$ confidence level for a combined Planck, DESI, and Union3 dataset Calderon et al. (2024). Due to the expected smooth behavior of scalar field dynamics, the coupling function $f(\phi)), x, w_\phi$, and $w_{\rm eff}$ all exhibit smoothness as well. At present, when $x = 0$, we have $w_\phi = -1$, which implies that $w_{\rm eff} = -1$. To maintain the smooth behavior of $w_{\rm eff}$, it would be impossible for $w_{\rm eff}$ to exceed -1 for the redshift range of $0 < z < 0.25$ for the combined dataset. Therefore, a freezing scenario with interaction is unlikely to adequately fit the DESI results in its simplest form.

5.6 Summary

In this study, we explore a scenario of a quintessence dark energy paradigm coupled with dark matter inspired by the framework proposed by Das et al. (2006a). A key feature of our approach is a scalar field that moves away from its minimum with significant kinetic energy in the present epoch, leading to a dynamical evolution of dark energy that effectively includes phantom crossing[¶]. This approach

[¶]The effects of kinetic energy in explaining DESI results have been discussed in Berghaus et al. (2024)

naturally accommodates the crucial observational constraints, especially from the Dark Energy Spectroscopic Instrument (DESI) survey. The distinctive capability of our model to cross the phantom divide, with the effective equation of state parameter $w_{\rm eff}$ transitioning from values below -1 in the distant past to values exceeding -1 in the present epoch, offers a compelling explanation for the observed signs of dark energy evolution. A crucial difference in comparison to many other attempts to explain the DESI results is that the dark energy sector is devoid of any pathologies, with the equation of state parameter $w_\phi > -1$ always.

Our investigation is further enhanced by numerically solving the modified Klein-Gordon equation for two distinct self-interaction potentials, namely exponential and polynomial, allowing us to explore the scalar field dynamics and compute the effective equation of state, $w_{\rm eff}$. The results, particularly when compared across various combinations of the parameters α and β, show strong agreement with data from the combined DESI, Planck, and Union3 datasets. We found that the set-up has enough flexibility for the $w_{\rm eff}$ to cross the phantom-divide for a range of z and also its present value reaching to be as large as $w_{\rm eff} \sim -0.8$.

This work provides a novel step toward a fundamental understanding of the complex interplay between dark energy and dark matter. Using current DESI data, we have shown that our framework offers a viable description, while a comprehensive Markov Chain Monte Carlo (MCMC) study remains to more precisely map the parameter space and to further improve the statistical robustness of the results. The continued release of DESI observations will be crucial to this effort, helping to close present gaps and to shed further insights on the dynamics of dark energy. In our setup, the dark energy field couples only to dark matter, and we have assumed that quantum corrections from the dark matter sector—being heavier than the dark energy mass—do not modify the latter's mass. Embedding these requirements in a concrete particle-physics model is nontrivial and will be pursued in future work.

Moreover, the proposed additional interactions in the dark matter-dark energy fluid naturally give rise to modified perturbation equations, which may lead to observational consequences in the CMB and LSS data. We have discussed the perturbation equations in the Appendix and have argued that the effect on the perturbations will be small and should be within the observational bounds. But a full cosmological analysis, including perturbations, is crucial to validate our model, and that is actively being pursued now.

Overall, this work contributes to the growing body of research aimed at unraveling the mysteries of dark energy and its role in the accelerated expansion of the universe. By offering a model that naturally accommodates evolving dark energy and phantom crossing, we pave the way for further investigations into alternative cosmological models that may better align with future observational data. While the present analysis demonstrates that interacting dark energy can reproduce the qualitative features suggested by DESI, the question of whether current data provide direct statistical evidence for a non-zero dark-sector coupling is addressed in the following chapter using the DESI DR2 dataset with an extended version of this model.

Chapter 6

Hint of dark matter-dark energy interaction in DESI DR2 and current cosmological dataset?*

Building on the interacting dark energy framework developed in the previous chapter, we now move to a quantitative test of whether current cosmological data provide evidence for a non-zero interaction in the dark sector. For context, the standard six-parameter phenomenological ΛCDM model has proven remarkably successful in accounting for the observed large-scale evolution of the universe Chen (2020); Semenaite et al. (2022); Sevilla-Noarbe et al. (2021); Dalal et al. (2023); Li et al. (2023). Nonetheless, with the advent of precision cosmology, several persistent discrepancies have emerged between different observational datasets, most notably the "Hubble tension" and the "S_8 tension", which have raised questions about the completeness of the ΛCDM framework Freedman (2017); Heymans *et al.* (2013). From a theoretical perspective, the exceedingly small value of the cosmological constant (Λ) continues to pose a profound challenge for fundamental

*This chapter is based on publication Chakraborty et al. (2026)

physics Weinberg (1989), motivating the exploration of departures from a pure cosmological constant description of dark energy.

As discussed in the previous chapter, a natural extension of ΛCDM is to consider a dynamical dark energy component with a time-dependent equation of state Caldwell et al. (1998); Liddle & Scherrer (1998); Sharma et al. (2022). Such scenarios naturally lead to distinctive imprints on the growth of large-scale structures, offering potential observational signatures that deviate from the predictions of the standard ΛCDM model. These models are increasingly within the reach of present and forthcoming cosmological surveys, which are capable of probing the expansion history and structure formation with unprecedented precision. In this context, recent DESI results have indicated mild tensions with the ΛCDM baseline, hinting at the possibility of a departure from a pure cosmological constant behavior Adame et al. (2024); Abdul-Karim et al. (2025); Lodha et al. (2025a); Roy Choudhury & Okumura (2024); Roy Choudhury (2025); Roy Choudhury et al. (2025). This, in turn, strengthens the case for exploring more general classes of dark energy models. As shown in the last chapter, one particularly promising class of such departures involves the presence of interactions within the dark sector—specifically, between dark energy and dark matter Wetterich (1988, 1995). Interacting dark energy models, reviewed in detail in the previous chapter, provide a theoretically well-motivated extension of the standard cosmological framework in which a scalar field naturally couples to the dark matter sector in the absence of a protecting symmetry Wetterich (1988). While such models were originally introduced to address the coincidence problem Amendola (2000) and have been extensively explored Amendola et al. (2003a); Amendola & Quercellini (2003a); Amendola (2001), existing studies have so far primarily yielded upper bounds on the interaction strength.

Here, we do not revisit these phenomenological motivations in detail but instead focus on whether current data provide statistical evidence for a Yukawa-type interaction in the case of a Chameleon dark energy model Khoury & Weltman (2004a),

discussed in the previous chapter. This model exhibits a particularly intriguing feature— that allows the DE equation of state parameter to drop below the phantom divide ($w < -1$) without violating the null energy condition or leading to catastrophic instabilities of ghost fields in the cosmic evolution Huey & Wandelt (2006); Štefančić (2004); Das et al. (2006b). The core dynamics of this model are governed by an interaction between dark matter and scalar-field dark energy, a coupling that emerges naturally from string-theory compactifications Damour & Polyakov (1994a), similar to what was discussed in the previous chapter. However, in particular, we make the additional assumption that the scalar field settles at the minimum of the effective potential at the present epoch. In this setup, energy flows from the dark energy field to the dark matter sector, modifying the expected dilution behavior of dark matter over cosmic time. For an observer unaware of such an interaction and interpreting the dark matter evolution within a ΛCDM-like framework, this energy exchange manifests as an apparent phantom behavior of the dark energy at earlier times.

This work presents a detailed numerical investigation of the Chameleon dark energy and its implications for cosmology. In contrast to earlier work Boriero et al. (2015a), where an approximate analytical solution of the scalar field was used, we solve the Klein-Gordon equation numerically by employing a shooting algorithm to accurately determine the initial condition of the scalar field. This more precise approach allows us to capture the field dynamics across all relevant redshifts, ensuring a consistent treatment throughout cosmic history. Previous works have also explored similar types of models and found a preference for non-zero coupling strength in the dark sector Gómez-Valent et al. (2020, 2022); Goh et al. (2023). Interestingly, we observe that the combined datasets of Planck, DESI DR2 BAO, and Pantheon+ datasets prefer a higher value of the coupling strength compared to the results of previous analyses. Recently, sign-changing interacting dark energy models, where flow of energy direction from dark matter to dark energy is reversed at a certain redshift, have also been able to constrain the interaction strength in

the dark sector Sabogal et al. (2025b). However, our model, which naturally arises from string compactifications, constrains the coupling strength with a preference for higher non-zero coupling strength without any sign of change in dark sector coupling. This intriguing result opens the door to further explorations, in particular, the effect on non-linear scales, which alter the history of structure formation due to the violation of the equivalence principle. With the advent of upcoming cosmological surveys capable of probing cosmic structures with unprecedented precision, the observational imprint of this interaction could be identified with greater statistical significance. Moreover, a non-zero coupling is expected to generate a distinct signature in the differential infall of dark matter and baryons into virialized halos Kesden & Kamionkowski (2006); Keselman et al. (2009); Secco et al. (2018). These effects will be systematically explored in our future work using dedicated N-body simulations, which will allow us to quantify the impact of the fifth force on structure formation in the non-linear regime.

6.1 The Chameleon Model

This work presents a comprehensive investigation of a Yukawa-type interaction between dark matter and a quintessential scalar field functioning as dark energy, which is an extension of the model described in Chapter 5. Such a light scalar degree of freedom can naturally emerge from string theory compactifications, enabling its coupling to the matter sector Damour & Polyakov (1994a). To remain consistent with the tight constraints from solar system gravity tests Will (2001); Kapner et al. (2007), the Chameleon mechanism typically restricts this interaction to the dark matter component alone Khoury & Weltman (2004a,b); Brax et al. (2004, 2006); Copeland et al. (2006b); Wang et al. (2012). As a result, the scalar field dynamically acquires a mass that depends on the local dark matter

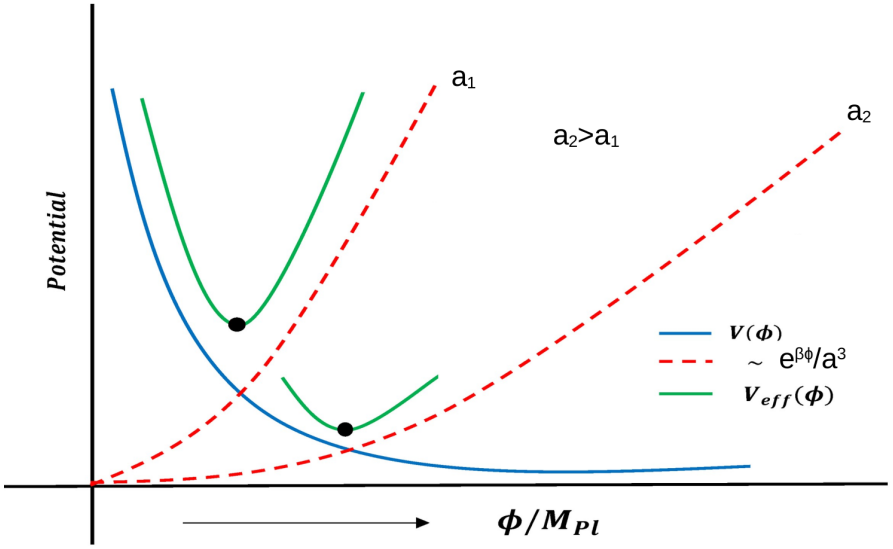


FIGURE 6.1: Schematic diagram of effective potential with evolving minima

density, giving rise to a screening effect that renders the field's influence negligible in high-density environments Das et al. (2006b); Wang et al. (2012).

In this chapter, we follow the model developed in Das et al. (2006b), where the quintessential scalar field, ϕ, couples to dark matter, ψ, through a Yukawa-type coupling of the form $f(\phi)\overline{\psi}\psi$. Here we extend the model described in Chapter 5 with an additional assumption of the scalar field being settled to the effective potential minima at present epoch. The dynamics of this field are governed by a modified Klein-Gordon equation, which includes an additional source term proportional to the dark matter energy density and the derivative of the coupling function.

$$\phi'' + 3H\phi' = -V_{,\phi}(\phi) - \frac{\rho_{\rm dm}^{(0)}}{a^3}\frac{f_{,\phi}(\phi)}{f(\phi_0)}. \tag{6.1}$$

Here ϕ' denotes the derivative with respect to standard time. Consequently,

the scalar field evolves under an effective potential that includes both the self-interaction potential and an interaction-induced term, which depends on the background dark matter density,

$$V_{\rm eff}(\phi) = V(\phi) + \frac{\rho_{\rm dm}^{(0)}}{a^3}\frac{f(\phi)}{f(\phi_0)}, \tag{6.2}$$

Here, ϕ_0 denotes the position of the scalar field in the present epoch. A schematic diagram of the effective potential with evolving minima is shown in Figure 6.1. In this context, we adopt the following form of the coupling function, motivated by string theory compactifications Damour & Polyakov (1994a),

$$f(\phi) = \exp\left(\frac{\beta\phi}{\sqrt{8\pi}M_{\rm Pl}}\right), \tag{6.3}$$

where $M_{\rm pl}$ is the reduced Planck mass. Due to the interaction with dark energy, the mass of dark matter becomes a function of the scalar field, causing its energy density to evolve as $\rho_{\rm dm} \sim f(\phi)/a^3$, which is slower than the standard ΛCDM evolution of $\sim a^{-3}$, since, similar to Das et al. (2006b), we assume that $f(\phi)$ monotonically increases at low redshifts, when dark energy effects become prominent. The corresponding Friedmann equation becomes,

$$3H^2M_{\rm Pl}^2 = \frac{\rho_{\rm dm}^0}{a^3}\frac{f(\phi)}{f(\phi_0)} + \rho_\phi + \rho_{\rm other} \tag{6.4}$$

where $\rho_\phi = \phi'^2/2 + V(\phi)$ and $\rho_{\rm other} = \rho_\gamma + \rho_\nu + \rho_{\rm b}$. $\rho_{\rm other}$ represents the total energy density of photons, neutrinos, and baryons. These components redshift in the same way as in the standard ΛCDM model, since they are not affected by the coupling between dark matter and dark energy.

Importantly, an observer who is unaware of this interaction—and assumes that

dark matter follows its standard evolution—would infer an effective non-interacting dark energy, fully described by an effective equation of state, $w_{\rm eff}$ and follows the following conservation equation,

$$\frac{d\rho_{\rm de}^{\rm eff}}{dt} = -3H(1+w_{\rm eff})\rho_{\rm de}^{\rm eff} \tag{6.5}$$

Correspondingly, the observer assumed the dark matter to be standard Cold Dark Matter (CDM), which results in the following Friedmann equation,

$$3H^2M_{\rm Pl}^2 = \frac{\rho_{\rm dm}^{(0)}}{a^3} + \rho_{\rm de}^{\rm eff} + \rho_{\rm other} \tag{6.6}$$

Due to the observer's assumption, this model would give rise to the effective dark energy density,

$$\rho_{\rm de}^{\rm eff} = \frac{\rho_{\rm dm}^{(0)}}{a^3}\left[\frac{f(\phi)}{f(\phi_0)} - 1\right] + \rho_\phi \tag{6.7}$$

Taking time derivative of the equation 6.7 and comparing it with equation 6.5 we get,

$$1 + w_{\rm eff} = \frac{1}{\rho_{\rm de}^{\rm eff}}\left\{\left[\frac{f(\phi)}{f(\phi_0)} - 1\right]\frac{\rho_{\rm dm}^{(0)}}{a^3} + (1+w_\phi)\rho_\phi\right\} \tag{6.8}$$

where, the equation of state of the true scalar field dark energy,

$$w_\phi = \left(\phi'^2/2 - V(\phi)\right) / \left(\phi'^2/2 + V(\phi)\right) \ . \tag{6.9}$$

From equation 6.8, we find that w_ϕ and $w_{\rm eff}$ are connected through the following relation,

$$w_{\rm eff} = \frac{w_\phi}{1-x} \quad \text{where,} \quad x = -\frac{\rho^0_{\rm dm}}{a^3\rho_\phi}\left(\frac{f(\phi)}{f(\phi_0)} - 1\right), \tag{6.10}$$

Although the quintessential scalar field itself does not exhibit any phantom behavior—remaining within the theoretical bounds of Null Energy Condition $-1 \leq w_\phi \leq -1/3$—an observer agnostic about the underlying dark sector interaction would still infer an effective equation of state that crosses into the phantom regime. This occurs because the parameter x remains strictly positive for a monotonically increasing coupling function, thereby amplifying the deviation between w_ϕ and $w_{\rm eff}$. Such a mechanism could potentially account for the mild preference for phantom-like dark energy observed in several independent analyses Alam et al. (2021); D'Amico et al. (2021); Abbott et al. (2019), and may serve as indirect evidence for an interaction within the dark sector.

We use the same runaway-type self-interaction potential given in Das et al. (2006b),

$$V(\phi) = M^4\left(\frac{M_{Pl}}{\phi}\right)^\alpha. \tag{6.11}$$

Here, M represents the characteristic energy scale associated with the scalar field, while α denotes the steepness of the potential. The evolution of the quintessential scalar field follows a thawing scenario, wherein the field remains nearly frozen at its initial value at earlier epochs due to strong Hubble friction, and gradually begins to evolve as the Hubble parameter decreases. This evolution drives the field toward the dynamically evolving minimum of the effective potential. In addition to this, we impose an important condition that the scalar field must settle at the present-day minimum of the effective potential with vanishing kinetic energy. This ensures that the total contribution to the dark energy density today arises purely

from the self-interaction potential. To implement this condition consistently, we normalize the self-interaction potential in the following way:

$$V(\phi) = 3H_0^2 M_{\rm pl}^2 \Omega_{\rm de}^0 \left(\frac{\phi_0}{\phi}\right)^{\alpha} \tag{6.12}$$

In our work, we use the analytical expression obtained in Das et al. (2006b) through minimizing the effective potential,

$$\frac{\phi_0}{\sqrt{8\pi} M_{\rm Pl}} = \frac{\alpha}{\beta} \frac{\Omega_{\rm de}^0}{\Omega_{\rm dm}^0} \tag{6.13}$$

Previous observations from Planck, BAO datasets (such as BOSS and eBOSS), and various supernova compilations have consistently pointed toward a present-day dark energy equation of state close to $w_{\rm de} = -1.0$, with strong statistical significance Aghanim et al. (2020); Semenaite et al. (2022); Sevilla-Noarbe et al. (2021). As demonstrated in Das et al. (2006b), the effective equation of state in the Chameleon framework naturally evolves toward $w_{\rm eff} \to -1$ as $z \to 0$, remaining compatible with these constraints. However, recent results from the DESI collaboration have provided strong evidence for evolving dark energy, thereby generating tension with the standard ΛCDM scenario Abdul-Karim et al. (2025). It is important to note that this tension arises only when an evolving dark energy component is assumed in the fiducial cosmology used for the analysis. Moreover, DESI's analysis reveals a crossing of the phantom divide in the reconstructed dark energy equation of state around redshift $z \sim 0.5$ and $w_{\rm de} > -1.0$ today, as observed across several model-independent reconstruction techniques Lodha et al. (2025a). While the statistical significance of this phantom crossing remains modest, a recent study has demonstrated an alternative realization of both of these behavior within the Chameleon framework Chakraborty et al. (2025b). This work has been

extensively discussed previously in Chapter 5. However, that approach differs substantially from the present one, particularly in the assumed scalar field mass and in allowing a non-zero kinetic energy for the field at the current epoch. Notably, in this work, the scalar field rolls down the effective potential after overcoming the Hubble friction and settles down eventually to the minima of the effective potential at the present epoch, leading to the dark energy equation of state, $w_{\rm de}$ close to -1. This eventually limits the model to the extent it can explain the DESI observation.

Due to the presence of an additional interaction in the dark sector, the perturbation equations will be modified accordingly. The equations take the following form in the synchronous gauge.

$$\begin{aligned}\dot{\delta}_{\rm dm} &= -\left(\frac{\theta_{\rm dm}}{a}+\frac{\dot{\tilde{h}}}{2}\right)+\frac{\beta}{\sqrt{8\pi}M_{\rm Pl}}\delta\dot{\phi}\ ,\\ \dot{\theta}_{\rm dm} &= -H\theta_{\rm dm}+\frac{\beta}{\sqrt{8\pi}M_{\rm Pl}}\left(\frac{k^2}{a}\delta\phi-\dot{\phi}\theta_{\rm dm}\right)\ ,\end{aligned} \tag{6.14}$$

Also, the perturbed Klein-Gordon equation becomes,

$$\ddot{\delta\phi}+3H\dot{\delta\phi}+\left(\frac{k^2}{a^2}+V_{,\phi\phi}\right)\delta\phi+\frac{1}{2}\dot{\tilde{h}}\dot{\phi}=-\frac{\beta}{\sqrt{8\pi}M_{\rm Pl}}\rho_{\rm dm}\delta_{\rm dm}\ , \tag{6.15}$$

where $\tilde{h}\equiv\tilde{h}^{i}{}_{i}$ is the trace of metric perturbation $\tilde{h}_{ij}$ in synchronous gauge.

Similarly, the perturbed Einstein equation determining the evolution of metric perturbation gets modified too in the following manner,

$$k^2\eta - \tfrac{1}{2}a^2H\dot{\tilde{h}} = -\frac{a^2}{2M_{\rm Pl}^2}\left(\sum_{i=\gamma,\nu,\rm b,dm}\rho_i\delta_i + \delta\rho_\phi\right), \tag{6.16}$$

$$k^2\dot{\eta} = \frac{a}{2M_{\rm Pl}^2}\left(\sum_{i=\gamma,\nu,\rm b,dm}(\rho_i + P_i)\,\theta_i + ak^2\dot{\phi}\,\delta\phi\right), \tag{6.17}$$

$$\ddot{\tilde{h}} + 3H\dot{\tilde{h}} - 2\frac{k^2}{a^2}\eta = -\frac{3}{M_{\rm Pl}^2}\left(\sum_{i=\gamma,\nu,\rm b,dm}\delta P_i + \dot{\phi}\,\delta\dot{\phi} - V_{,\phi}\,\delta\phi\right). \tag{6.18}$$

where $\delta\rho_\phi = \dot{\phi}\delta\dot{\phi} + V_{,\phi}\delta\phi$. From Eq. 6.2, it is evident that the dark matter density-dependent term dominates in the early universe due to the very small values of the scale factor. The self-interaction potential becomes comparable only once the scale factor is sufficiently large, which occurs around the epoch when dark energy starts to dominate. At this stage, the scalar field is gradually attracted toward the effective minimum, leading to a monotonic increase in its value. This late-time roll of the scalar field not only alters the background expansion history but also induces a time variation in the gravitational potentials.

An important observational imprint of this effect arises through the late-time Integrated Sachs–Wolfe (ISW) contribution to the CMB anisotropies. In standard cosmology, the gravitational potentials remain nearly constant during matter domination, and the ISW contribution is negligible. Once the expansion history deviates from pure matter domination, the potentials begin to evolve, leading to an ISW signal at large angular scales in the CMB. In chameleon models, the scalar–matter coupling modifies both the background acceleration and the growth of structure, thereby altering the time evolution of the potentials compared to ΛCDM. Although measurements of the ISW effect are fundamentally constrained by cosmic variance, correlating CMB temperature anisotropies with tracers of the large-scale matter distribution offers an independent handle on this characteristic

prediction of chameleon cosmology. The late-time ISW effect in the chameleon cosmology has been extensively discussed in previous works Boriero et al. (2015a).

In the next section, we present the procedure of implementing the model numerically in terms of both modified background and perturbation dynamics, and we present the results in Section 6.4 by putting constraints on the model parameters from various observational datasets.

6.2 Model Implementation: Shooting Algorithm

In this study, we implement the model in `CLASS` Lesgourgues (2011); Blas et al. (2011) and incorporate the background and perturbation equations relevant to the Chameleon dark energy model. In particular, we numerically solve the Klein-Gordon equation in conjunction with the Friedmann equations and the perturbed Einstein equations, following the formalism outlined in Corasaniti (2008). A critical aspect of this implementation involves the specification of the initial scalar field value, ϕ_i. An arbitrary choice of ϕ_i does not ensure that the scalar field will evolve to the correct present-day minimum of the effective potential, ϕ_0. As a result, this mismatch can lead to an inaccurate estimation of the present-day dark energy density, attributed to an incorrect treatment of the field's background evolution.

To ensure that the scalar field accurately reproduces the observed dark energy density today, our objective is to solve the Klein-Gordon equation such that the field evolves toward the minimum of the effective potential, ϕ_0 given in Eq. 6.13, with negligible kinetic energy at the present epoch. Achieving this behavior requires a careful choice of the initial field value and its velocity. To this end, we implement an automated shooting algorithm within `CLASS`, designed to iteratively

adjust the initial field value to match the analytically expected ϕ_0 at $z = 0$. Starting from a trial configuration of the initial scalar field and a fixed initial velocity set to zero, the code evolves the background cosmology and checks whether the final field value aligns with the target ϕ_0. If a deviation is detected, the algorithm updates the initial field position and repeats the integration until the field reaches the desired final value within a numerical accuracy of at least 10^{-5}.

This procedure is performed for each combination of the standard six ΛCDM cosmological parameters, along with input values of α and β. We have explicitly verified that the field velocity remains negligibly small at the present epoch, ensuring that its contribution to the total energy density is insignificant. Consequently, the present-day dark energy density arises almost entirely from the normalized self-interaction potential, as defined in Eq. 6.12. This method allows us to maintain high numerical precision in the evaluation of the energy density and enhances the robustness and accuracy of our results compared to previous studies that relied on approximate field dynamics.

Given the extremely light mass of the scalar field, its evolution is initially suppressed by Hubble friction, effectively freezing the field at its starting value in the early universe. The field begins to roll only at late times, and its dynamics are highly sensitive to the choice of α and β, which determine the slope and shape of the effective potential. At early epochs, the contribution from the dark matter coupling dominates the effective potential due to the small scale factor, while the self-interaction potential becomes relevant only at late times. As the field rolls down the effective potential, it can overshoot the minimum, leading to oscillatory behavior around ϕ_0. However, since the crossing of the minimum occurs at late times, the field does not acquire sufficient velocity to significantly affect the present-day energy budget. The detailed dynamics of the scalar field evolution, including the minima crossing and oscillations, will be discussed further in Section 6.4.

6.3 Method

We modify the Boltzmann code `CLASS` to incorporate the background and perturbed Einstein equations specific to the Chameleon dark energy model, following the formulation presented in Corasaniti (2008). This allows us to compute both the cosmic microwave background (CMB) anisotropy power spectra and linear matter power spectrum for Chameleon model.

To constrain the model parameters, we perform a comprehensive MCMC analysis using the following cosmological datasets:

- **Planck 2018:** High-ℓ temperature (TT), temperature-polarization (TE), and polarization (EE) power spectra, along with low-ℓ TT and EE measurements Chen (2020).

- **SDSS BAO:** Baryon Acoustic Oscillation measurements from SDSS-III BOSS DR12 galaxy sample at redshifts $z = 0.38,\ 0.51,\ 0.61$ Alam et al. (2017a), 6dF Galaxy Survey (6dFGS) at $z = 0.106$ Beutler et al. (2011a), and SDSS DR7 Main Galaxy Sample at $z = 0.15$ Ross et al. (2015a).

- **DESI DR2 BAO:** Baryon Acoustic Oscillation measurements from DESI DR2 Abdul-Karim et al. (2025), including tracers from galaxies, quasars, and the Lyman-α forest. The data provide both isotropic and anisotropic constraints across the redshift range $0.295 \leq z \leq 2.330$, divided into nine redshift bins as detailed in Table IV of Abdul-Karim et al. (2025).

- **Pantheon+ :** Type Ia supernovae measurements covering a redshift range of $z = 0.001$ to 2.26 Brout et al. (2022).

- **SH$_0$ES Cepheid sample:** Local distance ladder measurements using Cepheid variables in host galaxies of nearby Type Ia supernovae with $z \leq 0.01$ Riess et al. (2022).

Our baseline cosmological model includes the six standard ΛCDM parameters: [ω_b, ω_{dm}, θ_s, $\ln(10^{10}A_s)$, n_s, and τ_{reio}], in addition to the two Chameleon model parameters, α and β. Throughout our MCMC analysis, we consider uniform priors for all the cosmological parameters, and the corresponding prior range for the model parameters is presented in Table 6.1.

TABLE 6.1: Prior ranges considered for MCMC analysis for the cosmological parameters of Chameleon and ΛCDM model.

Parameters	Prior range
$100\omega_b$	$\mathcal{U}[0.50, 10.0]$
$\omega_{\rm dm}$[1]	$\mathcal{U}[0.0010, 0.99]$
$100 \times \theta_s$	$\mathcal{U}[0.50, 10.00]$
$\ln 10^{10} A_s$	$\mathcal{U}[1.60, 3.90]$
n_s	$\mathcal{U}[0.80, 1.20]$
τ_{reio}	$\mathcal{U}[0.04, 0.80]$
α	$\mathcal{U}[0.00, 16.00]$
β	$\mathcal{U}[0.00, 1.00]$

[1] for ΛCDM model, the 'dm' subscript means the CDM, and for the Chameleon model, it means the dark matter coupled with dark energy considered throughout the tables in this chapter.

The MCMC analysis is performed using the publicly available package `MontePython-v3` Brinckmann & Lesgourgues (2018), which employs the Metropolis-Hastings algorithm and interfaces directly with the modified version of `CLASS`. Parameter sampling efficiency is improved using Cholesky decomposition, which separates fast and slow directions in the parameter space Lewis et al. (2000). The convergence

of the MCMC chains is monitored using the Gelman-Rubin criterion, requiring $R-1 < 0.01$ for all parameters Gelman & Rubin (1992a). Additionally, we obtain the minimum χ^2 values using the Sequential Least Squares Programming (SLSQP) optimizer implemented within `MontePython`.

To further quantify the model preference, we calculate the AIC, which penalizes models with additional free parameters. The AIC difference between the Chameleon model and ΛCDM is given by Akaike (1974):

$$\Delta\text{AIC} = \chi^2_{\text{min,Model}} - \chi^2_{\text{min,}\Lambda\text{CDM}} + 2(N_{\text{Model}} - N_{\Lambda\text{CDM}})\,. \tag{6.19}$$

Here, the ΛCDM model is adopted as the reference. A negative value of ΔAIC indicates that the Chameleon model fits the data better than ΛCDM, given a combination of datasets; in contrast, positive values suggest an inferior fit. For this work we adopt the following criterion Wu (2025): In favor of the model, $\Delta\text{AIC} \in [-2, 0)$ indicates weak evidence; $\Delta\text{AIC} \in [-6, -2)$ indicates positive evidence; $\Delta\text{AIC} \in [-10, -6)$ indicates strong evidence; and $\Delta\text{AIC} < -10$ very strong evidence. Conversely, against the model $\Delta\text{AIC} \in (0, 2]$ indicates weak evidence; $\Delta\text{AIC} \in (2, 6]$ indicates positive evidence; $\Delta\text{AIC} \in (6, 10]$ indicates strong evidence; and $\Delta\text{AIC} > 10$ very strong evidence.

6.4 Results

In this section, we present the results of our MCMC analysis of the model. The results are given in Tables 6.2, 6.3, and 6.4, and illustrated in Figure 6.2, while the scalar field evolution and effective dark energy equation of state from the best-fit parameters are shown in Figures 6.3 and 6.4. We also compare our model relative to ΛCDM statistically using the Akaike Information Criterion (AIC) in Table 6.5 for each dataset combination used for the analysis.

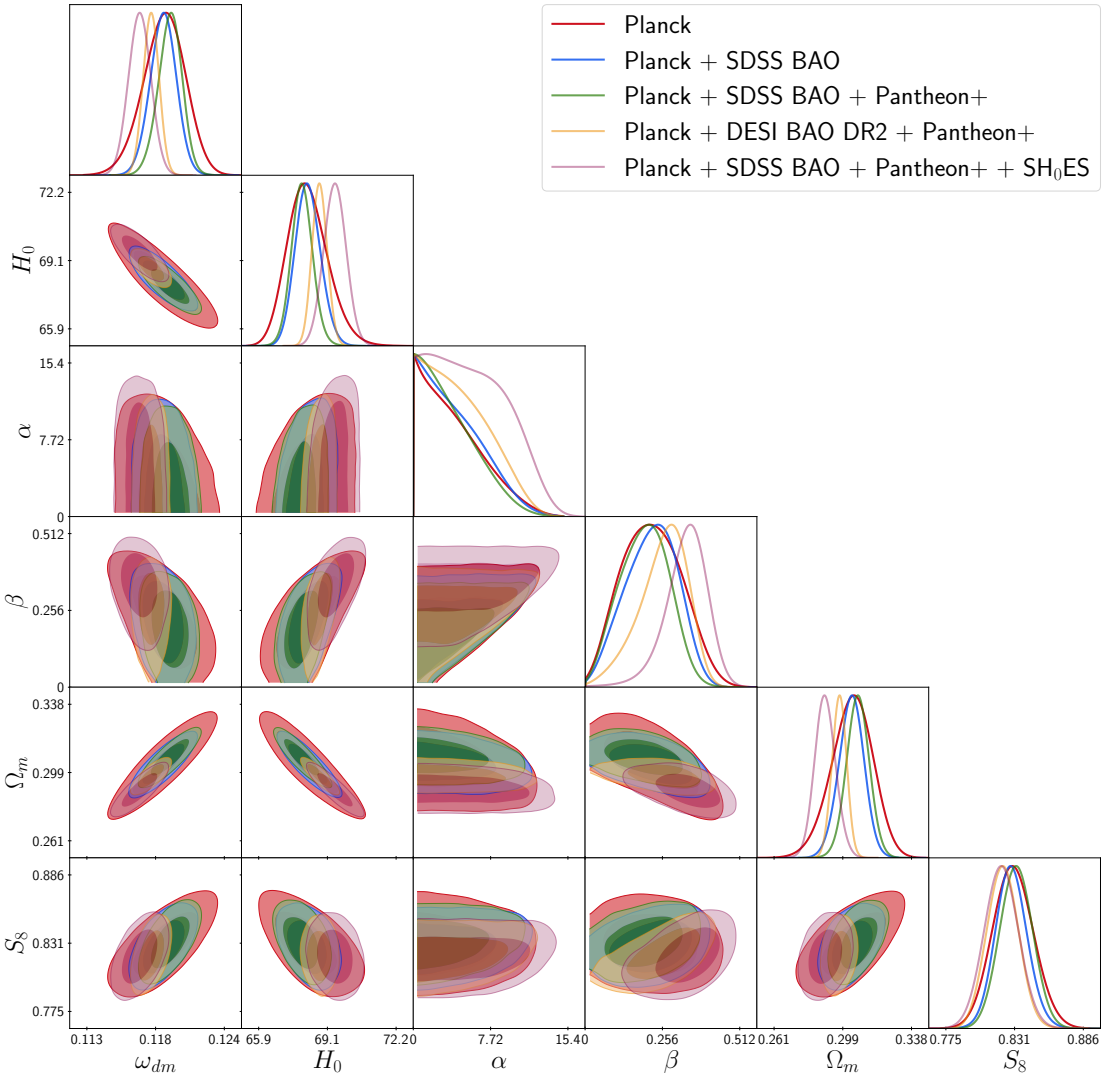


FIGURE 6.2: Two-dimensional marginalized posterior distributions of the model parameters ($\omega_{\rm dm}$, H_0, α, β, Ω_m, and S_8) obtained from our MCMC analysis with contours having 68% and 95% C.L. Different colors represent different dataset combinations: Planck-only, Planck+SDSS BAO, Planck+SDSS BAO+Pantheon+, Planck+DESI DR2 BAO+Pantheon+, and Planck+SDSS BAO+Pantheon+ + SH_0ES.

Figure 6.2 displays the one-dimensional marginalized posteriors and two-dimensional confidence contours for the model parameters. Notably, we find that although Planck alone restricts the allowed range of the coupling parameter β, the two-dimensional posteriors involving β are not fully closed at the 95% confidence level, while only an upper bound is obtained on α. Therefore, the Planck-only result does not provide enough evidence of a non-zero coupling. This is consistent with

the negligible improvement, $\Delta\chi^2_{\rm min} = -0.31$, over ΛCDM, presented in Table 6.5. We observe that the mean value of β remains close to ~ 0.200 with the inclusion of additional datasets such as SDSS BAO and Pantheon+, while the constraints tighten progressively as more data are incorporated. Remarkably, when substituting the BAO measurements with those from DESI DR2, it yields a higher value of interaction strength, $\beta \sim 0.256$, and significantly tighter bounds relative to earlier results due to the higher sensitivity and precision in measurement of the BAO scalae by the DESI collaboration. Also, we will later show that our model also shows features of an evolving dark energy with a phantom crossing like DESI, as shown in Figure 6.4. However, as mentioned in Section 6.1, departure of the effective dark energy equation of state from a cosmological constant remains tiny.

Furthermore, the inclusion of the DESI DR2 dataset leads to a modest upward shift in the Hubble constant, with $H_0 \sim 68.7$, compared to $H_0 \sim 68.0$ obtained from other datasets excluding DESI and closely aligned with the Planck baseline. When the full combination of Planck, SDSS BAO, Pantheon+, and $\rm SH_0ES$ data is considered, the model exhibits a preference for even higher dark sector interaction, with $\beta \sim 0.335$, along with the most stringent constraint on this parameter, as a result of the incredible precision of late-time dynamics from measurements of $\rm SH_0ES$ collaboration. The inclusion of $\rm SH_0ES$ also results in a further increase in the inferred Hubble constant, a trend that is clearly reflected in our analysis. For the Planck+SDSS BAO+Pantheon++$\rm SH_0ES$ combination, the Chameleon model yields $H_0 \simeq 69.4$, compared to $H_0 \simeq 68.6$ in ΛCDM. Although this upward shift is not sufficient to resolve the Hubble tension, the inclusion of $\rm SH_0ES$ strengthens the relative fit of the model, improving $\Delta\chi^2_{\rm min}$ from -1.96 without $\rm SH_0ES$ to -6.41 after its inclusion. This indicates a partial alleviation of the tension rather than a complete resolution.

Figure 6.2 also provides an upper bound on the parameter α, which characterizes

TABLE 6.2: The mean (bestfit) $\pm 1\sigma$ error for the cosmological parameters constrained with the datasets Planck and Planck + SDSS BAO for the ΛCDM model and Chameleon model are shown in this table. The 1σ error is obtained at 68% confidence level. The corresponding χ^2_{min} and $\Delta\chi^2_{min}$ values are also shown. Upper bounds are obtained from the marginalized distribution such that 95% of the samples lie below the quoted value, corresponding to the 95% credible level.

Dataset	Planck		Planck + SDSS BAO	
Model	ΛCDM	Chameleon	ΛCDM	Chameleon
$100\omega_b$	$2.24(2.25) \pm 0.0154$	$2.24(2.23)^{+0.0153}_{-0.0157}$	$2.24(2.24) \pm 0.0143$	$2.24(2.24) \pm 0.0140$
$\omega_{\rm dm}$	$0.120(0.119) \pm 0.00140$	$0.119(0.119)^{+0.00183}_{-0.00160}$	$0.119(0.120) \pm 0.00102$	$0.119(0.118)^{+0.00112}_{-0.00107}$
$100 \times \theta_s$	$1.04(1.04) \pm 0.000301$	$1.04(1.04)^{+0.000303}_{-0.000310}$	$1.042(1.042) \pm 0.000285$	$1.04(1.04) \pm 0.000293$
$\ln 10^{10} A_s$	$3.05(3.04)^{+0.0157}_{-0.0168}$	$3.04(3.04) \pm 0.0160$	$3.05(3.04)^{+0.0156}_{-0.0173}$	$3.04(3.04)^{+0.0162}_{-0.0167}$
n_s	$0.965(0.966)^{+0.00450}_{-0.00458}$	$0.966(0.966)^{+0.00462}_{-0.00465}$	$0.967(0.964) \pm 0.00388$	$0.966(0.968) \pm 0.00391$
τ_{reio}	$0.0545(0.0521)^{+0.00763}_{-0.00820}$	$0.0538(0.0537)^{+0.00776}_{-0.00804}$	$0.0557(0.0524)^{+0.00740}_{-0.00829}$	$0.0542(0.0535)^{+0.00771}_{-0.00817}$
α	–	< 9.83	–	< 9.55
β	–	$0.222(0.159)^{+0.0975}_{-0.105}$	–	$0.219(0.210)^{+0.0949}_{-0.0809}$
H_0	$67.3(67.7)^{+0.625}_{-0.635}$	$68.2(67.6)^{+0.776}_{-1.03}$	$67.7(67.7)^{+0.446}_{-0.470}$	$68.2(68.4)^{+0.538}_{-0.606}$
σ_8	$0.811(0.806)^{+0.00771}_{-0.00763}$	$0.824(0.813)^{+0.0104}_{-0.0143}$	$0.809(0.807)^{+0.00700}_{-0.00764}$	$0.823(0.832)^{+0.0103}_{-0.0137}$
$\chi^2_{\rm min}$	2772.09	2771.78	2777.08	2776.52
$\Delta\chi^2_{\rm min}$	0	−0.31	0	−0.56

the slope of the scalar field's self-interaction potential. For the theoretical consistency of the model, α must remain strictly positive. As a result, the MCMC analysis can only yield an upper bound on this parameter, rather than tightly constraining it. A very small value of α corresponds to an extremely flat potential, implying the absence of a well-defined minimum near the present epoch. In such cases, the scalar field continues to evolve slowly with a decreasing kinetic energy, never settling into a stable configuration. On the other hand, a large value of α results in a steeper potential, causing the field to become increasingly confined

and suppressing its evolution at late times. Therefore, an upper bound on α is an expected outcome, which is indeed observed in our analysis using Planck, SDSS BAO, and Pantheon+ datasets.

TABLE 6.3: Obtained parameter values with mean (bestfit) $\pm 1\sigma$ error using the datasets Planck + SDSS BAO + Pantheon Plus and Planck + SDSS BAO + Pantheon Plus + SH_0ES for the ΛCDM model and Chameleon model are shown in this table. The 1σ error is obtained at 68% confidence level. The corresponding χ^2_{min} and $\Delta\chi^2_{min}$ values are also shown. Upper bounds are obtained from the marginalized distribution such that 95% of the samples lie below the quoted value, corresponding to the 95% credible level.

Dataset	Planck + SDSS BAO + Pantheon+		Planck + SDSS BAO + Pantheon+ + SH_0ES	
Model	ΛCDM	Chameleon	ΛCDM	Chameleon
$100\omega_b$	$2.24(2.24)^{+0.0138}_{-0.0134}$	$2.24(2.24)^{+0.0137}_{-0.0140}$	$2.26(2.25)^{+0.0135}_{-0.0132}$	$2.25(2.26) \pm 0.0141$
$\omega_{\rm dm}$	$0.120(0.119)^{+0.000950}_{-0.000970}$	$0.119(0.120)^{+0.00103}_{-0.00101}$	$0.117(0.117)^{+0.000880}_{-0.000860}$	$0.117(0.117) \pm 0.000937$
$100 \times \theta_s$	$1.04(1.04)^{+0.000300}_{-0.000260}$	$1.04(1.04) \pm 0.000291$	$1.04(1.04)^{+0.000280}_{-0.000270}$	$1.04(1.04)^{+0.000295}_{-0.000292}$
$\ln 10^{10} A_s$	$3.04(3.04)^{+0.0155}_{-0.0161}$	$3.04(3.04)^{+0.0158}_{-0.0163}$	$3.05(3.04)^{+0.0164}_{-0.0180}$	$3.04(3.06)^{+0.0158}_{-0.0169}$
n_s	$0.966(0.965)^{+0.00363}_{-0.00379}$	$0.965(0.967)^{+0.00380}_{-0.00384}$	$0.972(0.973)^{+0.00374}_{-0.00364}$	$0.969(0.97)^{+0.00395}_{-0.00385}$
τ_{reio}	$0.0552(0.0513)^{+0.00750}_{-0.00776}$	$0.0536(0.0508)^{+0.00750}_{-0.00785}$	$0.0589(0.0574)^{+0.00752}_{-0.00903}$	$0.0550(0.0580)^{+0.00752}_{-0.00825}$
α	–	< 8.89	–	< 11.9
β	–	$0.197(0.154)^{+0.0859}_{-0.0815}$	–	$0.335(0.290)^{+0.0815}_{-0.0541}$
H_0	$67.5(67.8)^{+0.425}_{-0.430}$	$67.9(67.6)^{+0.484}_{-0.541}$	$68.6(68.6)^{+0.386}_{-0.398}$	$69.4(69.3) \pm 0.522$
σ_8	$0.810(0.803)^{+0.00726}_{-0.00689}$	$0.821(0.820)^{+0.00952}_{-0.0125}$	$0.804(0.803)^{+0.00727}_{-0.00778}$	$0.835(0.832)^{+0.0143}_{-0.0147}$
$\chi^2_{\rm min}$	4189.92	4187.96	4104.19	4097.78
$\Delta\chi^2_{\rm min}$	0	-1.96	0	-6.41

Interestingly, the inclusion of the DESI DR2 BAO dataset slightly relaxes the bound on α. This trend becomes more pronounced when the SH_0ES dataset is included, which further weakens the upper constraint on α. It is also noteworthy that both DESI DR2 and SH_0ES datasets tend to favor slightly lower values of $\omega_{\rm dm}$, compared to the combinations without them. This can be attributed to the

modified evolution of the dark matter energy density in the Chameleon framework, given by $\rho_{\rm dm} = \frac{\rho_{\rm dm}^{(0)}}{a^3} \frac{f_{,\phi}(\phi)}{f(\phi_0)}$, where the exponential coupling $f(\phi)$ depends on the interaction strength β as defined in Eq. 6.3. Since these datasets prefer higher values of both β and H_0, the resulting evolution of $\rho_{\rm dm}$ leads to a lower preferred value of $\omega_{\rm dm}$. Consequently, the total matter density Ω_m is slightly reduced, resulting in a mild downward shift in the preferred value of S_8 relative to other dataset combinations. A more detailed investigation into the growth of cosmic structures—and the corresponding inference of the matter fluctuation amplitude σ_8—requires a dedicated analysis involving small-scale non-linear dynamics, which are best captured through N-body simulations. We leave this aspect of the analysis to future work.

We also investigate the evolution of the scalar field and its dynamics by plotting the field value, its velocity, and the effective dark energy equation of state for the MCMC best-fit values obtained from various dataset combinations. These results are presented in Figures 6.3 and 6.4. The field evolution is computed by numerically solving the Klein-Gordon equation 6.1 using the shooting algorithm described in Section 6.2 to determine the appropriate initial field value that ensures consistency with present-day boundary conditions.

The left panel of Figure 6.3 shows the evolution of the scalar field, normalized by subtracting its initial value at the initial epoch, while the right panel displays the corresponding evolution of the field velocity. As the plots indicate, the scalar field remains nearly frozen at its initial value during the early universe due to strong Hubble friction, with its velocity remaining close to zero. As the Hubble parameter gradually decreases over time, the field begins to roll.

During the early evolution, the scalar field experiences an effective potential dominated by the dark matter coupling term, which is enhanced by the small scale

TABLE 6.4: Obtained parameter values with mean (bestfit) $\pm 1\sigma$ error using with the datasets Planck + DESI DR2 BAO + Pantheon Plus for the ΛCDM model and Chameleon model are shown in this table. The 1σ error is obtained at 68% confidence level. The corresponding χ^2_{min} and $\Delta\chi^2_{min}$ values are also shown. Upper bounds are obtained from the marginalized distribution such that 95% of the samples lie below the quoted value, corresponding to the 95% credible level.

Dataset	Planck + DESI DR2 BAO + Pantheon+	
Parameter	ΛCDM	Chameleon
$100\omega_b$	$2.25(2.26) \pm 0.0131$	$2.24(2.26)^{+0.0136}_{-0.0138}$
$\omega_{\rm dm}{}^{\dagger}$	$0.118(0.118)^{+0.000665}_{-0.000688}$	$0.118(0.117)^{+0.000677}_{-0.000673}$
$100 \times \theta_s$	$1.04(1.04) \pm 0.000278$	$1.04(1.04)^{+0.000285}_{-0.000296}$
$\ln 10^{10} A_s$	$3.05(3.05)^{+0.0160}_{-0.0177}$	$3.04(3.04)^{+0.0161}_{-0.0166}$
n_s	$0.971(0.972) \pm 0.00342$	$0.968(0.971) \pm 0.00371$
τ_{reio}	$0.0575(0.0580)^{+0.00764}_{-0.00845}$	$0.0550(0.0538)^{+0.00760}_{-0.00815}$
α	–	< 10.1
β	–	$0.256(0.23)^{+0.0924}_{-0.0629}$
H_0	$68.4(67.4) \pm 0.302$	$68.7(69.0)^{+0.348}_{-0.366}$
σ_8	$0.805(0.832)^{+0.00687}_{-0.00751}$	$0.825(0.823)^{+0.0121}_{-0.0143}$
$\chi^2_{\rm min}$	4200.94	4196.19
$\Delta\chi^2_{\rm min}$	0	−4.75

factor. This causes the field to roll down an exponentially shaped potential, leading to a monotonic decrease in its value. At later times, as the contribution from the self-interaction potential becomes comparable to the coupling term, a dynamically evolving minimum forms in the effective potential. The field accelerates toward this minimum, overshoots it due to its acquired velocity, and then begins to decelerate. After reaching a turning point—where its velocity momentarily vanishes—it reverses direction and begins to roll back down the potential.

This process leads to a damped oscillatory motion around the evolving minimum

of the effective potential. The field's velocity and position stabilize as it settles into the minimum with a negligible residual velocity, consistent with the boundary condition imposed at the present epoch. This behavior encapsulates the characteristic dynamics of the Chameleon mechanism and its late-time convergence to a potential-dominated dark energy state.

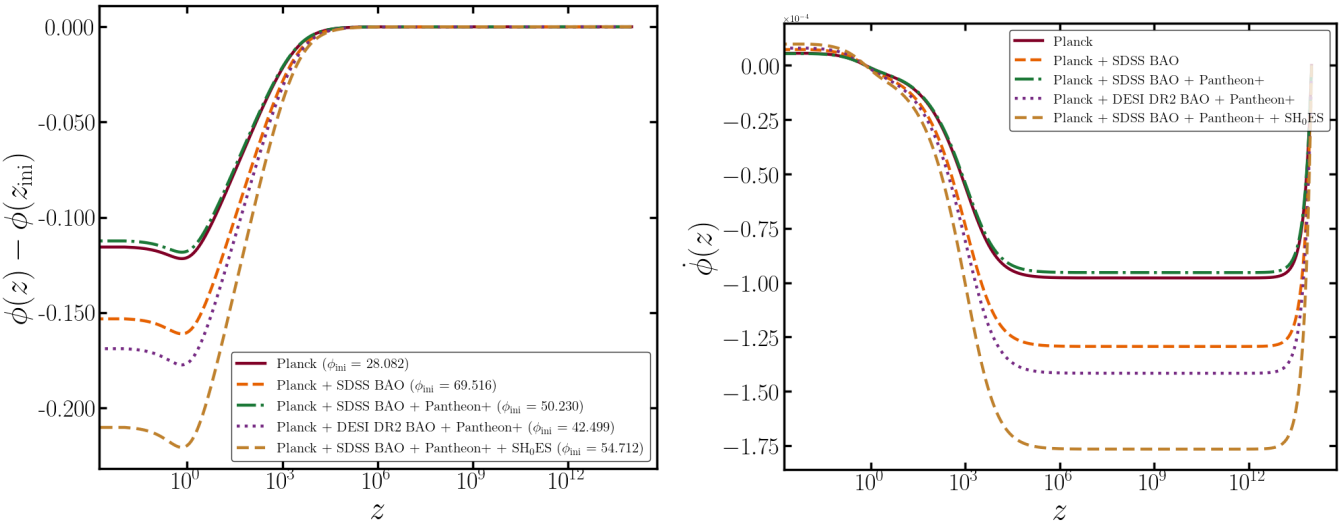


FIGURE 6.3: The scalar field dynamics with redshift is plotted here for best-fit values obtained from MCMC analysis for different combinations of datasets. The left panel shows the field value normalized to its initial value at the initial redshift, and the corresponding initial value is provided in the legend box. The right panel shows the corresponding dynamics of field velocity for the same set of best-fit values. Here $\dot{\phi}$ means derivative with respect to conformal time.

Using the scalar field dynamics obtained by numerically solving the Klein-Gordon equation, we compute the effective dark energy equation of state, $w_{\rm eff}$, using the Eqs. 6.10 & 6.9. The results are presented in Figure 6.4, which provides the evolution focused on the low-redshift regime, precisely where the Chameleon dark energy dynamics become observationally relevant.

In the context of recent evidence of dynamical dark energy from DESI observations, we analyze our Chameleon dark energy model using the DESI DR2 BAO dataset and find a preference for a non-zero dark sector coupling, with the interaction strength constrained to $\beta \sim 0.26$. Correspondingly, our model exhibits a crossing of the phantom divide in the effective dark energy equation of state around redshift

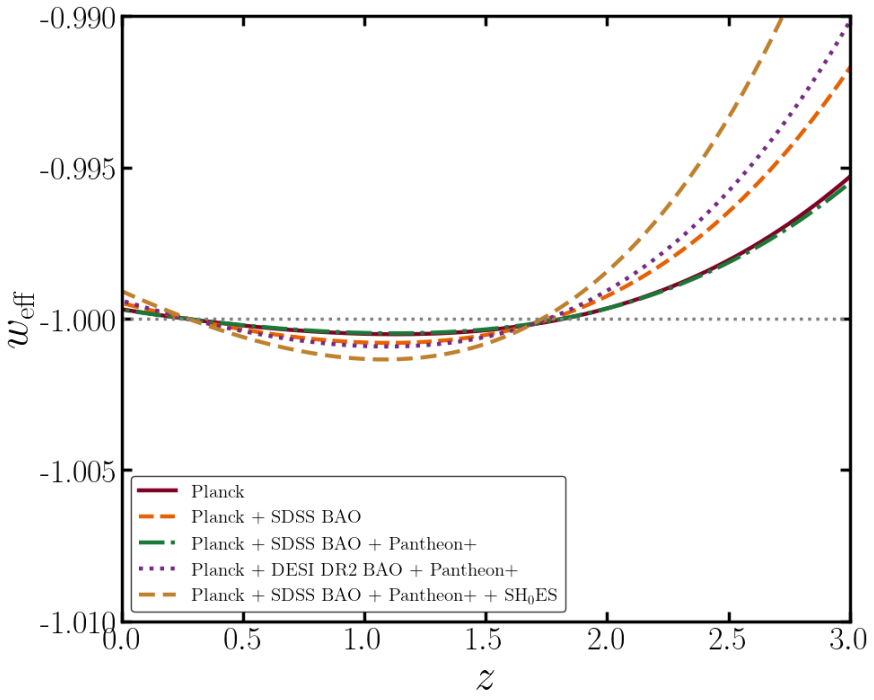


FIGURE 6.4: The effective dark energy equation of state for the chameleon model is plotted with redshift for best-fit values obtained from MCMC analysis for different combinations of datasets. It highlights a phantom crossing at low redshift.

$z \sim 0.5$, as illustrated in Figure 6.4. However, the evolution of $w_{\rm eff}$ remains very close cosmological constant at all relevant redshifts as a result of the assumptions of our model, mentioned in Section 6.1, which leads to $w_{\rm eff}$ close to -1 at present epoch. This conflicts with DESI observed preference of dark energy equation of state being higher than -1 today and explains the reduction of $\Delta\chi^2_{\rm min}$, as shown in Table 6.4 is not as significant as obtained by DESI collaboration for w_0w_aCDM model.

Although the statistical significance of the phantom crossing in the current DESI dataset remains moderate, the consistent emergence of this feature across independent analyses and within our framework suggests it may be more than a statistical fluctuation. Future DESI data—with improved redshift resolution and increased statistical power—will be essential in further probing the nature of dark energy. These forthcoming observations will allow for more stringent tests of interacting

dark sector models like ours, potentially confirming the presence of long-range interactions or ruling out this class of models entirely.

To assess the statistical significance of the Chameleon model relative to the standard ΛCDM scenario, we compute the difference in the minimum chi-squared value, $\Delta\chi^2_{\rm min}$, for each dataset combination used in our MCMC analysis. The results are summarized in Table 6.5. Across all combinations, we observe a reduction in $\chi^2_{\rm min}$ when the Chameleon model is used and when only Planck, SDSS BAO, and Pantheon+ datasets are considered; the amount of reduction remains consistent with other interacting dark energy modelsGiarè et al. (2024c). The most notable improvement occurs when the SH0ES dataset is included, yielding a maximum reduction of $\Delta\chi^2{\rm min} = -6.41$. A similarly significant reduction is observed when DESI DR2 BAO is used in place of SDSS BAO, with $\Delta\chi^2_{\rm min} = -4.75$, indicating a possible mild statistical preference for interaction in the dark sector in both cases of the combined datasets.

TABLE 6.5: Comparison of $\Delta\chi^2_{\rm min}$ and ΔAIC per experiment for Chameleon and ΛCDM models.

Dataset	Chameleon	
	$\Delta\chi^2_{\rm min}$	ΔAIC
Planck	-0.31	+3.69
Planck+ SDSS BAO	-0.56	+3.44
Planck + SDSS BAO + Pantheon+	-1.96	+2.04
Planck + DESI DR2 BAO + Pantheon+	-4.75	-0.75
Planck + SDSS BAO + Pantheon+ + SH_0ES	-6.41	-2.41

To statistically quantify the model preference, we calculate the ΔAIC using equation 6.19 by comparing our model with ΛCDM for each dataset combination used in our analysis. The results are presented in Table 6.5, and we base our conclusion on the adopted criterion mentioned in section 6.3. As shown in Table 6.5,

we get weak or positive evidence in terms of favoring the chameleon model relative to ΛCDM when either the DESI DR2 BAO or SH_0ES dataset is included, yielding ΔAIC values of -0.75 and -2.41, respectively. These results provide statistically meaningful (weak/positive) preference for interaction in the dark sector, with the combination of Planck, SDSS BAO, Pantheon+, and SH_0ES offering the positive evidence. This dataset combination is particularly sensitive to late-time cosmological dynamics, making it well-suited to probe deviations from the ΛCDM baseline. Furthermore, replacing SDSS BAO with DESI DR2 BAO also leads to weak evidence of dark sector interaction, suggesting that DESI data may offer a mild indirect indication of such interactions in the dark sector.

6.5 Summary

In this work, we investigate the possibility of an interaction within the dark sector using current cosmological datasets. Specifically, we consider the Chameleon dark energy model, where a quintessential scalar field is coupled to dark matter via a Yukawa-type interaction motivated by string compactification. In the absence of knowledge about this coupling, an observer would consider an incorrect evolution of the dark energy density, resulting in an observation of an effective dark energy that exhibits phantom-like behavior. The scalar field evolves under an effective potential comprising two contributions: the self-interaction potential and the interaction term sourced by the dark matter density, together forming a dynamically evolving minimum. We further impose the condition that the scalar field must settle at this minimum with vanishing velocity at the present epoch. To implement this scenario, we numerically solve the Klein-Gordon equation using a shooting algorithm, ensuring consistency with our boundary conditions. Based on the resulting scalar field dynamics, we compute the effective dark energy equation

of state, which exhibits phantom behavior at earlier epochs around $z \sim 2.0$, below which marks the onset of dark energy domination (around $z \sim 1.0$).

We perform an MCMC analysis of the Chameleon model using various combinations of datasets, including Planck, SDSS BAO, DESI DR2 BAO, Pantheon+, and SH0ES. We find that all dataset combinations are able to fully constrain the interaction strength β without requiring any sign-switching mechanism or additional exotic assumptions. We find higher non-zero interaction strength when incorporating the DESI DR2 and SH0ES datasets, yielding $\beta = 0.256^{+0.0924}_{-0.0629}$ and $\beta = 0.335^{+0.0815}_{-0.0541}$, respectively, compared to other dataset combinations which exclude either of these two. Previous works have also shown constraints on non-zero interaction; our analysis yields a comparatively higher value of it, when DESI or SH_0ES data were included in the analysis. Moreover, while some interacting dark sector models in the literature have required the introduction of sign-switching mechanisms at specific redshifts to fully constrain the interaction, our approach offers a more economical solution. It fully constrains the interaction strength without invoking any exotic modifications. Additionally, we obtain an upper bound on the slope of the scalar field self-interaction potential through the parameter α. Our AIC analysis further shows that the inclusion of $\mathrm{SH_0ES}$ and DESI DR2 BAO provides comparatively higher statistical preference in terms of positive and weak evidence in favor of the Chameleon model over the standard ΛCDM framework. These results suggest a mild preference for dark sector interaction in these particular two combinations of datasets, opening a promising avenue for new physics that could be further explored through small-scale structure observations by upcoming surveys, such as *Euclid* and *SPHEREx*.

Using the best-fit cosmological parameters obtained from the MCMC analysis for various dataset combinations, we extract the scalar field dynamics, which exhibit damped oscillations around the evolving minimum of the effective potential. From this, we compute the effective dark energy equation of state parameter, $w_{\rm eff}$, and

check its evolution, which crosses the phantom divide near $z \sim 0.5$. Even though the features like dynamical dark energy and phantom crossing are similar to the DESI observation, the assumption of the field to be at rest at the minima of the effective potential today, leads to an effective dark energy equation state value close to -1 at the present epoch. This does not agree with the DESI observations and as result it reflects in the weak statistical evidence in favor of the model relative to ΛCDM when Planck+DESI DR2 BAO+ Pantheon+ dataset combination is considered. It is also important to note that the current statistical evidence for phantom crossing from the DESI dataset remains moderate, future observations will offer the precision necessary to either confirm this feature or rule it out definitively.

This weak/positive statistical preference for a non-zero interaction strength β, derived from the analysis of linear cosmological scales, naturally motivates the extension of this investigation to smaller, non-linear scales. The best-fit values for β obtained here imply that the variation in the effective gravitational constant in the transition regime can be as large as $\sim 1/3$. Owing to the increased number of independent modes at these scales, the statistical power is significantly enhanced, offering the potential for a more robust detection of β or tighter constraints. A non-zero β would also produce distinct observational signatures, such as a differential infall rate between dark matter and baryonic matter onto virialized halos Kesden & Kamionkowski (2006); Keselman et al. (2009); Secco et al. (2018). Accurately quantifying these effects will require dedicated N-body simulations. Such simulations must be adapted to incorporate the Chameleon interaction and appropriately model the differing forces acting on dark matter and baryons. We plan to address these aspects in a forthcoming study.

Chapter 7

Summary and Future Work

7.1 Summary

This thesis has investigated a unified class of departures from the standard ΛCDM cosmology arising from non-standard properties of the dark sector, with a particular emphasis on scalar–fermion interactions and their cosmological consequences across widely separated epochs. The central theme connecting all chapters is the possibility that the microphysics of dark matter and dark energy need not be passive, but may involve dynamical interactions that leave observable imprints in both early- and late-time cosmology, which has been extensively discussed in earlier chapters and summarized below:

In Chapter 1, we presented a broad introduction to modern cosmology and the observational foundations of the standard ΛCDM model. We reviewed the basic framework of homogeneous and isotropic cosmology, the Friedmann equations, and the thermal history of the Universe, together with the key distance measures and

horizon scales relevant for precision cosmology. We then discussed the main cosmological probes, namely the CMB, BAO, and Type Ia supernovae, and summarized the emerging anomalies and tensions that motivate physics beyond ΛCDM and gave an overview on possible candidates of dark matter and dark energy. This chapter set the conceptual and observational context for the thesis, highlighting the role of the dark sector and motivating the exploration of early-time modifications of dark matter and late-time dynamics of dark energy.

In Chapter 2, we overviewed the statistical framework used throughout the thesis. We introduced the Bayesian approach to parameter inference, discussed the construction of likelihoods, and reviewed the role of priors, marginalization, and model comparison using Akaike information criteria. We presented the principles of Markov Chain Monte Carlo sampling, convergence diagnostics, and the analysis of correlated chains, together with practical aspects of goodness-of-fit and confidence-region estimation. This chapter established the methodological backbone for all subsequent analyses in the thesis.

In Chapter 3, we first examined whether the assumption of cold, non-relativistic dark matter prior to recombination is directly required by existing data. In the mass-varying dark matter (MVDM) framework, the dark matter mass was allowed to undergo an instantaneous transition from a relativistic to a non-relativistic phase at high redshift, described phenomenologically without committing to a specific particle-physics realization. The large free-streaming velocity during the relativistic phase suppresses power on small scales and modifies both the CMB anisotropies and the late-time clustering amplitude. A Bayesian analysis using Planck and ACT data, supplemented by BAO, supernovae, and weak-lensing priors, yielded a lower bound on the transition redshift and a mild preference for an eV-scale dark matter mass. While Planck data alone provide limited sensitivity at high multipoles, the inclusion of ACT significantly improved the constraints,

highlighting the importance of small-scale CMB measurements for probing early-time dark matter properties. The inclusion of weak-lensing priors further reduced the inferred value of S_8, demonstrating that early-time departures from cold dark matter can partially alleviate the S_8 tension.

In Chapter 4, building on the phenomenological framework in the previous chapter, we then constructed a concrete microscopic realization in which a Yukawa-type interaction between scalar and dark matter fermion leads to late-forming primordial black holes (PBHs) within the BBN and CMB epochs. In this scenario, dark matter becomes non-relativistic at $z \sim 10^6$, triggering an exponential growth of perturbations in the radiation-dominated era due to a force stronger than gravity. This mechanism naturally produces a population of early dense halos that cool through scalar radiation and collapse into PBHs with masses in the sublunar window, $10^{-16} - 10^{-14} M_\odot$. We derived the PBH mass function using a detailed treatment of halo formation and collapse, showing that it is narrow and that these PBHs can, in principle, constitute nearly the entire dark matter abundance while remaining consistent with current constraints.

In Chapter 5, the second part of the thesis, the same class of Yukawa-type scalar–fermion interactions was explored in the context of late-time cosmic acceleration. We first studied an interacting quintessence scenario in which the scalar field retains non-zero kinetic energy at the present epoch. Due to the interaction, an agnostic observer measures the evolution of the effective equation of state instead of the microscopic one. This allows the effective dark energy equation of state $w_{\rm eff}$ to cross the phantom divide while maintaining $w_\phi > -1$ at all times. Solving the modified Klein–Gordon equation for both exponential and polynomial potentials, we showed that the model can reproduce the qualitative features suggested by DESI, including early phantom behavior followed by a transition to $w_{\rm eff} > -1$ today. Although the present analysis was restricted to background evolution, it demonstrated that interacting dark energy with finite kinetic energy provides a

theoretically consistent mechanism for phantom crossing without invoking fundamental instabilities.

Finally in Chapter 6, we performed a full MCMC analysis of the chameleon model in which the scalar field settles at the evolving minimum of an effective potential with vanishing velocity today. Using combinations of Planck, SDSS BAO, DESI DR2 BAO, Pantheon+, and SH_0ES data, we obtained fully constrained posteriors for the interaction strength β without invoking any empirical sign-switching mechanisms or additional exotic assumptions. In particular, dataset combinations including DESI DR2 BAO or SH_0ES showed a mild preference for a non-zero coupling, with $\beta \sim 0.25 - 0.33$, and weak-to-positive statistical evidence relative to ΛCDM. Although the resulting present-day equation of state remains close to -1 due to zero velocity of the field today, the scalar dynamics exhibit phantom crossing near $z \sim 0.5$, in qualitative agreement with the DESI reconstruction. These results provide one of the most economical realizations of interacting dark energy compatible with current data.

7.2 Future Work

The results of this thesis naturally motivate several directions for future work, aimed at extending the present analysis beyond linear theory and background evolution to the fully non-linear regime and to upcoming high-precision datasets.

First, a non-linear investigation of the MVDM scenario using cosmological N-body simulations. The suppression of small-scale power induced by an early relativistic phase of dark matter directly impacts the Lyman-α forest and the internal structure of halos. Dedicated simulations, combined with emulator-based inference, would allow a joint analysis of CMB, galaxy clustering, and Lyman-α data

in a self-consistent framework. Such an approach could tighten the bound on the transition redshift and the dark matter mass.

Second, the late-forming PBH scenario provides a direct connection to current JWST observations of early structure formation. Since multiple PBHs can form in a single horizon, leading to early halo formation, this may have significant implications for the formation of the first stars and galaxies. A systematic study of the impact of these PBHs on high-redshift luminosity functions and the abundance of massive halos could be directly confronted with recent JWST observations. In parallel, incorporating the PBH formation that leads to the generation of scalar-induced stochastic gravitational waves can be worth considering for detection by future gravitational-wave detectors. This would provide an independent test of the formation mechanism.

Third, the interacting dark energy model discussed in Chapter 5, needs full implementation in Boltzmann code CLASS both in terms of background and perturbation; and an extensive MCMC analysis is required to perform to check whether the model can better fit DESI datasets and whether favoured strongly compared to ΛCDM compared to the extended model discussed in Chapter 6.

Fourth, the interacting dark energy models studied here call for a full treatment of cosmological perturbations and non-linear structure formation. The best-fit interaction strengths inferred from linear data imply order-unity modifications to the effective gravitational coupling in the transition regime. This naturally motivates the development of dedicated N-body simulations implementing chameleon interactions, with separate force laws for baryons and dark matter. Within this framework, one can search for robust, model-independent signatures such as differential infall, modified halo profiles, and scale-dependent galaxy bias. A particularly promising avenue is the application of the Effective Field Theory of Large-Scale Structure to interacting dark energy. By combining EFT predictions with DESI,

Euclid, and LSST full-shape clustering data, it may become possible to distinguish dark-sector interactions from standard modified gravity or massive neutrino effects in a controlled and systematic way.

Finally, embedding the phenomenological interactions studied in this thesis within a consistent particle-physics framework remains an important open problem. Constructing ultraviolet-complete models that generate the required Yukawa couplings while remaining stable under quantum corrections would provide a crucial link between cosmological observations and fundamental theory.

In summary, this thesis has shown that dark-sector interactions provide a flexible and testable framework capable of addressing both early- and late-time cosmological anomalies. With the advent of next-generation surveys and precision simulations, the coming decade offers a realistic prospect of determining whether these interactions represent a genuine extension of the standard cosmological model or a transient explanation for statistical fluctuations in current data.

✣ ✣ ✣ ✣

Bibliography

Abazajian, K., et al. 2022, Snowmass 2021 CMB-S4 White Paper. https://arxiv.org/abs/2203.08024

Abazajian, K. N., et al. 2015, Astropart. Phys., 63, 66, doi: 10.1016/j.astropartphys.2014.05.014

—. 2016, CMB-S4 Science Book, First Edition. https://arxiv.org/abs/1610.02743

Abbott, T. M. C., Abdalla, F. B., Avila, S., & et. al. 2019, Phys. Rev. D, 99, 123505, doi: 10.1103/PhysRevD.99.123505

Abbott, T. M. C., et al. 2022, Phys. Rev. D, 105, 023520, doi: 10.1103/PhysRevD.105.023520

Abbott *et al.*, T. M. C. 2018, Phys. Rev. D, 98, 043526, doi: 10.1103/PhysRevD.98.043526

Abdalla, E., et al. 2022, JHEAp, 34, 49, doi: 10.1016/j.jheap.2022.04.002

Abdul-Karim, M., Aguilar, J., et al. 2025, DESI DR2 Results II: Measurements of Baryon Acoustic Oscillations and Cosmological Constraints. https://arxiv.org/abs/2503.14738

Abdul Karim, M., et al. 2025. https://arxiv.org/abs/2503.14738

Abellán, G. F., Murgia, R., & Poulin, V. 2021, Phys. Rev. D, 104, 123533, doi: 10.1103/PhysRevD.104.123533

Abellán, G. F., Murgia, R., Poulin, V., & Lavalle, J. 2022, Phys. Rev. D, 105, 063525, doi: 10.1103/PhysRevD.105.063525

Adame, A., et al. 2025, Journal of Cosmology and Astroparticle Physics, 2025, 021, doi: 10.1088/1475-7516/2025/02/021

Adame, A. G., et al. 2024. https://arxiv.org/abs/2404.03002

Afshordi, N., Zaldarriaga, M., & Kohri, K. 2005, Phys. Rev. D, 72, 065024, doi: 10.1103/PhysRevD.72.065024

Agarwal, S., Corasaniti, P. S., Das, S., & Rasera, Y. 2015, Phys. Rev. D, 92, 063502, doi: 10.1103/PhysRevD.92.063502

Aghanim, N., et al. 2020, Astron. Astrophys., 641, A6, doi: 10.1051/0004-6361/201833910

Aiola, S., et al. 2020, Journal of Cosmology and Astroparticle Physics, 2020, 047, doi: 10.1088/1475-7516/2020/12/047

Akaike, H. 1974, IEEE Transactions on Automatic Control, 19, 716, doi: 10.1109/TAC.1974.1100705

Alam, S., Ata, M., Bailey, S., & et. al. 2017a, Monthly Notices of the Royal Astronomical Society, 470, 2617–2652, doi: 10.1093/mnras/stx721

Alam, S., Aubert, M., Avila, S., & et. al. 2021, Phys. Rev. D, 103, 083533, doi: 10.1103/PhysRevD.103.083533

Alam, S., et al. 2017b, Monthly Notices of the Royal Astronomical Society, 470, 2617, doi: 10.1093/mnras/stx721

Alexander, S., Bernardo, H., & Toomey, M. W. 2023, Journal of Cosmology and Astroparticle Physics, 2023, 037, doi: 10.1088/1475-7516/2023/03/037

Amendola, L. 2000, Phys. Rev. D, 62, 043511, doi: 10.1103/PhysRevD.62.043511

—. 2001, Phys. Rev. Lett., 86, 196, doi: 10.1103/PhysRevLett.86.196

Amendola, L., & Quercellini, C. 2003a, Phys. Rev. D, 68, 023514, doi: 10.1103/PhysRevD.68.023514

—. 2003b, Phys. Rev. D, 68, 023514, doi: 10.1103/PhysRevD.68.023514

Amendola, L., Quercellini, C., Tocchini-Valentini, D., & Pasqui, A. 2003a, Astrophys. J. Lett., 583, L53, doi: 10.1086/368064

—. 2003b, The Astrophysical Journal, 583, L53, doi: 10.1086/368064

Amendola, L., Rubio, J., & Wetterich, C. 2018, Phys. Rev. D, 97, 081302, doi: 10.1103/PhysRevD.97.081302

Amendola, L., & Tocchini-Valentini, D. 2001, Phys. Rev. D, 64, 043509, doi: 10.1103/PhysRevD.64.043509

Amendola, L., & Tsujikawa, S. 2020, Journal of Cosmology and Astroparticle Physics, 2020, 020, doi: 10.1088/1475-7516/2020/06/020

Amon, A., et al. 2022, Phys. Rev. D, 105, 023514, doi: 10.1103/PhysRevD.105.023514

Anderson, G. W., & Carroll, S. M. 1998, in COSMO-97 (WORLD SCIENTIFIC), doi: 10.1142/9789814447263_0025

Archidiacono, M., Hooper, D. C., Murgia, R., et al. 2019, Journal of Cosmology and Astroparticle Physics, 2019, 055, doi: 10.1088/1475-7516/2019/10/055

Asgari, Marika, et al. 2021, A&A, 645, A104, doi: 10.1051/0004-6361/202039070

Ashoorioon, A., Casadio, R., Cicoli, M., Geshnizjani, G., & Kim, H. J. 2018, Journal of High Energy Physics, 2018, 172, doi: 10.1007/JHEP02(2018)172

Ashoorioon, A., Rostami, A., & Firouzjaee, J. T. 2021, Journal of High Energy Physics, 2021, 87, doi: 10.1007/JHEP07(2021)087

Bachega, R. R., Costa, A. A., Abdalla, E., & Fornazier, K. 2020, Journal of Cosmology and Astroparticle Physics, 2020, 021, doi: 10.1088/1475-7516/2020/05/021

Baker, M. J., Breitbach, M., Kopp, J., & Mittnacht, L. 2021, Primordial Black Holes from First-Order Cosmological Phase Transitions

Baker, O., Afanasev, A., Lagouri, T., & et. al. 2022, Symmetry, 14, 2238, doi: 10.3390/sym14112238

Balazs, C., Bringmann, T., Kahlhoefer, F., & White, M. 2026, Astrophysics, 5, 17, doi: 10.1016/B978-0-443-21439-4.00070-5

Ballesteros, G., & Taoso, M. 2018, Phys. Rev. D, 97, 023501, doi: 10.1103/PhysRevD.97.023501

Bamba, K., Capozziello, S., Nojiri, S., & Odintsov, S. D. 2012, Astrophys. Space Sci., 342, 155, doi: 10.1007/s10509-012-1181-8

Banerjee, A., Cai, H., Heisenberg, L., et al. 2021, Phys. Rev. D, 103, L081305, doi: 10.1103/PhysRevD.103.L081305

Barkana, R., & Loeb, A. 2001, Phys. Rept., 349, 125, doi: 10.1016/S0370-1573(01)00019-9

Barrow, J. D., & Kittou, G. 2020, Eur. Phys. J. C, 80, 120, doi: 10.1140/epjc/s10052-020-7642-2

Baudis, L. 2014, Physics of the Dark Universe, 4, 50, doi: https://doi.org/10.1016/j.dark.2014.07.001

Baur, J., Palanque-Delabrouille, N., Yèche, C., et al. 2017, Journal of Cosmology and Astroparticle Physics, 2017, 013, doi: 10.1088/1475-7516/2017/12/013

Bean, R. 2001, Phys. Rev. D, 64, 123516, doi: 10.1103/PhysRevD.64.123516

Becker, N., Hooper, D. C., Kahlhoefer, F., Lesgourgues, J., & Schöneberg, N. 2021, Journal of Cosmology and Astroparticle Physics, 2021, 019, doi: 10.1088/1475-7516/2021/02/019

Bedroya, A., Obied, G., Vafa, C., & Wu, D. H. 2025. https://arxiv.org/abs/2507.03090

Benisty, D., Brax, P., & Davis, A.-C. 2023a, Phys. Rev. D, 107, 064049, doi: 10.1103/PhysRevD.107.064049

—. 2023b, Phys. Rev. D, 108, 063031, doi: 10.1103/PhysRevD.108.063031

Benisty, D., & Davis, A.-C. 2022, Phys. Rev. D, 105, 024052, doi: 10.1103/PhysRevD.105.024052

Benisty, D., Guendelman, E. I., Nissimov, E., & Pacheva, S. 2020a, Symmetry, 12, doi: 10.3390/sym12030481

Benisty, D., Guendemlan, E. I., Nissimov, E., & Pacheva, S. 2020b, Int. J. Mod. Phys. D, 26, 2050104, doi: 10.1142/S0218271820501047

Berbig, M. 2025, JCAP, 03, 015, doi: 10.1088/1475-7516/2025/03/015

Berghaus, K. V., Kable, J. A., & Miranda, V. 2024, Phys. Rev. D, 110, 103524, doi: 10.1103/PhysRevD.110.103524

Bertone, G., & Tait, T. M. P. 2018, Nature, 562, 51, doi: 10.1038/s41586-018-0542-z

Beutler, F., Blake, C., Colless, M., & et. al. 2011a, Monthly Notices of the Royal Astronomical Society, 416, 3017–3032, doi: 10.1111/j.1365-2966.2011.19250.x

Beutler, F., et al. 2011b, Monthly Notices of the Royal Astronomical Society, 416, 3017, doi: 10.1111/j.1365-2966.2011.19250.x

Bhattacharya, S., Borghetto, G., Malhotra, A., et al. 2024a, JCAP, 09, 073, doi: 10.1088/1475-7516/2024/09/073

—. 2024b. https://arxiv.org/abs/2410.21243

Bhattacharya, S., Das, A., & Dutta, K. 2021a, Journal of Cosmology and Astroparticle Physics, 2021, 071, doi: 10.1088/1475-7516/2021/10/071

—. 2021b, JCAP, 10, 071, doi: 10.1088/1475-7516/2021/10/071

Bird, S., Cholis, I., Muñoz, J. B., et al. 2016, Phys. Rev. Lett., 116, 201301, doi: 10.1103/PhysRevLett.116.201301

Blas, D., Lesgourgues, J., & Tram, T. 2011, Journal of Cosmology and Astroparticle Physics, 2011, 034, doi: 10.1088/1475-7516/2011/07/034

Blas, D., Lesgourgues, J., & Tram, T. 2011, Journal of Cosmology and Astroparticle Physics, 2011, 034, doi: 10.1088/1475-7516/2011/07/034

Blinov, N., Keith, C., & Hooper, D. 2020, Journal of Cosmology and Astroparticle Physics, 2020, 005, doi: 10.1088/1475-7516/2020/06/005

Bolotin, Y. L., Kostenko, A., Lemets, O. A., & Yerokhin, D. A. 2014, Int. J. Mod. Phys. D, 24, 1530007, doi: 10.1142/S0218271815300074

Boriero, D., Das, S., & Wong, Y. Y. 2015a, Journal of Cosmology and Astroparticle Physics, 2015, 033, doi: 10.1088/1475-7516/2015/07/033

Boriero, D., Das, S., & Wong, Y. Y. Y. 2015b, JCAP, 07, 033, doi: 10.1088/1475-7516/2015/07/033

Brax, P., Burgess, C. P., & Quevedo, F. 2023, JCAP, 08, 011, doi: 10.1088/1475-7516/2023/08/011

—. 2024, JCAP, 03, 015, doi: 10.1088/1475-7516/2024/03/015

Brax, P., van de Bruck, C., Davis, A., & Green, A. 2006, Physics Letters B, 633, 441, doi: https://doi.org/10.1016/j.physletb.2005.12.055

Brax, P., van de Bruck, C., Davis, A.-C., & et. al. 2004, Phys. Rev. D, 70, 123518, doi: 10.1103/PhysRevD.70.123518

Brinckmann, T., & Lesgourgues, J. 2018, MontePython 3: boosted MCMC sampler and other features. https://arxiv.org/abs/1804.07261

Brout, D., et al. 2022, The Astrophysical Journal, 938, 110, doi: 10.3847/1538-4357/ac8e04

Brouzakis, N., & Tetradis, N. 2006, JCAP, 01, 004, doi: 10.1088/1475-7516/2006/01/004

Burgess, C., & Quevedo, F. 2022, Journal of Cosmology and Astroparticle Physics, 2022, 007, doi: 10.1088/1475-7516/2022/04/007

Byrnes, C. T., Hindmarsh, M., Young, S., & Hawkins, M. R. 2018, Journal of Cosmology and Astroparticle Physics, 2018, 041–041, doi: 10.1088/1475-7516/2018/08/041

Cahn, R. N., de Putter, R., & Linder, E. V. 2008, Journal of Cosmology and Astroparticle Physics, 2008, 015, doi: 10.1088/1475-7516/2008/11/015

Cai, R.-G., Guo, Z.-K., Li, L., Wang, S.-J., & Yu, W.-W. 2021, Phys. Rev. D, 103, 121302, doi: 10.1103/PhysRevD.103.L121302

Cai, Y.-F., Saridakis, E. N., Setare, M. R., & Xia, J.-Q. 2010, Physics Reports, 493, 1, doi: https://doi.org/10.1016/j.physrep.2010.04.001

Calderon, R., et al. 2024, Journal of Cosmology and Astroparticle Physics, 2024, 048, doi: 10.1088/1475-7516/2024/10/048

Caldwell, R. 2002, Physics Letters B, 545, 23, doi: https://doi.org/10.1016/S0370-2693(02)02589-3

Caldwell, R. R., Dave, R., & Steinhardt, P. J. 1998, Phys. Rev. Lett., 80, 1582, doi: 10.1103/PhysRevLett.80.1582

Caldwell, R. R., Kamionkowski, M., & Weinberg, N. N. 2003, Phys. Rev. Lett., 91, 071301, doi: 10.1103/PhysRevLett.91.071301

Caldwell, R. R., Komp, W., Parker, L., & Vanzella, D. A. T. 2006, Phys. Rev. D, 73, 023513, doi: 10.1103/PhysRevD.73.023513

Caldwell, R. R., & Linder, E. V. 2005, Phys. Rev. Lett., 95, 141301, doi: 10.1103/PhysRevLett.95.141301

Cappelluti, N., Hasinger, G., & Natarajan, P. 2022, *Astrophys. J.*, 926, 205, doi: 10.3847/1538-4357/ac332d

Carr, B., Kohri, K., Sendouda, Y., & Yokoyama, J. 2021, Reports on Progress in Physics, 84, 116902, doi: 10.1088/1361-6633/ac1e31

Carr, B., Kohri, K., Sendouda, Y., & Yokoyama, J. 2021a, Reports on Progress in Physics, 84, 116902, doi: 10.1088/1361-6633/ac1e31

Carr, B., & Kühnel, F. 2020, Annual Review of Nuclear and Particle Science, 70, 355, doi: 10.1146/annurev-nucl-050520-125911

Carr, B., Kühnel, F., & Visinelli, L. 2021b, *Mon. Not. Roy. Astron. Soc.*, 501, 2029, doi: 10.1093/mnras/staa3651

Carr, B., Raidal, M., Tenkanen, T., Vaskonen, V., & Veermäe, H. 2017, Phys. Rev. D, 96, 023514, doi: 10.1103/PhysRevD.96.023514

Carr, B. J. 1975, *Astrophys. J.*, 201, 1, doi: 10.1086/153853

Carr, B. J., & Hawking, S. W. 1974, Monthly Notices of the Royal Astronomical Society, 168, 399, doi: 10.1093/mnras/168.2.399

Carr, B. J., & Lidsey, J. E. 1993, Phys. Rev. D, 48, 543, doi: 10.1103/PhysRevD.48.543

Carroll, S. M. 2019, Spacetime and Geometry: An Introduction to General Relativity (Cambridge University Press)

Casas, J. A., Garcia-Bellido, J., & Quiros, M. 1992, Classical and Quantum Gravity, 9, 1371–1384, doi: 10.1088/0264-9381/9/5/018

Chakraborty, A., Chanda, P. K., Das, S., & Dutta, K. 2025a, JCAP, 11, 047, doi: 10.1088/1475-7516/2025/11/047

—. 2025b, DESI results: Hint towards coupled dark matter and dark energy. https://arxiv.org/abs/2503.10806

Chakraborty, A., Chanda, P. K., Pandey, K. L., & Das, S. 2022a, The Astrophysical Journal, 932, 119, doi: 10.3847/1538-4357/ac6ddd

—. 2022b, Astrophys. J., 932, 119, doi: 10.3847/1538-4357/ac6ddd

Chakraborty, A., Das, A., Das, S., & Sethi, S. K. 2025c, Phys. Rev. D, 111, 063515, doi: 10.1103/PhysRevD.111.063515

Chakraborty, A., Ray, T., Das, S., Banerjee, A., & Ganesan, V. 2026, Astrophys. J., 998, 83, doi: 10.3847/1538-4357/ae2ff8

Chamings, F. N., Avgoustidis, A., Copeland, E. J., Green, A. M., & Pourtsidou, A. 2020, Phys. Rev. D, 101, 043531, doi: 10.1103/PhysRevD.101.043531

Chanda, P. K., & Das, S. 2017, Phys. Rev. D, 95, 083008, doi: 10.1103/PhysRevD.95.083008

Chen, C.-Y. 2020, International Journal of Modern Physics D, 30, 2150010, doi: 10.1142/s0218271821500103

Chevallier, M., & Polarski, D. 2001, Int. J. Mod. Phys. D, 10, 213, doi: 10.1142/S0218271801000822

Chimento, L. P., Jakubi, A. S., Pavón, D., & Zimdahl, W. 2003, Phys. Rev. D, 67, 083513, doi: 10.1103/PhysRevD.67.083513

Choptuik, M. W. 1993, Phys. Rev. Lett., 70, 9, doi: 10.1103/PhysRevLett.70.9

Choptuik, M. W. 1993, Phys. Rev. Lett., 70, 9, doi: 10.1103/PhysRevLett.70.9

Chudaykin, A., & Kunz, M. 2024, Phys. Rev. D, 110, 123524, doi: 10.1103/PhysRevD.110.123524

Chudaykin, A., Kunz, M., & Carron, J. 2025. https://arxiv.org/abs/2503.09893

Clark, S. J., Vattis, K., & Koushiappas, S. M. 2021, Phys. Rev. D, 103, 043014, doi: 10.1103/PhysRevD.103.043014

Clesse, S., & García-Bellido, J. 2015, Phys. Rev. D, 92, 023524, doi: 10.1103/PhysRevD.92.023524

Colgáin, E. O., & Sheikh-Jabbari, M. M. 2024. https://arxiv.org/abs/2412.12905

Comelli, D., Pietroni, M., & Riotto, A. 2003, Physics Letters B, 571, 115–120, doi: 10.1016/j.physletb.2003.05.006

Copeland, E. J., Sami, M., & Tsujikawa, S. 2006a, Int. J. Mod. Phys. D, 15, 1753, doi: 10.1142/S021827180600942X

—. 2006b, International Journal of Modern Physics D, 15, 1753–1935, doi: 10.1142/s021827180600942x

Corasaniti, P. S. 2008, Phys. Rev. D, 78, 083538, doi: 10.1103/PhysRevD.78.083538

Cortês, M., & Liddle, A. R. 2024, JCAP, 12, 007, doi: 10.1088/1475-7516/2024/12/007

Cotner, E., & Kusenko, A. 2017a, Phys. Rev. Lett., 119, 031103, doi: 10.1103/PhysRevLett.119.031103

—. 2017b, Phys. Rev. D, 96, 103002, doi: 10.1103/PhysRevD.96.103002

Cotner, E., Kusenko, A., Sasaki, M., & Takhistov, V. 2019, Journal of Cosmology and Astroparticle Physics, 2019, 077, doi: 10.1088/1475-7516/2019/10/077

Cotner, E., Kusenko, A., & Takhistov, V. 2018, Phys. Rev. D, 98, 083513, doi: 10.1103/PhysRevD.98.083513

Crawford, M., & Schramm, D. N. 1982, *Nature*, 298, 538, doi: 10.1038/298538a0

Dalal, N., & Kravtsov, A. 2022, Phys. Rev. D, 106, 063517, doi: 10.1103/PhysRevD.106.063517

Dalal, R., Li, X., Nicola, A., & et. al. 2023, Phys. Rev. D, 108, 123519, doi: 10.1103/PhysRevD.108.123519

D'Amico, G., Senatore, L., & Zhang, P. 2021, Journal of Cosmology and Astroparticle Physics, 2021, 006, doi: 10.1088/1475-7516/2021/01/006

Damour, T., Gibbons, G. W., & Gundlach, C. 1990, Phys. Rev. Lett., 64, 123, doi: 10.1103/PhysRevLett.64.123

Damour, T., Piazza, F., & Veneziano, G. 2002, Phys. Rev. Lett., 89, 081601, doi: 10.1103/PhysRevLett.89.081601

Damour, T., & Polyakov, A. 1994a, Nuclear Physics B, 423, 532–558, doi: 10.1016/0550-3213(94)90143-0

Damour, T., & Polyakov, A. M. 1994b, Nucl. Phys. B, 423, 532, doi: 10.1016/0550-3213(94)90143-0

Das, A., Das, S., & Sethi, S. K. 2023, Phys. Rev. D, 108, 083501, doi: 10.1103/PhysRevD.108.083501

Das, A., Dasgupta, B., & Khatri, R. 2019, JCAP, 04, 018, doi: 10.1088/1475-7516/2019/04/018

Das, S., Corasaniti, P. S., & Khoury, J. 2006a, Phys. Rev. D, 73, 083509, doi: 10.1103/PhysRevD.73.083509

—. 2006b, Phys. Rev. D, 73, 083509, doi: 10.1103/PhysRevD.73.083509

Das, S., Maharana, A., & Muia, F. 2021. https://arxiv.org/abs/2112.11486

Das, S., & Nadler, E. O. 2021a, Phys. Rev. D, 103, 043517, doi: 10.1103/PhysRevD.103.043517

—. 2021b, Phys. Rev. D, 103, 043517, doi: 10.1103/PhysRevD.103.043517

Das, S., & Weiner, N. 2011, Phys. Rev. D, 84, 123511, doi: 10.1103/PhysRevD.84.123511

Dasgupta, B., Laha, R., & Ray, A. 2020, Phys. Rev. Lett., 125, 101101, doi: 10.1103/PhysRevLett.125.101101

de Souza, J. S. T., Vicente, G. S., & Graef, L. L. 2024. https://arxiv.org/abs/2403.04970

Defillon, G., Granet, E., Tinyakov, P., & Tytgat, M. H. G. 2014, Phys. Rev. D, 90, 103522, doi: 10.1103/PhysRevD.90.103522

Di Valentino, E., Linder, E. V., & Melchiorri, A. 2018, Phys. Rev. D, 97, 043528, doi: 10.1103/PhysRevD.97.043528

Di Valentino, E., Melchiorri, A., Mena, O., Pan, S., & Yang, W. 2021, Monthly Notices of the Royal Astronomical Society: Letters, 502, L23, doi: 10.1093/mnrasl/slaa207

Di Valentino, E., Melchiorri, A., Mena, O., & Vagnozzi, S. 2020, Physics of the Dark Universe, 30, 100666, doi: https://doi.org/10.1016/j.dark.2020.100666

Di Valentino, E., Melchiorri, A., Mena, O., & Vagnozzi, S. 2020, Phys. Rev. D, 101, 063502, doi: 10.1103/PhysRevD.101.063502

Di Valentino, E., et al. 2025, Phys. Dark Univ., 49, 101965, doi: 10.1016/j.dark.2025.101965

Dutta Chowdhury, D., van den Bosch, F. C., van Dokkum, P., et al. 2023, The Astrophysical Journal, 949, 68, doi: 10.3847/1538-4357/acc73d

Einstein, A. 1916, Annalen der Physik, 354, 769, doi: https://doi.org/10.1002/andp.19163540702

Englert, F., & Brout, R. 1964, Phys. Rev. Lett., 13, 321, doi: 10.1103/PhysRevLett.13.321

Enqvist, K., Nadathur, S., Sekiguchi, T., & Takahashi, T. 2015, Journal of Cosmology and Astroparticle Physics, 2015, 067, doi: 10.1088/1475-7516/2015/09/067

Enzi, W., Murgia, R., Newton, O., et al. 2021, Monthly Notices of the Royal Astronomical Society, 506, 5848, doi: 10.1093/mnras/stab1960

Ezquiaga, J. M., García-Bellido, J., & Ruiz Morales, E. 2018, Physics Letters B, 776, 345, doi: 10.1016/j.physletb.2017.11.039

Fardon, R., Nelson, A. E., & Weiner, N. 2004, JCAP, 10, 005, doi: 10.1088/1475-7516/2004/10/005

—. 2006, Journal of High Energy Physics, 2006, 042–042, doi: 10.1088/1126-6708/2006/03/042

Farrar, G. R., & Peebles, P. J. E. 2004, The Astrophysical Journal, 604, 1–11, doi: 10.1086/381728

Ferrari, A. G., Ballardini, M., Finelli, F., & Paoletti, D. 2025. https://arxiv.org/abs/2501.15298

Fields, B., & Sarkar, S. 2006. https://arxiv.org/abs/astro-ph/0601514

Fikri, R., ElKhateeb, E., Lashin, E. S., & El Hanafy, W. 2024. https://arxiv.org/abs/2411.19362

Flores, M. M., & Kusenko, A. 2021a, Phys. Rev. Lett., 126, 041101, doi: 10.1103/PhysRevLett.126.041101

—. 2021b, Phys. Rev. D, 104, 063008, doi: 10.1103/PhysRevD.104.063008

Franciolini, G., Kehagias, A., Matarrese, S., & Riotto, A. 2018, Journal of Cosmology and Astroparticle Physics, 2018, 016, doi: 10.1088/1475-7516/2018/03/016

França, U., & Rosenfeld, R. 2004, Phys. Rev. D, 69, 063517, doi: 10.1103/PhysRevD.69.063517

Freedman, W. L. 2017, Nature Astronomy, 1, 0121, doi: 10.1038/s41550-017-0121

Freeman, K. C. 1970, *Astrophys. J.*, 160, 811, doi: 10.1086/150474

Friedmann, A. 1924, Zeitschrift für Physik, 21, 326, doi: 10.1007/BF01328280

Ganesan, V., Chakraborty, A., Ray, T., Das, S., & Banerjee, A. 2024. https://arxiv.org/abs/2403.14247

Gao, Q., Peng, Z., Gao, S., & Gong, Y. 2025, Universe, 11, doi: 10.3390/universe11010010

García-Bellido, J., Linde, A., & Wands, D. 1996, Phys. Rev. D, 54, 6040, doi: 10.1103/PhysRevD.54.6040

García-Bellido, J., & Ruiz Morales, E. 2017, Physics of the Dark Universe, 18, 47, doi: 10.1016/j.dark.2017.09.007

Gelman, A., & Rubin, D. B. 1992a, Statistical Science, 7, 457. http://www.jstor.org/stable/2246093

—. 1992b, Statistical Science, 7, 457 , doi: 10.1214/ss/1177011136

Gialamas, I. D., Hütsi, G., Kannike, K., et al. 2025, Phys. Rev. D, 111, 043540, doi: 10.1103/PhysRevD.111.043540

Giarè, W., Najafi, M., Pan, S., Di Valentino, E., & Firouzjaee, J. T. 2024a, JCAP, 10, 035, doi: 10.1088/1475-7516/2024/10/035

Giarè, W., Sabogal, M. A., Nunes, R. C., & Di Valentino, E. 2024b, Phys. Rev. Lett., 133, 251003, doi: 10.1103/PhysRevLett.133.251003

—. 2024c, Phys. Rev. Lett., 133, 251003, doi: 10.1103/PhysRevLett.133.251003

Gogoi, A., Sharma, R. K., Chanda, P., & Das, S. 2021, Astrophys. J., 915, 132, doi: 10.3847/1538-4357/abfe5b

Goh, L. W. K., Gómez-Valent, A., Pettorino, V., & Kilbinger, M. 2023, Phys. Rev. D, 107, 083503, doi: 10.1103/PhysRevD.107.083503

Gómez-Valent, A., Pettorino, V., & Amendola, L. 2020, Phys. Rev. D, 101, 123513, doi: 10.1103/PhysRevD.101.123513

Gómez-Valent, A., Zheng, Z., Amendola, L., Wetterich, C., & Pettorino, V. 2022, Phys. Rev. D, 106, 103522, doi: 10.1103/PhysRevD.106.103522

Green, A. M., & Liddle, A. R. 1999, Phys. Rev. D, 60, 063509, doi: 10.1103/PhysRevD.60.063509

Gross, C., Landini, G., Strumia, A., & Teresi, D. 2021, Journal of High Energy Physics, 2021, 33

Gross, D. J., & Wilczek, F. 1973, Phys. Rev. D, 8, 3633, doi: 10.1103/PhysRevD.8.3633

Gubser, S. S., & Khoury, J. 2004, Physical Review D, 70. http://dx.doi.org/10.1103/PhysRevD.70.104001

Guo, Z.-K., Piao, Y.-S., Zhang, X., & Zhang, Y.-Z. 2005, Physics Letters B, 608, 177, doi: https://doi.org/10.1016/j.physletb.2005.01.017

Guralnik, G. S., Hagen, C. R., & Kibble, T. W. B. 1964, Phys. Rev. Lett., 13, 585, doi: 10.1103/PhysRevLett.13.585

H. Hildebrandt *et al.* 2020, A&A, 633, A69, doi: 10.1051/0004-6361/201834878

Halder, S., de Haro, J., Saha, T., & Pan, S. 2024. https://arxiv.org/abs/2403.01397

Hannestad, S., & Madsen, J. 1995, Phys. Rev. D, 52, 1764, doi: 10.1103/PhysRevD.52.1764

Haridasu, B. S., & Viel, M. 2020, Monthly Notices of the Royal Astronomical Society, 497, 1757, doi: 10.1093/mnras/staa1991

Harvey, D., Massey, R., Kitching, T., Taylor, A., & Tittley, E. 2015, Science, 347, 1462, doi: 10.1126/science.1261381

Hastings, W. K. 1970, Biometrika, 57, 97, doi: 10.1093/biomet/57.1.97

Hawking, S. 1971, *Mon. Not. Roy. Astron. Soc.*, 152, 75, doi: 10.1093/mnras/152.1.75

Hawking, S. W. 1974, *Nature*, 248, 30, doi: 10.1038/248030a0

—. 1975, Communications in Mathematical Physics, 43, 199, doi: 10.1007/BF02345020

Hawking, S. W., Moss, I. G., & Stewart, J. M. 1982, Phys. Rev. D, 26, 2681, doi: 10.1103/PhysRevD.26.2681

Heavens, A. 2010, Statistical techniques in cosmology. https://arxiv.org/abs/0906.0664

Heckman, J. J., Ramadan, O. F., & Sakstein, J. 2025, Phys. Rev. D, 111, 023510, doi: 10.1103/PhysRevD.111.023510

Hernández-Almada, A., Mendoza-Martínez, M., García-Aspeitia, M. A., & Motta, V. 2024, Physics of the Dark Universe, 46, 101668, doi: https://doi.org/10.1016/j.dark.2024.101668

Heymans *et al.* 2013, Monthly Notices of the Royal Astronomical Society, 432, 2433, doi: 10.1093/mnras/stt601

Heymans *et al.*, C. 2021, A&A, 646, A140, doi: 10.1051/0004-6361/202039063

Higgs, P. 1964, Physics Letters, 12, 132, doi: https://doi.org/10.1016/0031-9163(64)91136-9

Hindmarsh, M., & Philipsen, O. 2005, Phys. Rev. D, 71, 087302, doi: 10.1103/PhysRevD.71.087302

Holm, E. B., Tram, T., & Hannestad, S. 2022, Journal of Cosmology and Astroparticle Physics, 2022, 044, doi: 10.1088/1475-7516/2022/08/044

Hu, W. 1998, Astrophys. J., 506, 485, doi: 10.1086/306274

Hu, W., Barkana, R., & Gruzinov, A. 2000, Phys. Rev. Lett., 85, 1158, doi: 10.1103/PhysRevLett.85.1158

Hu, W., Eisenstein, D. J., & Tegmark, M. 1998, Phys. Rev. Lett., 80, 5255, doi: 10.1103/PhysRevLett.80.5255

Huang, L., Cai, R.-G., & Wang, S.-J. 2025. https://arxiv.org/abs/2502.04212

Huey, G., & Wandelt, B. D. 2006, Physical Review D, 74. http://dx.doi.org/10.1103/PhysRevD.74.023519

Hütsi, G., Raidal, M., Vaskonen, V., & Veermäe, H. 2021, Journal of Cosmology and Astroparticle Physics, 2021, 068, doi: 10.1088/1475-7516/2021/03/068

Ibata, R., Nipoti, C., Sollima, A., et al. 2013, *Mon. Not. Roy. Astron. Soc.*, 428, 3648, doi: 10.1093/mnras/sts302

Ivanov, P., Naselsky, P., & Novikov, I. 1994, Phys. Rev. D, 50, 7173, doi: 10.1103/PhysRevD.50.7173

James, F., & Roos, M. 1975, Computer Physics Communications, 10, 343, doi: https://doi.org/10.1016/0010-4655(75)90039-9

Jedamzik, K. 1997, Phys. Rev. D, 55, R5871, doi: 10.1103/PhysRevD.55.R5871

—. 1998, Phys. Rep., 307, 155, doi: 10.1016/S0370-1573(98)00067-2

Jiang, J.-Q., Pedrotti, D., da Costa, S. S., & Vagnozzi, S. 2024, Phys. Rev. D, 110, 123519, doi: 10.1103/PhysRevD.110.123519

Käding, C., Pitschmann, M., & Voith, C. 2023, Eur. Phys. J. C, 83, 767, doi: 10.1140/epjc/s10052-023-11939-4

Kannike, K., Marzola, L., Raidal, M., & Veermäe, H. 2017, Journal of Cosmology and Astroparticle Physics, 2017, 020, doi: 10.1088/1475-7516/2017/09/020

Kapadia, S. J., Lal Pandey, K., Suyama, T., Kandhasamy, S., & Ajith, P. 2021, *Astrophys. J. Lett.*, 910, L4, doi: 10.3847/2041-8213/abe86e

Kapadia, S. J., Pandey, K. L., Suyama, T., & Ajith, P. 2020, Phys. Rev. D, 101, 123535, doi: 10.1103/PhysRevD.101.123535

Kaplan, D. B., Nelson, A. E., & Weiner, N. 2004, Phys. Rev. Lett., 93, 091801, doi: 10.1103/PhysRevLett.93.091801

Kapner, D. J., Cook, T. S., Adelberger, E. G., & et. al. 2007, Phys. Rev. Lett., 98, 021101, doi: 10.1103/PhysRevLett.98.021101

Karwal, T., Raveri, M., Jain, B., Khoury, J., & Trodden, M. 2021. https://arxiv.org/abs/2106.13290

Kase, R., & Tsujikawa, S. 2020a, Phys. Rev. D, 101, 063511, doi: 10.1103/PhysRevD.101.063511

—. 2020b, Physics Letters B, 804, 135400, doi: https://doi.org/10.1016/j.physletb.2020.135400

Katz, A., Kopp, J., Sibiryakov, S., & Xue, W. 2018, Journal of Cosmology and Astroparticle Physics, 2018, 005, doi: 10.1088/1475-7516/2018/12/005

Kawana, K., & Xie, K.-P. 2022, Physics Letters B, 824, 136791, doi: https://doi.org/10.1016/j.physletb.2021.136791

Kesden, M., & Kamionkowski, M. 2006, Physical Review D, 74, 083007. http://dx.doi.org/10.1103/PhysRevD.74.083007

Keselman, J. A., Nusser, A., & Peebles, P. J. E. 2009, Physical Review D, 80. http://dx.doi.org/10.1103/PhysRevD.80.063517

Khoury, J., Lin, M.-X., & Trodden, M. 2025, Phys. Rev. Lett., 135, 181001, doi: 10.1103/w4qb-plk8

Khoury, J., & Weltman, A. 2004a, Phys. Rev. Lett., 93, 171104, doi: 10.1103/PhysRevLett.93.171104

—. 2004b, Phys. Rev. D, 69, 044026, doi: 10.1103/PhysRevD.69.044026

—. 2004c, Phys. Rev. Lett., 93, 171104, doi: 10.1103/PhysRevLett.93.171104

Kodama, H., Sasaki, M., & Sato, K. 1982, Progress of Theoretical Physics, 68, 1979, doi: 10.1143/PTP.68.1979

Kogut, A., et al. 2003, Astrophys. J. Suppl., 148, 161, doi: 10.1086/377219

Konoplich, R. V., Rubin, S. G., Sakharov, A. S., & Khlopov, M. Y. 1998, Astronomy Letters, 24, 413

—. 1999, Physics of Atomic Nuclei, 62, 1593

Kreisch, C. D., Cyr-Racine, F.-Y., & Doré, O. 2020, Phys. Rev. D, 101, 123505, doi: 10.1103/PhysRevD.101.123505

Kumar, S., & Nunes, R. C. 2016, Phys. Rev. D, 94, 123511, doi: 10.1103/PhysRevD.94.123511

Kusenko, A., Sasaki, M., Sugiyama, S., et al. 2020, Phys. Rev. Lett., 125, 181304, doi: 10.1103/PhysRevLett.125.181304

La, D., & Steinhardt, P. 1989, Physics Letters, Section B: Nuclear, Elementary Particle and High-Energy Physics, 220, 375, doi: 10.1016/0370-2693(89)90890-3

Laha, R. 2019, Phys. Rev. Lett., 123, 251101, doi: 10.1103/PhysRevLett.123.251101

Laha, R., Muñoz, J. B., & Slatyer, T. R. 2020, Phys. Rev. D, 101, 123514, doi: 10.1103/PhysRevD.101.123514

Lee, B.-H., Lee, W., Colgáin, E. Ó., Sheikh-Jabbari, M. M., & Thakur, S. 2022, JCAP, 04, 004, doi: 10.1088/1475-7516/2022/04/004

Lee, T. D., & Pang, Y. 1987, Phys. Rev. D, 35, 3678, doi: 10.1103/PhysRevD.35.3678

Lemaître, A. G. 1931, Monthly Notices of the Royal Astronomical Society, 91, 483, doi: 10.1093/mnras/91.5.483

Lesgourgues, J. 2011. https://arxiv.org/abs/1104.2932

Lesgourgues, J. 2011, arXiv e-prints, arXiv:1104.2932. https://arxiv.org/abs/1104.2932

Lesgourgues, J., & Pastor, S. 2006, Phys. Rept., 429, 307, doi: 10.1016/j.physrep.2006.04.001

Lewis, A., Challinor, A., & Lasenby, A. 2000, The Astrophysical Journal, 538, 473, doi: 10.1086/309179

Lewis, A., & Chamberlain, E. 2024. https://arxiv.org/abs/2412.13894

Li, C., Ren, X., Khurshudyan, M., & Cai, Y.-F. 2020a, Physics Letters B, 801, 135141, doi: https://doi.org/10.1016/j.physletb.2019.135141

Li, H.-L., He, D.-Z., Zhang, J.-F., & Zhang, X. 2020b, Journal of Cosmology and Astroparticle Physics, 2020, 038, doi: 10.1088/1475-7516/2020/06/038

Li, T.-N., Du, G.-H., Li, Y.-H., et al. 2025. https://arxiv.org/abs/2501.07361

Li, T.-N., Wu, P.-J., Du, G.-H., et al. 2024a, The Astrophysical Journal, 976, 1, doi: 10.3847/1538-4357/ad87f0

—. 2024b, Astrophys. J., 976, 1, doi: 10.3847/1538-4357/ad87f0

Li, X., Zhang, T., Sugiyama, S., & et. al. 2023, Phys. Rev. D, 108, 123518, doi: 10.1103/PhysRevD.108.123518

Liddle, A. R., & Scherrer, R. J. 1998, Phys. Rev. D, 59, 023509, doi: 10.1103/PhysRevD.59.023509

Linder, E. V. 2003, Phys. Rev. Lett., 90, 091301, doi: 10.1103/PhysRevLett.90.091301

—. 2006, Phys. Rev. D, 73, 063010, doi: 10.1103/PhysRevD.73.063010

—. 2015, Phys. Rev. D, 91, 063006, doi: 10.1103/PhysRevD.91.063006

—. 2024. https://arxiv.org/abs/2410.10981

Liu, X.-W., Heneka, C., & Amendola, L. 2020, Journal of Cosmology and Astroparticle Physics, 2020, 038, doi: 10.1088/1475-7516/2020/05/038

Liu, Y., Liao, S., Liu, X., et al. 2022, Monthly Notices of the Royal Astronomical Society, 511, 3076, doi: 10.1093/mnras/stac229

Lodha, K., et al. 2025a, Extended Dark Energy analysis using DESI DR2 BAO measurements. https://arxiv.org/abs/2503.14743

—. 2025b, Phys. Rev. D, 111, 023532, doi: 10.1103/PhysRevD.111.023532

—. 2025c. https://arxiv.org/abs/2503.14743

Louis, T., et al. 2017, Journal of Cosmology and Astroparticle Physics, 2017, 031, doi: 10.1088/1475-7516/2017/06/031

Lucca, M., & Hooper, D. C. 2020, Phys. Rev. D, 102, 123502, doi: 10.1103/PhysRevD.102.123502

Ludwick, K. J. 2017, Modern Physics Letters A, 32, 1730025, doi: 10.1142/S0217732317300257

MacCrann, N., Zuntz, J., Bridle, S., Jain, B., & Becker, M. R. 2015, Monthly Notices of the Royal Astronomical Society, 451, 2877, doi: 10.1093/mnras/stv1154

Mangano, G., Miele, G., Pastor, S., et al. 2005, Nucl. Phys. B, 729, 221, doi: 10.1016/j.nuclphysb.2005.09.041

Marsh, D. J. E., & Niemeyer, J. C. 2019, Phys. Rev. Lett., 123, 051103, doi: 10.1103/PhysRevLett.123.051103

Martin, J. 2012, Comptes Rendus Physique, 13, 566, doi: 10.1016/j.crhy.2012.04.008

Maxon, M. S., & Corman, E. G. 1967, Phys. Rev., 163, 156, doi: 10.1103/PhysRev.163.156

Maxon, S. 1972, Phys. Rev. A, 5, 1630, doi: 10.1103/PhysRevA.5.1630

Metropolis, N., Rosenbluth, A. W., Rosenbluth, M. N., Teller, A. H., & Teller, E. 1953, The Journal of Chemical Physics, 21, 1087, doi: 10.1063/1.1699114

Miller, C., Erickcek, A. L., & Murgia, R. 2019, Phys. Rev. D, 100, 123520, doi: 10.1103/PhysRevD.100.123520

Miralda-Escude, J. 2003, Science, 300, 1904, doi: 10.1126/science.1085325

Montero-Camacho, P., Fang, X., Vasquez, G., Silva, M., & Hirata, C. M. 2019, Journal of Cosmology and Astroparticle Physics, 2019, 031, doi: 10.1088/1475-7516/2019/08/031

Moss, I. G. 1994, Phys. Rev. D, 50, 676, doi: 10.1103/PhysRevD.50.676

Mukherjee, P., & Sen, A. A. 2024, Phys. Rev. D, 110, 123502, doi: 10.1103/PhysRevD.110.123502

Mukhopadhyay, U., Paul, A., & Majumdar, D. 2020, Eur. Phys. J. C, 80, 904, doi: 10.1140/epjc/s10052-020-08457-y

Murgia, R., Gariazzo, S., & Fornengo, N. 2016, Journal of Cosmology and Astroparticle Physics, 2016, 014, doi: 10.1088/1475-7516/2016/04/014

Murgia, R., Iršič, V., & Viel, M. 2018, Phys. Rev. D, 98, 083540, doi: 10.1103/PhysRevD.98.083540

Murgia, R., Merle, A., Viel, M., Totzauer, M., & Schneider, A. 2017, Journal of Cosmology and Astroparticle Physics, 2017, 046, doi: 10.1088/1475-7516/2017/11/046

Naidu, R. P., et al. 2022, The Astrophysical Journal Letters, 940, L14, doi: 10.3847/2041-8213/ac9b22

Natarajan, A., & Yoshida, N. 2014, PTEP, 2014, 06B112, doi: 10.1093/ptep/ptu067

Odintsov, S. D., Sáez-Chillón Gómez, D., & Sharov, G. S. 2025, Eur. Phys. J. C, 85, 298, doi: 10.1140/epjc/s10052-025-14013-3

Olivares, G., Atrio-Barandela, F., & Pavón, D. 2005, Physical Review D, 71. http://dx.doi.org/10.1103/PhysRevD.71.063523

Palanque-Delabrouille, N., Yèche, C., Schöneberg, N., et al. 2020, Journal of Cosmology and Astroparticle Physics, 2020, 038, doi: 10.1088/1475-7516/2020/04/038

Paliathanasis, A. 2020, Class. Quant. Grav., 37, 195014, doi: 10.1088/1361-6382/aba667

—. 2023a, Phys. Dark Univ., 42, 101275, doi: 10.1016/j.dark.2023.101275

—. 2023b, Fortsch. Phys., 71, 2300088, doi: 10.1002/prop.202300088

—. 2024, Annals Phys., 468, 169724, doi: 10.1016/j.aop.2024.169724

Pan, S., de Haro, J., Yang, W., & Amorós, J. 2020, Phys. Rev. D, 101, 123506, doi: 10.1103/PhysRevD.101.123506

Pandey, K. L., Karwal, T., & Das, S. 2020, Journal of Cosmology and Astroparticle Physics, 2020, 026, doi: 10.1088/1475-7516/2020/07/026

Pandey, K. L., & Mangalam, A. 2018, Journal of Astrophysics and Astronomy, 39, 9, doi: 10.1007/s12036-018-9513-x

Pani, P., & Loeb, A. 2014, Journal of Cosmology and Astroparticle Physics, 2014, 026, doi: 10.1088/1475-7516/2014/06/026

Parashari, P., & Laha, R. 2023, Monthly Notices of the Royal Astronomical Society: Letters, 526, L63, doi: 10.1093/mnrasl/slad107

Park, C.-G., de Cruz Perez, J., & Ratra, B. 2024a. https://arxiv.org/abs/2410.13627

Park, C.-G., de Cruz Pérez, J., & Ratra, B. 2024b, Phys. Rev. D, 110, 123533, doi: 10.1103/PhysRevD.110.123533

Park, C.-G., & Ratra, B. 2025. https://arxiv.org/abs/2501.03480

Parker, L., & Raval, A. 2000, Phys. Rev. D, 62, 083503, doi: 10.1103/PhysRevD.62.083503

Peccei, R. D. 2005, Physical Review D, 71. http://dx.doi.org/10.1103/PhysRevD.71.023527

Peebles, P. J. E. 1993, Principles of Physical Cosmology (Princeton University Press)

Penzias, A. A., & Wilson, R. W. 1965, *Astrophys. J.*, 142, 419, doi: 10.1086/148307

Pi, S., li Zhang, Y., Huang, Q.-G., & Sasaki, M. 2018, Journal of Cosmology and Astroparticle Physics, 2018, 042, doi: 10.1088/1475-7516/2018/05/042

Piedipalumbo, E., Vignolo, S., Feola, P., & Capozziello, S. 2023, Phys. Dark Univ., 42, 101274, doi: 10.1016/j.dark.2023.101274

Poulin, V., Boddy, K. K., Bird, S., & Kamionkowski, M. 2018, Phys. Rev. D, 97, 123504, doi: 10.1103/PhysRevD.97.123504

Poulin, V., Serpico, P. D., & Lesgourgues, J. 2016, Journal of Cosmology and Astroparticle Physics, 2016, 036, doi: 10.1088/1475-7516/2016/08/036

Press, W. H., & Schechter, P. 1974, *Astrophys. J.*, 187, 425, doi: 10.1086/152650

Profumo, S. 2017, An Introduction to Particle Dark Matter (World Scientific), doi: 10.1142/q0001

Ramadan, O. F., Sakstein, J., & Rubin, D. 2024, Phys. Rev. D, 110, L041303, doi: 10.1103/PhysRevD.110.L041303

Ratra, B., & Peebles, P. J. E. 1988, Phys. Rev. D, 37, 3406, doi: 10.1103/PhysRevD.37.3406

Rice, J. R., & Zhang, B. 2017, Journal of High Energy Astrophysics, 13, 22, doi: 10.1016/j.jheap.2017.02.002

Riess, A. G., Yuan, W., Macri, L. M., & et. al. 2022, The Astrophysical Journal Letters, 934, L7, doi: 10.3847/2041-8213/ac5c5b

Riess, A. G., et al. 1998, The Astronomical Journal, 116, 1009, doi: 10.1086/300499

Riotto, A. 1998, in ICTP Summer School in High-Energy Physics and Cosmology, 326–436. https://arxiv.org/abs/hep-ph/9807454

Robertson, H. P. 1935, *Astrophys. J.*, 82, 284, doi: 10.1086/143681

Rogers, K. K., & Poulin, V. 2023. https://arxiv.org/abs/2311.16377

Ross, A. J., Samushia, L., Howlett, C., & et. al. 2015a, Monthly Notices of the Royal Astronomical Society, 449, 835–847, doi: 10.1093/mnras/stv154

Ross, A. J., et al. 2015b, Monthly Notices of the Royal Astronomical Society, 449, 835, doi: 10.1093/mnras/stv154

Roy Choudhury, S. 2025, Astrophys. J. Lett., 986, L31, doi: 10.3847/2041-8213/ade1cc

Roy Choudhury, S., & Okumura, T. 2024, Astrophys. J. Lett., 976, L11, doi: 10.3847/2041-8213/ad8c26

Roy Choudhury, S., Okumura, T., & Umetsu, K. 2025, Astrophys. J. Lett., 994, L26, doi: 10.3847/2041-8213/ae1a64

Rubin, D., et al. 2025, Astrophys. J., 986, 231, doi: 10.3847/1538-4357/adc0a5

Rubin, V. C., & Ford, Jr., W. K. 1970, *Astrophys. J.*, 159, 379, doi: 10.1086/150317

S. Joudaki *et al.* . 2020, A&A, 638, L1, doi: 10.1051/0004-6361/201936154

Sabogal, M. A., Silva, E., Nunes, R. C., Kumar, S., & Di Valentino, E. 2025a, Phys. Rev. D, 111, 043531, doi: 10.1103/PhysRevD.111.043531

—. 2025b, Phys. Rev. D, 111, 043531, doi: 10.1103/PhysRevD.111.043531

Sabogal, M. A., Silva, E., Nunes, R. C., et al. 2024, Phys. Rev. D, 110, 123508, doi: 10.1103/PhysRevD.110.123508

Sakharov, A. D. 1991, Phys. Usp., 34, 392, doi: 10.1070/PU1991v034n05ABEH002497

Salucci, P. 2019, The Astronomy and Astrophysics Review, 27, 2, doi: 10.1007/s00159-018-0113-1

Sarkar, A., Das, S., & Sethi, S. K. 2015, JCAP, 03, 004, doi: 10.1088/1475-7516/2015/03/004

Sarkar, A., Mondal, R., Das, S., et al. 2016, JCAP, 04, 012, doi: 10.1088/1475-7516/2016/04/012

Sarkar, A., Sethi, S. K., & Das, S. 2017a, Journal of Cosmology and Astroparticle Physics, 2017, 012, doi: 10.1088/1475-7516/2017/07/012

—. 2017b, JCAP, 07, 012, doi: 10.1088/1475-7516/2017/07/012

Sasaki, M., Suyama, T., Tanaka, T., & Yokoyama, S. 2016, Phys. Rev. Lett., 117, 061101, doi: 10.1103/PhysRevLett.117.061101

—. 2018, Classical and Quantum Gravity, 35, 063001, doi: 10.1088/1361-6382/aaa7b4

Savastano, S., Amendola, L., Rubio, J., & Wetterich, C. 2019, Phys. Rev. D, 100, 083518, doi: 10.1103/PhysRevD.100.083518

Schaeffer, T., & Schneider, A. 2021, Monthly Notices of the Royal Astronomical Society, 504, 3773, doi: 10.1093/mnras/stab1116

Secco, L. F., Farah, A., Jain, B., & et. al. 2018, The Astrophysical Journal, 860, 32, doi: 10.3847/1538-4357/aac271

Semenaite, A., Sánchez, A. G., Pezzotta, A., & et. al. 2022, Monthly Notices of the Royal Astronomical Society, 512, 5657, doi: 10.1093/mnras/stac829

Sevilla-Noarbe, I., Bechtol, K., Carrasco Kind, M., & et. al. 2021, The Astrophysical Journal Supplement Series, 254, 24, doi: 10.3847/1538-4365/abeb66

Shah, P., Samanta, G. C., Bamba, K., & Myrzakulov, R. 2023, Int. J. Geom. Meth. Mod. Phys., 20, 2350042, doi: 10.1142/S0219887823500421

Shah, R., Mukherjee, P., & Pal, S. 2024, Mon. Not. Roy. Astron. Soc., 536, 2404, doi: 10.1093/mnras/stae2712

—. 2025a, Interacting dark sectors in light of DESI DR2. https://arxiv.org/abs/2503.21652

—. 2025b. https://arxiv.org/abs/2503.21652

Sharma, R. K., Pandey, K. L., & Das, S. 2022, The Astrophysical Journal, 934, 113, doi: 10.3847/1538-4357/ac7a33

Shlivko, D., & Steinhardt, P. J. 2024a, Phys. Lett. B, 855, 138826, doi: 10.1016/j.physletb.2024.138826

—. 2024b, Physics Letters B, 855, 138826, doi: https://doi.org/10.1016/j.physletb.2024.138826

Silva, E., Zúñiga Bolaño, U., Nunes, R. C., & Di Valentino, E. 2024. https://arxiv.org/abs/2403.19590

Singh, A., Pradhan, A., & Beesham, A. 2023, New Astron., 100, 101995, doi: 10.1016/j.newast.2022.101995

Smoot, G. F., Bennett, C. L., Kogut, A., et al. 1992, *Astrophys. J. Lett.*, 396, L1, doi: 10.1086/186504

Solbi, M., & Karami, K. 2021, The European Physical Journal C, 81, 884, doi: 10.1140/epjc/s10052-021-09690-9

Suzuki, N., Rubin, D., Lidman, C., et al. 2012, *Astrophys. J.*, 746, 85, doi: 10.1088/0004-637X/746/1/85

Tada, Y., & Terada, T. 2024, Phys. Rev. D, 109, L121305, doi: 10.1103/PhysRevD.109.L121305

Trodden, M. 1999, Rev. Mod. Phys., 71, 1463, doi: 10.1103/RevModPhys.71.1463

Trotta, R. 2008, Contemp. Phys., 49, 71, doi: 10.1080/00107510802066753

Tsujikawa, S. 2013a, Class. Quant. Grav., 30, 214003, doi: 10.1088/0264-9381/30/21/214003

—. 2013b, Classical and Quantum Gravity, 30, 214003, doi: 10.1088/0264-9381/30/21/214003

Tytler, D., O'Meara, J. M., Suzuki, N., & Lubin, D. 2000, Phys. Scripta T, 85, 12, doi: 10.1238/Physica.Topical.085a00012

van der Westhuizen, M. A., & Abebe, A. 2024, Journal of Cosmology and Astroparticle Physics, 2024, 048, doi: 10.1088/1475-7516/2024/01/048

Vattis, K., Koushiappas, S. M., & Loeb, A. 2019, Phys. Rev. D, 99, 121302, doi: 10.1103/PhysRevD.99.121302

Verde, L. 2007. https://arxiv.org/abs/0712.3028

Viel, M., Becker, G. D., Bolton, J. S., & Haehnelt, M. G. 2013a, Phys. Rev. D, 88, 043502, doi: 10.1103/PhysRevD.88.043502

—. 2013b, Phys. Rev. D, 88, 043502, doi: 10.1103/PhysRevD.88.043502

von Marttens, R., Borges, H. A., Carneiro, S., Alcaniz, J. S., & Zimdahl, W. 2020a, Eur. Phys. J. C, 80, 1110, doi: 10.1140/epjc/s10052-020-08682-5

von Marttens, R., Lombriser, L., Kunz, M., & et. al. 2020b, Physics of the Dark Universe, 28, 100490, doi: 10.1016/j.dark.2020.100490

Walker, A. G. 1937, Proceedings of the London Mathematical Society, s2-42, 90, doi: https://doi.org/10.1112/plms/s2-42.1.90

Wang, B., Abdalla, E., Atrio-Barandela, F., & Pavón, D. 2024, Reports on Progress in Physics, 87, 036901, doi: 10.1088/1361-6633/ad2527

Wang, H., & Piao, Y.-S. 2024. https://arxiv.org/abs/2404.18579

Wang, J., Hui, L., & Khoury, J. 2012, Phys. Rev. Lett., 109, 241301, doi: 10.1103/PhysRevLett.109.241301

Wang, M.-Y., Croft, R. A. C., Peter, A. H. G., Zentner, A. R., & Purcell, C. W. 2013, Phys. Rev. D, 88, 123515, doi: 10.1103/PhysRevD.88.123515

Wei, H., & Cai, R.-G. 2005, Phys. Rev. D, 71, 043504, doi: 10.1103/PhysRevD.71.043504

Weinberg, S. 1989, Rev. Mod. Phys., 61, 1, doi: 10.1103/RevModPhys.61.1

Wetterich, C. 1988, Nuclear Physics B, 302, 668, doi: https://doi.org/10.1016/0550-3213(88)90193-9

Wetterich, C. 1995, Astronomy & Astrophysics, 301, 321, doi: 10.48550/arXiv.hep-th/9408025

Widerin, P., & Schmid, C. 1998, arXiv e-prints, astro. https://arxiv.org/abs/astro-ph/9808142

Will, C. M. 2001, Living Reviews in Relativity, 4. http://dx.doi.org/10.12942/lrr-2001-4

Wolf, W. J., Ferreira, P. G., & García-García, C. 2025a, Phys. Rev. D, 111, L041303, doi: 10.1103/PhysRevD.111.L041303

Wolf, W. J., García-García, C., Bartlett, D. J., & Ferreira, P. G. 2024a, Phys. Rev. D, 110, 083528, doi: 10.1103/PhysRevD.110.083528

Wolf, W. J., García-García, C., Bartlett, D. J., & Ferreira, P. G. 2024b, Phys. Rev. D, 110, 083528, doi: 10.1103/PhysRevD.110.083528

Wolf, W. J., García-García, C., & Ferreira, P. G. 2025b. https://arxiv.org/abs/2502.04929

Wright, A. H., et al. 2025, Astron. Astrophys., 703, A158, doi: 10.1051/0004-6361/202554908

Wu, P.-J. 2025, Phys. Rev. D, 112, 043527, doi: 10.1103/mcgb-ntwr

Yang, W., Pan, S., Nunes, R. C., & Mota, D. F. 2020, Journal of Cosmology and Astroparticle Physics, 2020, 008, doi: 10.1088/1475-7516/2020/04/008

Yang, Y., Wang, Q., Li, C., et al. 2025. https://arxiv.org/abs/2501.18336

Ye, G., Martinelli, M., Hu, B., & Silvestri, A. 2024. https://arxiv.org/abs/2407.15832

Yin, W. 2022, Phys. Rev. D, 106, 055014, doi: 10.1103/PhysRevD.106.055014

—. 2024, JHEP, 05, 327, doi: 10.1007/JHEP05(2024)327

Zaroubi, S. 2013, in Astrophysics and Space Science Library, Vol. 396, The First Galaxies, ed. T. Wiklind, B. Mobasher, & V. Bromm, 45, doi: 10.1007/978-3-642-32362-1_2

Zel'dovich, Y. B., & Novikov, I. D. 1967, *Soviet Astron.*, 10, 602

Zhang, H.-C. 2022. https://arxiv.org/abs/2210.10204

Zhao, C., Variu, A., He, M., et al. 2022, *Mon. Not. Roy. Astron. Soc.*, 511, 5492, doi: 10.1093/mnras/stac390

Zlatev, I., Wang, L., & Steinhardt, P. J. 1999, Phys. Rev. Lett., 82, 896, doi: 10.1103/PhysRevLett.82.896

Štefančić, H. 2004, The European Physical Journal C, 36, 523–527, doi: 10.1140/epjc/s2004-01970-6